Scanning Tunnelling Microscopy of Epitaxial Nanomaterials on $SrTiO_3$



Yakun Gao

Lincoln College

University of Oxford

A thesis submitted for the degree of

Doctor of Philosophy

Trinity Term 2017

Abstract

This thesis focuses on the study of epitaxial nanomaterials grown on $SrTiO_3$ substrates including their morphologies, their epitaxial relationship, the energetics of equilibrium crystals and the interactions with the substrates.

The formation of ordered TiO_x-rich dilines on the $SrTiO_3(001)$ surface was achieved following UHV annealing of sputtered surfaces. Upon extensive UHV annealing, leading to a significant TiO_x surface enrichment, anatase $TiO_2(001)$ islands are nucleated on nanostructured $SrTiO_3(001)$. These (1×4) and (1×3) reconstructed islands are strained on the $SrTiO_3(001)$. Further Ti deposition encourages islands growth into a film with a relaxed (1×4) reconstruction. Both the dilines and the anatase film present close-packed rows aligning in the <100> direction and are suitable to study the epitaxially-grown Pd nanocrystals.

Elongated Pd nanocrystals are formed at a low temperature and grow towards to an equilibrium hexagonal shape upon high temperature anneal. The adhesion energies are calculated to be 2.55 ± 0.09 J/m^2 and 2.05 ± 0.05 J/m^2 for Pd-dilines and Pd-anatase systems respectively. High temperature anneals (above 600°C) bring Pd-diline and Pd-anatase systems into the SMSI state, along with the formation of (7×7) wagon wheel and $(4 \times 4)R1.5°$ hexagonal superstructures attributed to moiré patterns. These moiré patterns are successfully interpreted by atomic models, via superposition of Ti layer on Pd(111). The moiré dots, resolved by STM at an atomic level, indicate seven-Ti atoms units in two configurations. Encapsulation of Pd nanocrystals by a TiO_x layer can reduce the surface energy by 0.35 ± 0.19 J/m^2 for the dominant (111) facets from 1.64 J/m^2 for bare Pd nanocrystals to 1.29 ± 0.19 J/m^2 for encapsulated Pd nanocrystals supported on anatase.

Depending on the crystallographic interface of MoS_2 with the $SrTiO_3$ substrate, two shapes can be created: a regular triangle ($MoS_2(0001) \| SrTiO_3(111)$) and a right-angled triangle ($MoS_2(0001) \| SrTiO_3(001)$). MoS_2 crystals grown on the symmetry-disparate (001) surface are more strained, as evidenced by the red-shift of the A peak in photoluminescence spectra and the softening of the E^1_{2g} mode in Raman spectra.

These findings provide an understanding of how epitaxy is achieved on $SrTiO_3$ surfaces and of the interactions between these heterogeneous structures. This opens up a platform for the growth of tailored nanomaterials for electronics and catalysis applications.

Preface

The work reported in this thesis is original work that was carried out by the author, unless indicated otherwise, from October 2013 to September 2017, under the supervision of Prof. M. R. Castell, in the Department of Materials at the University of Oxford. Some of the work contained in this thesis has been presented at scientific conferences and is in preparation for scientific journal submission. These include:

Oral presentation:

- The International Functional Oxide Surfaces and Interfaces (FOXSI) Conference (2016) - Vienna, Austria.

Poster presentations:

- 13th European Conference on Surface Crystallography and Dynamics (ECSCD-13) (2017) - Donostia-San Sebastián, Spain.
- COST CM1104 Final Meeting (2016) - Osnabrück, Germany.
- Studying Surfaces: in vacuo, in situ, in silico Meeting (2016) - London, UK.
- 3rd ICSOS Workshop on Surface Structures (2015) – Łódź, Poland.
- Imaging Surfaces Meeting (2015) - London, UK.

Acknowledgement

First and foremost, I would like to thank my supervisor, Professor Martin R. Castell, who brought me into the microscopic world to investigate the structures down to the nanometre scale. I also want to express my appreciation for his patience on spending many hours on meetings with me and discussing the work. He always encouraged me to explore the insight of the research and motivate me to solve the problem from different aspects. I am also thankful to Martin for suggesting me to attend several international scientific conferences in Germany, Latvia, Austria and Poland. This allowed me to share my research ideas with other researchers around the world and spark inspirations on my research projects.

Working with a group of people during my DPhil is an invaluable experience for me. I would like to say thank you to my colleagues in the research group, Shams ur Rahman for training me on using UHV-STM, Xiao Hu for teaching me how to make tips and going to several conferences together, and Shuqiu Wang for her advice on making images better using the SmartAlign software. It was a pleasant time to work with Peiyu Chen on MoS_2 project together during my fourth year when we had shared the knowledge and made progress. Thank you also to my officemate Merel Lefferts for a great working atmosphere in the office and an unforgettable time having sandwiches in the University Park. Other colleagues during my time in the STM group have been a pleasure to work with: Chen Wu, Krishnan Murugappan, Aatif Rasheed, Ben Armitage and Fubiao Gu, and thanks for their peer support. I appreciate our engineer Chris Spencer for the technical assistance and solutions for any difficult situation that happened to me while I am using STM.

I would like to thank the administrative and technical support staffs from our department: the kind supports from Marion Beckett and Adrian Taylor from Department Graduate Office, and Paul Warren, Chris Akinola and Robert Saunders from Department IT Serve for saving my PC.

Great thanks to my College, Lincoln College, which provided a great social and comfortable living environment and has supported several conferences I have attended. I would also like to thank Chinese Scholarship Council for the generous funding which supported me to fulfil my DPhil research without the burden.

Many thanks to my friends no matter how long we have met, who made my life in Oxford spectacular: Yeli Guma, Qingji Shen and Jingyi Ma, we spent lots of fantastic time together; a group of friends, Yudong Liu, Binxin Ru, Cheng Chen, Xin Liu, Zhixin Zeng and others from OXCSSA, we brainstormed many interesting activities and have achieved lots of meaningful and amazing thing together; Yue Zhang, Shixiang Zhao, Rui Guo, Shen Xiang and Junan Jiang since five of us came to UK together, studied in the University of Birmingham and continued to study or work in UK until now; and friends from Lincoln College, we watched scary movies and spent some fantastic time hiking and camping to explore beautiful sceneries in UK. I should not forget to say thank you to my childhood friends: Zhen Hu, Jiarui Wang, Yuqiong Wang, Jin Chen, for sending their best wishes far away from China.

Last but not least, I would like to thank my boyfriend Zhu Li who stands by my side, giving me confidence and encouragement, and shares happiness and sorrows. My families, Mom and Dad, who trust me I can do better and support me for the study abroad through the years. My cousins, uncles and aunts for encouraging me. My grandmothers, while they are no longer here, I am sure they would be happy to see me complete the DPhil at the University of Oxford.

Contents

1 Introduction 1
1.1 Background 1
1.2 Outline of the Thesis 4
2 Experimental Techniques 6
2.1 Introduction 6
2.2 Scanning Tunnelling Microscopy (STM) 7
2.2.1 History of STM 7
2.2.2 Principle of STM 8
2.2.3 Custom-built UHV-STM 11
2.3 Methods and Procedures 13
2.3.1 Sample preparation 13
2.3.2 Sputtering 15
2.3.3 Tip making 17
2.3.4 STM imaging 20
2.3.5 STM calibration 24
2.3.6 STM system baking 26
2.3.7 Metal deposition 28
2.3.8 Photoluminescence spectroscopy (PL) 29
2.3.9 Raman spectroscopy 30
2.3.10 Scanning electron microscopy (SEM) 32
2.4 Summary 33
3 Literature Review 34
3.1 Introduction 34
3.2 Metal Oxides and Perovskites 34
3.2.1 Metal oxides 34
3.2.2 Perovskite structures, ideal (001) and (111) surfaces 35
3.3 Reconstructions and Surface Nanostructures 39
3.3.1 Surface unit cell and notation 39
3.3.2 Surface relaxation and reconstruction 41
3.4 Properties of Nanostructures and Surfaces 44
3.4.1 Catalytic property 46
3.4.2 Optical property 47
3.5 The Surface Structures of $SrTiO_3$, Nanostructures, Anatase and Properties 48
3.5.1 Introduction to $SrTiO_3$ 48
3.5.2 Reconstructions on $SrTiO_3$(001) and (111) surfaces 49
3.5.3 Nanostructures on $SrTiO_3$(001) surface 62
3.5.4 Anatase on $SrTiO_3$(001) surface 67
3.6 Metal Nanocrystals on $SrTiO_3$ and Anatase 73

3.6.1 Theory of nanocrystal formation 73
3.6.2 Strong metal-support interaction (SMSI) 75
3.6.3 Metal nanocrystals on $SrTiO_3$ 78
3.6.4 Metals on anatase 84
3.7 The Surface of Transition Metal Dichalcogenides (TMDs) 88
3.7.1 Introduction to TMDs and monolayer TMDs 88
3.7.2 Characterisations and properties of monolayer MoS_2 92
3.8 Summary 104
3.9 Research Objectives 105
3.9.1 Nucleation and growth of anatase TiO_2(001) on the $SrTiO_3$(001) substrate 105
3.9.2 Characterisation of Pd on anatase grown on $SrTiO_3$(001) 106
3.9.3 Effect of substrate structures on the growth of monolayer MoS_2 106
4 Nucleation and Growth of Anatase TiO_2(001) on $SrTiO_3$(001) Substrates 108
4.1 Introduction 108
4.2 Experimental Methods 109
4.3 Results 109
4.3.1 Nucleation of anatase islands 109
4.3.2 Growth of anatase islands 112
4.3.3 Anatase (1 × 3) nanostructures 120
4.4 Discussion 124
4.4.1 Formation of anatase TiO_2 on $SrTiO_3$ 124
4.4.2 Formation of anatase TiO_2-(1 × 3) nanostructure 127
4.5 Conclusion 129
5 Growth of Pd on Ordered Diline-(6 × 2) Substrates 131
5.1 Introduction 131
5.2 Experimental methods 132
5.3 Results 133
5.3.1 Diline-terminated $SrTiO_3$(001) surfaces 133
5.3.2 Growth of Pd nanocrystals on dilines substrates 134
5.3.3 Size distributions of Pd nanocrystals 136
5.4 Discussion 141
5.4.1 Growth of elongated Pd nanocrystals 141
5.4.2 Adhesion energy of Pd nanocrystals on dilines 146
5.5 Conclusion 149
6 Growth of Pd on Anatase Substrates 150
6.1 Introduction 150
6.2 Experimental Methods 151
6.3 Results 152
6.3.1 Shapes and size distributions of Pd 152

6.3.2 Height-to-width (*h*/*w*) ratio of Pd nanocrystals 160
6.4 Discussion 165
6.4.1 Adhesion energy of Pd nanocrystals on anatase 165
6.4.2 Comparison of surface energies between bare and encapsulated Pd nanocrystals 166
6.5 Conclusion 170
7 Encapsulation of Pd on Dilines and Anatase Substrates 171
7.1 Introduction 171
7.2 Experimental method 172
7.3 Results 173
7.3.1 Encapsulation of Pd nanocrystals supported on dilines 173
7.3.2 Encapsulation of Pd nanocrystals supported on anatase 177
7.3.3 Encapsulation of Pd islands supported on anatase 178
7.4 Discussion 184
7.4.1 Stacking sequence of encapsulated layer on Pd(111) 184
7.4.2 Atomic models of the superstructures and moiré patterns 185
7.5 Conclusion 198
8 Growth of MoS_2 on $SrTiO_3$ Substrates 199
8.1 Introduction 199
8.2 Experimental Methods 200
8.3 Results 202
8.3.1 MoS_2 on $SrTiO_3$(111) substrate 202
8.3.2 MoS_2 on $SrTiO_3$(001) substrate 209
8.3.3 Comparison between (111) and (001) substrates 215
8.4 Discussion 216
8.5 Conclusion 219
9 Conclusions 221
9.1 Overview 221
9.2 Anatase Nanostructures and Film 222
9.3 Epitaxial Pd Nanocrystals 223
9.4 Epitaxial Monolayer MoS_2 crystals 225
9.5 Future work 226
References 228

Chapter 1

Introduction

1.1 Background

$SrTiO_3$ is a typical perovskite and is part of the metal oxides group, which has garnered much research interest in the last few decades. Surfaces of $SrTiO_3$ have been studied since 1970, when the initial interests were focused on surface defects in the catalytic reaction [1]. The outstanding properties of $SrTiO_3$ such as tuneable dielectric properties [2,3], electric conductivity by doping [4] and photocatalytic properties [5] have driven it to a wide variety of applications such as photonics devices [6], gas sensors [7], grain boundary barrier layer capacitors [8], thermoelectric materials [9] and photocatalysts [5]. It has been recognised that the surface structures and compositions of $SrTiO_3$ play a decisive role in its performance in these applications. Meanwhile, as one of the typical perovskites, understanding the surface structures and properties of $SrTiO_3$ will benefit the study of other oxide surfaces.

Growth of self-assembled arrays of nano-sized structures is crucial in developing novel electronic devices. $SrTiO_3$ has been widely used as a substrate for growth of superconducting thin films [10]. This encourages researchers to fully explore the functionality of employing $SrTiO_3$ as a substrate for the growth of other materials. Many studies have reported the formation of epitaxially ordered nanostructures, that remain stable at room temperature, such as nanolines and nanodots, on $SrTiO_3$ surfaces [11-14]. It is

suggested that if the nanolines are found to be electrically conducting, they can be potentially used as nanowires. If they are insulating, the patterned surfaces can be used as templates for the growth of self-assembled molecular, semiconducting or metallic structures [11]. It was also shown by Auger spectroscopy (AES) that these nanolines are TiO_x-rich [12], suggesting Ti atoms are able to segregate at the surface and form titanium oxides or even TiO_2 if the proper surface treatment is conducted.

Titanium oxides are significantly important in the environmental and energy-related field. The physicochemical properties such as adsorption, catalytic reactivity and selectivity are determined by both surface atomic configurations and level of exposure of reactive crystal surfaces [15,16]. Anatase TiO_2 is believed to be more catalytically active than the other two polymorphs in the photocatalytic production of hydrogen from water [17-19]. The anatase TiO_2(001) surface is more reactive than its thermodynamically stable (101) surface [20]. However, the higher surface energy makes it difficult to produce stable large-area (001) surfaces. Epitaxial growth methods on suitable substrates are considered an effective method to produce high-quality and stable anatase TiO_2(001) single crystals with a large surface of exposure. Owing to the small lattice mismatch of 3.3%, a self-assembly epitaxial growth method has recently been established by our research group to produce anatase TiO_2-(1 × 4) islands on $SrTiO_3$(001) substrates [21,22].

Oxide-supported metal nanocrystals have become functionally important in catalysis applications [17,23-25] . For instance, loading noble metal nanoparticles (e.g., Au, Ag, Pt and Pd) on TiO_2 supported substrates could help to obtain higher catalytic efficiencies by inhibiting the charge recombination process [26]. Their catalytic properties can be improved by modification of the morphology of metal nanocrystals [27]. This thesis presents the study of epitaxial Pd nanocrystals on titanium oxide supports. The rationale behind this work arises from the prevalent use of Pd nanocrystals as catalysts, whose

catalytic activity is sensitive to the nanocrystal shape. Therefore, understanding the compositions, morphologies and locations of metal Pd nanocrystals grown on ordered titanium oxide supports (e.g., dilines and anatase) plays a vital role in the shape control, which could further optimise catalytic performance in the metal-oxide heterogeneous-catalyst system.

Meanwhile, many studies found that the catalytic activity of noble metal-oxide system such as Pd and Pt on titanium supports is significantly influenced by high temperature treatments, when they enter the strong metal support interaction (SMSI) state [28-36]. It is also important to understand the fundamental interaction between the metallic particles and the oxide supports. This thesis reports results from study of SMSI in the Pd-system at atomic scale, especially the top surface layer, to understand the atomic arrangement that is the most dominant region where the catalytic reaction occurs. This could potentially improve an understanding of the origin of the selectivity of the catalytic reaction for the heterogeneous catalysts in the SMSI state.

$SrTiO_3$ is a versatile substrate which can accommodate a wide range of surface reconstructions with different stoichiometry and unit cell structures on (001) and (111) surfaces [37-42]. These surfaces are atomically flat with long range order which enables the growth of uniform and flat overlayers, such as 2D materials for the heterogeneous structures.

1.2 Outline of the Thesis

This thesis has focused on understanding of the TiO_x nanostructures e.g., dilines and anatase TiO_2(001) on $SrTiO_3$(001) substrates, the epitaxial and encapsulated Pd nanocrystals on dilines and anatase, the epitaxial relationship of monolayer MoS_2 crystals grown on a $SrTiO_3$ single crystal terminated with (111) and (001) surfaces. An outline of the thesis follows below.

Chapter 2 introduces the main experimental techniques applied in this thesis to characterise the surface structures (by scanning tunnelling microscopy (STM) and scanning electron microscopy (SEM)) and properties (by photoluminescence (PL) and Raman Spectroscopy) of the nanomaterials. As most of the work in this thesis has been carried out using ultra-high vacuum (UHV) STM, the operation principle and methods, introduction of the equipment and calibration methods are also described. This is followed with a general description of the experimental procedure including sample preparation, sputtering, tip making and metal deposition.

An introduction of the perovskite, surface relaxation and reconstruction and nanostructure properties is provided in the beginning of Chapter 3. Previous published work in related fields is reviewed. This includes surface reconstructions and nanostructures formed on $SrTiO_3$, properties and growth methods of TiO_2 especially in its anatase phase, and noble metals grown on TiO_2 and $SrTiO_3$ substrates along with strong-metal-support-interaction (SMSI) in this system. Next, the current research progress in understanding physical properties and characterisation methods of monolayer MoS_2 is presented. The research objectives are outlined at the end of this chapter.

From Chapter 4 onwards, the original work is presented. Chapter 4 reports the formation of anatase TiO_2(001) with (1 × 3) nanostructure and (1 × 4) film on the nanostructured

$SrTiO_3$(001) substrate using the self-assembly epitaxial growth method. The well-ordered anatase (1 × 4) thin film is used as the substrate to grow Pd nanocrystals in Chapter 6 and Chapter 7.

In Chapter 5, the epitaxially-grown Pd nanocrystals on ordered (6 × 2) dilines are studied. This includes the change of shapes and sizes of Pd nanocrystals grown at different temperatures, as well as the calculation of adhesion energy in this system.

Chapter 6 presents the study of the epitaxially-grown Pd nanocrystals on anatase substrates. It concerns the shape and size distributions, especially the height-to-width (*h/w*) ratio of Pd nanocrystals grown at different temperatures. The adhesion energy in the Pd-anatase system is included. This chapter also involves the comparison between bare and encapsulated Pd nanocrystals regarding the calculation of surface energy change.

Chapter 7 reports the characterisation of encapsulated Pd nanocrystals supported on dilines and anatase substrates. A (7 × 7) wagon wheel and a (4 × 4)*R*1.5° hexagonal superstructure are formed on the encapsulated Pd, which is attributed to moiré patterns. The atomic models are built to interpret the formation of these two moiré patterns.

Chapter 8, which is the final experimental results chapter, reports the study of the monolayer MoS_2 grown on $SrTiO_3$(111) and (001) substrates with different lattice symmetries. The morphologies and properties of MoS_2 crystals of the two systems are compared using STM, SEM, Raman and PL.

A summary of the work presented in this thesis is provided in Chapter 9 along with the conclusions. The work in this thesis focuses on the study of epitaxial nanomaterials grown on $SrTiO_3$ surfaces and provides the fundamental understanding of the SMSI at the atomic scale. The scope of the future work is depicted by further explorations of the formation mechanism and how to functionalise these nanomaterials are also discussed in final chapter.

Chapter 2

Experimental Techniques

2.1 Introduction

The invention of the microscope enabled us to explore the world which cannot be seen by the bare eyes. The resolution of different types of microscopes influences the object sizes which can be observed. Fig. 2.1 presents the size resolving range of human eyes, optical microscopes and electron microscopes. In general, the smallest objects the naked eyes can see are in the range of 10^{-4} m. In order to study smaller objects in detail, various techniques have been invented which allow to us resolve objects from the millimetre down to the nanometre scale. Optical microscope uses visible light to observe the objects. However, the wavelength of the visible light (400∼700 nm) limits the resolution of the optical microscope to a resolution size in the range of 10^{-6} m. Electron microscope applies an electron beam source instead of light. It works under the mechanism of the electron-sample interaction in the form of scattering for scanning electron microscope [43] and transmission electron microscope [44]. The electron beam has smaller wavelength compared to light (3.88 to 2.24 pm at accelerating voltage from 100 to 300 keV). The sufficiently small wavelength of the electron beam enables to resolve the objects with sizes from 10^{-10} m to 10^{-5} m. Sophisticated analytical tools can also be applied to study even smaller objects in the nanoscale range. Currently, scanning tunnelling microscope (STM) is one of the most powerful tools to characterise surface in atomic scale and provide topographical and

electronic information. The imaging process relies on the electron tunnelling in the quantum mechanical condition and detailed operation principle of STM is described in the Sec. 2.2.2.

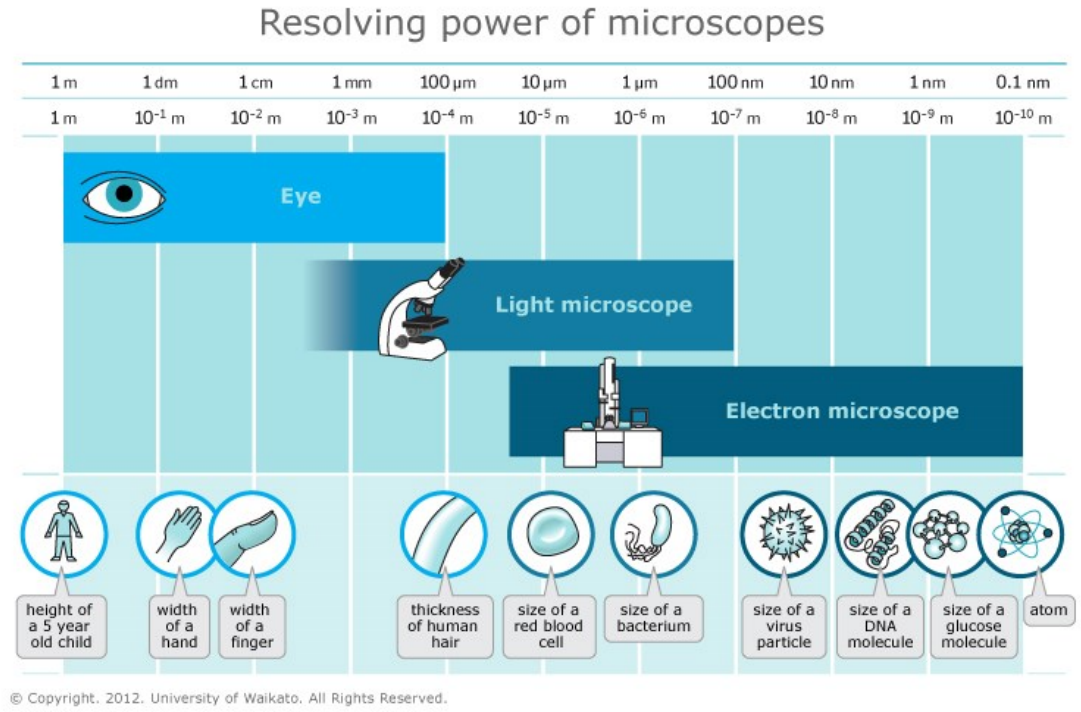


Fig. 2.1 Comparison of the resolving sizes of human eyes, light microscope and electron microscope (taken from Ref. [45]).

2.2 Scanning Tunnelling Microscopy (STM)

2.2.1 History of STM

The scanning tunnelling microscope (STM) wasinvented by Gerd Binnig and Heinrich Rohrer in the IBM Zurich Research Laboratories in 1981 [46], who were awarded the Nobel Prize in Physics in 1986. The invention of STM achieves the significance in directly applying quantum mechanics theory to practical work, which brings a new era of studying surface nanoscience and technology. It shows the capability to image and manipulate individual atoms and molecules on the surface in the nanoscale.

To meet the different demands of surface analysis, STM equipment has been improved to operate in different environment such as UHV, atmosphere, liquid and gas. Besides, heating and cooling systems are also applied in STM to enable hot or cold imaging. STM is a very delicate equipment and sensitive to vibrations. Various designs for vibration isolation systems and specimen stage (e.g., arrangement of tip and sample position) have been applied to reduce the vibration and drift during the imaging process. Other surface analysis techniques such as Low energy electron diffraction (LEED), X-ray photoelectron spectroscopy (XPS) and Auger electron spectroscopy (AES) can also be installed alongside STM to make the whole surface analysis system more versatile and enable in-situ study of surface structures.

2.2.2 Principle of STM

STM is operated by scanning a conductive sample surface with a sharp metallic tip. It works by using the principle of quantum mechanics of electron tunnelling. Tunnelling happens when the gap between the tip and sample is in the order of a few angstroms (Å) (10^{-10} m) wide. The electrons in the tip can tunnel to the sample surface and vice versa.

As shown in Fig. 2.2a, when the sample and the tip are separated by a macroscopic distance, they are two independent systems where both electron energy in the vacuum near by the surface (E_{vac}) are the same. E_{vac} is a reference energy level. The Fermi energy describes the upper limit of the filled state of the materials. The tip and sample have their individual Fermi energies (E_{Fs} and E_{Ft}). The Work function is the minimum energy required to move an electron from the bulk into the vacuum ($\phi = E_{vac} - E_F$). The electron wave functions of tip present the exponential decay from the surface to the gap and no electrons can travel between two materials. As the separation between the tip and the sample is narrowed to the

order of a few Å (10^{-10} m), electrons can tunnel through the gap from high energy level material to the lower one. These tunnelling electrons fill in the empty state of the material with lower energy level. This process leads to the thermodynamically equilibrium condition which the Fermi energy of these two materials are equal ($E_{Fs} = E_{Ft}$) (Fig. 2.2b).

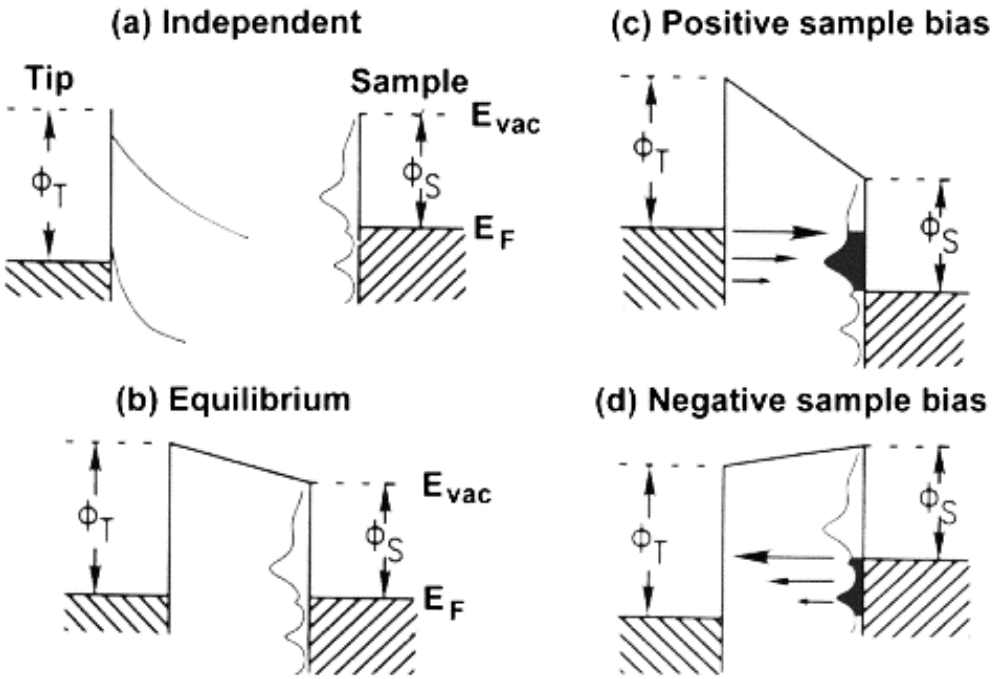


Fig. 2.2 Energy band diagrams for the STM tip and the sample. (a) The tip and the sample are separated by a macroscopic distance and are two independent systems. The vacuum energy of them are considered to be the same. (b) Narrowing the vacuum gap between the tip and the sample causes the electron tunnelling effect. The whole system has reached the equilibrium condition and have equalisation of Fermi energy. (c) Applying positive sample bias leads to the electron tunnelling from the filled state of the tip to the empty state of the sample. (d) Applying a negative sample bias leads to the electron tunnelling from the filled state of the sample to the empty state of the tip (taken from Ref. [47]).

Tunnelling current is generated when the bias is applied between the sample and the tip. The bias is usually applied on the sample and the tip is grounded. The bias applied on the sample causes the relative shift in Fermi energy of sample to the tip. The tunnelling electrons are those which energy states are located between the Fermi energy of tip and sample. If the sample is applied with the positive bias, its Fermi energy shifts down by the

amount of | eV | with respect to the tip. This allows the tunnelling electrons to access the empty electron states in the sample. The electrons will transfer from the filled state of the tip to the empty state of the sample (Fig. 2.2c). If the sample is negatively biased, the relative Fermi energy of the sample rises up by the value of | eV | . The electrons will tunnel from the filled state of the sample to the empty state of the tip (Fig. 2.2d).

The tunnelling current is determined by several parameters and can be described in the following relation according to Tersoff and Hamann Theory [47-49]:

$$I_t \propto V\rho_s\rho_t e^{-2\kappa d} \tag{2.1}$$

Where $\kappa = \sqrt{2m\phi}/\hbar$ for low bias voltages

Where I_t is the tunnelling current, V is the voltage applied between the sample and the tip, ϕ is the work function, ρ_s is the density of states of the sample, ρ_t is the density of states of the tip, κ is the decay constant and related to the inverse decay length for the wave functions in vacuum, d is the distance between the sample and the tip.

This shows that the tunnelling current decays exponentially with the sample-tip distance, proportionally to local densities of states and proportionally to the bias voltage. The inverse exponential relationship between the tip-sample separations illustrates that a slight change of the separation will produce a huge difference in tunnelling current. The closer they are, the higher the tunnelling current density is. The closest distance between the tip and the sample surface is at the apex atom of the tip which tunnels the majority of the electrons.

Two operation modes i.e., constant height mode and constant current mode can be applied for STM imaging. Constant height mode (Fig. 2.3a) operates as the tip is scanning over the sample surface at the same plane. It produces the tunnelling current as a function of the distance X and Y on the sample surface. Because the sample surface could be rough, using

constant height scanning mode may risk crashing the tip and damaging the sample surface. Constant current mode is widely used as it can operate over a larger distance in the vertical direction (Z-axis) than the constant height mode. As for constant current mode (Fig. 2.3b), the tunnelling current is set as a constant value. The tip adjusts its height during scanning to maintain the constant tunnelling current (I_t). The equilibrium Z position is adjusted by the voltage induced shape transformation of the Z-piezo. The contour of the equilibrium Z position gives the trace of the surface having the same tunnelling current i.e., outputs the height as the function of the X and Y. By measuring the variation of the height, it constructs a 3D mapping of the atomic corrugation of the surface which gives the topographic information of the sample.

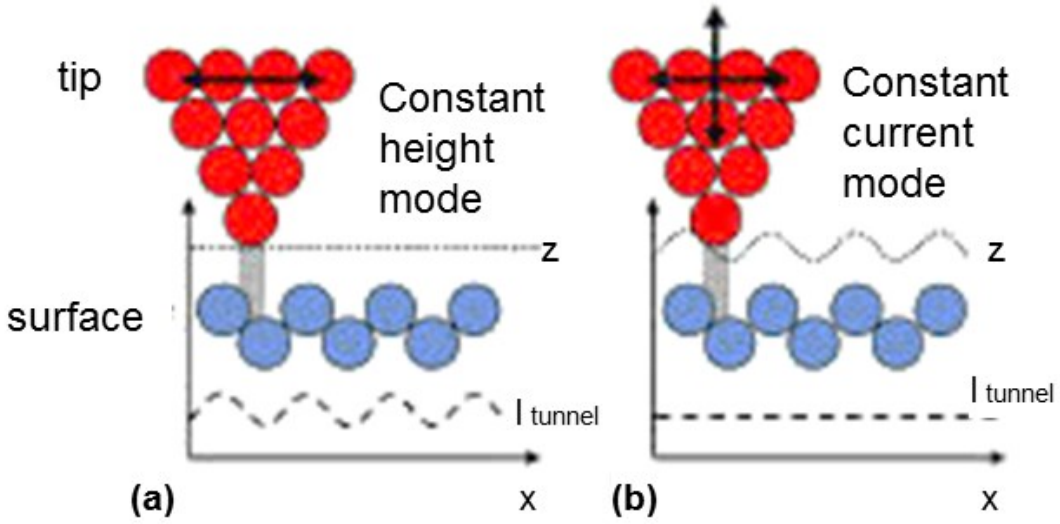


Fig. 2.3 Diagram shows two STM imaging modes: (a) Constant height mode which the distance between the tip and sample keeps constant. (b) Constant current mode which the tunnelling current keeps constant during the imaging (taken from Ref. [50]).

2.2.3 Custom-built UHV-STM

The JSPM-4500S is used in this experiment. It is specially designed for the UHV environment to maintain the cleanness of the sample. Because STM is a superficial surface

analysis technique, it is desirable for the sample surface to be free of contamination in order to obtain the high resolution STM images for surface study. The custom-built UHV-STM used in this thesis is shown in Fig. 2.4.

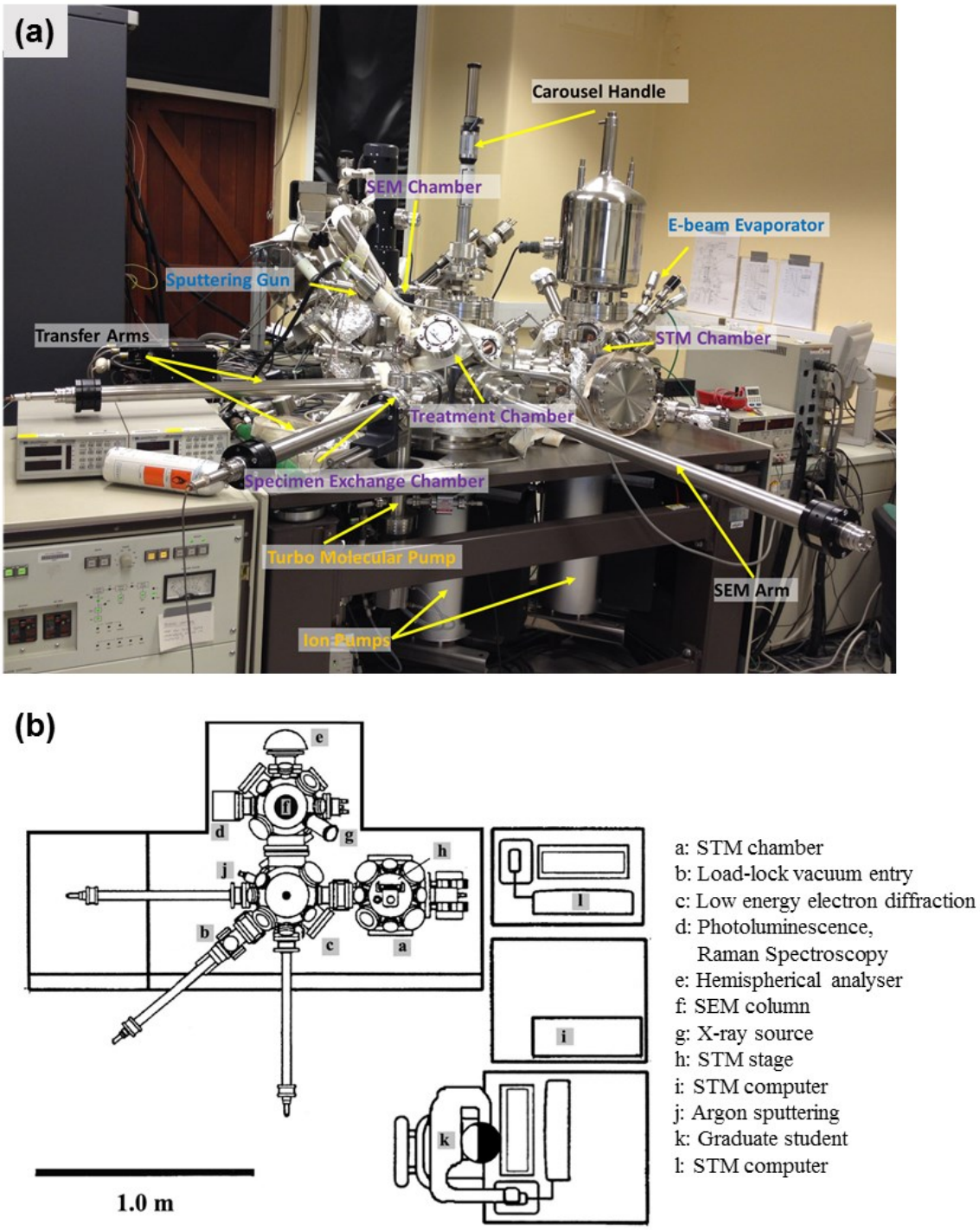


Fig. 2.4 (a) Photo of custom-built ultra-high vacuum scanning tunnelling microscope (UHV-STM), Model JEOL JSTM-4500s system designed by Japanese Electron Optics Laboratories (JEOL). (b) Schematic diagram of JEOL-4500s microscope (taken from Ref. [51]).

There are two main chambers which are treatment chamber and the STM chamber. The sample is transferred by the transport mechanics from specimen exchange chamber to treatment chamber for sample preparation (degassing, sputtering and annealing), and to the STM chamber for imaging. The Turbo-molecular Pump (TMP) is located below the specimen exchange chamber to keep the pressure into the 10^{-5} Pa range or lower. The vacuum condition in both the treatment chamber and the STM chamber are maintained by ion pumps located below the main console table. They maintain the pressure in both chambers in the range of 10^{-8} Pa or less. An e-beam evaporator is attached to the STM chamber for metal deposition.

2.3 Methods and Procedures

2.3.1 Sample preparation

Single crystal epipolished $SrTiO_3$(001) and $SrTiO_3$(111) with 0.5 wt% Nb doping provided by PI-KEM Ltd., UK are used in this experiment. The sample size is 7.0 × 2.0 × 0.5 mm. Pure stoichiometric $SrTiO_3$ sample is a good insulator with a band gap of about 3.2 eV at room temperature. Slightly doping $SrTiO_3$ with an electron donor Nb changes it from insulator to n-type semiconductor. Modification of the sample conductivity enables the surface preparation and experimental analysis by STM. Samples are ultrasonically cleaned in acetone and methanol separately for three minutes, dried with air duster and then mounted on the sample holder. Heating sample holder is used in this experiment (Fig. 2.5).

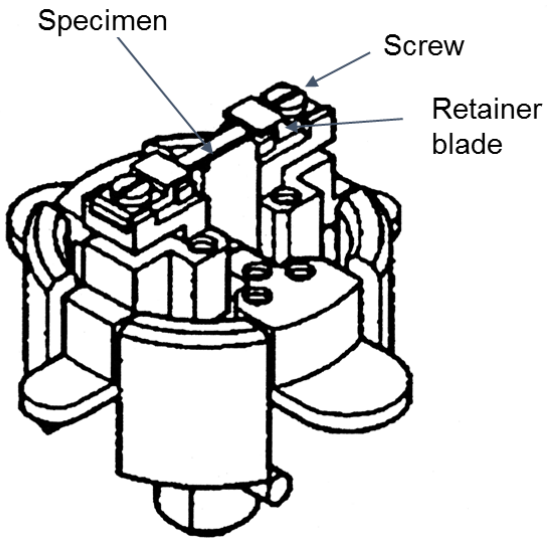


Fig. 2.5 Sample heating holder (taken from Ref. [52]).

The mounting procedure is illustrated in Fig. 2.6. Sample is placed on the two molybdenum posts and screwed in carefully using two tantalum clips to secure the sample in place. The resistance of the sample is desired to be less than 3Ω. The mounted sample is then put into the specimen exchange chamber (base pressure of 10^{-5} Pa) and transported into the treatment chamber (base pressure of 10^{-8} Pa).

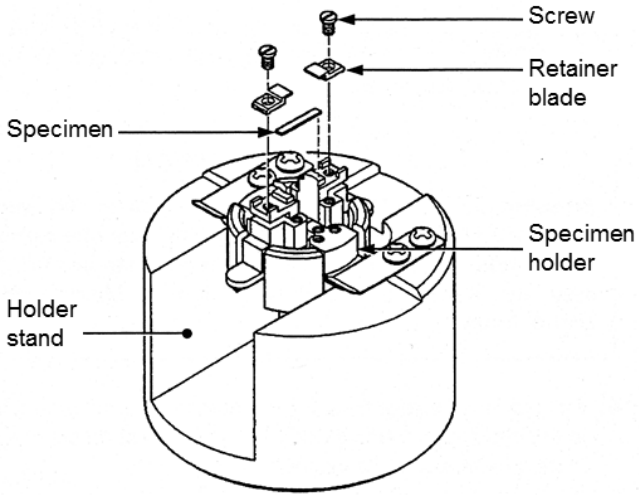


Fig. 2.6 Mounting the sample on the heating holder (taken from Ref. [52]).

The direct heating method is used to prepare the sample surface. As shown in Fig. 2.7, the electric terminals for direct heating are located at the top and bottom of the specimen stage block. The external power supply connects these two terminals to provide the voltage bias and produce the direct current passing through the sample for heating. The sample is degassed and annealed (in UHV or O_2) to prepare different reconstructed surfaces. The temperature of sample is measured by the disappearing filament optical pyrometer from HeatWave Labs, Inc..

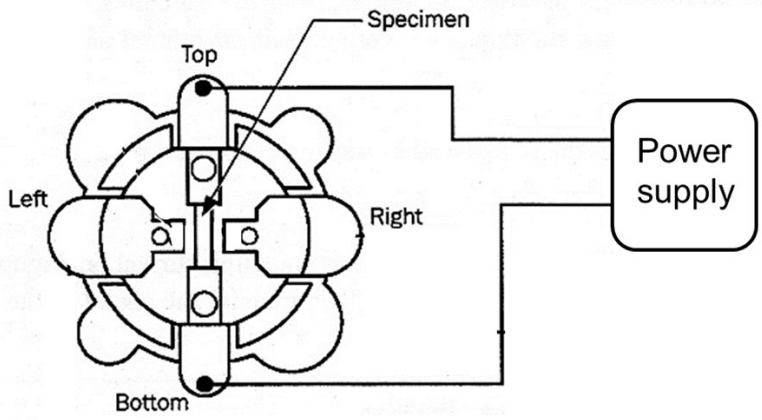


Fig. 2.7 Heating connection for direct heating method (adapted from Ref. [52]).

2.3.2 Sputtering

An EX03 Ion gun system is installed onto the treatment chamber for sputtering purposes. This system can generate ions with 300 eV to 3 keV energy with current of 10 μA to 20 μA respectively. The ion gun is composed of gas line cover and lens column. Inert Ar gas is introduced into the source region of the ion gun through a gas pipe. The pressure value determines the quantity of Ar atoms in the source region i.e., ionisation region.

The sputtering process is decribed in Fig. 2.8. There are two filaments installed in the ion gun. During sputtering, one of the filaments is heated up to the temperature where the

electrons are emitted. The emitted electrons are accelerated and travel through the cage of the source region to the region where is occupied by inert Ar gas. The flow of electrons is the indication of the emission current.

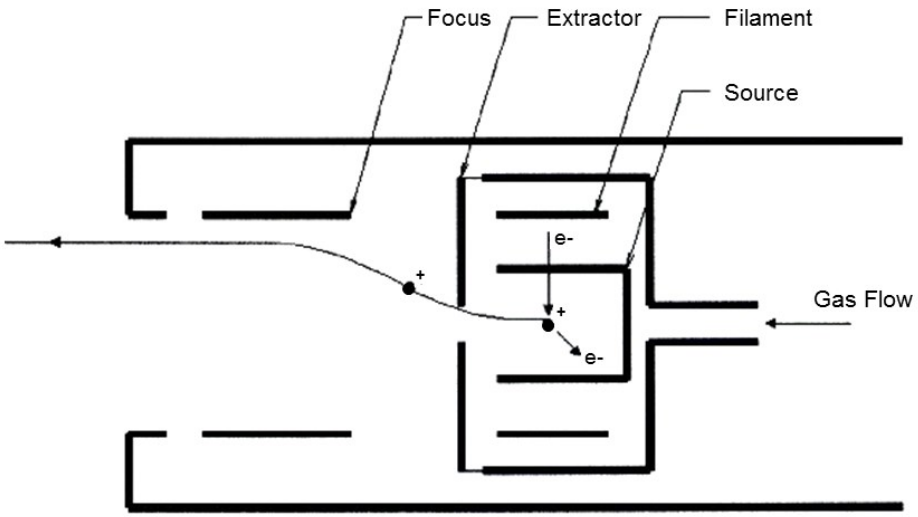


Fig. 2.8 Schematic diagram of the EX03 ion gun (taken from Ref. [53]).

The collision between the electrons and Ar atoms causes the ionisation of Ar species and form positively charged Ar ions (Ar^+). The high positive potential is applied in the ion gun which allows Ar^+ ions to accelerate through the aperture in the extractor lens and travel to the sample. Several lenses are installed in the lens column to focus and shape the Ar^+ ion beam. The beam current, as an indication of the quantity of Ar^+ ions striking to the target sample, can be controlled by the pressure and the emission current [53].

Ar^+ ions bombarded at the sample surface can remove contaminations and create the surface defects. The non-stoichiometric sample surface after sputtering is favourable for surface reconstructions and formation of new structures during annealing process.

2.3.3 Tip making

A high quality tip, which allows the tunnelling current to focus on its single apical atom, is essential to obtain high resolution STM images. A tungsten (W) tip is used in the experiment. It is prepared by electrochemical etching of a tungsten wire (diameter 0.3mm) in a 2 mol/L NaOH solution. Firstly, a piece of W wire (~10 mm) is ultrasonic cleaned by acetone and methanol for 3 minutes and then dried with air duster. The cleaned W wire is placed into JEOL tip holder (Fig. 2.9a). It is then fastened by a special wrench to secure the tip in place and leave the suitable tip height (11 mm) (Fig. 2.9b).

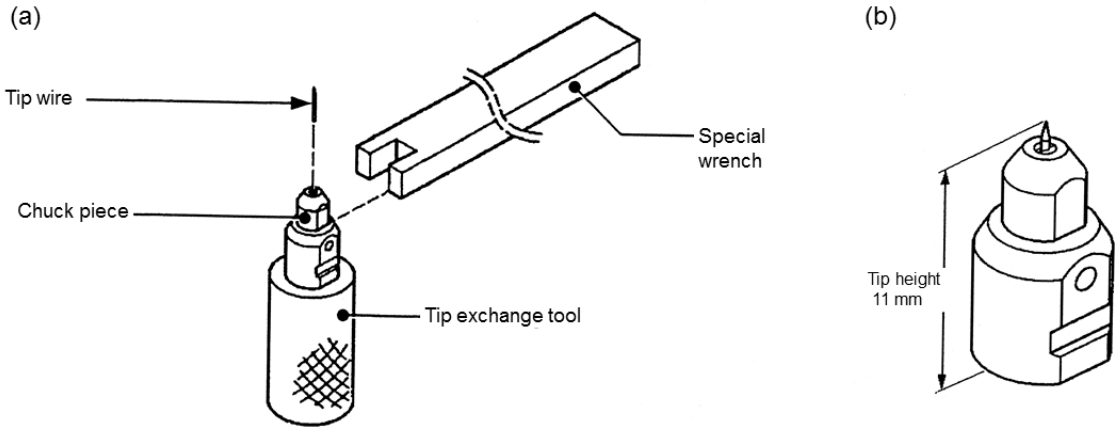


Fig. 2.9 (a) Tip wire mounting in the tip holder. (b) JEOL tip holder showing the suitable tip height (taken from Ref. [52]).

Next, the tip holder is loaded into a special tip port (Fig. 2.10) and put through the centre of Pt wire loop. The rest of the W wire is cut off with 4 mm left between the Pt loop and the end of the W wire. The set up apparatus for tip making is illustrated in Fig. 2.11. The Pt loop is connected to the cathode and the tip holder is connected with anode. The electrical power is supplied by the special designed power supply. The Pt loop is placed very close to the liquid level of NaOH solution in order to forms the NaOH solution meniscus and close the electrical circuit.

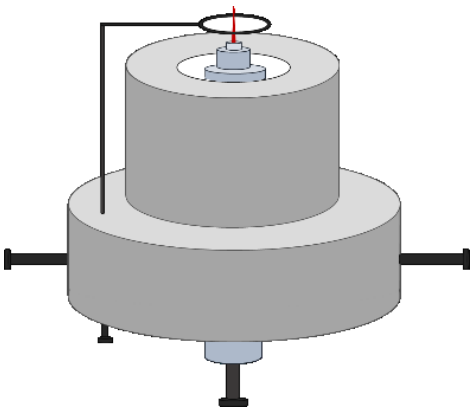


Fig. 2.10 Schematic diagram of the special tip port for tip making. The W tip is in red.

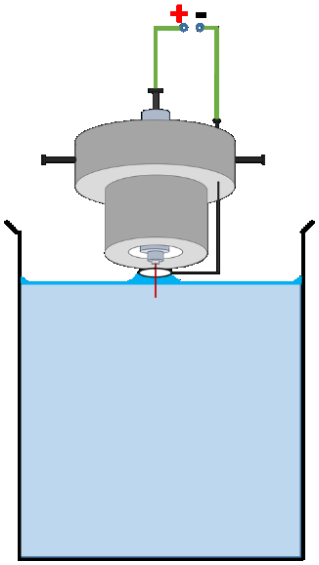


Fig. 2.11 Apparatus set up for the tip making in the 2 mol/L NaOH solution. The W wire is marked in red and acted as the anode. The Pt loop is acted as the cathode.

During electrochemical etching process, the W tip which is connected to the tip holder acts as the anode and Pt loop acts as the cathode. The etching occurs at the air-electrolyte interface where the meniscus of the NaOH solution forms. The chemical reactions are described as follows:

Anode reaction: $W+8OH^- \rightarrow WO_4^{2-}+4H_2O+6e^-$

Cathode reaction: $6H^++6e^- \rightarrow 3H_2$

Total reaction: $W+2H_2O+2OH^- \rightarrow WO_4^{2-}+3H_2$

During etching, the anode material of the W wire is constantly consumed. It becomes thinner at the etching interface (Fig. 2.12). Once it becomes thin enough, the bottom part of the tip in the solution drops off and leaves a sharp fracture surface at the etching interface [54]. The power supply for the tip making apparatus is sensitive to the change of the resistance, and automatically shuts down once the electrical circuit breaks to stop further etching.

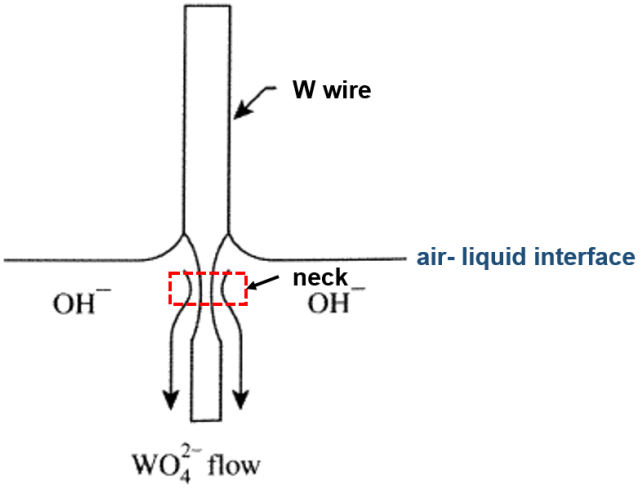


Fig. 2.12 Schematic diagram showing the electrochemical etching process of the W wire in the 2 mol/L NaOH electrolyte solution. The neck marked becomes thinner during etching (marked by red dash rectangle) (adapted from Ref. [54]).

The tip is then rinsed with de-ionised water, acetone and methanol to remove the excess NaOH, dried with an air duster and inspected under an optical microscope. An example of the fresh sharp tip prepared by the electrochemical etching method is shown in Fig. 2.13. Because the OH^- is consumed during each reaction, NaOH solution should be changed after several etching process in order to obtain the proper etching speed.

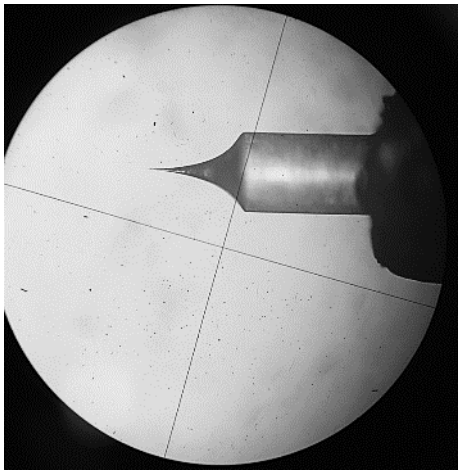


Fig. 2.13 Example of a sharp W tip prepared by electrochemical etching in the 2 mol/L NaOH solution. Tip is inspected under an optical microscope.

2.3.4 STM imaging

After the sample is prepared in the treatment chamber, it is transported to the STM chamber for imaging. STM stage unit consists of a specimen stage, a scanner, coarse specimen drive mechanisms and a pre-amplifier case.The sample holder is positioned in the specimen stage by the transfer arm.

The coarse movement of the specimen stage relies on the motor drive mechanisms. X- and Y- axis motors control the stage movement along X and Y directions within $\pm$2 mm from the sample centre. The Z-axis motor moves the scanner table and drives the tip in the Z direction for the function of tip approaching and retract with approximate drive distance of 3 mm. As the tunnelling current is usually very weak, of the order of 0.1-0.5 nA, pre-amplifier is therefore applied to detect the weak tunnelling current and amplifies it to the reasonable output value. The output signal is transferred to the SPM control unit for analysis.

To start imaging, the lever at the side of the STM chamber is released towards the sample. Then the tip approaching function is activated in the WinSPM software. Z-axis motor slowly drives the tip towards to the sample. The Z-axis motor stops when the value of

tunnelling current is detected as the same as the value shown in the "Current/nA" in the WinSPM software.

STM images can be influenced by both topography and surface electronic states of samples. One of typical examples of topography dominant effect is present when the tip scans over the $SrTiO_3$(001) substrate grown with Pd nanocrystals, which was imaged at constant current mode (Fig. 2.14). The height of the tip is recorded while the tunnelling current is kept at constant. This produces the STM image which the structurally prominent Pd nanocrystals (Fig. 2.14b) appear brighter compared to the substrate (Fig. 2.14a) [55]. The dominant effect from surface electronic structure on STM images can be seen in the STM study of the rutile TiO_2(110) surface (Fig. 2.15) [56]. In its crystal model (Fig. 2.15b), rows of bridging O atoms (labeled by A) are structurally prominent compared to the surrounding five-fold coordinated Ti atoms (labeled by B), which one may expect the bright rows in this empty state STM image are originated from bridging O. However, theoretical analysis has confirmed that bright rows in the empty state STM image (Fig. 2.15a) are attributed to the under-coordinated Ti atoms (i.e. five-coordinated Ti) due to their higher local density of electronic state allowing more electrons tunnelling into, compared to that of the surface bridging O atoms (Fig. 2.15c) [47].

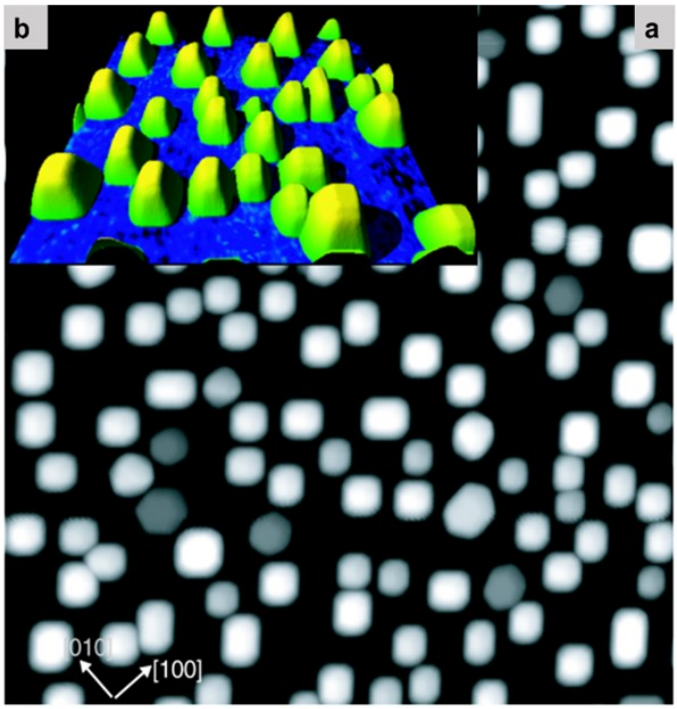


Fig. 2.14 Examples of the contrast in STM images which is dominated by the topographic effect. (a) STM image of Pd nanocrystal grown on $SrTiO_3(001)$-$c(4 \times 2)$ substrate (image size: 140×140 nm^2, imaging conditions: $V_s = +0.8$ V, $I_t = 0.3$ nA). (b) 3D model of Pd nanocrystals are structurally prominent compared to the substrate (taken from Ref. [55]).

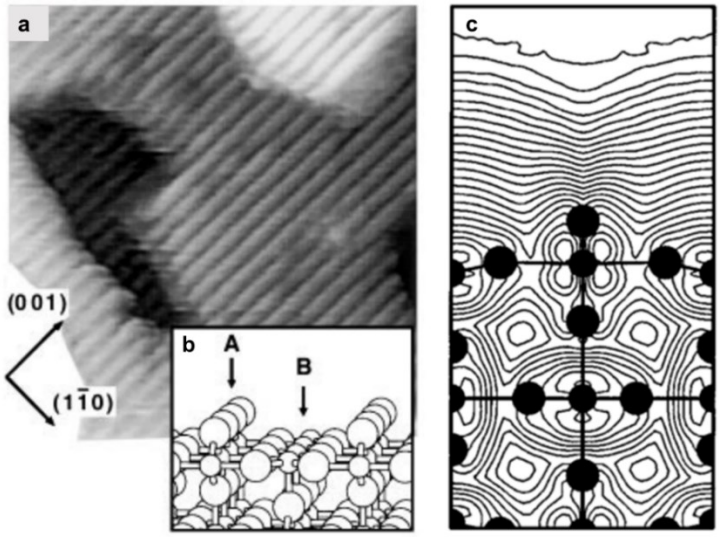


Fig. 2.15 Example of the contrast in STM images which is dominant by the electronic-structure effect. (a) Empty state STM image of stoichiometric rutile $TiO_2(110)$-(1×1) surface, bright rows are observed (image size 14×14 nm^2, imaging conditions: $V_s = +1.6$ V, $I_t = 0.38$ nA). (b) Ball-and stick model of the rutile $TiO_2(110)$-(1×1), the prominent bridging oxygen atoms rows are labelled by A and five-fold coordinated Ti atoms are labelled by B. (c) Contour plot of [001]-averaged charge densities of electron states for the relaxed stoichiometric rutile $TiO_2(110)$-(1×1) surface (the conduction band minimum is 2 eV) (taken from Ref. [56]).

JEOL JSTM-4500s system has an imaging resolution of 0.14 nm in lateral direction and 0.01 nm in vertical direction. The scanner especially its piezoelectric tube scanner elements is the key component to precisely control the movement of the tip for STM imaging in sub-nanometre control range. The piezoelectric (PZT) materials are mounted on the scanner basic unit (Fig. 2.16). The tip holder is placed at the end of the Z-axis PZT element. The movement of the tip is controlled by the PZT elements in X, Y and Z directions. The PZT elements controlling X and Y direction are attached on the side surface of the scanner basic unit to control the tip scanning over sample surface. The PZT element controlling the Z direction is mounted on the end of the scanner basic unit [57]. In the constant current mode, the Z-axis PZT element is controlled in order to give the constant detected tunnelling current.

The quality of STM images is affected by the vibration from the environment, quality of the tip, noises from either surrounding electronics or environment, tunnelling current and the surface condition of the sample [47].

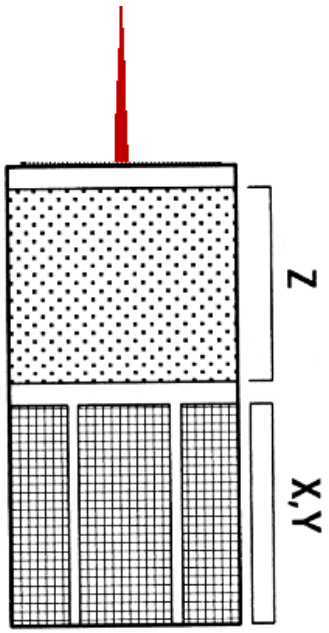


Fig. 2.16 Scanner basic unit and the position of attaching PZT elements controlling X-,Y- and Z- axis movement of the tip (adapted from Ref. [57]).

2.3.5 STM calibration

The piezoelectric materials Lead Zirconate Titanate ceramics (PZT) are widely used in STM equipment to control the movement of the scanner during imaging. As the voltage is applied on the PZT elements, the shape of these piezoelectric elements changes by a small amount of distance. This displacement of the PZT elements gives the distance measured in X, Y and Z directions in STM images. STM have correlation equations between the applied voltage and the displacement of the piezo in X, Y and Z directions. High temperature operation and long-term use may cause the aging of piezoelectric elements, which the piezo is relaxed and its displacement does not respond correctly with the applied voltage.

Periodically, the STM equipment needs to be calibrated in order to obtain the correct measurements of the sample surfaces in X, Y and Z directions. The recent calibration on our equipment was done in 2015 after we found a significant offset of the measurements on STM images. The offset value was 58.9 % in Z, 11.3 % in X and 12.7 % in Y directions since the previous calibration done in 2009. The STM calibration method is described below.

STM calibration in the X and Y directions

The Si(111)-(7 × 7) reconstructed sample has a relatively flat surface and well-defined unit cell. So it is chosen as the reference to carry out the STM calibration in the X and Y directions. The sample was imaged at the centre of the off-site region during each scan, to obtain the STM images with different sizes i.e., 20 × 20, 30 × 30, 40 × 40 and 50 × 50 nm^2. Measurements in X and Y directions were taken as parallel as possible to the horizontal X and vertical Y directions (red dashed lines in Fig. 2.17a and b). Specifically, the X direction was chosen across three horizontally neighbouring (7 × 7) unit cells indicated by the black line in Fig. 2.17a. The measurement in Y direction was taken across two vertically

neighbouring (7 × 7) unit cells indicated by the black line in Fig. 2.17b. The experimental measurement in X and Y directions (X_1 = 10.8 nm and Y_1 = 8.02 nm) were compared to their true values (X_0 = 9.70 nm and Y_0 = 7.12 nm) respectively. Next, we updated the calibration equations from: $X = 7.3\ V_x$; $Y = 7.6\ V_y$ to $X = 6.56\ V_x$; $Y = 6.75\ V_y$, which V_x is the voltage applied on X-piezo and V_y is the voltage applied on Y-piezo. The scanner sensitivities in the X and Y directions are then calibrated in the WinSPM software installed in the STM operating computer.

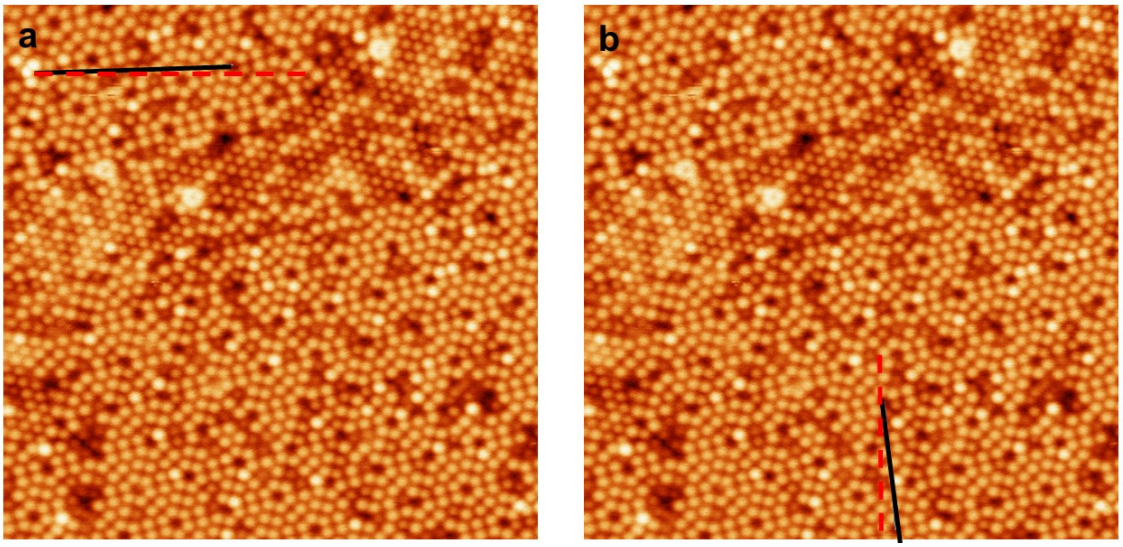


Fig. 2.17 STM images of Si(111)-(7 × 7) reconstruction. (a) Measurement taken in the X direction (trace in black line). (b) Measurement taken in the Y direction (trace in black line). The red dashed lines are the reference in horizontal and vertical directions (image size: 30 × 30 nm^2, imaging conditions: V_s = +1.874 V, I_t = 0.525 nA).

STM calibration in the Z direction

$SrTiO_3$(001)-*c*(4 × 2) has flat terraces with well-structured straight step edges. So it is chosen as a reference sample to carry out the STM calibration in the Z direction. The sample was imaged at the centre of the off-site region during each scan to minimise the influence from scanning in the X and Y directions. Sample was imaged at different imaging sizes (100 × 100, 200 × 200 and 300 × 300 nm^2) with STM images shown in Fig. 2.18. Step

heights were obtained by averaging the data from selected areas indicated by the red rectangles in Fig. 2.18. Then, the experimentally measured step height (Z_1 = 0.62 nm) was compared to its true value Z_0= 0.3905 nm. Next, we updated the calibration equation from $Z = 1.55\ V_z$ to $Z = 0.96844\ V_z$, which V_z is the voltage applied on Z-piezo. The scanner sensitivity in the Z direction is then calibrated in the WinSPM software.

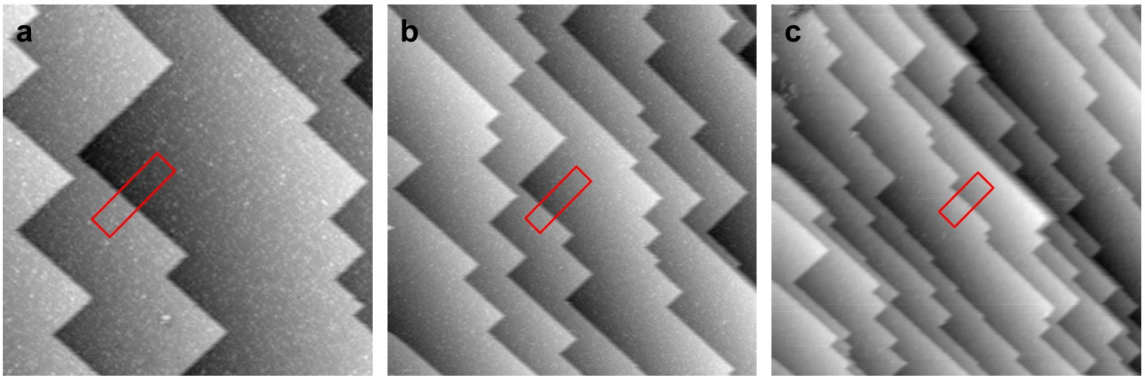


Fig. 2.18 STM images of $SrTiO_3$(001)-c(4 × 2) reconstruction with image sizes of (a) 100 × 100 nm^2; (b) 200 × 200 nm^2 and (c) 300 × 300 nm^2 (imaging conditions: V_s = +2.503 V, I_t = 0.23 nA).

2.3.6 STM system baking

Sample surface treatments (e.g., degassing, annealing and evaporation) may introduce contamination for both STM and treatment chambers. This breaks the UHV environment and affects the cleanness of the sample surface for high quality STM imaging. In order to maintain the UHV condition, it is necessary to carry out a "baking" operation.

Before starting the baking operation, the ion pumps should be switched off but the Turbo-molecular Pump (TMP) should be left running. The glass observation windows must be covered by aluminium foil to avoid cracking due to the dramatic change of the thermal gradient. All the electronics attached to the STM chamber should be removed in case of any heat damage. Other attached components such as the sputtering gun and the e-beam gun

should be removed. The magnets on the transferring arms should be removed in case of demagnetisation under high temperature. Because baking is carried out at temperature around 150°C, every inflammable or heat sensitive materials should be kept away from the chambers. Then, wind the ribbon heater around the transferring arms, treatment and STM chambers to heat up the components.

Baking can work for either the treatment chamber or both the treatment and STM chambers. Only the Turbo-molecular Pump (TMP) attached to the specimen exchange chamber is running in the baking process. During the baking, hydrocarbon and moisture contamination are removed from the chamber wall and pumped out by the TMP. Baking usually takes at least two days. The ion pumps, Titanium Sublimation Pumps (TSPs) are degassed when turning off the baking operation. The pressure in each chamber is usually in the 10^{-5} Pa range when turning off the baking. The chambers are then self-cooled to the room temperature when the baking heater is switched off. An UHV condition in the 10^{-8} Pa range will be reached in 8-12 hours after baking is finished.

It is necessary to vent the entire machine when fixing existing apparatus or installing a new apparatus onto the STM equipment. The chambers are vented by introducing N_2 gas through specimen exchange chamber to the main chambers. Every apparatus is sealed on machine with copper gaskets. Copper gaskets should be replaced by a fresh one every time when re-attaching the apparatus to the machine. Baking is required after venting the entire machine and follows the procedure described above.

2.3.7 Metal deposition

The e-beam evaporator (Model EGCO4) is used in this experiment (Fig. 2.19). The evaporator is attached onto the STM chamber and operated in the UHV environment [58]. The deposition rate is controlled from less than 0.1 Å/min to over 50 Å/min [58]. Metal deposition is achieved through electron beam induced thermal evaporation of materials. A high voltage is applied on the target rod which generates a voltage gradient between the filament and the rod. The electrons are emitted from the filament by increasing the filament temperature through adjusting the current. The emitted electron is at earth potential and accelerated towards to the tip of the target rod. The bombardment of the emitted electrons (emission current can be up to 100 mA) to the rod gives the total available power of 200 W [58]. This is a sufficiently high power to evaporate some high melting point metals such as tungsten. Only the target rod is required to heat up to the evaporation temperature. The rods in other pockets are protected from melting by running chilled water to keep the rods at ambient temperature.

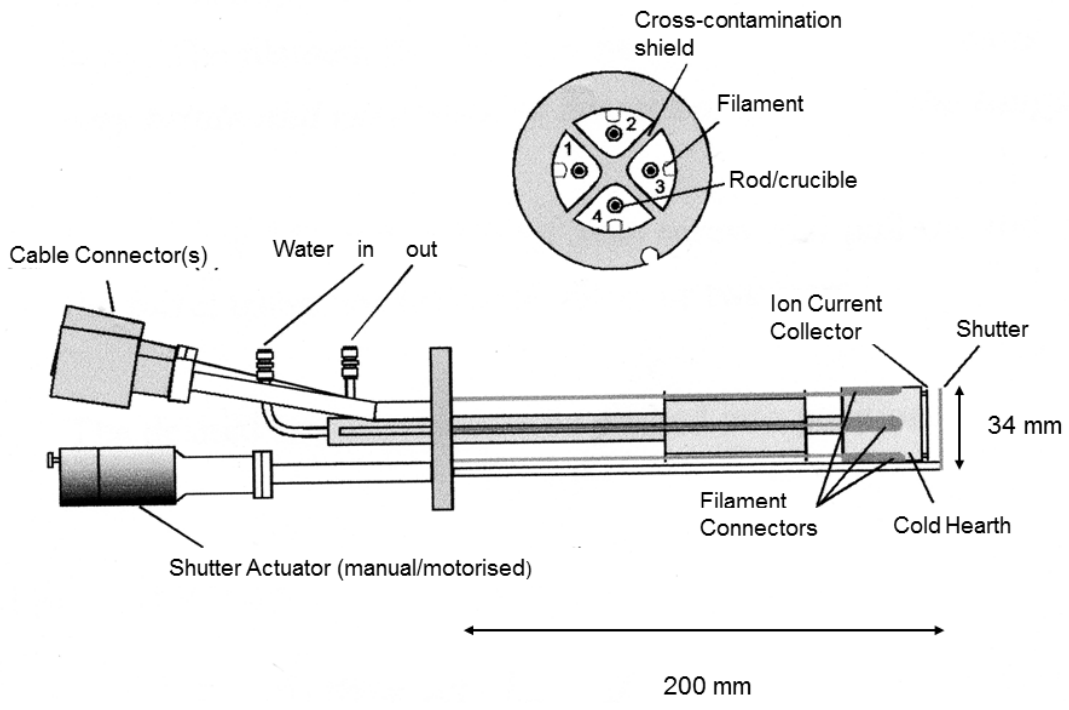


Fig. 2.19 Schematic picture of EGCO4 e-beam evaporator (taken from Ref. [58]).

To start the evaporation process, firstly, EHT (unit: kV) which controls the hearth potential is adjusted to 2 kV. This is the voltage applied onto the target metal rod to create the voltage gradient between the rod and the filament. Next, the targeted metal rod with its pocket number is selected. Then, the filament current is gradually increased until reaching the desired value for electrons emitting from filament. The flux is monitored during this process in order to decide the quantity of the evaporation species. Finally, the shutter is opened with timer running to count the deposition time. Deposition can be carried out on either warm or room temperature substrates. After deposition, the shutter is closed immediately. Filament current and EHT are carefully reduced to zero by following the procedure in the reverse order described above. Post annealing may be carried out directly after deposition for the crystallisation of the metal particles.

2.3.8 Photoluminescence spectroscopy (PL)

JY Horiba LabRAM ARAMIS imaging confocal Raman microscope was applied to perform the PL experiment on 2D-MoS_2 samples.

Photoluminescence analysis (PL) is a non-destructive and sensitive technique to characterise the surface and interface of the sample. This is because that PL is sensitive to the discrete electronic states and most of these electronic states lie near to the surfaces and interface [59]. PL performs well for the high radiative efficiency materials that can emit light under the light source. However it is difficult to study the indirect bandgap semiconductors via PL that have low radiative efficiency.

The typical set-up of the PL instrument is shown in Fig. 2.20. It consists of an optical source and an optical power meter or spectrophotometer. In general, a laser source emits light with

sufficient energy to excite the sample. Initial state electrons in the sample are excited to a higher energy state through absorbing sufficient energy from the incoming light. These electrons eventually relax to the ground state, combine with holes and emit the fluorescent light. The light travels through the lenses, the spectrophotometer and is collected by the photo-detector. The colour of light is directly related to the electronic energy level of the sample. The PL spectra are generated after this process, presented by the intensity versus wavelength of the light. Through carefully analysing the PL spectra such as the peak position and intensity of the signal, one could obtain the information to identify the surfaces and interfaces, the impurity level, disorder of materials and interface roughness [59].

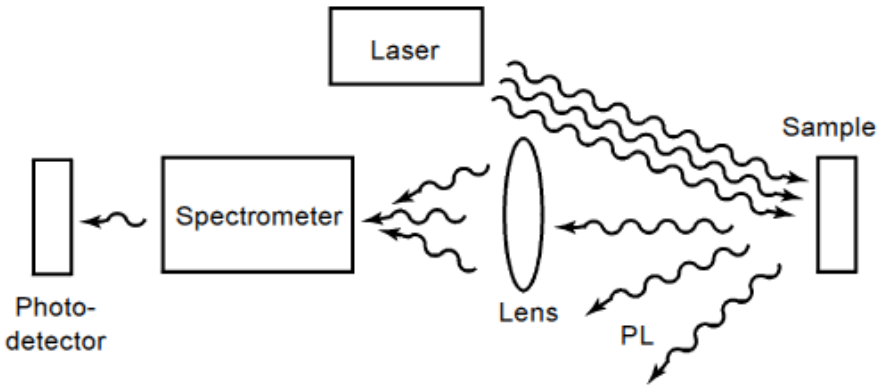


Fig. 2.20 Typical experimental set-up for the PL measurement with the components of optical source, and an optical power meter or spectrophotometer (taken from Ref. [59]).

2.3.9 Raman spectroscopy

JY Horiba LabRAM ARAMIS imaging confocal Raman microscope was used in this experiment to characterise the structural properties of the 2D MoS_2 crystals.

In general, Raman spectroscopy is used to observe vibrational, rotational, and other low-frequency modes in materials. A laser source is usually applied to produce a monochromatic radiation with the wavelength in the visible or near infrared range. As the photons collide

with the molecules in the sample, they could either be elastically scattered or inelastically scattered. The elastic scattered radiation is called Rayleigh scattering where the scattered photons have the same wavelength as the incoming laser radiation (Fig. 2.21). Raman spectroscopy relies on the inelastically scattered photon radiation. After the collision, the molecules are excited to the virtual state and immediately emitted back to the vibrational state. The energy level of the original vibrational state of the molecule and its final state determines whether the phenomenon is Stokes scattering or anti-Stokes scattering (Fig. 2.21). If the molecule is excited from the lowest vibrational state and relax back to the higher vibration state, the scattered photons will have the energy which is lower than the incoming photons (Stokes radiation). If the molecule is excited from the higher vibrational state and relax back to the lowest vibration state, the inelastically scattered photon will have a higher energy than that of the incoming photons (anti-Stokes radiation). The inelastically scattered photons travel through lenses, a spectrometer and are then collected by the detector.

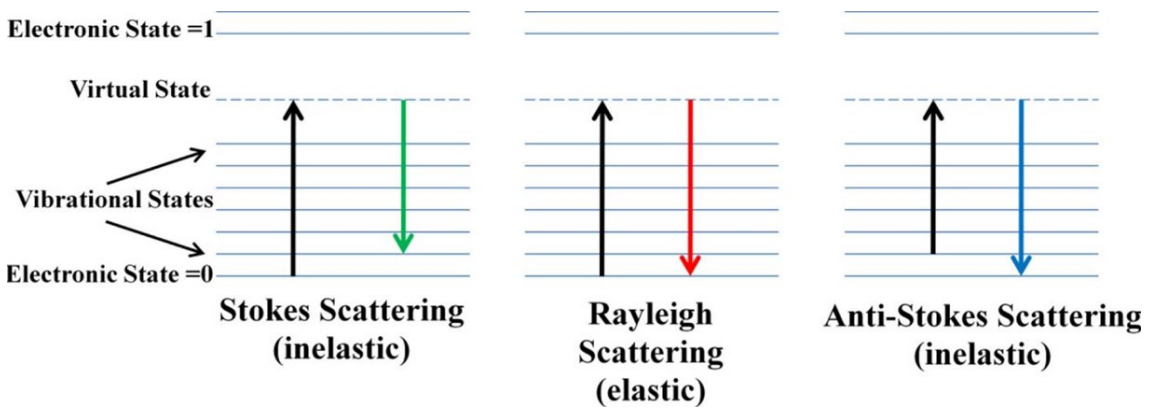


Fig. 2.21 Energy diagrams of Stokes, Rayleigh and Anti-Stokes Raman scattering (taken from Ref. [60]).

The photon energy after Rayleigh scattering is used as a reference to measure the energy shift of those photons which are inelastically scattered (Raman shift). Because different molecules have different vibration frequency i.e., vibration energy, the Raman shift of Strokes and anti-Strokes scattering is a direct measurement of the vibrational energy of the molecules. Through carefully studying the Raman shift in the Raman spectra, we can obtain the chemical and structural information of the molecules. Besides, the peaks in the Raman spectra are related to the characteristic vibration modes of the materials. For example, it is possible to determine the layer numbers of the 2D crystals by measuring the frequency differences between two characteristic peaks i.e., E_{2g}^{1} and A_{1g} [61]. Raman spectroscopy is also useful in determining the lattice strain, doping levels and the van der Waals interaction at the interface for 2D crystals [61].

2.3.10 Scanning electron microscopy (SEM)

Hitachi-S-4300 field emission scanning electron microscope was used to study the MoS_2 samples described within the thesis. The electron beam is accelerated at 0.5 kV to 30 kV. The operation pressure is in the 10^{-5} to 10^{-6} Pa range.

Scanning electron microscopy applies electron beam instead of light to deliver the images of the sample surface [43]. In general, a beam of electrons is emitted from the filament in the electron gun. Then, the electron beam is shaped and focused by electromagnetic lenses and accelerated to the sample surface. The emission of secondary electrons [62] is caused by the inelastic scattering between electron beam and free electrons in the sample close to the surface (Fig. 2.22). The free electrons absorb sufficient energy to resist the attraction force from the nuclei and escape from the solid surface. The escaping SEs are collected by the detector and displayed as the SEM images showing surface morphology and topography.

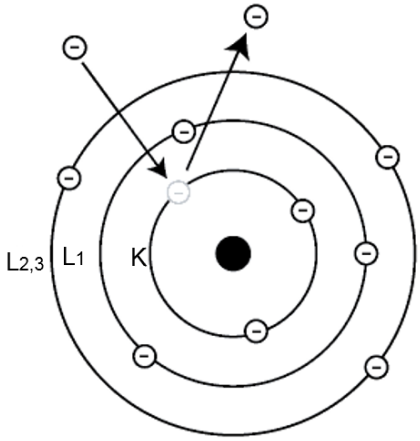


Fig. 2.22 Diagram of the secondary electron emission caused by the inelastic scattering (taken from Ref. [63]).

2.4 Summary

This chapter has introduced the main experimental technique i.e., STM in the concepts of history, operation principle and equipment functionality. STM is applied for surface characterisation and analysis in studying atomic structures, periodicity and electronic structures of the samples in this work. Besides, other supporting techniques such as PL spectroscopy, Raman spectroscopy and SEM were also included in this chapter. These techniques are applied for characterisation of MoS_2 2D materials. The methodology for tip making and surface preparation including sputtering, annealing and metal vapour deposition have also been described. To obtain the accurate measurement, the STM calibration methods in X, Y and Z directions have been summarised along with the detailed description for each procedure.

Chapter 3

Literature Review

3.1 Introduction

This chapter begins with an introduction of metal oxides, in particular perovskites, the properties and potential applications and concepts of surface reconstructions, and nanostructure formations. The review then concentrates on specific types of perovskite, i.e., $SrTiO_3$ related reconstructions, nanostructures and nanocrystal formation on (001) and (111) surfaces. The studies of anatase TiO_2 surfaces are also reviewed in terms of their properties and the metal-TiO_2 system. Finally, the 2D TMDs are introduced including a review of the physical properties and characterisation methods.

3.2 Metal Oxides and Perovskites

3.2.1 Metal oxides

Metal oxides are a class of materials which exhibit a wide range of electrical conductivity behaviour from metals to semiconductors and insulators. Metal oxide surfaces or interfaces between oxides and other materials play an important role in catalysis, chemical sensing and energy-related applications. Based on the fascinating applications, in the field of surface science, a great deal of attention has been drawn to study the metal oxide surfaces. Due to

the difference in the ion coordination, metal oxides are classified into different crystal structures such as perovskite, fluorite, rocksalt and wurtzite [64]. The complexity in the crystallography of the oxide structures and electronic structures brings the difficulty to study metal oxide surfaces, compared to those of the semiconductors. The complex crystallography can simply lead to the complexity in both chemical and physical properties. Many elements in metal oxides usually present more than one oxidation state. This brings chemical complexity and causes deviation in composition and properties. Also, the physical properties of metal oxides can be changed very easily when the imperfection is induced into the crystal lattice. For instance, the defects in the lattice cause the changes in electronic conductivity and colour of the metal oxides [64,65].

3.2.2 Perovskite structures, ideal (001) and (111) surfaces

Perovskite was initially named for Calcium Titanium Oxide mineral ($CaTiO_3$). Nowadays, perovskite is widely represented by a structural family of the metal oxides whose general formula is ABO_3 (A is usually larger than B) [66,67]. The ideal perovskite oxide structure is shown in Fig. 3.1. Generally, three distinct ions are located at different sites of the basic unit [64,66]. Commonly, cations A are from alkaline earth or rare earth elements and can be monovalent, bivalent or trivalent [68]. They are located at the centre of each cubic cell and coordinated with the O anions in the 12-fold arrangement [66]. Transition metal elements are usually represented by cation B and located at the corner of the cube in the octahedral 6-fold coordination with O [68]. O anions are located at the centre of 12 edges of the cubic structure [64].

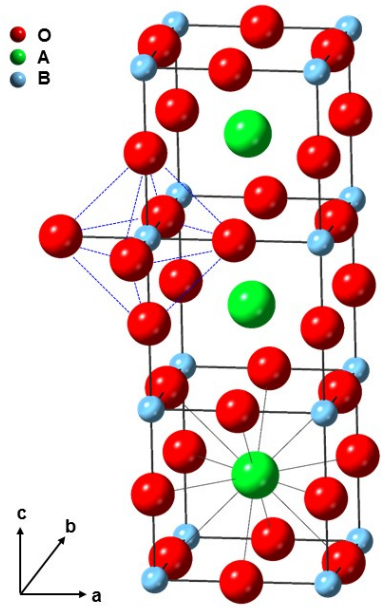


Fig. 3.1 ABO_3 ideal perovskite structure

Perovskite exhibits a large variety in ferroelectric, piezoelectric, dielectric, ferromagnetic and multiferroic properties. These physical properties enable the perovskite to be applied in the applications such as ferroelectric random access memories [69], multilayer ceramic capacitors [70], sensors and actuators [71], potential new types of multiple-state memories and spintronic devices controlled by electric and magnetic fields [72].

Ideal perovskite (001) surface

The (001) surface is the most popular surface in studying the perovskite surface structures. The ideal perovskite (001) surface is atomically flat and alternates in the composition of AO and BO_2 planes (Fig. 3.2). Both planes are charge-neutral with non-polar behaviour [64]. Each A cation in the surface AO plane, which has a comparable size of oxygen anion, bonds with eight O^{2-}. While in the bulk perovskite structure, A cation is coordinated with 12-fold oxygen. Each B cation in the surface BO_2 plane has a total of five oxygen ligands,

with four nearest O^{2-} anions located in the outmost surface plane and one O^{2-} anion located directly below the B cation [64]. Because AO and BO_2 surfaces will exhibit different surface energies, different ratios of these two types of surfaces can be generated by the surface preparation process such as ion bombardment and annealing [73]. Different treatment conditions (e.g., pressure, temperature or atmosphere) can lead to the different valences and coordination numbers of the transition metal oxide surface, leading to a more complex oxide structures [74].

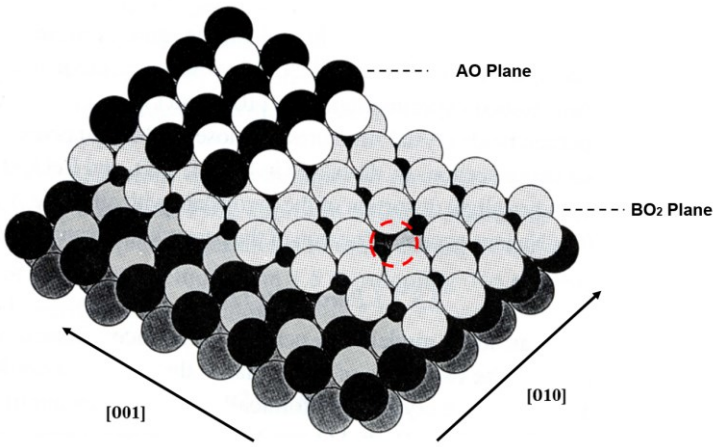


Fig. 3.2 Ideal model of perovskite (001) surface. Two steps to (001) terraces are shown. O-vacancy defect is shown in BO_2 plane. Large black balls are A cations, small black balls are B anions and large white balls are O anions (adapted from Ref.[73]).

Oxygen vacancies are the most common point defect observed in the metal oxides. It is generated during heating and quenching or particle bombarding. The red circle in Fig. 3.2 shows one missing oxygen anion, i.e., oxygen vacancy in the BO_2 plane. In this way, the adjacent B cation losses one coordinate and presents four-fold coordination with O^{2-}. Two type of [001] steps are shown in Fig. 3.2 with reduction of the O^{2-} ligand numbers for atoms on both step edges [73]. However, no evidence shows that perovskite (001) surface with ideal surface geometry shown as Fig. 3.2 has been observed in the real case, as surface reconstruction occur easily once a (001) surface has been created. The surface reconstructions are explained in Sec. 3.3.

Ideal perovskite (111) surface

The surface structure of unrelaxed perovskite (111) surface in few atomic layers is depicted in Fig. 3.3. Plane cleaving creates two sets of atomically flat planes which are AO_3 and B planes (B ions lies above the AO_3 plane). However, different from ideal perovskite (001) surface, (111) surface either presented by the B plane or the AO_3 plane would be polar. Dipole is usually present on the unrelaxed polar (111) surfaces. The B ions at the surface have only 3 oxygen ligands which are three fewer than those in bulk. Annealing the perovskite (111) surface causes reconstructions which removes the net dipole moments and increases the surface cation coordination. Also, these rearrangement processes may not be restricted to the top layer [64].

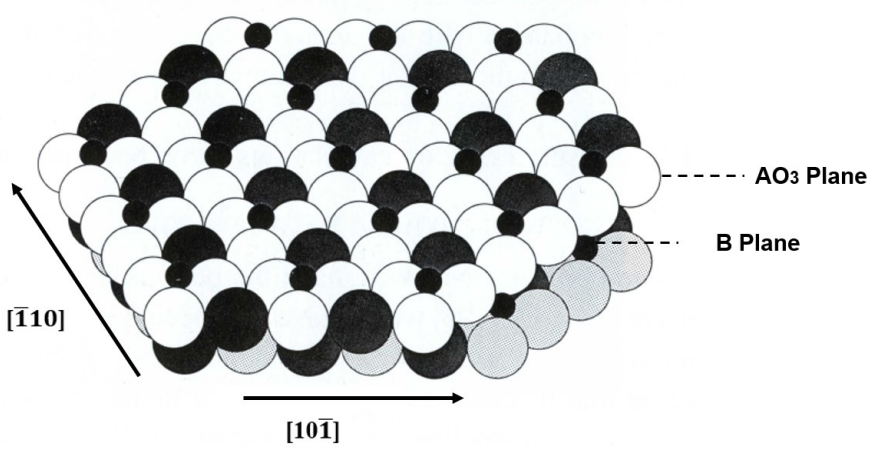


Fig. 3.3 Ideal model of unrelaxed perovskite (111) surface. Large black balls are A cations, small black balls are B cations and large white balls are O anions (adapted from Ref. [64]).

3.3 Reconstructions and Surface Nanostructures

3.3.1 Surface unit cell and notation

Defining the basic constructing unit of the surface i.e., surface unit cell is the primary step to analyse surface structures. A surface unit cell is the simplest periodically repeated unit constructed from an array of surface atoms. Through repeatedly translating the primitive unit cell, the surface can be constructed into an ordered manner. Two vectors (e.g., $\boldsymbol{a_1}$ and $\boldsymbol{a_2}$) are involved to define the shape, size and symmetry of the bulk terminated surface unit cell without any atom rearrangement. They share the common origin and point along two sides of one unit cell (Fig. 3.4). The other two vectors (e.g., $\boldsymbol{b_1}$ and $\boldsymbol{b_2}$) are used to define the new superficial unit cell.

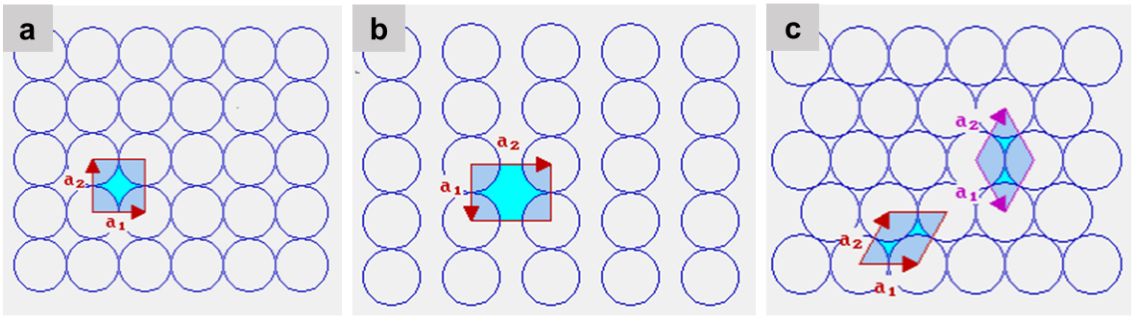


Fig. 3.4 Examples of the original surface unit cell defined by two vectors (e.g., $\boldsymbol{a_1}$ and $\boldsymbol{a_2}$) on the overlayer structure of fcc: (a) (100); (b) (110) and (c) (111) surfaces without atom rearrangement (taken from Ref. [75]).

Woods notation and matrix notation are the two principal methods applied to define the surface unit cell. Woods notation is the simplest and most frequently used method. The expression format is shown as the length ratio of the surface unit cell vectors ($\boldsymbol{b_1}$ and $\boldsymbol{b_2}$) with respect to the substrate unit cell vectors ($\boldsymbol{a_1}$ and $\boldsymbol{a_2}$) (i.e., $\left(\frac{|\boldsymbol{b_1}|}{|\boldsymbol{a_1}|} \times \frac{|\boldsymbol{b_2}|}{|\boldsymbol{a_2}|}\right)$. For examples, a (2×2) unit cell is defined by scaling up the surface unit cell side length with respect to

those in the substrate in the factor of two (Fig. 3.5a). Sometimes, (2 × 2) can also be written as $p(2 \times 2)$ where p represents the primitive unit cell. If there is a crystallographically equivalent atom at the centre of the surface unit cell (Fig. 3.5b), 'c' which represents 'centre', is added in front of the $(\frac{|\boldsymbol{b_1}|}{|\boldsymbol{a_1}|} \times \frac{|\boldsymbol{b_2}|}{|\boldsymbol{a_2}|})$. The $c(2 \times 2)$ unit cell where there is one atom located at the centre of the primitive (2 × 2) unit cell is highlighted in Fig. 3.5b.

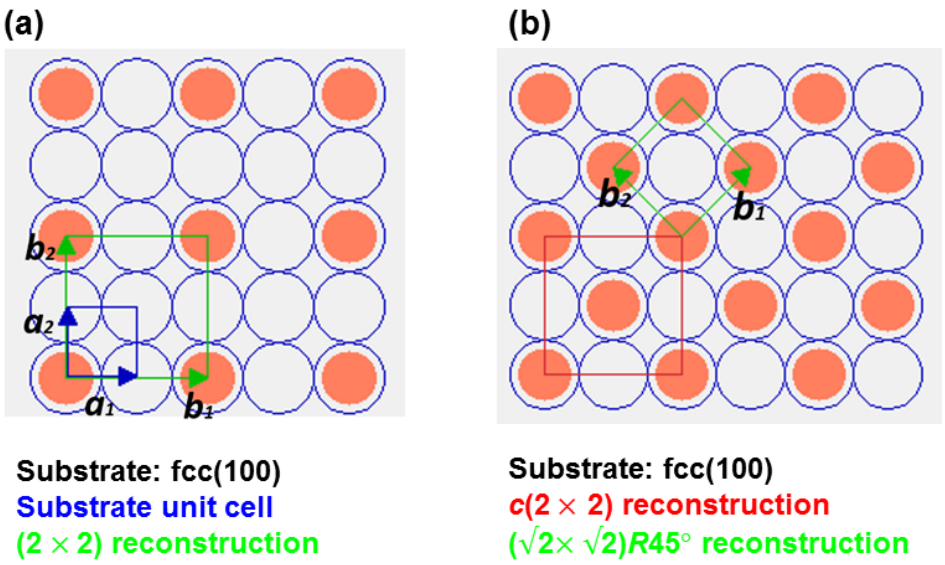


Fig. 3.5 Woods notation of the examples: (a) (2 × 2) and (b) $c(2 \times 2)$ unit cell on fcc (100) surface (adapted from Ref.[75]).

Woods notation links the surface and substrate unit cell closely and clearly shows the length fraction in the form of simple multiples of $\boldsymbol{a_1}$ and $\boldsymbol{a_2}$ respectively. Sometimes, there is a relative rotation from the common origin between the surface unit cell and the substrate unit cell (Fig. 3.5b). The rotation angle measured between $\boldsymbol{b_1}$ and $\boldsymbol{a_1}$ is added after the length ratio $(\frac{|\boldsymbol{b_1}|}{|\boldsymbol{a_1}|} \times \frac{|\boldsymbol{b_2}|}{|\boldsymbol{a_2}|})$. Meanwhile, the unit cell of $(\sqrt{2} \times \sqrt{2})R45°$ in Fig. 3.5b can also be rewritten as $c(2 \times 2)$ to describe the same surface atom arrangement. Applying Woods notation is restricted to the situation which the surface and substrate unit cells are in the same or almost the closely-related symmetries. This means the angle between $\boldsymbol{b_1}$ and $\boldsymbol{b_2}$ must be the same as the angle between $\boldsymbol{a_1}$ and $\boldsymbol{a_2}$) [75].

Matrix notation is suitable for the general system to describe all ordered array of the surface structures. It relates $\boldsymbol{b_1}$ and $\boldsymbol{b_2}$ to the substrate unit cell vectors $\boldsymbol{a_1}$ and $\boldsymbol{a_2}$ in the matrix format i.e., $\begin{pmatrix}\boldsymbol{b}_1\\ \boldsymbol{b}_2\end{pmatrix}$ =**M** $\begin{pmatrix}\boldsymbol{a}_1\\ \boldsymbol{a}_2\end{pmatrix} = \begin{pmatrix}\boldsymbol{m_{11}} & \boldsymbol{m_{12}}\\ \boldsymbol{m_{21}} & \boldsymbol{m_{22}}\end{pmatrix}\begin{pmatrix}\boldsymbol{a}_1\\ \boldsymbol{a}_2\end{pmatrix}$ which $\boldsymbol{b}_1 = m_{11}\boldsymbol{a}_1 + m_{12}\boldsymbol{a}_2$, $\boldsymbol{b}_2 = m_{21}\boldsymbol{a}_1 + m_{22}\boldsymbol{a}_2$. Vectors $\boldsymbol{b}_1$ and $\boldsymbol{b_2}$ are decomposed along the direction of substrate unit cell vectors $\boldsymbol{a_1}$ and $\boldsymbol{a_2}$, and defined independently as the linear combination of $\boldsymbol{a_1}$ and $\boldsymbol{a_2}$ in the matrix format. For example, in the (2 × 2) unit cell (Fig. 3.6a), the unit cell vectors $\boldsymbol{b}_1$ and $\boldsymbol{b_2}$ are resolved as $\boldsymbol{b}_1 = 2\boldsymbol{a}_1 + 0\boldsymbol{a}_2$, $\boldsymbol{b}_2 = 0\boldsymbol{a}_1 + 2\boldsymbol{a}_2$. Then it can be converted to the matrix format as **M**= $\begin{pmatrix}2 & 0\\ 0 & 2\end{pmatrix}$. Similarly, in the *c*(2×2) unit cell (Fig. 3.6b), $\boldsymbol{b}_1 = 1\boldsymbol{a}_1 + 1\boldsymbol{a}_1$, $\boldsymbol{b}_2 = -1\boldsymbol{a}_1 + 1\boldsymbol{a}_2$, which gives **M** = $\begin{pmatrix}1 & 1\\ -1 & 1\end{pmatrix}$.

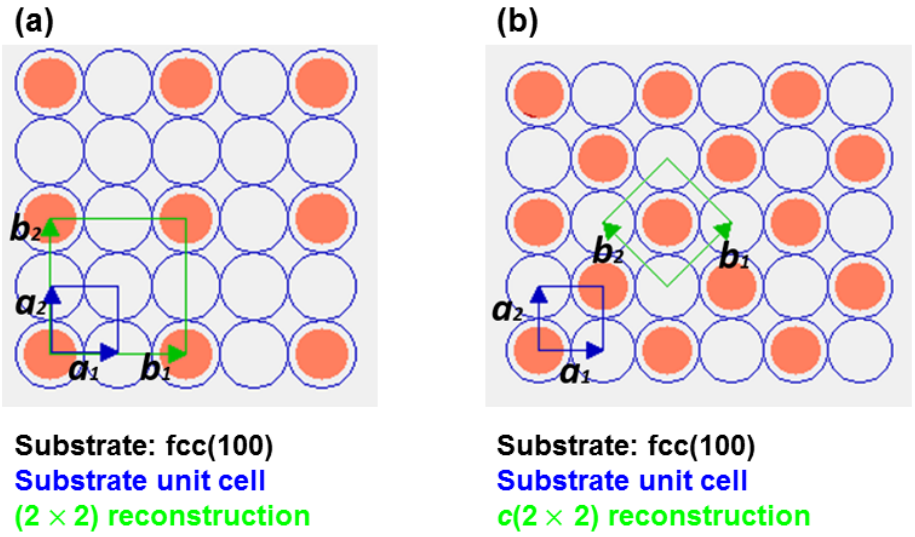


Fig. 3.6 Matrix notation of the surface unit cell examples: (a) (2 × 2) and (b) (√2 × √2) unit cell on the fcc (100) substrate surface (adapted from Ref.[75]).

3.3.2 Surface relaxation and reconstruction

The formation of a new surface from bulk entails the destruction of bonds. Fig. 3.7a shows the ideal bulk truncated surface which the top few atomic layers all present the same periodicity and interplanar distance to the inside layers. However, in reality, atoms on the

surface will no longer have as full a complement of co-ordinations as those in the bulk. This leaves the surface with high energy configuration therefore seeking to minimise the surface free energy through relaxation and reconstruction.

Surface relaxation

Even for the flat surface with low miller index plane, top atomic layer still undergoes the process of changing bonding geometry to form new surface [76]. In the meantime, based on the electron smoothing concept, electrons left around the surface atoms have the tendency to spread over the surface in order to lower their kinetic energy [77]. Redistribution of these charges leads to the increase of the charge density between the first and the second atomic layers. These electrons tend to move downwards to the bulk crystal and create the electrostatic attraction that attracts the surface ions moving towards them. This electrostatic force between the surface atoms and the bulk atoms causes surface stressed and narrows the interplaner spacing between these layers [76,78]. Relaxation relieves the surface stress in the most vertical directions and produces a new surface structure with the distinct bonding coordination [76]. Relaxation changes the bond length and angle by a few percentage and adjusts the layer spacing perpendicularly to the surface. It does not change the periodicity that is parallel to the symmetry of the surface (Fig. 3.7b).

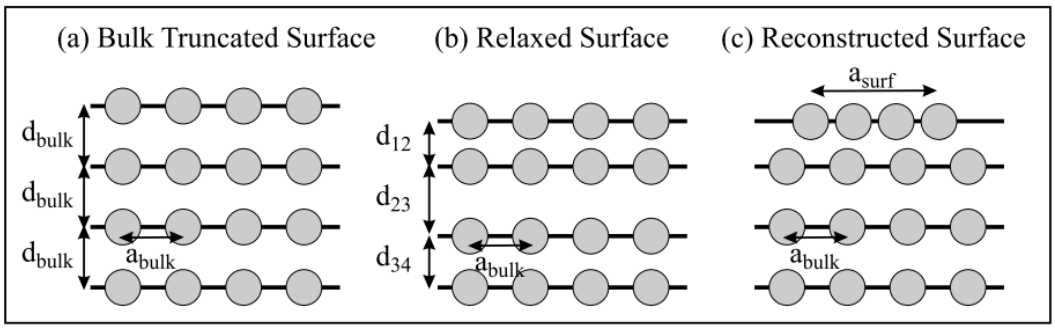


Fig. 3.7 Schematic side views of (a) a bulk truncated surface; (b) a relaxed surface; and (c) a reconstructed surface (taken from Ref.[76]).

In some cases, rearrangement of the charge by surface relaxation in the first atomic layer cannot relieve all stresses and still generate the in-plane stress. This in-plane stress can then be relieved by reconstruction of surface atoms to more dense close-packed structures [77].

Surface reconstruction

For those surfaces that cannot be fully stabilised by simple relaxation, their surface atoms undergo drastic arrangement, i.e., reconstruction. This process happens when the stress in the surface exceeds its elastic limit [76,79]. Surface reconstruction changes the equilibrium position and bonding of the surface atoms, resulting in the difference in periodicity and fundamental structures compared to those of in the bulk (Fig. 3.7c). This perturbation caused by the surface reconstruction propagates towards to the inner atomic layers until the bulk lattice is recovered [76,80]. Reconstruction occurs quite often on the semiconductors and polar surfaces. The presence of the high-energy dangling bonds on the covalent surfaces can be modified by the drastic atom arrangement. Reconstruction is driven by reduction of surface free energy. It is capable to minimise or even eliminate the quantity of dangling bonds and facilitate rebonding of surface atoms [81].

Many metal oxide structures are formed by interstitially locating metal cations in the oxide close-packed structures [64]. Based on the scientific interest on the different crystallographic planes, metal oxide surfaces can be created by different methods to form either non-polar or polar surfaces. Three main methods were mentioned by Freund *et al*. [82], which are 1) cleavage along the specific crystal plane to form the non-polar surface; 2) fracture a crystallographic plane mechanically or spark erosion followed by the surface polishing; 3) grow oxide film on the metallic substrate to form polar or non-polar surfaces.

Polar metal oxide surfaces such as NiO(111) and $SrTiO_3$(110) are electrostatically unstable due to the divergent of their surface potential per unit charge [83]. These unstable surfaces can be stabilised by modification of the numbers of surface ions though geometric reconstruction. Most metal oxide (especially the transition metal oxide) surfaces present non-stoichiometric features, which can be accommodated by either surface reconstructions or surface stabilisation of substoichiometric phases [84].

Surface treatment facilitates reconstructions on metal oxide surfaces [84]. Beyond the surface reconstruction, more fascinating features such as the nanostructures are formed. The formation of nanostructures on the oxide surfaces has attracted much more scientific attention since the 1990s. Reconstructed surfaces could act as a template for the growth of ordered nanostructures with dimension range of 1-100 nm. Several studies have shown that the linear and dots nanostructures can form on the $SrTiO_3$(001) surfaces [11,12,85-87] (details are described in Sec. 3.5.3).

3.4 Properties of Nanostructures and Surfaces

Nanostructures are produced when the dimension scales in the periodic infinite solid crystals on surfaces are reduced into the small amount of atom groups. For nanomaterials, the proportion of atoms on the surface is much greater than that of in the bulk, and the percentage increases with decreasing the nanostructure size.

The structure, symmetrical coordination, and even stoichiometry of the surface can be different from bulk [88]. For instance, the bond percolation, coordination numbers and electron-lattice coupling of one-dimensional metal oxide differ substantially from those of in the bulk [89] . Other examples can be found in the studies of metal oxides nanostructures

such as ZnO [90-98], SnO_2 [99,100], TiO_2 [15,101,102], In_2O_3 [103], WO_3 [104,105], TeO_2 [106], CuO [107,108], CdO [109,110], Fe_2O_3 [111,112] and MoO_3 [113], which are reported to exhibit fascinating novel properties compared to their bulk analogues. This highlights the importance of the surface structures in the discovery of novel properties of nanomaterials.

The electronic structures on the surface are different compared to those of in the bulk. The electron constraint within the surface is highly influenced by the composition, size and shape of the materials which yields the specific chemical, physical, electrical and optical properties [87,100,107,108]. Structure dimensionality also presents a strong effect in determining the properties of the nanomaterials [114,115]. Importantly, control of the size and shape of the nanomaterials can extend their application in nanodevices. Discovery of the carbon nanotube has sparked the scientific interest and attention on the one-dimensional nanostructures with the demand of the fabrication of the low cost, small size and low power consumption devices [115,116]. Recently, various materials such as Si [117,118], Ge [119,120], SiO_2 [121], MgO [122], GaN [123,124], β-SiC [125] and ZnO [126,127] have been synthesised into nanowires, showing good performance in the relevant applications. Also, quantum dots made from semiconducting materials have attracted scientific interest because they present atom-like behaviour with discrete energy of electrons and holes. Study of adsorption and luminescent spectra on the quantum dots has been carried out for a few decades. It found that these two properties are highly dependent on the properties of semiconductors and the size of quantum dots [128].

3.4.1 Catalytic property

Catalysis is one of the important applications for nanomaterials. Catalysis process generally occurs at the surface of the materials. The catalytic efficiency and reactivity are highly depended on the distribution of the active sites which are primarily affected by the material structures [129]. Active catalysts generally contain small particles in either single or polycrystals form with sizes less than 10 nm and sometimes even smaller than 1 nm [43,130,131]. Careful control of crystal sizes and their surface atom arrangement are likely to change the physical and chemical properties of the heterogeneous catalysts, leading to the modification of their activity and selectivity in the practical applications [132,133].

Mostly, catalytic activity is improved as increase of surface area, by reduction the size of the catalyst particles [129]. For example, bulk Au is known as chemically and catalytically inert. However, if the size of Au particle is reduced to 2-5 nm and finely disperse them in the reducible oxide matrix, the whole system will turn to be highly active towards CO oxidation at low temperature [134].

A high-performance of the metal-oxides catalysts relies on a controlled size and shape distribution of metal particles in this system. However, some fabrication routes such as wet chemistry and evaporation methods still bring the problem in obtaining uniform objects [135,136]. To tackle this problem, some studies have been carried out to grow metal crystals epitaxially on oxide supports which formed the nanocrystals in controlled and tailored shapes [24,55].

3.4.2 Optical property

Nanostructures have potential use in optical devices because of their high surface-to-volume ratio, chemical stability and high exciton binding energy [100]. Optical property is achieved by electron transport in the way either from the valence band to the conduction band or vice versa. Many studies showed that chemical, physical and electrical properties in the nanoscale are mainly determined by the composition, size and shape of the materials [92,99,100]. Tawale *et al*. studied the shape effect on the nanostructure properties using SnO_2 nanostructures [100]. Three different shapes (spherical, octahedral and facet) of SnO_2 nanostructures were studied, showing the blue and green emission from these nanostructures in the visible region with altered optical properties from different shapes. They concluded that optical properties i.e., absorption and photoluminescence are strongly depended on the shapes of the oxide structures. The luminescence properties are changed after the shapes of nanomaterials are modified, suggesting a potential use in optical applications which requires different luminescence properties.

Similar shape and size effects were also noticed by other researchers who studied the ZnO nanostructures [92]. The shape-varied ZnO nanostructures, produced by different synthesis methods, showed different room temperature photoluminescence emission spectra with varied peak positions. Since the defect density at the surface is higher than those of in the bulk, it suggested that the variation of peaks may be due to the difference in the defect concentration on the nanostructures with various shapes that present different surface-to-volume ratios [92].

3.5 The Surface Structures of $SrTiO_3$, Nanostructures, Anatase and Properties

3.5.1 Introduction to $SrTiO_3$

$SrTiO_3$ is one type of perovskites. It has a cubic crystalline structure at room temperature with lattice parameter of 0.3905 nm. Stoichiometric $SrTiO_3$ is a good insulator with the band gap value about 3.2 eV at room temperature. Slightly doping $SrTiO_3$ with other elements can change it to semiconductor by substitution of Ti^{4+} and Sr^{2+} sites. N-type semiconductor is formed by doping with high pentavalent elements such as Nb^{5+}, Sb^{5+} and V^{5+}. P-type semiconductor is created by doping with trivalent elements such as Sc^{3+} [137]. Electronic structure calculation suggested that the top of valence band is mainly composed of O 2p state while the bottom of the conduction band is made up of Ti 3d state [138]. The interaction of Ti 3d-O 2p forms the corner-shared TiO_6 octahedra network which is the most important component dominating the electronic property of $SrTiO_3$ [138].

The unit cell of $SrTiO_3$ is shown in Fig. 3.8. The ionic charges are Sr^{2+} (at the cube centre), Ti^{4+} (at the cube corner) and O^{2-}(at the cube edge) [37]. Surfaces of $SrTiO_3$ have been studied since 1970, with the initial interest concerning the important role of surface defect in surface catalytic reaction [1]. Surface structures of the $SrTiO_3$ have now attracted more interest in the applications such as photonics devices [6,139], gas sensors [7], grain boundary barrier layer capacitors [8], thermoelectric materials [9] and photocatalysts [5]. Besides, $SrTiO_3$ can also be used as the substrate for growing thin film superconducting materials [10]. Also, two-dimensional electron gas can be formed between $SrTiO_3$ and $LaAlO_3$, which could use as novel oxide heterostructures [140,141]. There is no doubt that how $SrTiO_3$ performs in these applications strongly depends on the surface structures and

compositions. Meanwhile, as one of typical perovskites, understanding surface structures and properties of $SrTiO_3$ will benefit the study of other oxide surfaces.

3.5.2 Reconstructions on $SrTiO_3$(001) and (111) surfaces

Recently, reconstructions of the substrate surface have been reported as an important role to influence the epitaxial growth of perovskite oxide thin film (e.g., titanium and barium oxide) on $SrTiO_3$(001) surfaces [142]. Therefore, understanding and controlling surface terminations tend to become more important in the atomic layer-by-layer growth.

Surface reconstructions on $SrTiO_3$(001) surface

Viewing from <001> directions of $SrTiO_3$ crystal structure, alternating SrO and TiO_2 layers are stacked up to form bulk terminations with individual surface shown in Fig. 3.8 [37]. The distance between two similar planes (SrO and SrO or TiO_2 and TiO_2) is of the magnitude of 0.3905 nm.

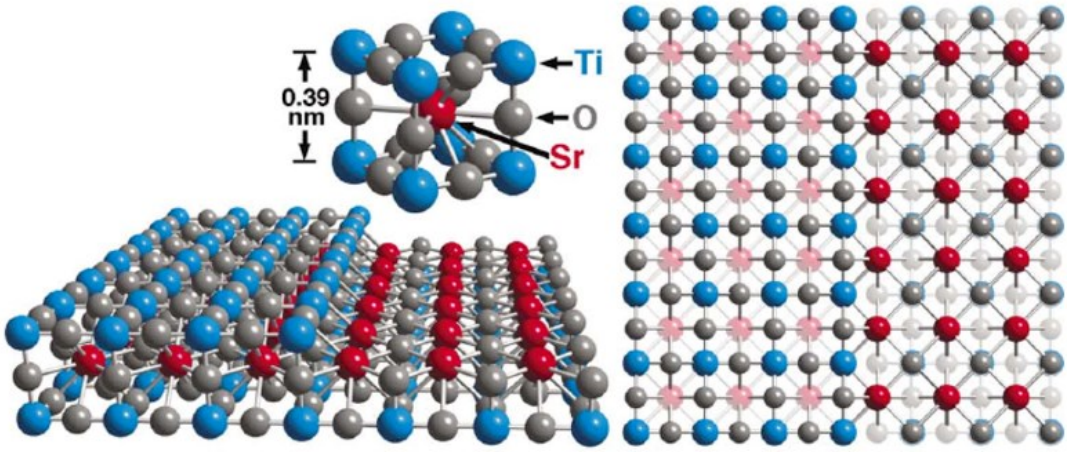


Fig. 3.8 $SrTiO_3$ unit cell and model of SrO and TiO_2 surface (taken from Ref. [37]).

Scanning tunnelling microscopy is used to investigate the atomic structures of Nb-doped $SrTiO_3(001)$ surfaces. To date, some types of reconstructions have been observed which are formed by annealing at different temperatures in UHV with or without Ar^+ ion sputtering. These reported reconstructions are (2×1) [37,74,143], (2×2) [40,144,145], $c(4 \times 4)$ [37,40], $c(4 \times 2)$ [37,146,147], $c(6 \times 2)$ [41,148], $(\sqrt{5} \times \sqrt{5})R26.6°$ [42,149-151] and $(\sqrt{13} \times \sqrt{13})R37.7°$ [150,152]. Tab. 3.1 summarised the relevant reconstructions including treatment conditions and descriptions.

Tab. 3.1 Summary of reconstructions reported on $SrTiO_3(001)$ surfaces

Reconstruction	**Treatment conditions**					**Description**	**Ref.**
	Ar^+ sputtering		**Annealing**			**Step height Å**	
	Energy keV	**Time min**	**Temp °C**	**Time**	**Environ-ment**		
(2×1)	BHF etching		600-800	30 mins	UHV	4.0	[37]
(2×2)	NH_4F–HF etching		950	2hrs	UHV	3.95±0.14	[40]
$c(4 \times 4)$	NH_4F–HF etching		1030 1100	1hr 20mins	UHV UHV	- -	[40] [37]
c(4×2)	0.5	10	900-1400	15mins	UHV	4.0	[37]
$c(6 \times 2)$	-	-	1100	3hrs	H_2 and O_2	4	[41]
$(\sqrt{5} \times \sqrt{5})R26.6°$	-	-	1400-1450	1hr+	UHV	3.91±0.07	[149]
$(\sqrt{13} \times \sqrt{13})R37.7°$	-	-	1100	15hrs	O_2	-	[152]

Erdman *et al*. solved TiO_2-riched (2×1) surface structure on $SrTiO_3(001)$ surface using high-resolution electron microscopy and the theoretical direct method including DFT calculation [74]. The (2×1) reconstruction was also observed by STM (Fig. 3.9) [37]. It exhibits the wavy step edges which are not aligned in any crystallographic directions. The step height is 4.0 Å which corresponds to one bulk $SrTiO_3$ unit cell.

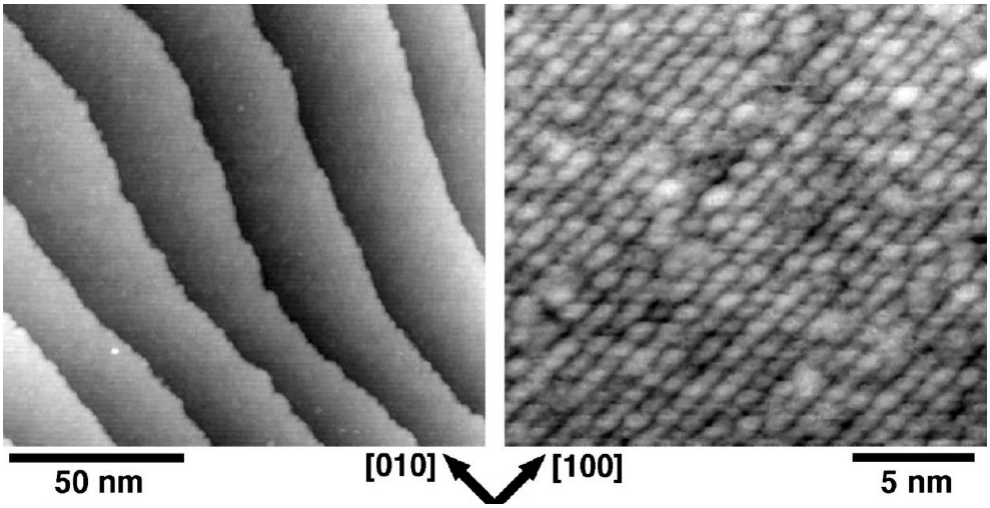


Fig. 3.9 STM images of $SrTiO_3$(001)-(2 × 1) reconstructed surface (imaging conditions: V_s= +2.3 V, I_t = 0.1 nA) (taken from Ref. [37]).

Silly *et al*. observed (2 × 2) reconstruction by STM. This surface structure was produced by UHV annealing of HF etched $SrTiO_3$(001) at temperature around 950°C for 2 hours [40]. (2 × 2) reconstructed surface has bright dots in four-fold symmetry (Fig. 3.10), which has also been confirmed by Density Functional Theory (DFT) calculation [145]. The step edges of (2 × 2) surface show wavy morphology without preferential crystallographic orientation [40]. The transformation from (2 × 2) into *c*(4 × 4) domains was observed when the (2 × 2) reconstructed sample was further annealed to the temperature around 1050°C [40].

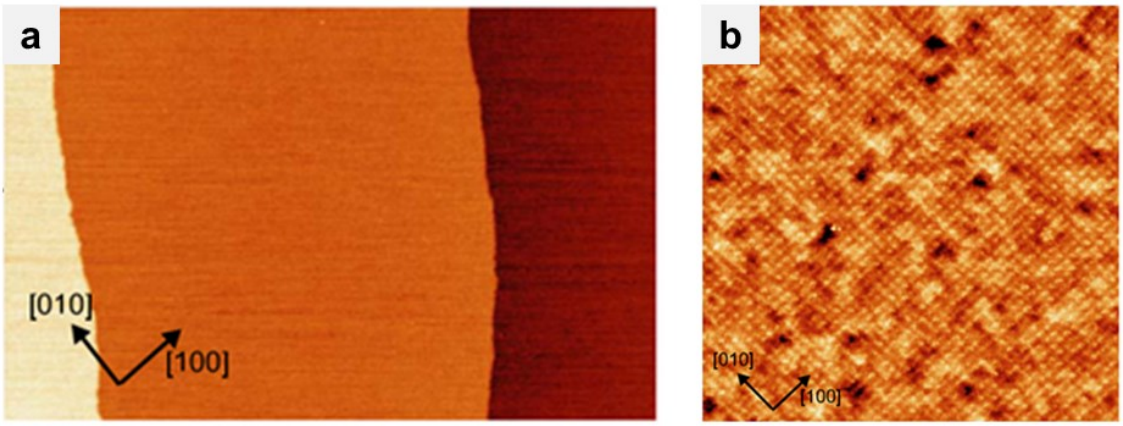


Fig. 3.10 STM images of (2 × 2) reconstruction formed on the $SrTiO_3$(001) surface.(a) STM image showing the terraces with wavy step edges (image size: 510 × 325 nm^2, V_s= +0.8 V, I_t = 0.3 nA). (b) STM image showing the detail of the reconstruction (image size: 35 × 35 nm^2 , V_s= +0.7 V, I_t = 0.3 nA) (taken from Ref. [40]).

Castell reported $c(4 \times 4)$ reconstruction in 2002 [37]. The $c(4 \times 4)$ structure was described as "brickwork" pattern and appeared short line structures broken down at every 1.6 nm (4 bulk unit cells) in [100] direction (Fig. 3.11a). In his study, the $c(4 \times 4)$ reconstruction was suggested to form from (2×1) area through ordering the defects [37].

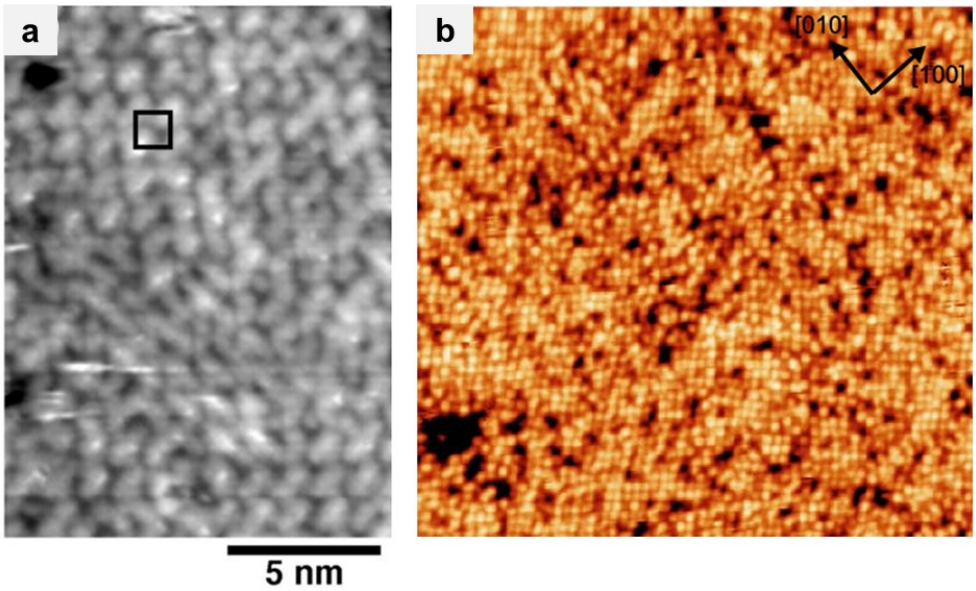


Fig. 3.11 (a) STM image of the (2×1)+$c(4 \times 4)$ reconstructed surface mainly with $c(4 \times 4)$ reconstruction, showing "brickwork pattern" reported by Castell [37] (V_s= +0.2 V, I_t = 10 nA). (b) STM image of $c(4 \times 4)$ reconstruction reported by Silly *et al*. [40] (image size: 75 × 72 nm^2, V_s= +2.0 V, I_t = 0.1 nA).

Silly *et al*. reported that $c(4 \times 4)$ reconstruction can also be formed by annealing the (2×2) reconstructured surface [40]. His finding of $c(4 \times 4)$ ordering (Fig. 3.1b) was announced to be not the same as the "brickwork" pattern (Fig. 3.1a) reported by Castell [37]. Dotted row structures (different as reported nanolines) were found in the (2×2) surface, suggesting as the precursor to evoke the formation of $c(4 \times 4)$ structure [40].

$c(4 \times 2)$ terminated surface shows straight step edges aligned in [010] and [100] directions with one unit cell step height (Fig. 3.12a). The atomic resolved structure was observed using STM by Castell (Fig. 3.12b) [37]. The $c(4 \times 2)$ reconstruction was also solved by Erdman *et al*.[147] using transmission electron diffraction combined with density function theory

(DFT). The structure unit of $c(4 \times 2)$ reconstruction was studied theoretically by Becerra-Toledo *et al*. [146]. Nanolines were reported to form on the $c(4 \times 2)$ reconstructed $SrTiO_3(001)$ surface after the sample was annealed at the temperature above 900°C. It suggests that these nanostructures are acted as the precursor or coexisted with nanolines [11,146].

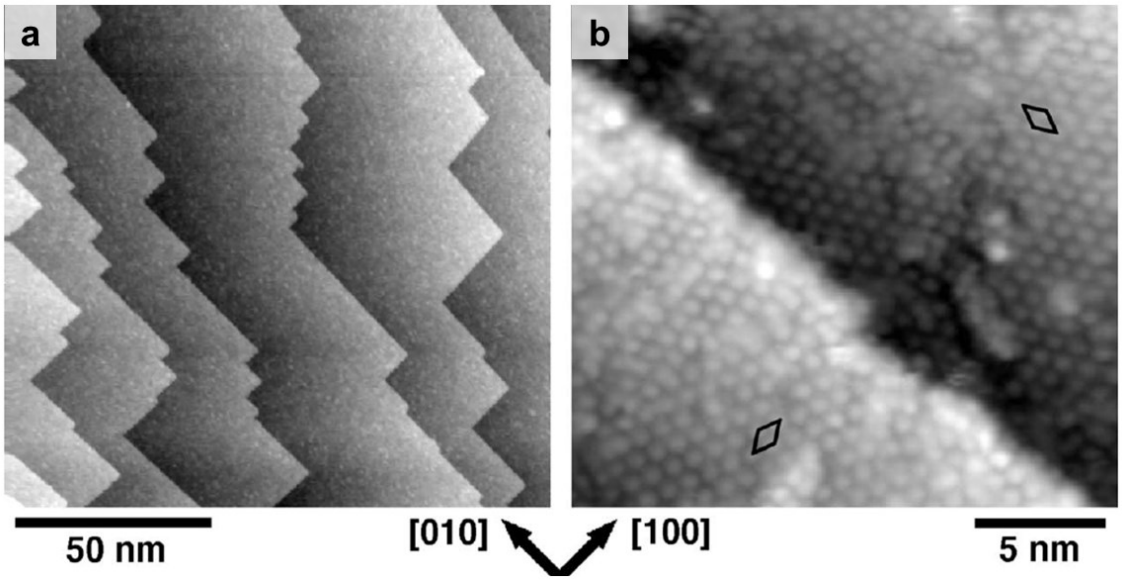


Fig. 3.12 STM images of the $c(4 \times 2)$ reconstructed surface. (a) STM image showing the straight step edges (V_s= +2.5 V, I_t = 0.2 nA). (b) Atomic resolved $c(4 \times 2)$ structure (V_s= +2.0 V, I_t = 0.1 nA) (taken from Ref. [37]).

$c(6 \times 2)$ type shows well-ordered and featureless terraces with 2 Å (half unit cell) step height (Fig. 3.13a). The close-up STM image (Fig. 3.13b) shows the row structure with spacing of 12 Å aligned in [010] and [100] directions [148]. This study showed $c(6 \times 2)$ surface was extremely stable in UHV and even retained the structure when the sample was exposed into 200 mbar oxygen for 5 minutes, ambient air for 30 minutes and air to 10 days [41,148].

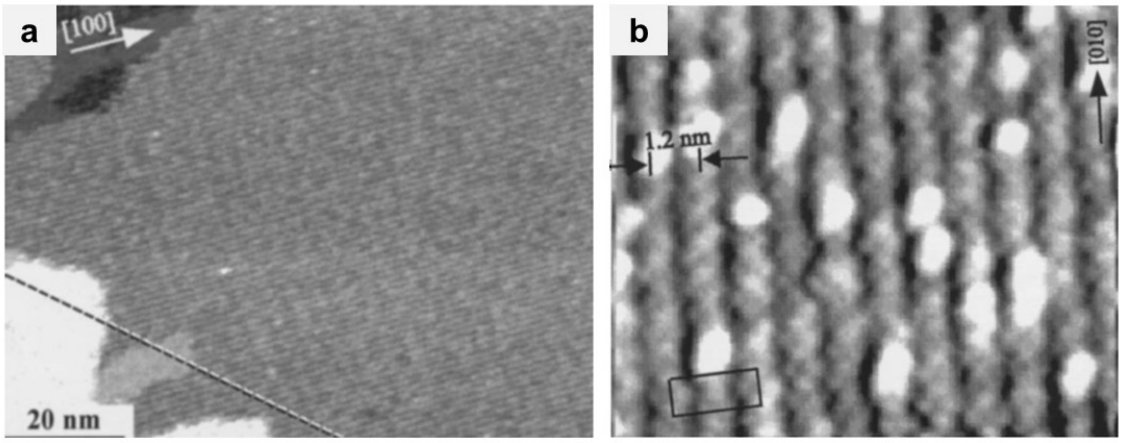


Fig. 3.13 STM images of $c(6 \times 2)$ surface reconstruction. (a) Large-scale STM image showing long-range ordered $c(6 \times 2)$ surface (V_s = +1.8 V, I_t = 0.31 nA). (b) High resolution STM image (V_s= +2.1 V, I_t = 0.28 nA) (taken from Ref. [41]).

The first atomic resolution image of $(\sqrt{5} \times \sqrt{5})R26.6°$ surface was reported by Matsumoto *et al*. in 1992 [151]. $(\sqrt{5} \times \sqrt{5})R26.6°$ surface shows disordered terraces separated by wavy step edges with step height of 3.9 Å. Kubo and Nazoye [42,150] also found the same structure on the $SrTiO_3(100)$ sample after $c(4 \times 4)$ terminated surface was annealed at 1200°C for several seconds. The atomic resolved STM image of $(\sqrt{5} \times \sqrt{5})R26.6°$ is shown in Fig. 3.14 [150]. Newell *et al*. found that some islands formed on $(\sqrt{5} \times \sqrt{5})R26.6°$ surface which was suggested to be TiO islands [149].

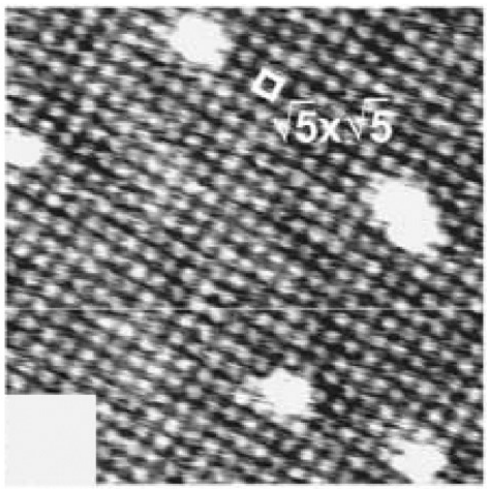


Fig. 3.14 STM image of $(\sqrt{5} \times \sqrt{5})R26.6°$ reconstruction on the $SrTiO_3(100)$ surface (image size: 20 × 20 nm^2, V_s = +0.55 V, I_t = 0.01 nA) (taken from Ref. [150]).

Naito and Sato reported the formation of $(\sqrt{13} \times \sqrt{13})R37.7°$ reconstruction using Reflection High-energy Electron Diffraction (RHEED) in 1994 [152]. The structure was prepared by annealing the sample at 800-1100°C in oxygen atmosphere. The $(\sqrt{13} \times \sqrt{13})R37.7°$ reconstruction (Fig. 3.15) was later observed by Kubo and Nozoye in 2003 [150], when the $(\sqrt{5} \times \sqrt{5})R26.6°$ terminated sample was further annealed at 1250°C for several seconds. Kubo and Nozoye also proved a phase transition between $(\sqrt{5} \times \sqrt{5})R26.6°$ and $(\sqrt{13} \times \sqrt{13})R37.7°$ using the Sr adatom structure model [150].

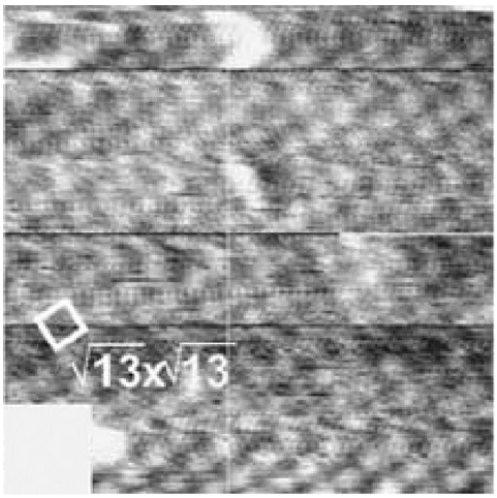


Fig. 3.15 STM image of $(\sqrt{13} \times \sqrt{13})R37.7°$ reconstruction formed on $SrTiO_3(100)$ surface (image size: 20 × 20 nm^2, V_s = +0.5 V, I_t = 0.01 nA) (taken from Ref. [150]).

Surface reconstructions on $SrTiO_3(111)$ surfaces

The (111) surface of $SrTiO_3$ unit cell is shown in Fig. 3.16. View from <111> directions, the surface is made up of the alternating Ti^{4+} and SrO_3^{4-} planes. The interplanar spacing between two similar planes (Ti^{4+} and Ti^{4+} or SrO_3^{4-} and SrO_3^{4-}) is of the magnitude of 0.225 nm (i.e., d_{111}). The spacing between two dissimilar planes (Ti^{4+} and SrO_3^{4-}) is 0.113 nm (i.e., $\frac{1}{2}d_{111}$). The negatively and positively charged planes create a macroscopic dipole perpendicular to the surface. In order to stabilise the polar surface such as $SrTiO_3(111)$, it needs to remove the dipole on the surface. Four mechanisms are suggested

to remove the surface dipole [39]. They are changing the surface stoichiometry; redistribution of electrons in the surface region; adsorption of atoms or molecules and faceting. These allow to form different reconstructions with different compositions on $SrTiO_3$(111) surfaces. The reconstructions reported are (1 × 1) [153,154], (2 × 2) [155], (3 × 3) [38,155,156], (4 × 4) [38,153,155,157], (5 × 5) [38,157], (6 × 6) [38,156,157], (9/5 × 9/5) [38,156], ($\sqrt{7} \times \sqrt{7}$)*R*19.1° [39] and ($\sqrt{13} \times \sqrt{13}$)*R*13.9° [39].

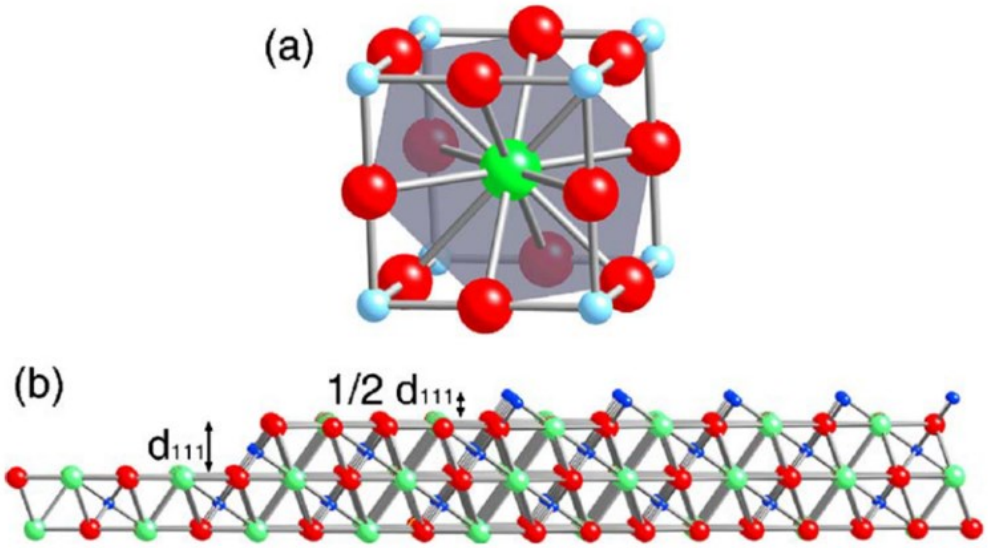


Fig. 3.16 (a) Unit cell of $SrTiO_3$ with (111) surface indicated; (b) Side view of the bulk terminated $SrTiO_3$(111) surface. It is composed of Ti^{4+} plane and SrO_3^{4-} plane. The spacing between two dissimilar planes (Ti^{4+} and SrO_3^{4-} plane) is marked as $1/2d_{111}$), the distance between two similar planes (Ti^{4+} and Ti^{4+} or SrO_3^{4-} and SrO_3^{4-} planes) is marked as d_{111} (taken from Ref. [39]).

The first major work on $SrTiO_3$(111) surface was studied by Lo and Somorjai in 1978 [158]. Due to the lack of surface-sensitive techniques such as STM to explore the structure of (111) surface, most works before the 1990s on $SrTiO_3$(111) surface were focused on studying the composition and ion species termination of the (111) and clean (111)-(1 × 1) surfaces. The samples were treated at high-temperature, room temperature with or without Ar^+ ion sputtering and analysed by the available techniques such as LEED, AES and UPS. Somorjai with his co-worker Ferrer explored the photo-dissociative properties of (111) surface when

the sample was interacted with water [159,160]. In 1998, Haruyama *et al*. produced the (4 × 4) and (1 × 1) reconstructions on $SrTiO_3$(111) surface with surface structures confirmed by LEED [153].

The surface termination and topography of the $SrTiO_3$(111) is influenced by annealing temperature, environment (UHV, air or P_{O2}) and also whether the sample is sputtered before anneal. The preparation methods and description of reported reconstructions are summarised in Tab. 3.2.

Tab. 3.2 Summary of reconstructions reported on $SrTiO_3$(111) surfaces

Reconstruction	**Treatment conditions**					**Description**		**Ref.**
	Ar^+ sputtering		**Annealing**			**Step height nm**	**Surface termination ***	
	Energy keV	**Time min**	**Temp °C**	**Time**	**Environment**			
(1 × 1)	N	N	800	1hr	UHV	-	-	[153]
(2 × 2)	0.5	6	1280	5hrs	PO_2=6×10^{-4} Pa	-	-	[155]
(3 × 3)	0.5	10	1150	5hrs	PO_2=4.0×10^{-4} Pa	0.22	Ti/Sr=1.56	[38]
	0.5	6	1150	5hrs	PO_2=4.5×10^{-4} Pa	-		[155]
(4 × 4)	0.5	10	950	30mins	UHV	0.217±0.016	Ti/Sr=2.43	[38]
	N	N	1200	5mins	UHV	-	-	[153]
	1	10	900	1hr+	P_{O_2}=5×10^{-6} mbar	0.223±0.008	-	[157]
	0.5	6	1000	1hr	UHV	-	-	[155]
(5 × 5)	0.5	20	1000	30mins	UHV	0.224±0.012	Ti/Sr=2.26	[38]
(6 × 6)	0.5	10	950	30mins	UHV	0.217±0.016	Ti/Sr=1.24	[38]
(9/5 × 9/5)	0.5	10	1100	10hrs	1 atm air	0.219±0.014	Ti/Sr=1.24	[38]
(√7 × √7)*R*19.1°	N	N	850	30mins	UHV	0.21±0.02	Ti/Sr=1.13	[39]
(√13 × √13)*R*13.9°	N	N	850	30mins	UHV	0.21±0.02	Ti/Sr=1.13	[39]
TiO(111)-(2 × 2)	Y	Y	1400	variable	UHV	-	-	[38]

*For cleaved surface Ti/Sr=1, all data are compared to the cleaved surface.

TEM and transmission diffraction pattern studied by Chiaramonti *et al.* [156] suggested that the formation of different reconstructions on $SrTiO_3$(111) surfaces were determined by annealing atmosphere, durations and temperatures. For the shortest annealing duration (0.5h), the reconstruction was mainly dependent on the oxygen partial pressure. For the longest annealing duration (10h), the reconstruction was primarily influenced by the annealing temperature. The reconstructions produced by the intermediate annealing duration showed the effect from both temperature and oxygen partial pressure, which produced the co-existence of three reconstructions, i.e., (3×3), (6×6) and (9×9). The (9×9) named in their study is the same reconstruction as the $(9/5 \times 9/5)$, which observed by other researchers. Chiaramonti *et al.* also reported that same reconstruction can form at different annealing conditions [156]. For instance, (6×6) was produced after short anneals with high oxygen partial pressure as well as long anneals at lower temperature.

Tanaka and Kawai [161] showed that a smooth surface assigned with Sr-O_{3-x} termination, with step height of integral multiple of d_{111} lattice spacing, can be produced when sample was annealed in UHV at 1180°C. A more granular surface terminated with a Ti layer, with step height equivalent to d_{111} lattice spacing, was formed when the sample was annealed at 1220°C. RHEED analysis showed that both surfaces had the (1×1) periodicity. When the sample was annealed at the same UHV condition at 1200 °C, a terraced surface was produced with the step height of integral multiple of $\frac{1}{2}d_{111}$.

Sigmund *et al*. [162] observed a smooth and terraced surface by SEM when the sample was annealed at 950°C for 2 hours in UHV. The step height, measured using STM, was reported to be as 12-30 Å corresponding to 4-10 d_{111} lattice spacing. Sekiguchi *et al*. [163,164] analysed the structures of $SrTiO_3$(111) polar surface using AFM and XPS. Trench structures with step height of even multiples of 0.225 nm (i.e., d_{111}) were observed when the sample

was annealed in oxygen. When sample was annealed in Ar gas, large triangular terraces with step height multiples of 0.113 nm (i.e.. $0.5d_{111}$) were formed on $SrTiO_3(111)$ surface. The formation of the structure in a fractal shape (called Sierpinski's gasket structures) with different sizes was observed when the sample was annealed in air. Also, the STM/MEIS study by Gomann *et al*. [165] showed that high temperature annealing (up to 1000°C) for 1 hour in UHV or synthetic air caused microfaceting of the topmost layer of the $SrTiO_3(111)$ surface. Pojani *et al.* [166,167] suggested that Ti species is a dominant and most stable termination in the O-rich condition, while SrO_3 species become a more stable termination in the O-poor condition.

Russell and Castell [39] reported a group of reconstructions formed on $SrTiO_3(111)$ surfaces. The atomic resolved STM images of these reconstructions are shown in Fig. 3.17. Sputtered and non-sputtered surface preparation methods produce different surface reconstructions. Direct UHV annealing the sample without Ar^+ sputtering give the formation of $(\sqrt{7} \times \sqrt{7})R19.1°$ and $(\sqrt{13} \times \sqrt{13})R13.9°$ reconstructions (Fig. 3.17g and h). These two reconstructions are usually co-existed on (111) surface prepared by the same condition, suggesting a similar surface energy and composition between these two structures. In addition, they reported the most complete works of the (n × n) reconstruction families on the (111) surfaces [38]. Group of the samples were prepared by Ar^+ sputtering and annealing in either UHV or O_2 conditions. Varing the sputtering conditions and O_2 pressures cause the variations in oxygen stoichiometry and produce a family of (n × n) reconstructions i.e. (5 × 5), (6 × 6)/(4 × 4), (3 × 3) and (9/5 × 9/5) reconstructions on $SrTiO_3(111)$ surfaces (Fig. 3.17a-e). TiO-(111)-(2 × 2) nanophase was also formed by extensive UHV annealing (Fig. 3.17f). Their ASE study of these (n × n) reconstructions, regarding the compositions of Ti, Sr and O species, suggests that:

Ti-rich TiO-(111)-(2 × 2)>(5 × 5)>(6 × 6)/(4 × 4)>(3 × 3)>(9/5 × 9/5) **Sr-rich**

O-rich (9/5 × 9/5)>(3 × 3)>(4 × 4)>(6 × 6)>(5 × 5) **O-depleted**

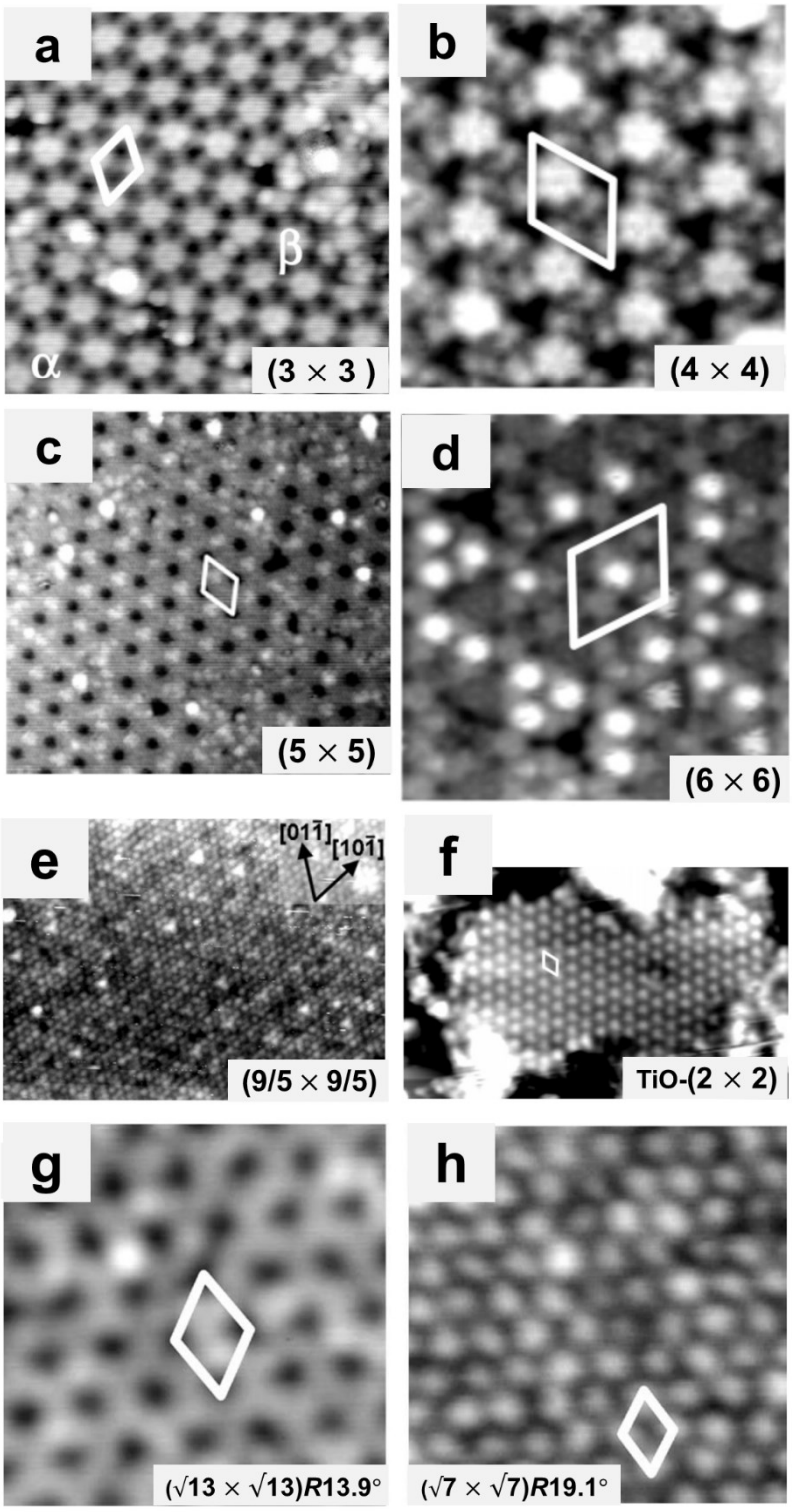


Fig. 3.17 STM images of reconstructions formed on $SrTiO_3$(111) surfaces. The reconstruction types are indicated in each images with surface unit cell highlighted. The image size and imaging conditions for each image are: (a) 14 × 14 nm^2, V_s = +2.0 V, I_t = 0.4 nA; (b) 9 × 9 nm^2, V_s = +2.0 V, I_t = 0.5 nA; (c) 28 × 32 nm^2, V_s = +2.6 V, I_t = 0.2 nA; (d) 13 × 13 nm^2, V_s = +1.86 V, I_t = 0.17 nA; (e) 42 × 32 nm^2, V_s = +2.0 V, I_t = 0.1 nA; (f) 14 × 8.5 nm^2, V_s = -1.0 V, I_t = 0.5 nA; (g) 12 × 12 nm^2, V_s = +3.6 V, I_t = 0.12 nA; (h) 12 × 12 nm^2, V_s= +2.14 V, I_t = 0.1 nA (adapted from Refs. [38,39]).

Some theoretical studies were also carried out to analyse $SrTiO_3$(111) and its reconstructed surfaces. Marks *et al*. studied the (1 × 1) reconstruction unit cell by DFT calculation [168]. They compared the different methods of the atomic-level structure solution for the (1 × 1) surface and generated a more accurate low energy TiO_2-rich configurations with octahedral co-ordination. They suggested this modified model could act at the template for building either TiO or Ti_2O_3 layer to satisfy with experimental observations. Their later study, combined with TEM/DFT modelling and STM, reported the structures for the (n × n) reconstructions ($2 \leq n \leq 4$). The detail of the structure models with corresponding STM images can be found in Ref. [155].

In summary, $SrTiO_3$(001) and (111) surfaces can accommodate a wide range of surface reconstructions, and various techniques have been applied to resolve their structures and compositions. The structures are studied by LEED, TEM and STM and compositions are analysed by XPS and AES. DFT calculation gives the knowledge in atomic configuration of these structures from the theoretical aspect. The formation of different types of reconstructions is determined by several factors such as pre-treatment preparations i.e. if the surface has been sputtered or not, annealing temperatures, durations and environment. The majority of the surface reconstructions are formed at a specific temperature range and annealing duration. Further annealing of one reconstruction at higher temperatures may cause the transformation into another reconstructions e.g. (2×2) to *c*(4×4) [40] and ($\sqrt{5} \times \sqrt{5}$)*R*26.6° to ($\sqrt{13} \times \sqrt{13}$)*R*37.7° [150] on $SrTiO_3$(001) surfaces. Some reconstructions can co-exist on the surface e.g. ($\sqrt{7} \times \sqrt{7}$)*R*19.1° and ($\sqrt{13} \times \sqrt{13}$)*R*13.9° [39] on $SrTiO_3$(111), suggesting a similar surface energy and compositions. Therefore, by carefully changing the treatment conditions, certain types of reconstructions are able to form on $SrTiO_3$(001) and (111) surfaces for further studies.

3.5.3 Nanostructures on $SrTiO_3$(001) surface

Nanostructures are useful in novel electronic devices such as single electron transistors and quantum dot lasers. The good performance of these products relies highly on the growth of the self-assembled nanostructures. Most scientific interest was initially focused on the semiconductor materials systems, for instance, growth of Ge island on Si substrate [169,170], creation of $ErSi_2$ nanowires on Si [171,172]. These materials systems work well to some extent. However, a large scattering of the size distribution of these nanostructure grown on semiconductor substrates may hinder their use in more precise-restrictive applications. These drawbacks encourage the researchers to explore the growth of nanostructures on other substrates such as insulating oxide crystals to precisely control the size and ordering of the nanostructures. Oxide surfaces such as $SrTiO_3$, which is electrical insulating, is a competitive candidate to grow nanostructures. Formation of the array of nanostructures (e.g., nanowires and nanodots) on $SrTiO_3$ surfaces shows the potential use in novel electronic application [11-13,85,86].

Castell first observed the nucleation of nanolines on the $c(4 \times 2)$ surface under STM in 2002 [11]. Since then, several studies reported the formation of nanostructures on $SrTiO_3$(001) surfaces [12,13,85,86,146]. These experiments involved Ar^+ ion sputtering and annealing at temperature from 850 to 1200°C, which produces the non-stoichiometry and TiO_x-rich one dimensional nanostructures on $SrTiO_3$(001) surfaces. These nanostructures have close-packed domains aligning in the <001> crystallographic directions. The relevant surface nanostructures are summarised in Tab. 3.3 with corresponding STM images depicted in Fig. 3.18a-f.

Tab. 3.3 Summary of TiO_2-rich nanostructures formed on $SrTiO_3$(001) surfaces

	Types	Treatment conditions					Recon.	Ref.
		Ar^+ sputtering		Annealing				
		Energy keV	Time mins	Temp °C	Time mins	Enviro -ment		
Nanolines	Dilines	1	10	800-880	40-60	UHV	(6 × 2)	[85]
	Meta-diline	0.5-3	7-15	1000			(6 × 2)	[12]
	triline	1	10	890-900	45	UHV	(9 × 2)	[85]
	tetraline	1	10	1000*	>1h	UHV	(12 × 2)	[12]
Trenches or waffles		0.5-3	7-15	950 (on meta-diline surface) UHV			(6 × 8)	[12]
Cross-dot (nanodots)		0.5-3	7-15	930-970*	30	UHV	(7 × 4)	[12]

*Means repeat annealing

The unit cell of each type of nanostructure is marked with a rectangle in the STM images. Nanolines (dilines, meta-dilines, trilines, tetraline), trenches or waffles and nanodots are the six common nanostructures formed on $SrTiO_3$(001) surfaces. All nanolines consist of parallel rows oriented in <001> directions with certain periodicity in the closed packed domains. Specifically, dilines are made up of two parallel rows of well-ordered domains (Fig. 3.18a), where the bright spots are composed of the linked group of 4 titanium atoms and 7.5 oxygen atoms [85]. Square configuration and zigzag configuration are the two typical features observed in the diline nanostructures. Dilines exhibit (6 × 2) periodicity with referencing to the $SrTiO_3$(001) bulk unit cell. The spots separation along the rows is 0.8 nm corresponding to the twice of bulk unit cell. Meta-diline structures (Fig. 3.18b) appear to be the degenerated dilines however still exhibits same symmetry as diline structures. The periodicity in each domain shows (6 × 2) configuration. Each triline nanostructure consists of three parallel rows (two outer rows and one backbone) aligned in

<001> directions (Fig. 3.18c). It exhibits (8 × 2) or (9 × 2) periodicity in the closed packed domains [12,85,146]. Separation between bright spots along the aligning direction is 0.8 nm (twice of the lattice constant) in outer rows and 0.39 nm (one lattice constant) in the backbone. The height ratio of backbone to side rows varies with STM imaging voltage (Fig. 3.19), signifying the electronic effect which convolutes the topography effect. Meanwhile, the variation of ratio indicates that the local density of states (LDOS) of backbones differs from that of surrounding structures [12]. Similar to trilines, tetraline structures (Fig. 3.18d) consist of three rows with (12 × 2) periodicity in a close-packed domain. The appearance of two outer rows of tetralines is same to those observed in other nanolines. However, unlike triline structures, tetraline nanostructures show the irregular nature of central row, presenting no discernible structure along the backbone. Meanwhile, the backbone appears bright under all imaging voltages and does not show voltage-dependent appearance [85]. Trenches or waffles structures with (6 × 8) periodicity (Fig. 3.18e) were found at meta-dilines sample when sample was further annealed at 950°C [12]. The trench structures are more than 0.2 nm in depth and cross-like structures are around 0.1 nm in height [12]. The cross dots (nanodots) structures with (7 × 4) periodicity (Fig. 3.18f) were formed at higher temperature and are more close-packed than the trench structures. Cross dots have the same height as dilines (0.2 nm) and 4 unit cells longitudinal periodicity arrayed in [100] and [010] directions [12]. It is suggested that nanolines are the precursor structures to form nanodots [11].

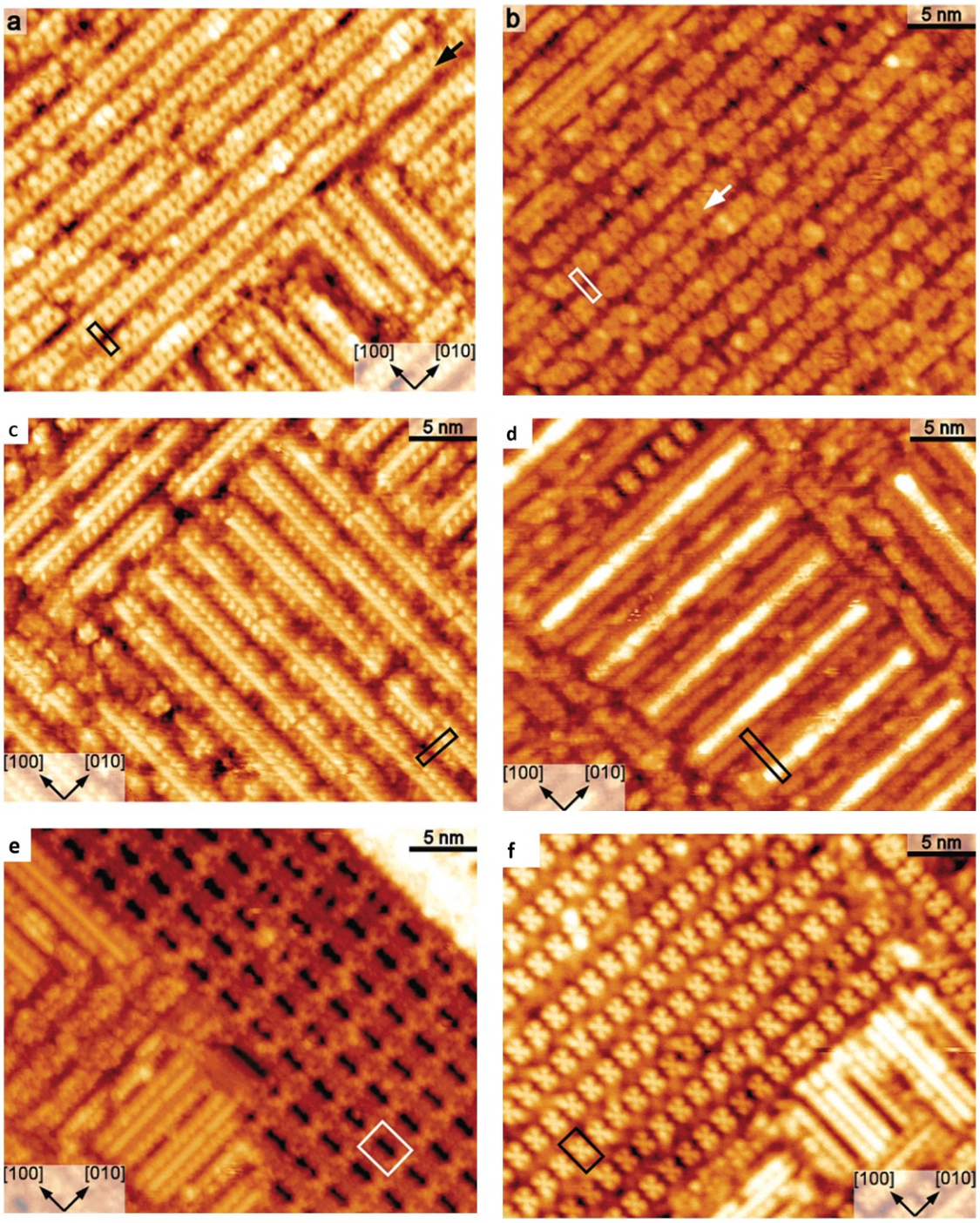


Fig. 3.18 STM images of different nanostructure phases on $SrTiO_3$(001) surfaces.(a) Dilines (image size: 35.0 × 28.5 nm^2, V_s = +1.4 V, I_t = 0.10 nA). (b) Meta-dilines (V_s = +1.4 V, I_t = 0.10 nA). (c) Trilines (V_s = +1.5 V, I_t = 0.30 nA). (d) Tetralines (V_s = +1.7 V, I_t = 0.30 nA). (e) Trench array or waffles (V_s = +0.8 V, I_t = 0.30 nA). (f) Cross dots (V_s = +1.1 V, I_t = 0.10 nA) (taken from Ref. [12]).

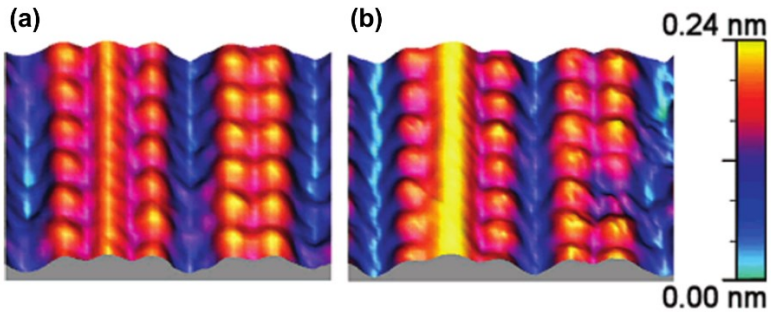


Fig. 3.19 3D-rendered STM images showing the height of the triline backbone varies as a function of the imaging bias (image size: 7.2 × 5.0 nm^2). (a) V_s = +0.8 V, I_t = 0.30 nA; (b) V_s = +2.2 V, I_t = 0.09 nA. The triline backbone in (b) is about 0.02 nm higher than in (a) (taken from Ref. [12]).

Surface compositions of dilines, trilines and tetralines nanostructures were studied by Marshall *et al*. using Core-level XPS [85]. It shows a notable difference in core-level XPS of Ti $2p_{3/2}$ peak of each of these three linear nanostructure. As shown in the XPS spectra (Fig. 3.20), the dilines decorated surface (Fig. 3.20a) is dominated by Ti^{4+} (90.5% of Ti $2p_{3/2}$ peak). Triline nanostructured sample (Fig. 3.20b) exhibits a significant proportion of Ti^{2+} which suggests a structural feature of this nanostructure. Tetraline structures contain no Ti^{2+} state and less Ti^{3+} than trilines (Fig. 3.20c). Since annealing nanostructured surface can induce the formation of anatase islands, Marshall *et al.* speculated that the central row of the tetralines contains TiO_2 [85].

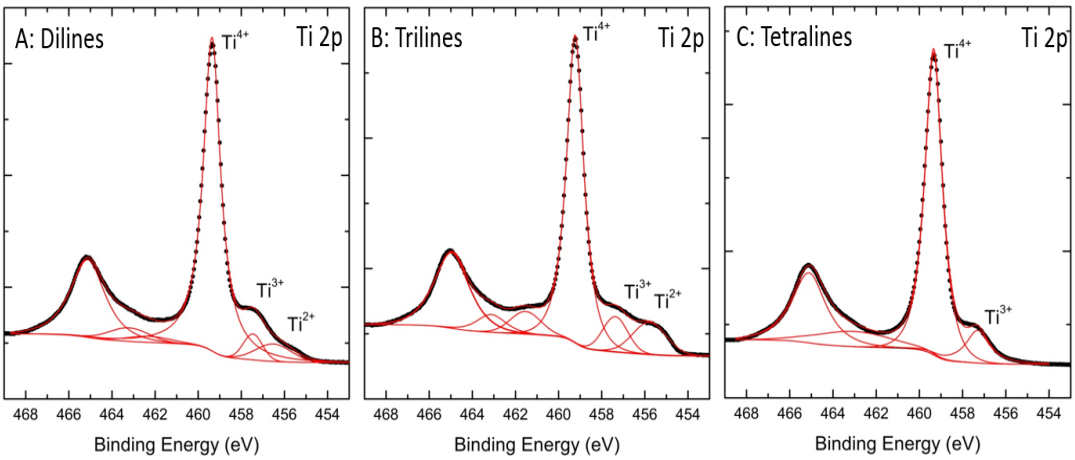


Fig. 3.20 Core level XPS: Ti 2p peaks of linear nanostructures. (a) Dilines; (b) Trilines and (c) Tetralines (taken from Ref. [85]).

3.5.4 Anatase on $SrTiO_3$(001) surface

Nanostructured titanium dioxide (TiO_2) is significantly important in the applications for environmental and energy-related field e.g., photocatalyst [15,173-175], catalyst supports [176-178], solar cell devices [179,180], optical devices [181,182], gas and humidity sensors [183], optoelectronic [184] and spintronic [185] devices. The unique physical and chemical properties of the TiO_2 crystal are derived from the intrinsic electric structure, size, shape and surface conditions [15]. The differences in crystallographic planes, phases and surface defects could affect the electronic and optical properties as well as interfacial transport of ionic species [15]. Especially for physicochemical properties such as adsorption, catalytic reactivity and selectivity, they are influenced by both surface atomic configurations and degree of exposure of reactive crystal surfaces [15,16].

TiO_2 has three polymorphs: anatase (tetragonal), rutile (tetragonal) and brookite (orthorhombic). Different from tetragonal rutile, tetragonal anatase composed of TiO_6 chain shows the different distortion inside of each octahedron (Fig. 3.21) [186]. The significant distorted octahedron in anatase leads its symmetry lower than that of orthorhombic structure. The distance between Ti-Ti ionic bonds becomes 3.79 Å and 3.04 Å. The interionic distance of Ti-O becomes 1.91 Å and 1.95 Å [186].

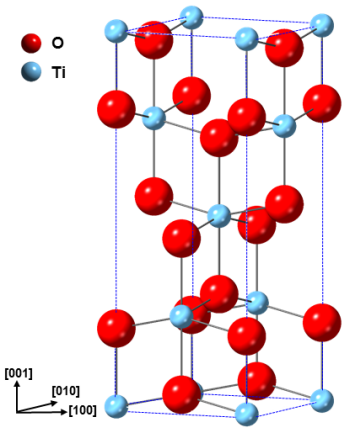


Fig. 3.21 Ball-and-stick model of an anatase unit cell. The blue balls represent Ti atoms. The red ball are O atoms.

Considering the extensive study on rutile TiO_2 [187-192], more research interest has now focused on the study of anatase phase [21,22,191-199]. Anatase TiO_2 shows promising properties in photocatalysis application based on its active surface chemistry, large band gap energy (~3.2 eV at room temperature) [200], and high electron mobility [201]. It has been reported that anatase TiO_2 polymorph is more catalytically active under ultraviolet irradiation than the other two polymorphs rutile and brookite, especially in the application of photocatalytic production of hydrogen from water [17-19].

The mineral anatase has a truncated bipyramidal structure exposed with pyramid (101) and capped with (001) surfaces in the natural environment [197]. Even though for a high purity mineral anatase, it still contains small amount of impurities. These impurities may affect the properties of anatase. For example the iron impurity in the mineral anatase may influence the surface electronic and chemical properties [202-204]. Meanwhile, natural anatase crystal is existed in a small size and thermodynamically unstable compared to rutile phase. The commercial anatase nanocrystallines or nanoparticles formed at low temperature is metastable and transform into the rutile phase irreversibly at higher temperature around 600-1100°C [201,205-207]. Also, the study conducted by Lazzeri and Selloni using Wulff construction and surface energy calculation showed that the equilibrium anatase crystal exposes large (101) surfaces and small (001) surfaces [208].

Various methods have been employed to produce stable anatase structures. Chemical transport reactions using reducing transport agents are reported as an efficient way to synthesise anatase TiO_2 single crystal [193,204]. It forms bipyramidal structures with exposure of either {111} [204] or {101} [19,186,204] pyramid faces. Berger *et al*. in 1993 first used chemical transport reaction method to syntheses single anatase crystal using NH_4Cl and CCl_4 or HCl and Cl_2 [209]. By studying the anatase crystals, they addressed that understanding electronic band structures of anatase can better explore the electrical and

optical properties of this type of materials. In the same institute, Sanjinés *et al*. carried out their first electron spectroscopy study on anatase TiO_2(101) formed by chemical transport reaction using reducing transport agent NH_4Cl or HCl [186]. Meanwhile, research done by their institute also showed that the electrical and optical properties of anatase are different from rutile. Specifically, anatase crystal showed a metallic-like resistivity behaviour with high mobility of n-type carriers at the temperature above 60 K. When the temperature is below 60 K, anatase crystals showed semiconducting behaviour with high photoluminescence response [210-212]. Kavan *et al*. applying the same method to grow anatase crystals using $TeCl_4$ as transporting agent to react with TiO_2 [19], produces the colourless transparent bipyramids anatase with well-developed and highly reflecting (101) faces. They also did the first electrochemical and photoelectrochemical investigation on single crystal anatase.

Anatase produced by chemical transport reaction method usually generates (101) surface. Because anatase (001) surface has higher surface energy (0.90 J/m^2) compared to that of (101) surface (0.44 J/m^2), its (001) surface is more reactive than thermodynamically stable (101) surface [20]. The fact of higher surface energy brings the difficulty in the production of large and stable anatase TiO_2(001). Considerable efforts have been devoted to produce high quality anatase single crystal with large stable (001) surface exposed using chemical transport reactions [209,213], chemical [187,214] and physical [204,215-219] deposition methods. Because anatase synthesised by transport reactions are often conducted with high-temperature gas phase reactions (around 1000°C), rutile phase is sometimes formed as a by-products during this process [220]. Among the above growth techniques, the chemical and physical deposition techniques involving epitaxial growth method such as chemical vapour deposition (CVD) [187,214], pulse laser deposition (PLD) [216-218], molecular beam epitaxy (MBE) [204,215,221] and reactive electron beam evaporation (REBE) [219] on

suitable substrates are considered effective to produce high quality and stable anatase TiO_2(001) single crystalline with large exposure surfaces. Most high quality anatase TiO_2(001) thin films were reported to grow epitaxially on the oxide substrates such as $SrTiO_3$(001) [21,22,142,194,200,204,214-219,221-223], $LaAlO_3$(110) [224] and $LaAlO_3$(001) [196,221,225,226] substrates.

Epitaxial growth of TiO_2 on $SrTiO_3$(001) substrates could well control the growth of anatase (001) surface. This is achieved due to the small degree of lattice mismatch between two materials i.e., -3.3% of parameter *a* between tetragonal anatase unit cell (a = 3.78 Å) and that of the cubic $SrTiO_3$(001) (a = 3.91 Å), compared to +17.4% for tetragonal rutile (a = 4.59Å). Herman and Gao [204] successfully produced anatase TiO_2(001) film on $SrTiO_3$(001) surface by oxygen plasma-assisted molecular beam epitaxy method. The experimental analysis using RHEED and LEED showed that the anatase surface was terminated with two-domain (1 × 4) reconstructions. Liang *et al*. [215] also applied MBE method to grow TiO_2(001) film on $SrTiO_3$(001) substrate in oxidising atmosphere. Ciancio *et al*. [216] used pulsed laser deposition method to grow epitaxial TiO_2 anatase thin film layer on $SrTiO_3$ and $LaAlO_3$ substrates. They found the inter-diffusion phenomenon occurred during TiO_2 deposition on the $SrTiO_3$ substrate where Sr atoms from the substrate diffused towards to the films. The pure TiO_2 film can only be produced after reaching the critical thickness of 20 nm [216].

Most epitaxial growth methods mention above are conducted by depositing Ti or TiO_2 powder onto warm substrates in oxygen environment. The film prepared by this process is relatively thick. The thickness ranges from 20 to 600 nm [204,216,219]. The anatase formed by direct TiO_2 deposition may be distributed non-uniformly on substrate with varied grain sizes or domain sizes of anatase [216,219].

Silly and Castell have established a self-assembly epitaxial growth method to create single domain anatase TiO_2-(1 × 4) islands on $SrTiO_3$(001) substrates in 2004 [21]. This method involves changing near-surface stoichiometry of $SrTiO_3$ crystal by sputtering and annealing the sample in UHV. Anatase TiO_2 islands were formed on the nanostructured $SrTiO_3$(001) surface (Fig. 3.22). Extensive anneals carried on the $SrTiO_3$(001) surface in UHV cause Ti and O enrichment on the surface. It is likely to initiate the formation of the epitaxial island of anatase TiO_2(001) on $SrTiO_3$(001) substrate [22].

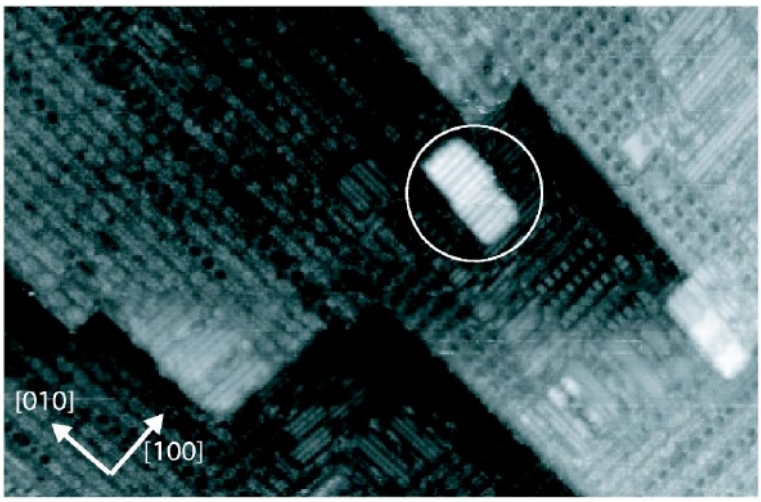


Fig. 3.22 STM image of anatase TiO_2 islands on the nanostructured $SrTiO_3$(001) surface (circled) (image size: 100 × 65 nm^2, V_s = +0.8 V, I_t = 0.3 nA) (taken from Ref. [21]).

Marshall and Castell studied the shape transition during the epitaxial growth of anatase islands on $SrTiO_3$(001) surface [22]. The lattice mismatch induces strain between substrate and anatase islands which is likely to be relieved by the shape transition. They reported that detachment of the O and Ti atoms were likely to occur when the sample was annealed at 1000-1030°C. It caused the strain-induced shape evolution and was predicated by Tersoff's theory [227]. When the sample was annealed at 930-1000°C, the strain was relieved by the formation of trenches accompanied by the minimal amount of mass transport of Ti and O atoms.

Because the surface energy of anatase (001) is high, it undergoes reconstruction to form low energy stable structures. The dominant reconstruction observed on anatase (001) surface is (1 × 4) reconstruction [21,191,199,214,223,228-230]. Only few studies reported the observation of small region with (1 × 3) reconstruction [223,229]. Stabilisation of (1 × 3) reconstruction is still unknown because most metastable (1 × 3) reconstruction was transformed into (1 × 4) reconstruction during sample surface preparation.

Several models have been proposed for anatase (001)-(1 × 4) reconstruction including microfacet model (MFM) (Fig. 3.23a) [214], added-and missing row model (AMR) (Fig. 3.23b) [215], ad-molecule model (ADM) (Fig. 3.23c) [230] and some modified ADMs [199,228].

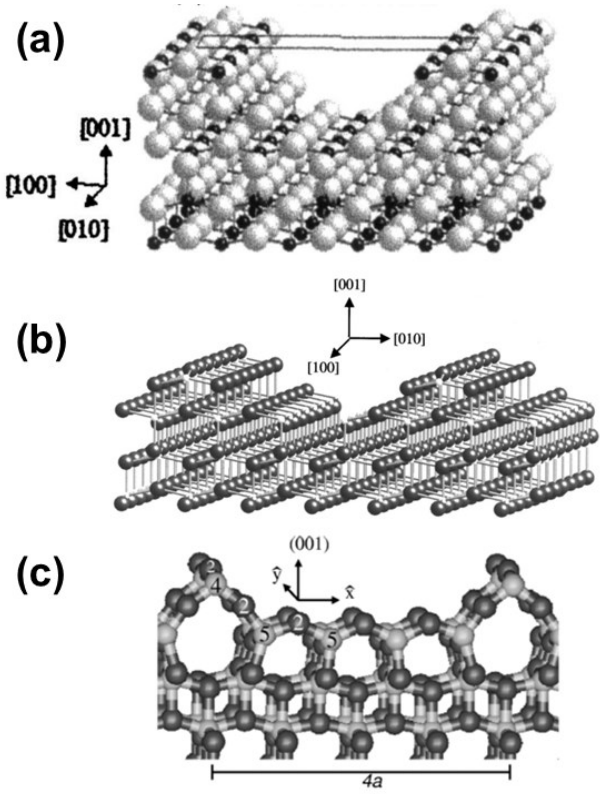


Fig. 3.23 Models proposed for anatase TiO_2(001)-(1 × 4) reconstruction. (a) Microfacet model viewing along [010] direction proposed by Herman *et al*.. Ti is represented as dark circle and O as light circle (taken from Ref. [214]). (b) AMR model of anatase TiO_2(001)-(1 × 4) reconstruction proposed by Liang *et al*.. Large balls represent O atoms and small balls are Ti atoms. (taken from Ref. [215]). (c) Relaxed structure of ADM model of (1 × 4) reconstruction proposed by Lazzeri and Selloni. Dark ball is O atoms and light ball is Ti atoms (taken from Ref. [230]).

Among these models, ad-molecule model (ADM) originally proposed by Lazzeri and Selloni (Fig. 3.23c) [230] is widely accepted and recently has been proved by Yuan *et al*. when they conducted real-time observations of the surface reconstruction of TiO_2(001) using environmental transmission electron microscopy (ETEM) [229].

3.6 Metal Nanocrystals on $SrTiO_3$ and Anatase

3.6.1 Theory of nanocrystal formation

Theoretical studies proved that surface energy is important to determine the equilibrium shape of nanocrystals grown on supported substrates. Winterbottom did his theoretical-mathematic study in the equilibrium shape of particle placed on the substrate [231]. He started the analysis by assuming that the whole system remains in the isothermal condition while the particle shape changes when volume is constant. Detailed mathematical calculation can be found in his work [231]. The theory developed by Winterbottom to predict the shapes of the particles at the interface is based on surface energy. He defined γ^*as the general surface energy of the particle. The γ^* value is determined by the surface energy of particle-substrate interface (γ_{SP}) and substrate-vapour surface (γ_{SV}), which $\gamma^* = \gamma_{SP} - \gamma_{SV}$ in particle-substrate system. Four types of substrate-particle configurations were studied based on the different wetting conditions, which $\gamma_{SP} - \gamma_{SV}$ represents the degree of binding or wetting between the particle and the substrate (summarised in Tab. 3.4). In the particle-substrate system, Winterbottom generalised a geometric construction from an orientation-dependent γ^* polar plot (Fig. 3.24) based on the Gibbs-Wulff construction.

Tab. 3.4 Wetting condition for different surface energy relations

Case	Surface energy relation	Configuration
Non- wetting	$(\gamma_{SP} - \gamma_{SV}) \geq \gamma_{PV}$	Fig. 3.24a
Partial-wetting 1	$0 < (\gamma_{SP} - \gamma_{SV}) < \gamma_{PV}$	Fig. 3.24b
Partial- wetting 2	$-\gamma_{PV} < (\gamma_{SP} - \gamma_{SV}) \leq 0$	Fig. 3.24c
Complete wetting	$(\gamma_{SP} - \gamma_{SV}) \leq -\gamma_{PV}$	Fig. 3.24d

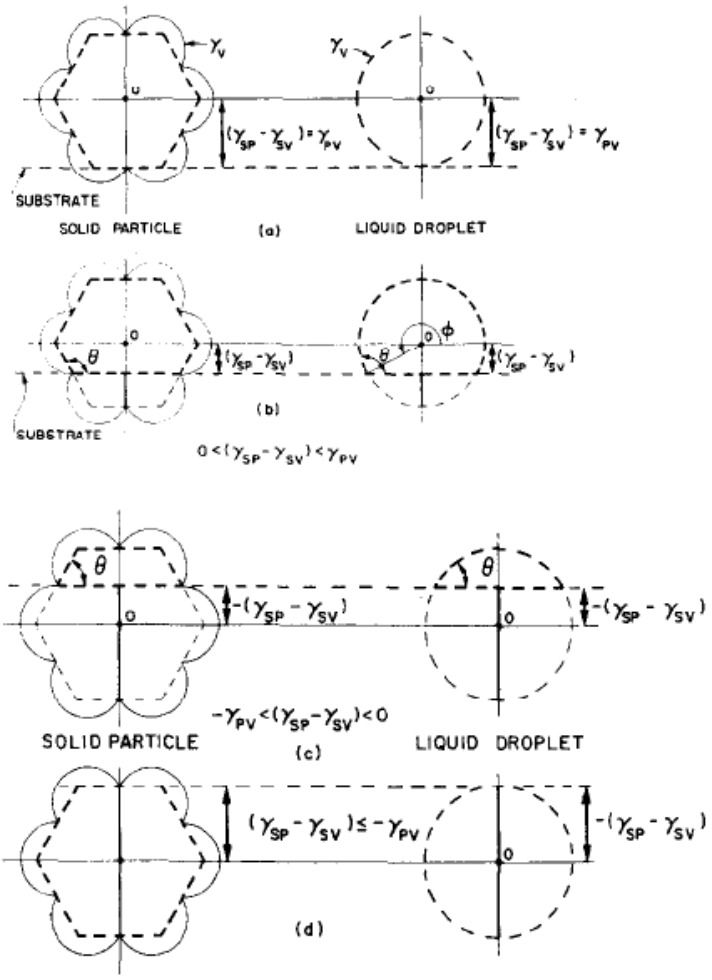


Fig. 3.24 γ^* plot and corresponding equilibrium shapes for the two dimensional solid and liquid system. (a) Non-wetting; (b) Partial wetting 1; (c) Particle wetting 2 and (d) Complete wetting. The configurations in 2D construction were meant to better illustrate the shape theory studied by Winterbottom and construction in 3D can be analogues. Dashed curve is the construction line for the equilibrium particle shape (taken from Ref. [231]).

Note that the plot still satisfies the statement which the ratio between the surface energy of any free surface (γ_{hkl}) and the perpendicular distance (h_{hkl}) from the Wulff point is constant (i.e., $\gamma_{hkl} = \lambda h_{hkl}$). This γ^* plot also depicts the corresponding four types of equilibrium shape of two dimensional solid and liquid substrate-particle configurations summarised in Tab. 3.4.

3.6.2 Strong metal-support interaction (SMSI)

Strong metal support interaction was first termed by Tauster *el al*. in 1978 [232]. They found the noble metals/TiO_2 system became less capable in chemisorption of H_2 and CO at high temperature (500°C) compared to that of in low-temperature reactions (200°C). The adsorption behaviour was reversible when the sample was annealed in oxidation environment. After they excluded the possibility of encapsulation or poisoning by impurities, they came up with the idea about the existence of the chemical interaction between the metals and the support to explain the unique reversible adsorption behaviour. This interaction was then referred as the strong metal-support interactions (SMSI). They claimed that SMSI effect was related to the formation of bonds between the noble metal and Ti cations or Ti atoms and further forms the intermetallic compounds. Later study by Tauster *et al.* in 1987 [233] suggested that the reduced titanium oxide was migrated to the metal surfaces and formed TiO_x top layer ($x < 2$). The thickness of the encapsulation layer was generally limited to one or two monolayer [82]. The interaction occurs directly between reduced titanium ions (e.g., Ti^{3+}) and group VIII (8-10) metals (Fe, Ni, Rh, Pt, Pd and Ir) and form the interfacial bond between them.

Noble metal on titanium oxide support is one of the popular systems to observed SMSI. Besides noble metal grown on TiO_2 substrate, SMSI effect was also found on the Fe_3O_4

[234], CeO_2(111) [235] and Nb_2O_5 [236] substrates. Specifically, efforts have been made to understand composition and geometric of the TiO_x layer on the noble metal surface. Some surface sensitive techniques such as STM was applied to reveal the atomic arrangement of the TiO_x suboxide layer on the noble metals e.g., Pt [28,29] and Pd [32,33] surfaces. Dulub *et al*. [29] first reported atomically resolved STM images of ordered titanium oxide overlayer on Pt clusters supported by TiO_2(110) substrate (Fig. 3.25a). It showed the capability of STM in analysing the surface structure of the encapsulation layer in the SMSI state. Based on the atomic STM images, they built the structure model of the encapsulation layer which is composed of two layers of titanium oxide with overall composition close to $TiO_{1.1}$ (Fig. 3.25b).

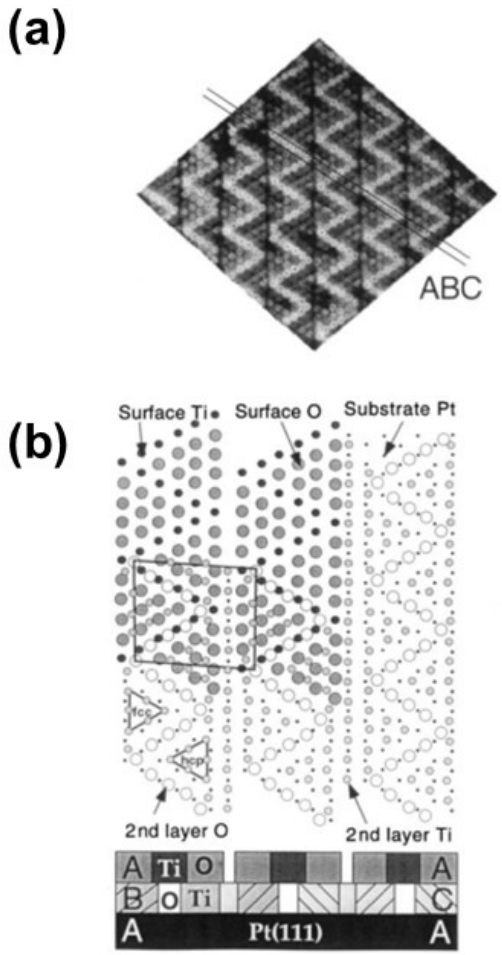


Fig. 3.25 (a) Atomically resolved STM image of the encapsulated Pt cluster (image size: 0.1×0.1 nm^2. (b) Top view of the proposed atomic model for the encapsulation layer on the Pt cluster (taken from Ref. [29]).

Atomic resolved STM image of encapsulation layer was also observed on Pd nanocrystals supported by nanoline-structured $SrTiO_3(001)$ surfaces [32]. Silly and Castell found there were two superstructures formed on the surface of the TiO_x covered Pd nanocrystals, which are named as wagon wheel (Fig. 3.26a) and hexagonal structures (Fig. 3.26b). Two distinct moiré patterns were observed in STM. The atomic models of wagon wheel and hexgonal superstructures were interpreted by superposition of Ti and O layers, giving $TiO_{1.36}$ and $TiO_{1.37}$ stoichiomoteires respectively (Fig. 3.27) [32].

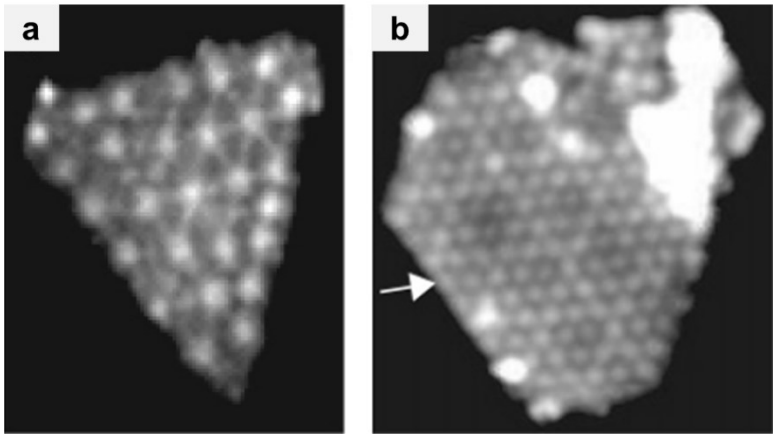


Fig. 3.26 STM images of encapsulated Pd nanocrystals on $SrTiO_3(001)$ surfaces with (a) the wagon wheel superstructure (image size: 21×22 nm^2, V_s = +0.8 V, I_t = 0.3 nA). (b) the hexagonal superstructure (image size: 19 × 18 nm^2, V_s = +0.8 V, I_t = 0.3 nA) (taken from Ref. [32]).

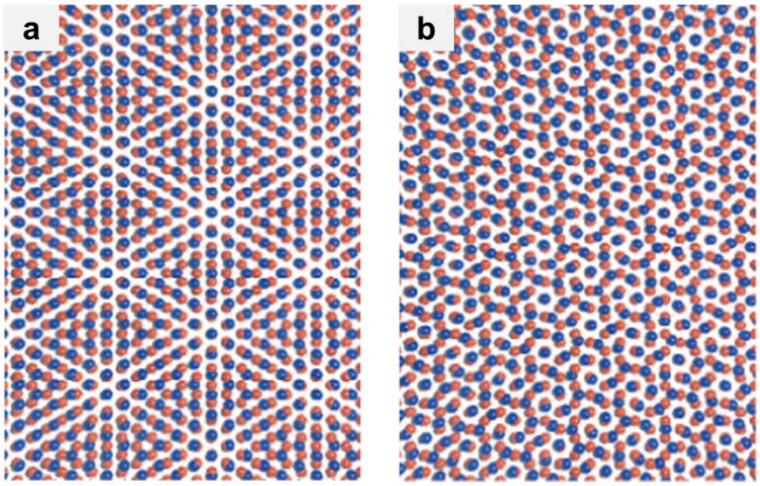


Fig. 3.27 Atomic models of (a) wagon wheel structure. The Ti layer has the lattice spacing of 3.21 Å, O layer has the lattice spacing of 2.75 Å; (b) hexagonal structure. The Ti layer has the lattice spacing of 3.22 Å and rotation at 19.6° to the O lattice. O layer has the lattice spacing of 2.75 Å (blue balls are Ti atoms, red balls are O atoms which located at the 3-fold hollow site of Pd) (taken from Ref. [32]).

SMSI effect was also studied on the TiO_2 support with different sizes. Weerachawanasak *et al*. [36] reported that the strong SMSI on the nano-sized TiO_2 in the reducing H_2 environment at 500 °C, which showed an enhanced selectivity in hydrogenation of phenylacetylene. SMSI effect was not detected when the Pd was supported by the micro-sized TiO_2 [36].

On the one hand, SMSI effect cause drastic reduction or even vanish of the chemisorption ability of CO and H_2 in the metal-oxide support catalysts [34,232,237]. Some studies reported the methods to overcome or optimise the SMSI state in order to increase the catalytic efficiency [236,238]. On the other hand, competitive hydrogenation versus hydrogenolysis reaction are greatly favoured in SMSI system [29]. This allows the tailored selectivity for catalytic reaction e.g., enhanced methanation production from CO or CO_2 and H_2 by 3 orders of magnitude [239], and selective hydrogenation process such as alkenes from long-chain alkadienes [240], ethylene in acetylene [241] and styrene in phenylacetylene [36].

3.6.3 Metal nanocrystals on $SrTiO_3$

As described Secs. 3.5.2 and 3.5.3, $SrTiO_3$(001) undergoes several surface reconstructions after the sample is sputtered and annealed. $SrTiO_3$(001) is suggested as a suitable substrate for the growth of high T_c superconductors, metals and semiconducting thin films [242]. Oxide-supported metal nanocrystals have become functionally important in catalysis [17,23-25], gas sensing [243] and optical applications [244]. The physical and chemical properties such as luminescence, conductivity, and catalytic activity of these functional devices are determined by the morphology of the nanocrystals [24,55].

Nanocrystals such as Fe[245], Co[144], Ag[246], Au [242], Ni[24] and Pd[55,247] have been reported to grow on reconstructed $SrTiO_3$(001) surfacess. The equilibrium shape of the nanocrystals grown on the $SrTiO_3$(001) substrate is determined by surface energy of the nanocrystal facets and substrate, and interface energy between them. The reported morphologies and the adhesion energies of these nanocrystals grown on $SrTiO_3$(001) surfaces are summarised in Tab. 3.5.

Tab. 3.5 Summary of the metal nanocrystals grown on $SrTiO_3$(001) substrates

Crystal type	Morphology	Substrate	Interface crystallography	Adhesion energy (J/m^2)	Ref.
Fe	truncated pyramid	$SrTiO_3$(001)-$c(4 \times 2)$	$(001)_{Fe} \parallel (001)_{SrTiO_3}$ $[100]_{Fe} \parallel [110]_{SrTiO_3}$	3.05±0.15	[245]
Co	truncated pyramid	$SrTiO_3$(001)-(2×2)	$(001)_{Co} \parallel (001)_{SrTiO_3}$ $[100]_{Co} \parallel [100]_{SrTiO_3}$	3.96±0.37	[144]
Ag	icosahedron	$SrTiO_3$(001)-(2×1)	-	-	[246]
Pd	hut	$SrTiO_3$(001)-(2×1)	$(011)_{Pd} \parallel (001)_{SrTiO_3}$ $[110]_{Pd} \parallel [100]_{SrTiO_3}$	-	[55,247]
	hexagonal	$SrTiO_3$(001)-$c(4 \times 2)$	$(111)_{Pd} \parallel (001)_{SrTiO_3}$ $[110]_{Pd} \parallel [110]_{SrTiO_3}$	-	
	truncated pyramid	$SrTiO_3$(001)-$c(4 \times 2)$	$(001)_{Pd} \parallel (001)_{SrTiO_3}$ $[100]_{Pd} \parallel [100]_{SrTiO_3}$		
Au	truncated triangle	$SrTiO_3$(001)-(2×1)	$(111)_{Au} \parallel (001)_{SrTiO_3}$ $[110]_{Au} \parallel [110]_{SrTiO_3}$ and $(111)_{Au} \parallel (001)_{SrTiO_3}$ $[110]_{Au} \parallel [100]_{SrTiO_3}$	1.732±0.091	[242]
Ni	truncated pyramid	$SrTiO_3$(001)-$c(4 \times 2)$	$(001)_{Ni} \parallel (001)_{SrTiO_3}$ $[100]_{Ni} \parallel [100]_{SrTiO_3}$	3.28 ±0.17	[24]

Silly and Castell investigated the growth behaviour of these metal nanocrystals on the reconstructed $SrTiO_3$(001) surface [55,144,242,245-247]. They managed to epitaxially grow the bcc Fe nanocrystals with a truncated pyramid shape on the $SrTiO_3$(001)-$c(4 \times 2)$ substrate [245] (Fig. 3.28). The adhesion energy is (3.05±0.15) J/m^2. They also produced Co nanocrystals on the $SrTiO_3$(001)-(2 × 2) surface (Fig. 3.29) [144]. Co nanocrystal exhibits a truncated pyramid shape with one (001) top facet and four (111) side facets. The adhesion energy was calculated as $\gamma_{adh} = 3.96 \pm 0.37$ J/m^2.

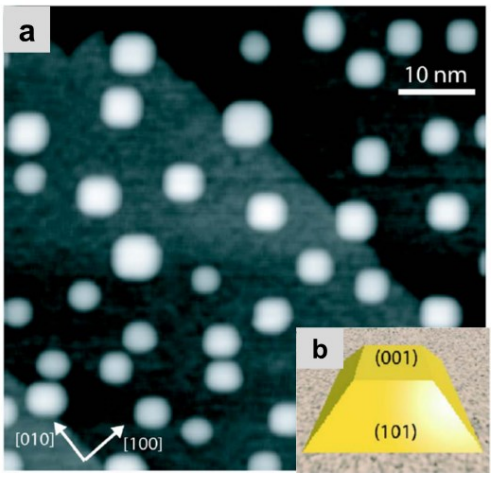


Fig. 3.28 (a) STM image of Fe nanocrystal formed on a $SrTiO_3$ (001)-$c(4 \times 2)$ substrate (V_s = +1.0 V, I_t = 0.1 nA). (b) 3D model of truncated pyramid-shape Fe nanocrystals (taken from Ref. [245]).

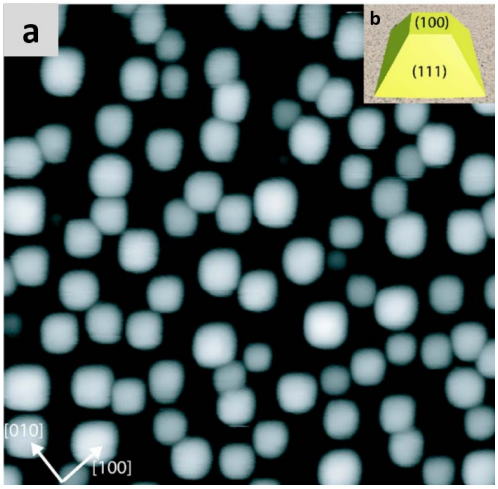


Fig. 3.29 (a) STM image of Co nanocrystal formed on a $SrTiO_3$(001)-(2 × 2) surface (image size: 60 × 60 nm^2, V_s = +1.0 V, I_t = 0.3 nA). (b) 3D model of truncated pyramid shaped Co nanocrystals (taken from Ref. [144]).

Ag icosahedral nanocrystals (Fig. 3.30) were also grown on the $SrTiO_3(001)$-(2 × 1) substrate by Silly and Castell [246]. Ag nanocrystals were self-assembled and organised into multiply twinned crystals with five-fold symmetry. Three different orientations (e.g., face, edge, and point orientation) were observed. It was suggested that these Ag nanocrystals were not partially buried since STM tip was still able to dislodge the icosahedral nanocrystals from the substrate [246].

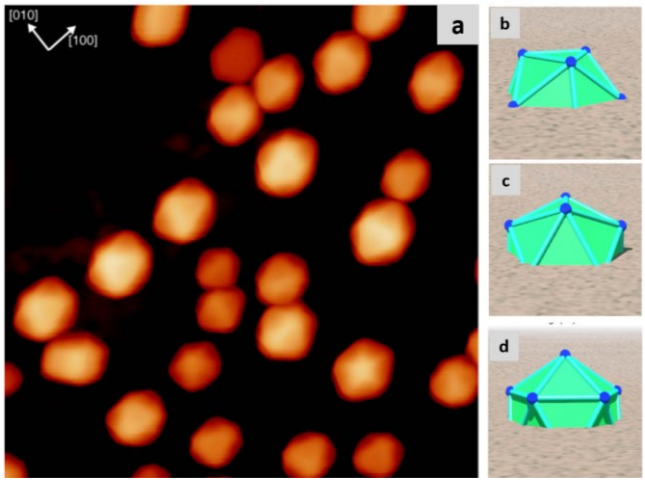


Fig. 3.30 STM image of five-fold symmetry Ag nanocrystals formed on a $SrTiO_3(001)$-(2 × 1) substrate (image size: 80 × 80 nm^2, V_s = +4.0 V, I_t = 30 pA). 3D model of icosahedral Ag nanocrystal with (b)face orientation; (c) edge orientation and (d) point orientation (taken from Ref. [246]).

Growth of Pd nanocrystals on $SrTiO_3(001)$ substrate was studied by Silly and Castell [55,247], giving a good explanation of the factors such as crystallography, interface energy between metal and oxide substrate in determining the morphology of metal nanocrystals grown on oxide supports. Different shapes of Pd nanocrystals e.g., hut, hexagonal disk and pyramid shaped were formed on the reconstructed $SrTiO_3(001)$ substrates [55,247]. The shapes of Pd nanocrystals grown on $SrTiO_3(001)$ substrate is dependent on the crystallographic interface between Pd and substrate, types of surface reconstruction on substrate and Pd deposition temperatures. The hut-shaped Pd nanocrystal exhibits an (011) interface with (001) end facets and (111) side facets (Fig. 3.31a). Both hexagonal disk and

truncated pyramid shaped Pd nanocrystals were observed on the $SrTiO_3(001)$-$c(4 \times 2)$ substrates. The hexagon transferred into truncated pyramids shape when the Pd deposition temperature was increased. The hexagonal Pd nanocrystal (Fig. 3.31b) has a (111) interface with substrate, one (111) top facet, three (111) side facets and the other three (001) side facets. The truncated pyramid Pd nanocrystals were formed on the $SrTiO_3(001)$-$c(4 \times 2)$ surface (Fig. 3.31c). Among these three shapes, thermodynamic model analysis relating nanocrystal energy to the shape and modified surface energy γ^* were calculated. The calculation indicated that the truncated pyramid and hut shapes are the two stable structures while Pd nanocrystals in hexagonal shapes are metastable [55]. The shape evolution of Pd nanocrystals in each morphology was also studied by increasing the Pd deposition temperature and concentrations [247].

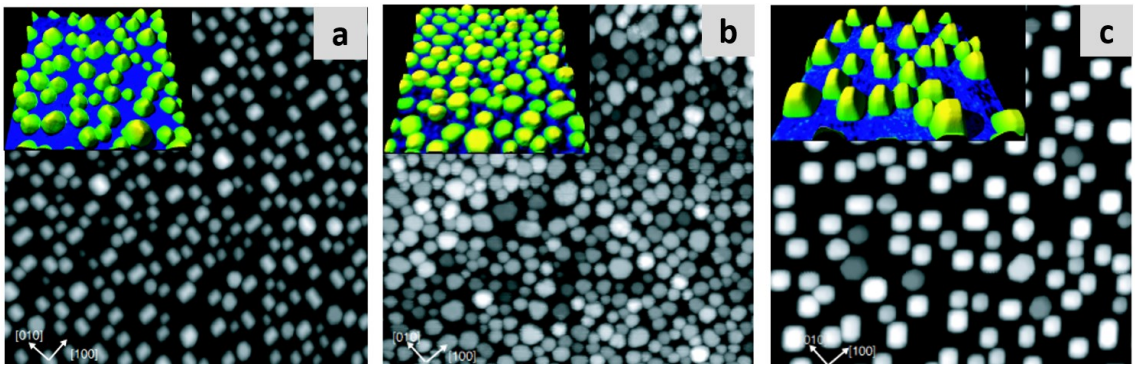


Fig. 3.31 STM images showing Pd nanocrystals in a (a) hut; (b) hexagonal and (c) truncated pyramid shape with 3D models shown on the top left corner. The substrates are $SrTiO_3(001)$ (image size: 140×140 nm^2, V_s= +0.8 V, I_t = 0.3 nA) (taken from Ref. [55]).

Biomodal growth of Au nanocrystals on $SrTiO_3(001)$-(2×1) substrates was thoroughly studied by Silly and Castell [242]. The Au nanocrystals have hexagonal shapes with six side facets and a truncated triangle top surface parallel to the substrate (Fig. 3.32). A small amount of icosahedral Au nanocrystals were also observed which they believed it is the first STM image reported about this type of shape for Au nanocrystals. Through varying the Au

coverage, they illustrated that the growth mode changed from monolayer wetting (Frank van der Merwe growth) when $\gamma_{STO} > \gamma_{Au} + \gamma_i$ into nanocrystal growth (Stranski-Krastanov growth). They also elucidated that crystals are most likely nucleated at the wetted monolayer and grow by de-wetting of incoming surrounded Au [242]. Adhesion energy between the Au and $SrTiO_3(001)$ was obtained as $\gamma_{adh} = 1.732 \pm 0.091$ J/m^2.

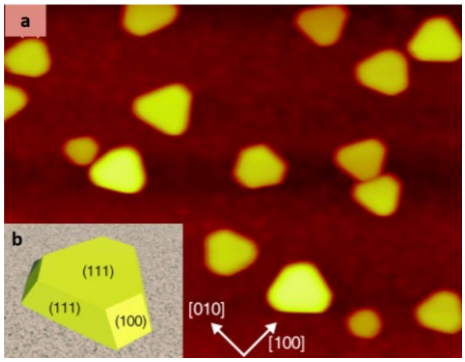


Fig. 3.32 (a) STM image of truncated triangle-shaped Au nanocrystals on a $SrTiO_3(001)$-(2 × 1) substrate (image size: 100 × 78 nm^2, V_s = +2.0 V, I_t = 0.1 nA). (b) 3D model of truncated triangle shaped Au nanocrystal (taken from Ref. [242]).

Sun *et al*. recently studied the growth of Ni nanocrystals on *c*(4 × 2) terminated $SrTiO_3(001)$ substrate (Fig. 3.33) [24]. The Ni nanocrystals formed truncated pyramid equilibrium shapes. Each Ni nanocrystal is constructed of one {001} top facet and four {111} side facets. Its adhesion energy was calculated to be $\gamma_{adh} = 3.28 \pm 0.17$ J/m^2.

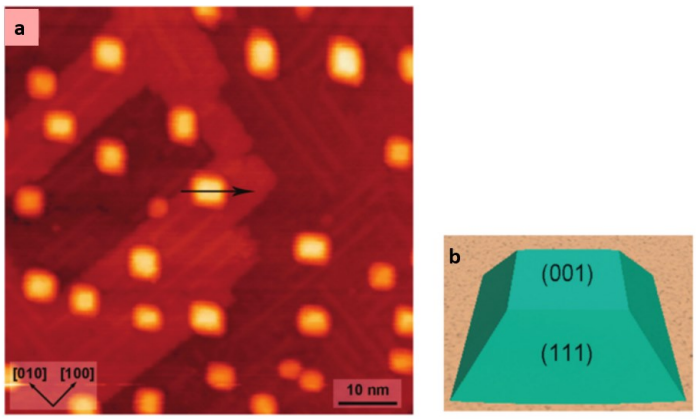


Fig. 3.33 (a) STM image of truncated pyramid shaped Ni nanocrystals grown on the $SrTiO_3(001)$-*c*(4 × 2) surface (V_s = +1.0 V, I_t = 0.4 nA). (b) 3D model of an fcc truncated pyramid shaped Ni nanocrystal (taken from Ref. [24]).

3.6.4 Metals on anatase

TiO_2 is one of the popular semiconductor material used in the heterogeneous photocatalytic application. The photocatalyst made by TiO_2 is stable, low cost and nontoxic [26,248,249]. However, its photocatalytic behaviour is limited by the rapid recombination of photogenerated electron (e^-) and hole (h^+) in TiO_2 [26,250-252]. Deposition of noble metal nanoparticles (e.g., Au, Ag, Pt, Pd) on TiO_2 supports is suggested as an effective way to tackle this limitation and is likely to inhibit the charge recombination process [26].

Metal nanoparticles or clusters grown on a well-ordered metal oxide surface is important in the catalysis application. TiO_2 acting as a support to grow transition metal nanoparticles or clusters has been investigated since recent decades. Studies have been explored the use of TiO_2 in promoting catalytic activity [23,253,254] and chemical reactions such as CO oxidization [253,255,256], hydrogenation [36,257,258] and water splitting [259-261]. Most research has been carried out on the rutile TiO_2 especially for its (110) surface [191,262-264]. The studies related to the metal particles grown on the well-ordered anatase TiO_2 are still scarce and most of them focused on catalytic aspect [26,254,262,265-269].

Among a group of noble metals, Au, Pt and Pd nanoparticles are widely employed to improve the catalytic especially photocatalytic efficiency of anatase. Understanding of composition, morphology and location of the metal nanoparticles grown on anatase substrates plays a vital role in optimising catalytic performance in the metal-oxide catalyst system [26].

Photocatalytic oxidation with O_2 has been investigated mostly on the semiconductor surfaces such as TiO_2 [270-274]. Recent studies suggested that Pt nanoparticles supported on anatase TiO_2 can efficiently promote the aerobic oxidation under the visible light irradiation at room temperature [268,269]. The strong affinity between the Pt nanoparticles

and the anatase substrate brings a high activity in Pt/anatase catalyst system (7.1% quantum yield for reaction) compared to that of Au catalyst (3.8% quantum yield for reaction) [268]. Shiraishi *et al*. also studied the alloying Pd with Cu on anatase [269]. The TEM results showed that the Pt-Cu bimetallic nanoparticles were formed and finely dispersed on the support and structured into the bcc cuboctahedron shape [269].They also demonstrated that this bimetallic system can significantly enhance the aerobic oxidation under visible light irradiation (17% quantum yield for reaction) [269]. The reason was explained as alloying elements can reduce the work function of the nanoparticles (i.e., Schottky barrier) which promotes the electron transport from photoactivated nanoparticles to anatase [269].

Au nanoparticles supported on TiO_2 are used for catalytic application in low-temperature CO oxidation, selective propene oxidation and other catalytic and photocatalytic oxidation reactions [23,191,275-278]. Gong *et al*. [254] investigated the role of different surface sites (e.g., terraces, step edges, oxygen vacancies) in nucleation and growth of small Au and Pt clusters on the anatase TiO_2(101) (Fig. 3.34). Combined with DFT calculation and STM results, he suggested that Au clusters were highly favourable to nucleate and grow at the steps on the clean anatase TiO_2(101) and O vacancies on the electron-irradiated surfaces [254]. Unlike Au clusters, Pt clusters were shown no preference of growth at the sites mentioned above [254].

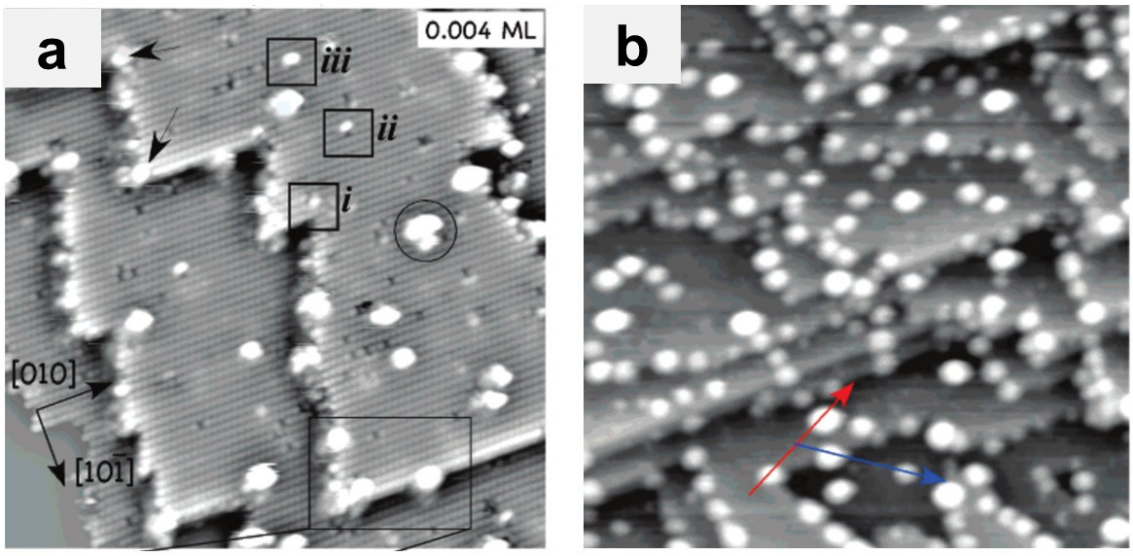


Fig. 3.34 STM images of (a) Pt nanoparticles grown on anatase (101) (image size: 30 × 30 nm^2, V_s = +1.5 V, I_t = 0.3 nA). (b) Au nanoparticles grown on anatase (101) (image size: 70 × 70 nm^2, V_s= +1.4 V, I_t = 0.8 nA) (taken from Ref. [254]).

Balasanthiran and Hoefelmeyer recently developed a low-cost and effective method to load transition metal ions (Cr(III), Mn(II), Fe(II), Co(II), Ni(II), and Cu(II)) on the surface of anatase TiO_2 nano-rods in the metal chloride hydrate solution [267]. The host nanocrystals retained their morphology and phases after the quantity of the attaching metal ions reached up to monolayer coverage. This hybrid system may be important in mediating electron transfer reaction which can be potentially used in photocatalytic application.

Bian *et al*. used the simple photodeposition method to grow the noble metal nanocrystals (Au, Pt) onto the anatase TiO_2 mesocrystal (Meso-TiO_2) superstructures [26]. TEM images showed that these metal nanoparticles were preferentially located at the edge of TiO_2 mesocrystals (Fig. 3.35). Further investigation in electron transport and photocatalytic properties indicated an enhanced photocatalytic oxidation activity after the meso-TiO_2 sample was loaded with noble metal nanoparticles.

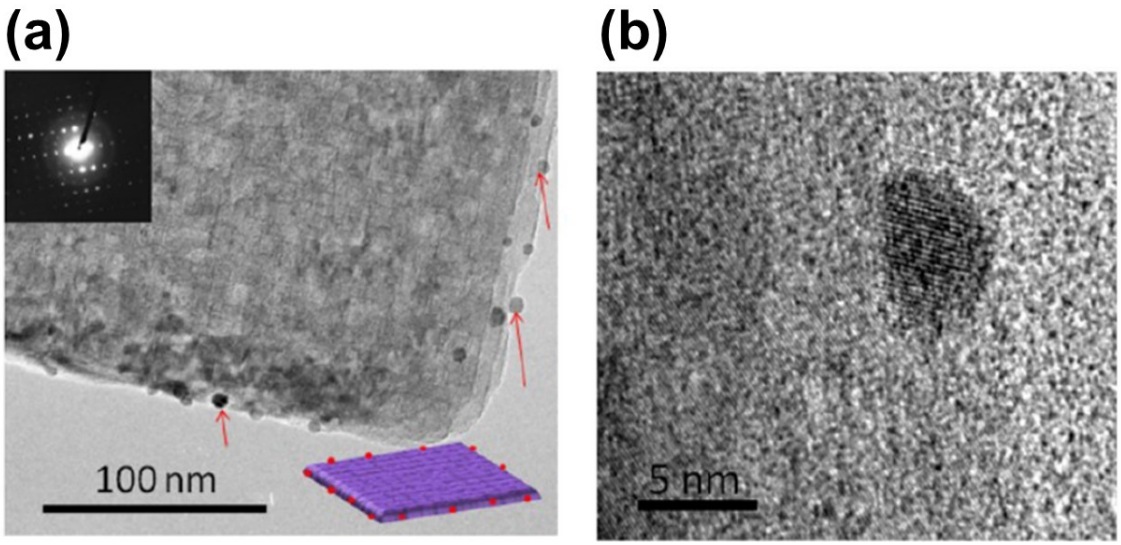


Fig. 3.35 (a) TEM images of 0.04wt% Au/ Mesco-TiO_2 (Au particles are pointed by red arrows). (b) HRTEM image on the edge of 0.04wt% Au/Mesco-TiO_2 (taken from Ref. [26]).

Vittadini and Selloni did extensive theoretical DFT analysis on the interaction between Au nanoparticles and anatase surface to study the behaviour of titania-supported gold catalyst [266]. It reported that single Au tended to locate at the top site of a five-coordinated Ti atom on perfect anatase surfaces and nucleate at oxygen vacancies on the defective surfaces. They suggested that the oxygen vacancy performed as the nucleation centre and induced the "wetting" behaviour of the clusters [266]. These findings were later confirmed by Gong *et al*. who studied the location of deposited Au and Pt on anatase surfaces using STM (Fig. 3.34) [254].

Zhang *et al*. studied the nucleation and growth of Pd clusters supported on anatase TiO_2(101) surface using periodic supercell model and density function theory [279]. They elucidated that single Pd adatom is preferentially located at the bridging site formed by two-coordinated oxygen atoms at the step edge on the perfect anatase TiO_2 (101) surface. While on the defective surface, oxygen vacancy could act as a nucleation site for the growth of Pd nanoparticles but this effect is not as strong as growing Au and Pt nanoparticles. Also, the calculation indicated that adsorbed Pd_3 clusters tended to form planar triangle structures,

Pd_4 and Pd_5 adsorbates tended to form three-dimension structures on both perfect and defective anatase TiO_2 surfaces.

It should be noticed that most current work about the formation of noble metal nanoparticles or clusters on anatase TiO_2 especially on (101) surface were studied using SEM or TEM. The STM study of the growth of noble metals on anatase especially on its active (001) surface are scarce. Even though anatase (001) has been reported to form on $SrTiO_3$(001) surfaces, the growth of metal particles on anatase (001) structured $SrTiO_3$ substrate is still less studied.

3.7 The Surface of Transition Metal Dichalcogenides (TMDs)

3.7.1 Introduction to TMDs and monolayer TMDs

Transition metal dichalcogenides (TMDs) are a group of the materials with formula of MX_2. M represents a transition metal atom from group 4-10. X represents a chalcogen atom (e.g., S, Se or Te). Around 40 TMDs are found to have layered structures from group 4-7. TMDs from group 8-10, excepted Pd and Pt, normally exhibit non-layer structures or partial layered structures (Co, Rh, Ir and Ni) (Fig. 3.36) [280,281].

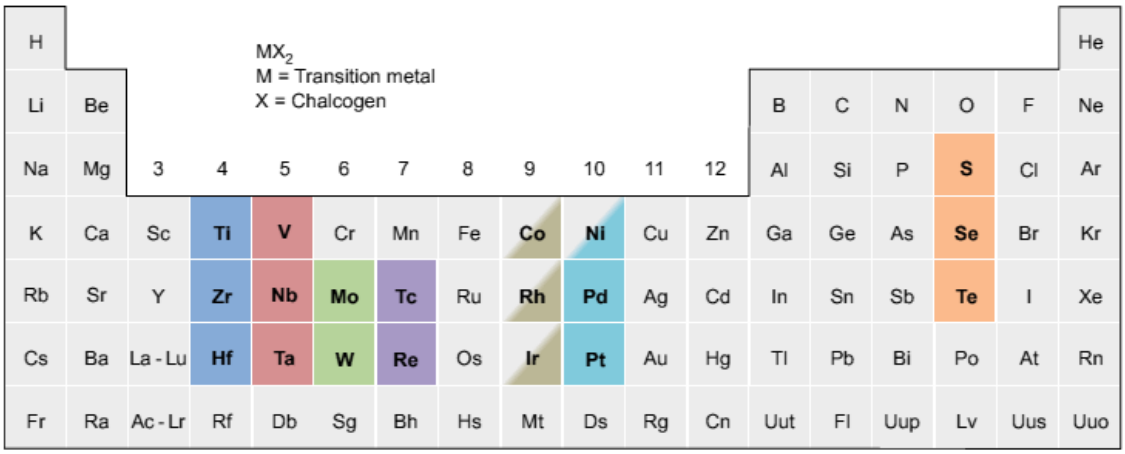


Fig. 3.36 Periodic table shows the composition of TMDs. The fully highlighted transition metals are found to form layered structures. The partial highlighted element are found to form partial layered structures depending on which chalcogen they are bonded to (taken from Ref. [281]).

Bulk TMD usually exhibits two types of crystal structures with trigonal prismatic (2H) phase (Fig. 3.37a) or octahedral (1T) phase (Fig. 3.37b). These two phases have different stacking configurations. In the 2H-MX_2 structure (Fig. 3.37a), transition metal atom (represented by M) locates at the centre of the prismatic unit cell and coordinated with six surrounding chalcogen atoms (represented by X). Chalcogen atoms are located at the corner of the unit cell. As for metastable 1T-MX_2 phase (Fig. 3.37b), six X atoms sit at the corner of the distorted octahedral unit cell with one M atom in the centre. Simple transition occurs between these two phases by intralayer atomic gliding. 2H-MX_2 structure is more thermodynamically stable compared to 1T-MX_2 [282,283]. The electronic behaviour between these two phases could be different. Taking MoS_2 as an example, two phases exhibit two different electronic behaviour which 2H-MoS_2 in the bulk form is a semiconductor with an indirect band gap energy of ~1.2 eV [284,285], while 1T-MoS_2 is metallic[286,287].

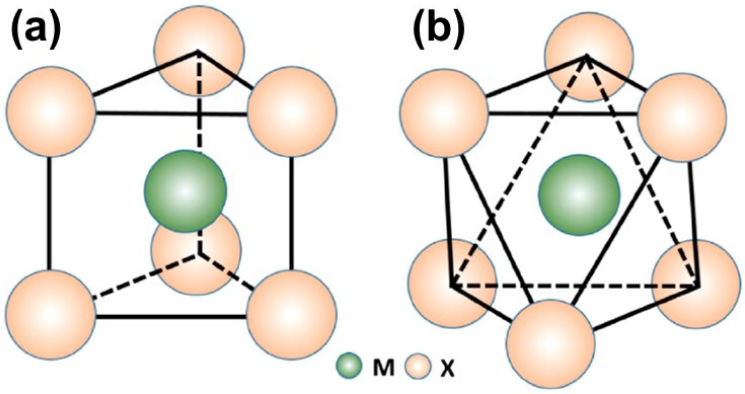


Fig. 3.37 Crystal structures of bulk MX_2 with unit cell structures: (a) 2H-MX_2 phase; (b) 1T-MX_2 phase (taken from Ref. [288]).

Monolayer or multi-layer TMDs are formed by repeating each type of unit cell (Fig. 3.38). Individual monolayer TMDs is generally around 6~7 Å thick. It is composed of three atomic (X-M-X) layers (Fig. 3.38a and b). Transition metal layer is sandwiched between two chalcogen layers. The intralayer i.e., M-X layer is strong covalent bonded and each interlayer i.e., X-M-X is weakly bonded by van der Waals interaction.

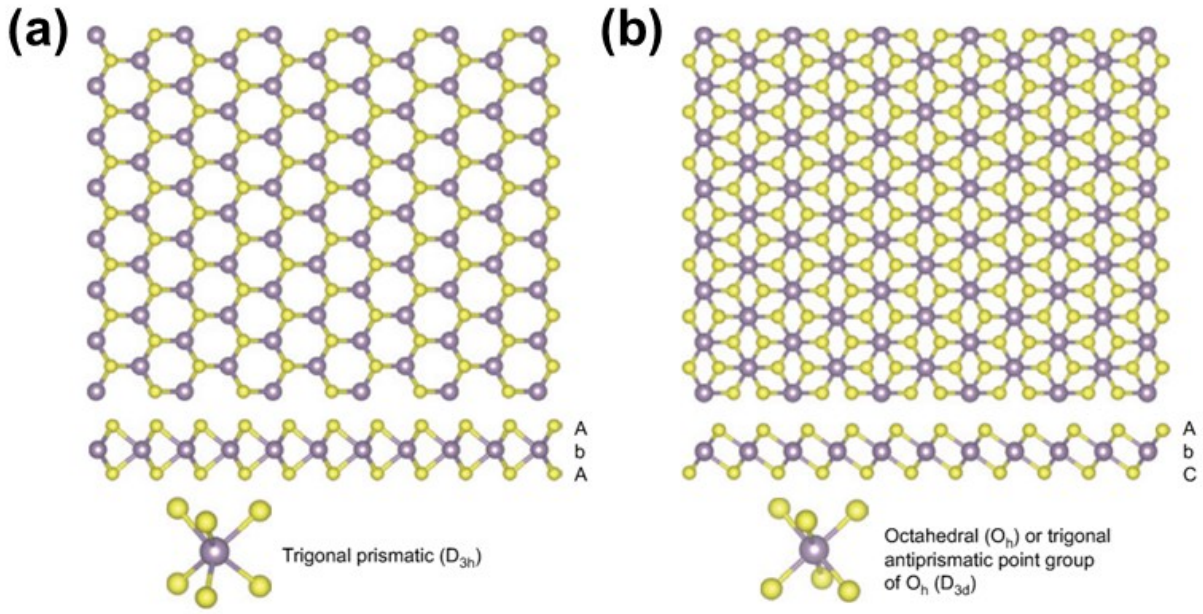


Fig. 3.38 Monolayer structures of TMDs constructed with (a) Trigonal prismatic phase; (b) Octahedral phase. Top view, side view and unit cell are shown (taken from Ref. [281]).

Monolayer TMDs

After the discovery of the novel transport properties in field effect of individual graphene sheet by Novoselov *et al*. in 2004 [289], the intensive interests have been ignited on the study of 2D materials in recent years. Unlike graphene showing mainly semimetallic character, diverse electronic behaviours, depending on the composition, are found on TMDs such as semiconductor (MoS_2 and WS_2), semimetals (WTe_2 and $TiSe_2$), true metals (NbS_2 and VSe_2) and superconductor ($NbSe_2$ and TaS_2) [288]. Also, TMDs exhibit tuneable band gap structures by simply changing the thickness of the layers. The band gap value of the common TMDs is summarised in Fig. 3.39. Generally, the TMDs such as MoS_2, WS_2, WSe_2 and $MoSe_2$ exhibit indirect band gap as bi or multilayers while present direct bandgaps as a monolayer [290].

Bandgap (eV)		Mo	W	Ti	Zr	Hf	V	Nb	Ta	Ni	Pd	Pt
S	monolayer	1.8-2.1	1.8-2.1	~0.65	~1.2	~1.3	~1.1	metal	metal	~0.6	~1.2	~1.9
	Bulk	1.0-1.3	1.3-1.4	~0.3	~1.6	~1.6	metal	metal	metal	~0.3	~1.1	~1.8
Se	monolayer	1.4-1.7	1.5-1.7	~0.51	~0.7	~0.7	metal	metal	metal	~0.12	~1.1	~1.5
	Bulk	1.1-1.4	1.2-1.5	metal	~0.8	~0.6	metal	metal	metal	metal	~1.3	~1.4
Te	monolayer	1.1-1.3	~1.03	~0.1	~0.4	~0.3	metal	metal	metal	metal	~0.3	~0.8
	Bulk	1.0-1.2	metal	metal	metal	metal	metal	metal	metal	metal	~0.2	~0.8

Fig. 3.39 Summary of the band gap for common TMDs taken from Ref. [280]

Monolayer transition metal dichalcogenide, as one of the popular 2D materials, has gained great attention. Owing to the excellent physical properties such as strong spin-orbit coupling, strong quantum confinement and direct-indirect band gap transition, monolayer TMDs show the promising applications in the field of transistors [285], sensors [291], memory devices [292], electronics and optoelectronics such as valleytronics [293,294] and photodetectors [295-297].

3.7.2 Characterisations and properties of monolayer MoS_2

MoS_2 is one of the typical layered TMDs materials that its monolayer has been obtained great attention. MoS_2 crystal is composed of the layered structures shown in Fig. 3.40. The thickness of a single MoS_2 layer is 6.5 Å. Bulk MoS_2 is semiconductor with indirect band gap of 1.2 eV [284,285]. When the thickness is reduced to a single layer, MoS_2 became semiconducting with band gap of 1.8 eV [298]. Monolayer MoS_2 also exhibits strong adsorption in the solar spectrum region, enhanced PL quantum yield after indirect-to-direct band transition ($\sim 10^4$) [298], large in-plane carrier mobility ($\sim$200-500$cm^2/(V\ s)$) [299] and high current on/off ratio exceeding 10^8 at room temperature (the normal desirable ratio is between 1×10^4 and 1×10^7) [285,291,300]. All these properties enable 2D MoS_2 to be fabricated for the optical and optoelectronics devices [291].

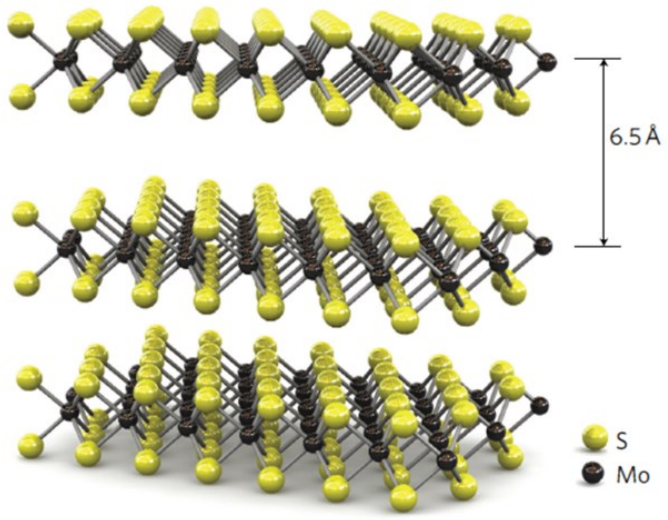


Fig. 3.40 3D representation of the MoS_2 structure (taken from Ref. [285]).

Four main methods have been reported to fabricate monolayer MoS_2 which are micromechanical exfoliation [285,291,298,301-303], liquid exfoliation [281], lithium intercalation [286,304-307] and chemical vapour deposition [61,308-314].

Several well established techniques have been applied to characterise surface quality of the synthesised 2D MoS_2 in terms of it electronic, optical and topographical properties. These well-established techniques are optical microscopy (OP), atomic force microscopy (AFM), scanning tunnelling microscopy (STM), Raman spectroscopy and photoluminescence spectroscopy (PL).

Layer uniformity and thickness measurements

Optical microscopy gives a direct view of the uniformity of the as-grown MoS_2 layers. MoS_2 with different thickness shows different contrast under the optical microscope (Fig. 3.41a), which the thinner layers appear brighter. The accurate measurement of the thickness can be obtained by AFM (Fig. 3.41b and c). The monolayer MoS_2 thickness (0.6-0.9 nm) measured by AFM were reported by many literatures [313,315,316]. This data is comparable to its theoretical value of the single layer thickness (0.65 nm). The slight difference between the measurement and its theoretical value may be caused by absorbents such as contaminations formed on the MoS_2 surface during synthesis [317]. More detailed and higher resolution of the thickness uniformity can be observed by Raman mapping (Fig. 3.42) [303,313].

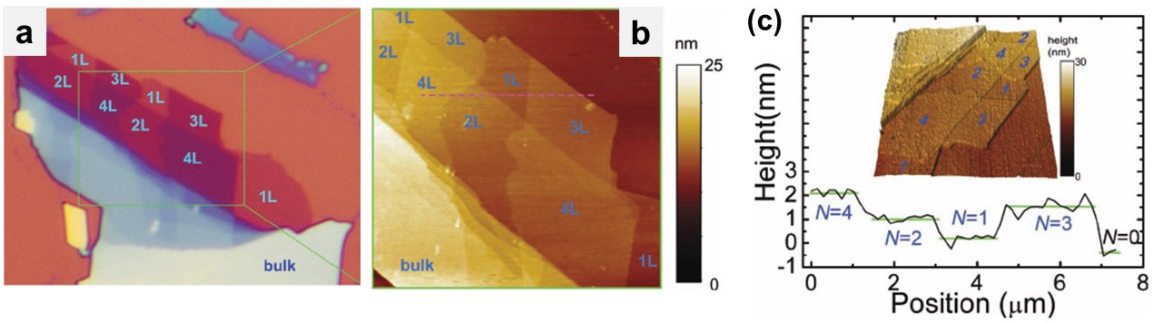


Fig. 3.41 MoS_2 with different thickness observed by (a) OP; (b) AFM (the nL means number of layers). (c) Height profile of MoS_2 surface measured by AFM (taken from Ref. [303]).

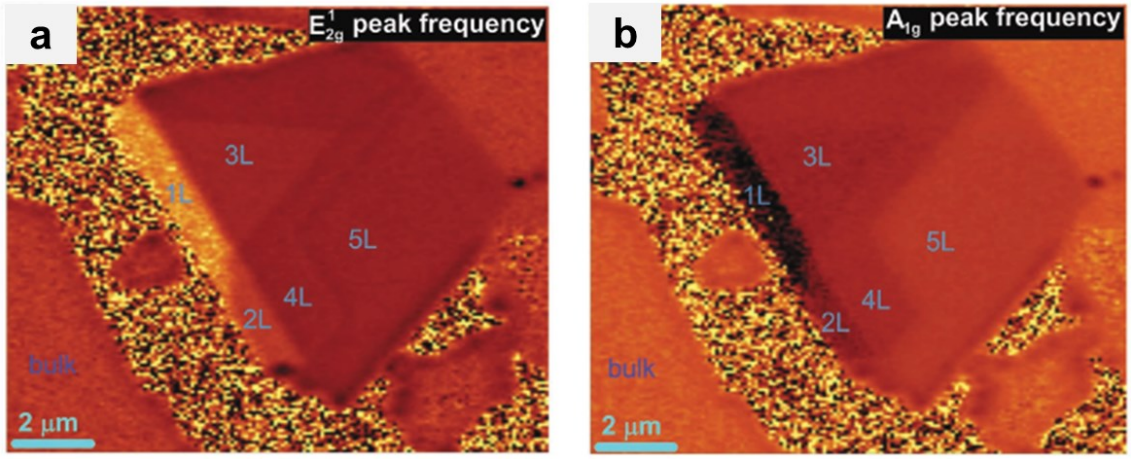


Fig. 3.42 Raman mapping images with (a) E^1_{2g} and (b) A_{1g} peak frequency showing the contrast in dependence of layer numbers (taken from Ref. [303]).

Surface topography and atomic structure

The contrast in STM imaging comes from both topographic roughness and also the density of the state. Topographic effect is suggested as the primary effect in studying MoS_2 surface [314]. Also, Zhou *et al*. found that MoS_2 surface became smoother as increasing the layer thickness, which is attributed to the increase of the bending stiffness with the layer thickness [314].

STM can also reveal the atomic arrangement of the MoS_2 crystals. The hexagonally arranged bright spots were observed in the STM images showing the atomic resolution of the MoS_2 (Fig. 3.43). These bright spots were first claimed as the Mo atoms by early theoretical studies, but later STM image calculation concluded them as surface S atoms [318-321]. Defects such as S vacancies were quite often observed at the edge of the MoS_2 crystals. The S vacancies are indicated as a catalytic active site for the hydrodesulphurization (HDS) application [322,323].

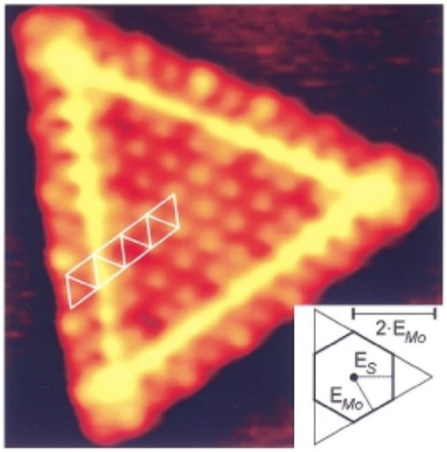


Fig. 3.43 STM image of the atomic resolved monolayer MoS_2 nanocluster (taken from Ref. [323]).

Thickness related features

The operation principle of Raman spectroscopy has been described in Sec. 2.3.9. There are two vibrational modes for the layered materials. One is inside the layer (intralayer mode) and the other is the movement of the whole layer (interlayer mode). The interlayer mode is usually observed on the low frequency range while intralayer mode is at the high-frequency range. The position of intralayer mode depends on chemical compositions and layer numbers. The position of interlayer mode mainly depends on the layer numbers [324]. Both vibration modes can be used to determine the layer numbers of MoS_2.

For the bulk MoS_2, four active modes are generally observed which are E_{2g}^2 (32cm^{-1}), E_{1g} (286cm^{-1}), E_{2g}^1 (383cm^{-1}) and A_{1g} (408cm^{-1}) [303]. As depicted in Fig. 3.44, E_{2g}^2 mode generates from vibration of an S-Mo-S layer against adjacent layers. E_{2g}^1 mode is the in-plane vibration arising from vibration of two S atoms with respect to one Mo atom. E_{1g} mode is usually forbidden on the back-scattering experiment on the basal plane. A_{1g} mode is the out-of-plane vibration of S atoms in opposite directions [325].

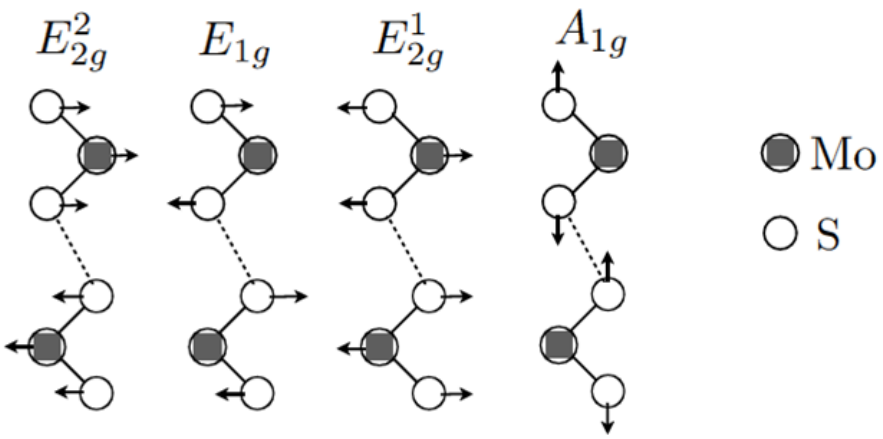


Fig. 3.44 Schematic presentation of the four vibrational modes in bulk MoS_2 (taken from Ref. [326]).

Most studies used intralayer mode (i.e., two characteristic modes E^1_{2g} and A_{1g}) to determine layer numbers of MoS_2 [61,303,313]. This is achieved by calculating the frequency difference Δk between E^1_{2g} and A_{1g}peaks. Fig. 3.45 gives an example of the change in the Raman spectra as the function of the layer numbers. Apparently, monolayer (1L) MoS_2 shows the smallest frequency difference Δk between two characteristic E^1_{2g} and A_{1g} peaks at the range of 384-385 and 402-405 cm^{-1} respectively [61,303,313]. It may vary slightly due to the different laser energy and synthesis methods [303,313].

Normally, the frequency difference of Δk<20.5 cm^{-1} indicated the formation of monolayer MoS_2 [313]. Many studies reported the E^1_{2g} softening (red-shift) and A_{1g} stiffening (blue-shift) with increasing the layer thickness [303,327,328].

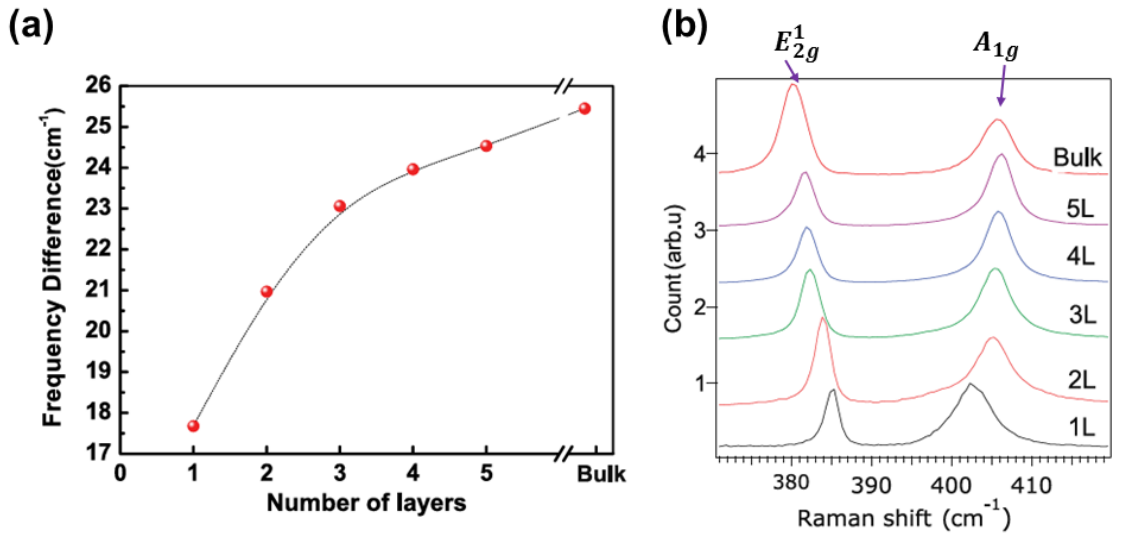


Fig. 3.45 (a) Example of the energy difference of the E^1_{2g} and A_{1g} modes verse the layer numbers. (b) The function of the Raman spectra with different layer numbers of MoS_2 (adapted from Ref. [327]).

Even though most studies were reported to use the frequency difference between E^1_{2g} and A_{1g} modes to determine the layer numbers, Plechinger *et al*. found A_{1g} was almost complete suppressed for the polarised spectrum (Fig. 3.46a) which was hard to determine the layer thickness [315] . Therefore, they used the interlayer shear mode (E^2_{2g}) to determine the layer numbers. From their Raman spectra results (Fig. 3.46b and c), they suggested that the shear mode showed well-defined transitions with large frequency difference of the peaks among the MoS_2 with different thickness [315]. The main challenge of this method by using interplane shear mode is that it can only be applied for determine more than two layered MoS_2. Because shear mode (E^2_{2g}) is focused on the interplane vibration, it is not suitable for determining the monolayer MoS_2.

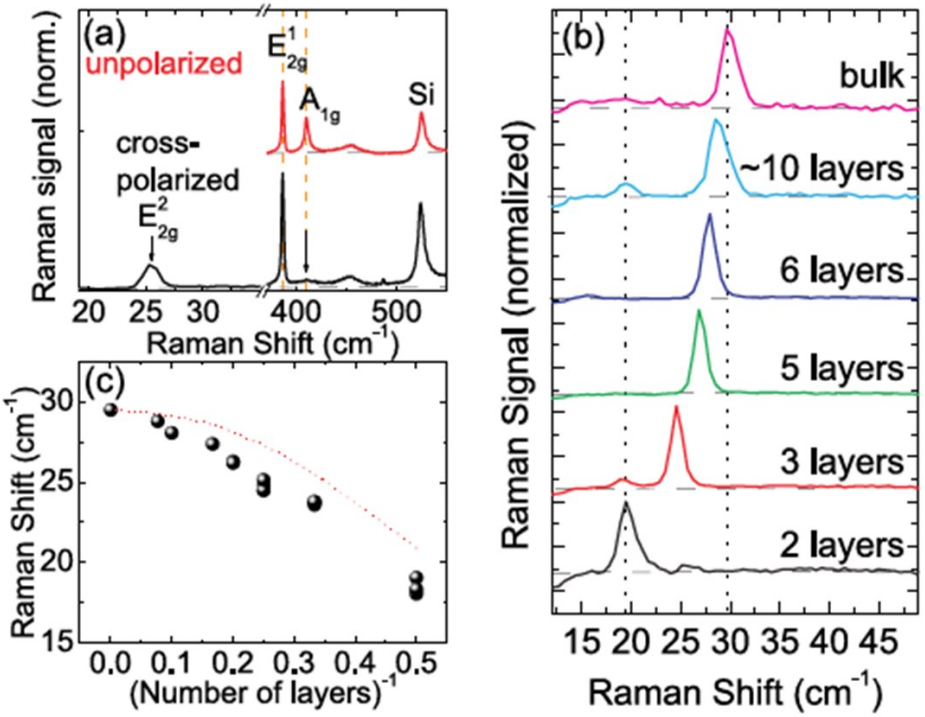


Fig. 3.46 (a) Comparison of unpolarised and polarised Raman spectra of MoS_2 flakes. (b) Normalised Raman spectra of shear mode measured on the MoS_2 flakes in the function of the layer thickness. (c) Spectral position of the shear mode as a function of (number of layers)$^{-1}$ (taken from Ref. [315]).

The principle of PL spectroscopy was introduced in Sec. 2.3.8. PL works under the photon-excited system which presents excited electrons in conduction band and holes in valence band. The excitons form through binding these electrons and holes by electrostatic Coulomb force. These excitons were observed in the PL spectra for the thin film with characteristic strong A and broad B peaks. The normalised PL spectra for peak A of monolayer MoS_2 was located at 1.9 eV [298].

The peak position (blue and red shift), intensity and shape of peak A varies with substrate materials. The PL peak intensity is depended on quantum yield. As thickness is reduced, the PL quantum yield is significantly enhanced for the monolayer MoS_2, showing the ability of effectively light emitting (Fig. 3.47b). PL intensity between monolayer and bilayer MoS_2

is significantly different (Fig. 3.47a), for example the enhancement in the order of 10^4 was observed for monolayer MoS_2 compared to that of from the bulk [298].

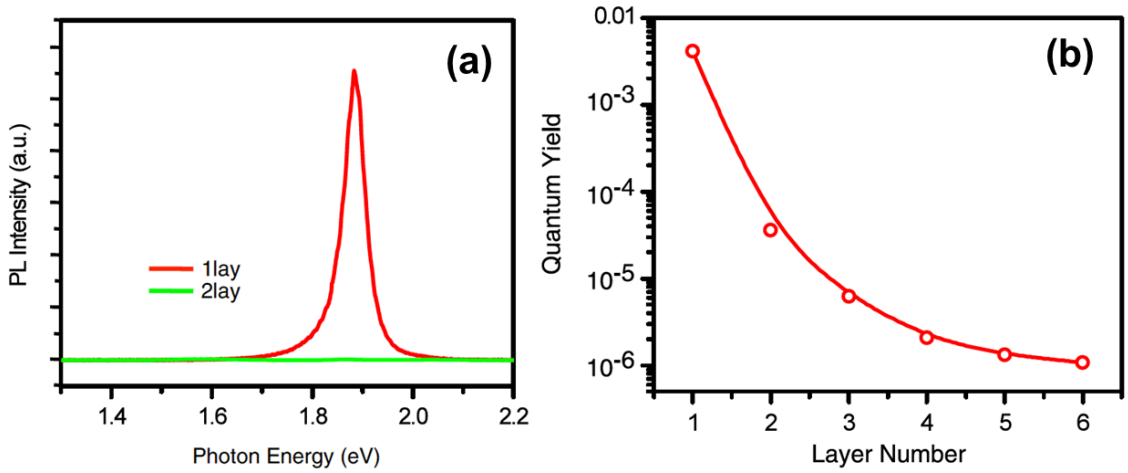


Fig. 3.47 (a) PL spectra for the monolayer and bilayer MoS_2 samples. It shows an enhancement of the PL for monolayer MoS_2. (b) Quantum yield of the MoS_2 with different layer thickness (taken from Ref. [298]).

Domain shapes of monolayer MoS_2 crystals

Different shapes of MoS_2 crystals were observed after synthesising with CVD method. These reported shapes were hexagon, triangles, truncated triangles, three point stars and six point stars [313,329-331]. It is suggested that the growth shape of MoS_2 crystals is highly influenced by the Mo to S ratio [313,323].

The shape evolution of monolayer MoS_2 crystals was symmetrically studied by Wang *et al*. [313]. Two terminations, i.e., S-zigzag (S-zz) and Mo-zigzag (Mo-zz) are commonly existed for the MoS_2 domain. Either of element terminated edges growing faster will eventually become smaller or even disappear. The growth speed is related to the edge free energy in the 2D MoS_2 system. They proved that the Mo to S ratio affects the growth shape of MoS_2 crystals (referential ratio is 1:2). As illustrated in Fig. 3.48, if Mo:S= 1:2, it forms hexagon; if Mo:S>1:2, un-saturated S atoms exposed outside is more energetic and grow faster. It ended up with forming Mo terminated triangle. If Mo:S <1:2 it forms S terminated

triangles. Truncated triangle shape forms if Mo:S is slight above 1:2. The formation of the pointed star shape is due to the slower growth rate at one termination surface compared to the other face. The Mo to S ratio can be affected by evaporation temperature of the precursors and deposition position where the substrate is placed [313].

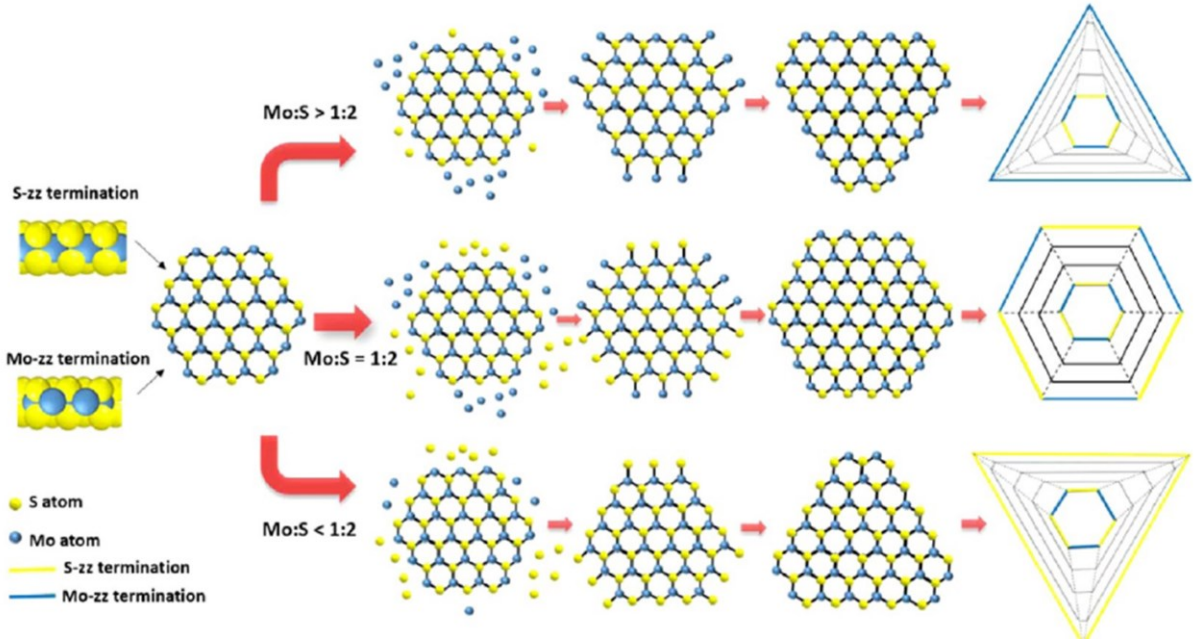


Fig. 3.48 Schematic illustration of the relationship between the Mo:S to the growth shape of MoS_2 domain (taken from Ref. [313]).

Substrate related feature

Several materials have been used as the substrates to grow monolayer MoS_2. They are SiO_2/Si [298,308-314,330,332], sapphire [308,333,334], *h*-BN [61,335], Au [323,335-337], mica [335,338], graphite [335,339], graphene [340], $SrTiO_3$ [341-343] and $LaAlO_3$[341,344].

In the thin film-substrate heterostructures system, the physical properties of the thin film become more depended on the interaction from the substrate with reducing the thickness of the film. The possible effects induced by the substrate are: 1) structural strain from lattice

mismatch and 2) electronic doping by charge transfer between two materials [341]. Several studies reported the substrate influences on the monolayer MoS_2 using Raman and PL spectroscopy [326,335,341]. Raman spectroscopy was used to study the structural strain of monolayer MoS_2. PL was applied for analysing the electronic doping on the MoS_2 via charge transfer from the substrate.

When the thin film is grown on a substrate with different lattice parameters, the strain is built up in the thin film due to the lattice mismatch, which may lead the film to modify its lattice structure [341]. E_{2g}^1 mode is originated from the in-plane vibration of two S atoms with respect to the Mo atom, and could be influenced by the substrate [341]. Many studies focused on the effect of the substrate-induced-strain on E_{2g}^1 mode. Li *et al*. [341] and Buscema *et al*. [335] studied the substrate effect on monolayer MoS_2 using the Raman and PL. The normalised Raman spectra measured by both groups are shown in Fig. 3.49. Even though they chose different substrates, both groups did not observe the significant E_{2g}^1 peak shift in the Raman spectra for MoS_2 grown on the different substrates. Only small variation about less than 0.4cm^{-1} was reported by Buscema *et al*. which thet suggested that E_{2g}^1 mode was insensitive to the substrate [335]. The frequency shift of A_{1g} mode was found not obvious from Li's group. While a sizable shift of the A_{1g} peak (~2cm^{-1}) towards to the high frequency (stiffening) was observed by Buscema's group [335]. Only large strain can cause the notable Raman peak shift as reported by Rice *et al*., who observed a uniaxial strain-induced Raman shift on the monolayer MoS_2 [326]. They reported a large shift of E_{2g}^1 mode (rate: 2.1cm^{-1} per % strain) and a small shift of the A_{1g} mode (rate: 0.4 cm^{-1} per % strain) to the low frequency (red-shift).

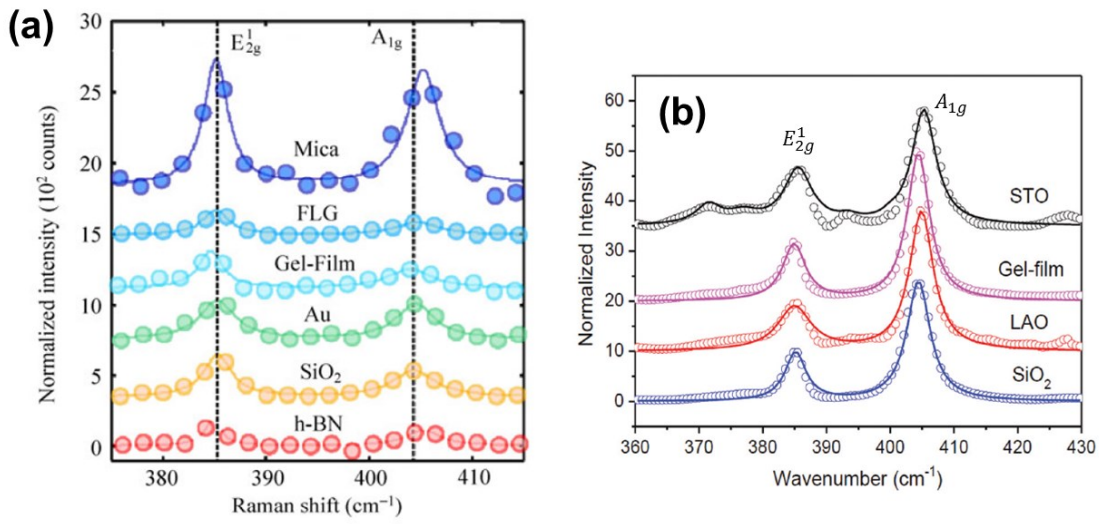


Fig. 3.49 Normalised Raman spectra of monolayer MoS_2 grown on the different substrate. (a) Data from Buscema group (taken from Ref. [335]). (b) Data from Li group (taken from Ref. [341]).

However, significant difference in PL spectra was observed by both Li and Buscema groups (Fig. 3.50). The peak position, intensity, shape varies with different substrates. They suggested the effect was as the result of the substrate inducing doping and causing the charge transfer to the monolayer MoS_2. Both groups reported that MoS_2/SiO_2 sample showed the lowest PL intensity, probably attributed to the scattering of the surface optical phonons [335]. The peak A of MoS_2/SiO_2 were found at lower energy and other materials were blue-shifted. The blue-shift of conducting substrate was observed by Buscema *et al*. due to the relative increase of the luminesce from neutral exciton [335].

The excitons in the monolayer MoS_2 evolves trions (charged excitons) and neutral excitons. The trion emission intensity, in terms of the concentration of trions, is depended on the excess charge. The excitons change their charge states and optical response when additional charges are introduced into the 2D materiasl. The two resonances charged excitons i.e., trions (A^-) and neutral excitons (A^0) contribute to the A exciton peak. A^- is formed by adding one electron with neutral exciton ($e + A^0 \rightarrow A^-$) and located at the lower energy range

compared to the A^0 peak [341,345]. The charge could come from the doping which may be attributed to interface impurities or defects. Weaker doping level and charge transfer gives the smaller spectrum weight ratio (I_{A^-}/I_{A^0}), which I is the integrated emission intensity for neutral exciton (I_{A^0}) and trions (I_{A^-}). Also, full width at half maximum (FWHM) of the peak for trions and neutral excitons becomes broader with the increase of the charge transfer [341]. Buscema *et al*. also claimed that the substrate can affect the radiative decay rates of neutral and charged excitons which caused the difference in the PL spectra [335].

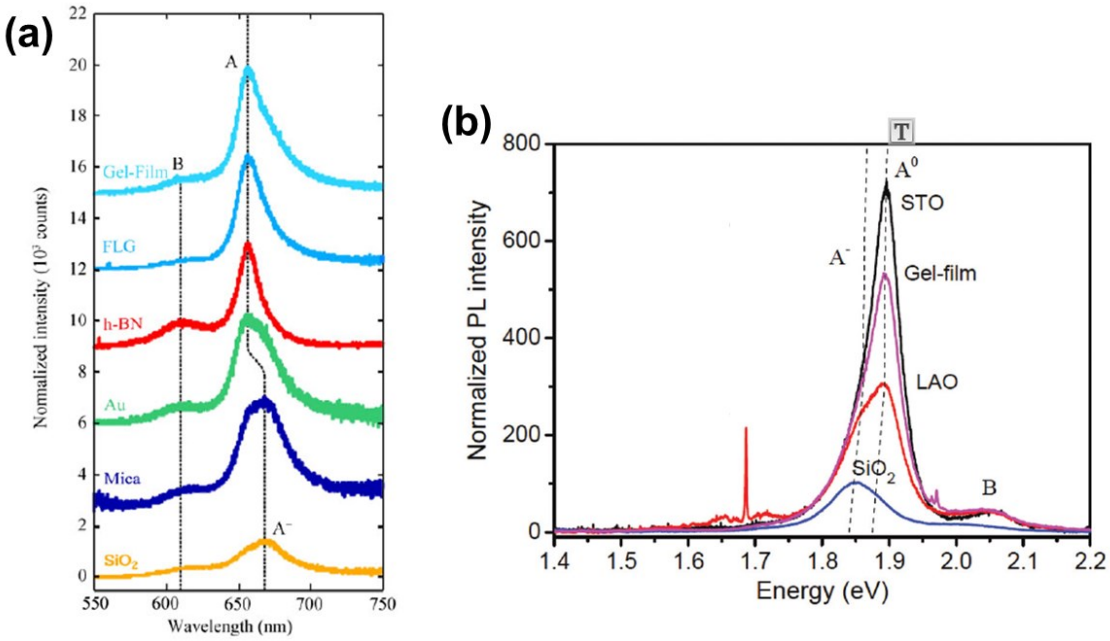


Fig. 3.50 Normalised PL spectra of monolayer MoS_2 grown on the different substrates. (a) Data from Buscema group (taken from Ref. [335]). (b) Data from Li group (taken from Ref. [341]).

3.8 Summary

Study of surface science on nanomaterials allows us to gain a deeper understanding of the distinctive properties compared to its bulk. Surface structures, reconstructions and nanostructures grown on $SrTiO_3$ have been reviewed in detail in terms of the research outcomes and breakthroughs from different research groups. Other metal oxides such as TiO_2 especially its anatase phase is a useful material in catalysis application. The literatures relating surface structures, properties and growth methods of TiO_2 and its anatase phase have been reviewed in Sec. 3.5.4. This review also showed that more scientific attention has been dedicated to explore the growth of metal nanocrystals on the reconstructed $SrTiO_3(001)$ and anatase TiO_2 surfaces because of their capability in modifying the catalytic property. Other 2D materials TMDs especially monolayer MoS_2 have also attracted scientific attention due to its promising electronic and optical properties used in electronics and optoelectronics devices. The current research progress in understanding of the physical properties and characterisation methods of monolayer MoS_2 were reviewed in Sec. 3.7. Also, it showed that the quality and physical behaviour of monolayer MoS_2 are depended on the substrate materials.

3.9 Research Objectives

Study of surface science highlights the importance of surface structures in determining the novel chemical and physical properties of materials in general and metal oxides in particular. Atomic arrangements and electronic structures on the surface are different from those in the bulk. It is the motivation to study $SrTiO_3$ surfaces in order to fully explore their properties and behaviours. The objectives of my research project are to study the epitaxial nanomaterials grown on $SrTiO_3$ substrates which includes the topics as follows.

3.9.1 Nucleation and growth of anatase TiO_2(001) on the $SrTiO_3$(001) substrate

Different growth methods have been established to synthesis TiO_2. Most methods produce anatase TiO_2 with (101) surface. Because the surface energy of anatase (001) is higher than its (101) surface, it is still a challenge to grow energetic and highly reactive anatase (001) surface with a large exposed surface suitable for STM study. Our research group has established a self-assembly epitaxial growth method to create single domain anatase TiO_2(001)-(1 × 4) islands on $SrTiO_3$(001) substrates [21,22]. In this thesis, we will apply this established method to produce high-quality epitaxially-grown anatase islands. The uniformly distributed anatase islands will act as the nucleation sites which are favourable for the growth of the extended anatase (001) thin film. Constraint from substrate $SrTiO_3$(001) lattice will stabilise the anatase with a large exposure of the (001) surface. These surfaces are ideally suited for the study of epitaxially grown metal nanoparticles (e.g., Pd).

3.9.2 Characterisation of Pd on anatase grown on $SrTiO_3$(001)

Epitaxial growth method pointed out a way to produce high quality and stable anatase TiO_2(001) surface. These surfaces are ideally suited to grow metal nanoparticles (e.g., Pd). Most noble metal-TiO_2 catalyst system use rutile TiO_2 phase. Nowadays, anatase especially its (001) surface is found more catalytically active. Only a few work have been conducted on anatase and were mainly focused on its (101) surface. No prior work has been reported about growth of metal particles on anatase (001) terminated $SrTiO_3$(001) surface. As described in Sec. 3.4, the control of crystal sizes and surface atom arrangement is likely to alter the physical and chemical properties of heterogeneous catalysts. Thus, it will be a great opportunity to study the interaction between noble metal crystals with active anatase (001) surface, to understand the growth behaviour and shape evolution of Pd nanocrystals, and the SMSI state in this system. This will be a useful analogue for a catalytic system in which Pd nanocrystals are loaded on small anatase crystal supports.

3.9.3 Effect of substrate structures on the growth of monolayer MoS_2

As 2D materials become thinner to monolayer, the interface between substrate and monolayer becomes more important. As reviewed in Sec. 3.7, substrate induces electronic doping (electron transfer) and strain to the monolayer MoS_2. This effect influences the electronic and optical properties of monolayer MoS_2 that can be analysed by PL and Raman spectroscopy. Among the reported substrate materials, $SrTiO_3$ is the insulator which is suitable to grow MoS_2 to avoid charge transfer between the substrate and MoS_2. Also, $SrTiO_3$ can be easily doped by other elements if the charge transfer is required for thin film-

substrate heterostructures system. In the meantime, a wide range of surface reconstructions with different stoichiometries and unit cell structures have been observed on $SrTiO_3$(001) and (111) surfaces. Theses surfaces are atomically flat with long range order which enables the growth of uniform and flat monolayer MoS_2 crystals. Also the surfaces can be used to study the epitaxial relationship of monolayer MoS_2 crystals with substrates terminated with different surfaces or reconstructions. Substrates with different symmetries may induce different levels of strain for the MoS_2 crystals grown on them, resulting in the change of the bandgap of MoS_2. It will be a useful phenomenon in the thin film-substrate heterostructures system that engineering the electronic and optical properties of monolayer MoS_2 can be achieved by modifying the substrate structures.

Chapter 4

Nucleation and Growth of Anatase TiO_2(001) on $SrTiO_3$(001) Substrates

4.1 Introduction

Nanostructured titanium dioxide (TiO_2) is of great importance in environmental and energy-related applications, e.g., photocatalysts [15,173-175], catalyst supports [176-178], solar cell devices [179,180], optical devices [181,182], gas and humidity sensors [183], optoelectronic [184] and spintronic devices [185]. Research on anatase TiO_2 shows that the anatase TiO_2 polymorph is more catalytically active under ultraviolet irradiation than the other two polymorphs (i.e., rutile and brookite) especially in the photocatalytic production of hydrogen from water [17-19]. The anatase TiO_2(001) surface is more reactive than the thermodynamically stable (101) surface [20]. However, the higher surface energy makes it difficult to produce stable large-area (001) surfaces. Our research group has recently established a self-assembly epitaxial growth method to create anatase TiO_2-(1 × 4) islands on $SrTiO_3$(001) substrates by Ar^+ ion sputtering and extensive UHV annealing [21,22]. This method is based on the substrate stabilisation of anatase because of the small lattice mismatch (3.3%) between the anatase unit cell (a = 3.78 Å) and that of the $SrTiO_3$(001) unit cell (a = 3.91 Å).

In this chapter, we apply this established method to produce high-quality stable anatase (001) surfaces with a large coverage. Anatase islands and films with the (1 × 4) reconstruction and anatase nanostructures with (1 × 3) are studied using STM. The relevant atomic models are also presented in this chapter. The evolution of the anatase (001) surface from islands and the stabilisation of the anatase (1 × 3) reconstruction by the formation of complex nanostructures is discussed in Sec. 4.4.

4.2 Experimental Methods

$SrTiO_3$(001) was used in this experiment. Firstly, the sample was sputtered by Ar^+ ion at 1.5 keV for 12 minutes followed by direct-current anneals in UHV at set temperatures for different lengths of time to prepare nanostructured surfaces. Next, an e-beam evaporator was used for Ti deposition. All depositions were carried out at room temperature followed by annealing at temperatures ranging from 600 to 900°C for different time durations to encourage island growth.

4.3 Results

4.3.1 Nucleation of anatase islands

Upon extensive UHV annealing leading to significant TiO_x surface enrichment, the TiO_2(001) anatase phase started to nucleate on the nanostructured $SrTiO_3$(001) surface. This occurred after several annealing cycles at temperatures of 900-950°C. Fig. 4.1a shows the island nucleation (highlighted by yellow rectangles) on the

nanostructures after repeated cycles of annealing at temperatures of 900-950°C for 48 hours in total. The average height of the anatase islands is 2.25±0.23 nm with respect to the nanostructured $SrTiO_3$(001) substrate. The close-up STM image in Fig. 4.1b shows that these anatase islands are comprised of close packed bright rows aligned with the [010] direction. A line profile was measured along the direction of the black arrow in Fig. 4.1b. The spacing between the rows are 11.99±0.14 Å and 15.62±0.15 Å as indicated in Fig. 4.1e, corresponding to three and four times the lattice constant of $SrTiO_3$(001), a_{SrTiO_3}= 3.91 Å.

Faint rows were observed between two adjacent anatase ridges as indicated by the white arrows in both the STM image (Fig. 4.1b) and the 3D image (Fig. 4.1d). When closely inspected, each of the bright rows is comprised of well-aligned ovals. These ovals, highlighted by red dots in Fig. 4.1c, with a periodicity of 3.95±0.07 Å are in agreement with the lattice constant of $SrTiO_3$ unit cell. Therefore, islands formed on the nanostructured $SrTiO_3$(001) substrate adopt the $SrTiO_3$(001) lattice constant and have (1 × 3) and (1 × 4) reconstructions.

There are also some other features observed on anatase TiO_2(001) islands. When two anatase islands are next to each other as shown in Fig. 4.2a, the bright rows on "island A" are slightly offset compared to those on "island B". The shift is 4.02±0.07 Å which matches to one unit cell constant of $SrTiO_3$. Point defects (Fig. 4.2b) were also observed on anatase islands ridges and some examples are highlighted in Fig. 4.2c.

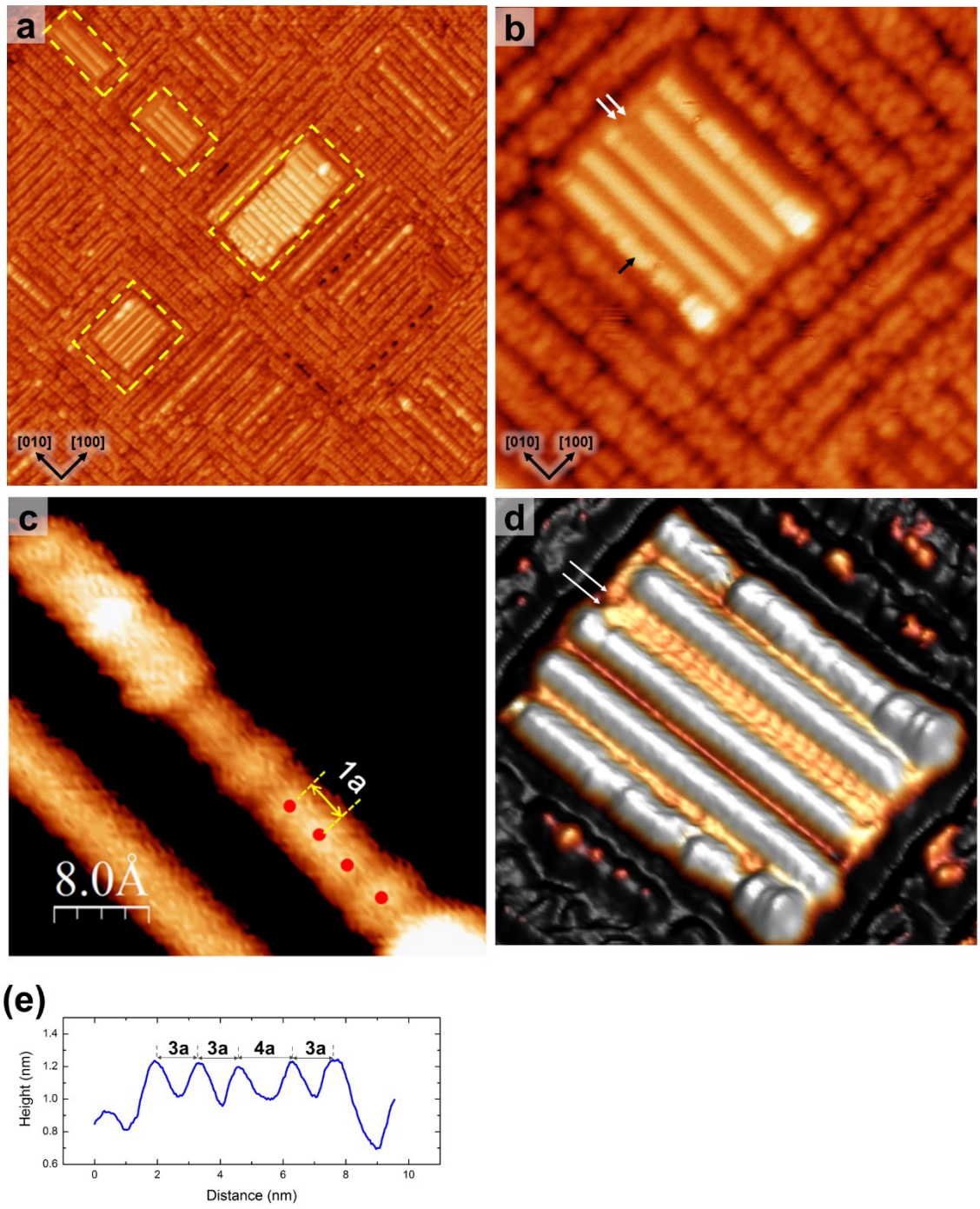


Fig. 4.1 STM images showing the formation of TiO_2 anatase islands on nanostructured $SrTiO_3$(001) surfaces. (a) Nucleated islands after several anneals at temperatures of 900-950°C for 48 hours in total. These islands are highlighted by yellow rectangles (image size: 80 × 80 nm^2, imaging conditions: V_s = +1.367 V, I_t = 0.225 nA). (b) STM image of a single anatase island (image size: 20 × 20 nm^2, imaging conditions: V_s = +1.795 V, I_t = 0.230 nA). The faint rows are highlighted by white arrows. (c) Periodical oval structures (highlighted by red dots) on anatase ridges. (d) 3D image of Fig. 4.1b. Faint rows are highlighted by white arrows. (e) Line profile taken across the islands ridges in the direction of the black arrow in Fig. 4.1b. It shows that the separations between anatase ridges are $3a$ and $4a$ (a = 3.91 Å).

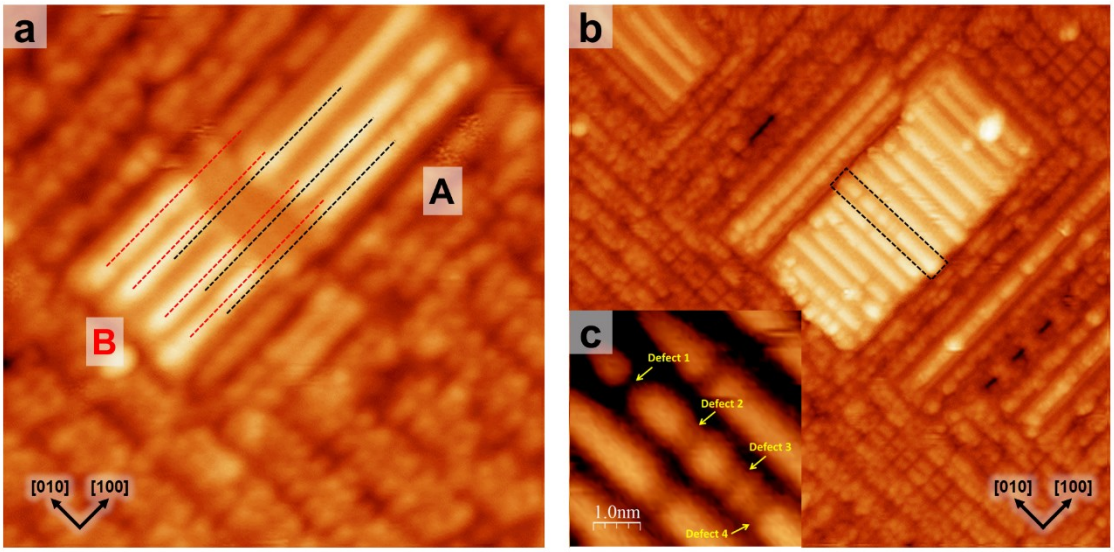


Fig. 4.2 STM images of some features observed on anatase islands. (a) The offset between the bright rows between two adjacent islands A and B (image size 20 × 20 nm^2, imaging conditions: V_s = +1.87 V, I_t = 0.285 nA). (b) Point defects on anatase island ridges (image size: 40 × 40 nm^2, imaging conditions: V_s = +1.367 V, I_t = 0.225 nA). (c) Magnified image of selected area in Fig. 4.2b showing the defects on anatase ridges.

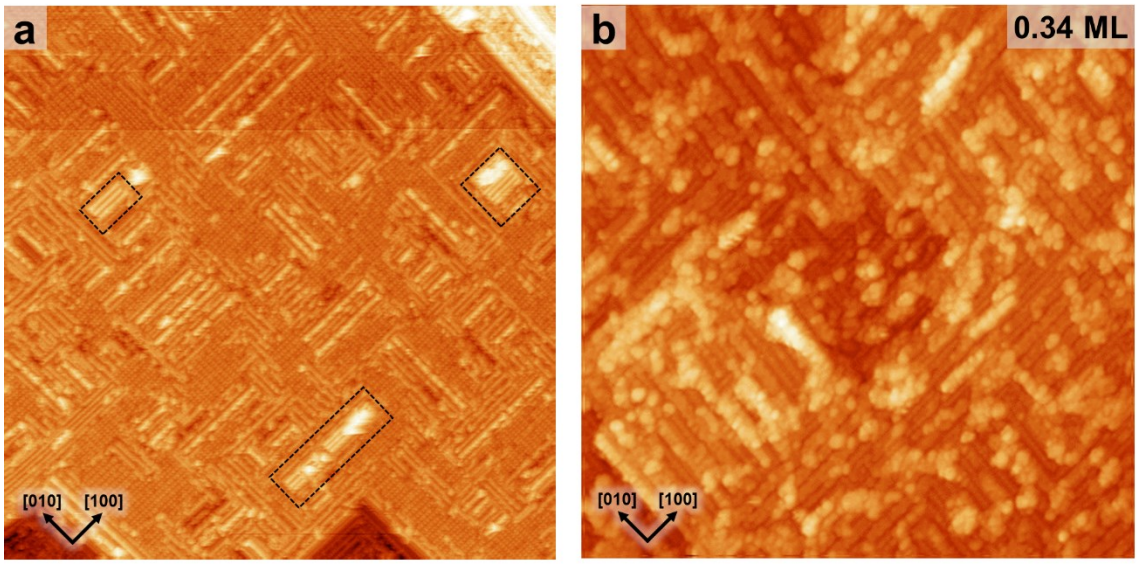
4.3.2 Growth of anatase islands

Extensive UHV anneals at temperatures of 900-950°C led to the nucleation of anatase islands on the $SrTiO_3$(001) substrate. Growth of anatase TiO_2(001) can be further enhanced by depositing Ti onto the nanostructured $SrTiO_3$(001) substrate, followed by an anneal at 600-900°C. Ti was deposited onto the sample which was already decorated by small anatase islands. The sample surface is shown in Fig. 4.3a and anatase islands are highlighted. Fig. 4.3b-f are the STM images of the substrate surface taken after post-deposition anneals at temperature from 600 to 850°C.

0.34 ML of Ti was first deposited onto the sample surface. Fig. 4.3b shows the surface annealed in UHV at 600°C for 30 minutes. Ti clusters formed oval shapes and were evenly distributed on the nanostructured $SrTiO_3$(001) substrate. They preferentially locate along the nanolines. In some regions nanolines that have not been covered by Ti clusters can still

be seen. After the sample was annealed at 650°C, the oval-shaped clusters started to join together and form islands. These islands grew preferentially along the substrate nanostructures (Fig. 4.3c). Some islands in linear shapes formed on the surface and grew along the [010] and [100] directions. The height of the linearly-shaped islands is approximately 1.5 nm. After the sample was further annealed at 750°C for 4 hours, more anatase islands started to form around the nanostructures (Fig. 4.3d). Around 1/3 of the area was covered by anatase and the rest was mainly tetraline-structured. Some small anatase islands are located far apart. Some relatively big anatase islands formed at this stage gathered very closely and stacked onto each other. The heights of the islands vary from 8 Å to 14 Å.

A further 0.17 ML of Ti was deposited on the nanostructured $SrTiO_3$(001) sample before it was annealed at temperatures in the range of 800-900°C. The number of anatase islands has increased after Ti deposition and a post-deposition anneal at 800°C for 1 hour (Fig. 4.3e). Next this sample was further annealed at 850°C for 1 hour. After this anneal, few stacked islands were seen and most anatase islands were found in elongated shapes along the length of the ridges (Fig. 4.3f).



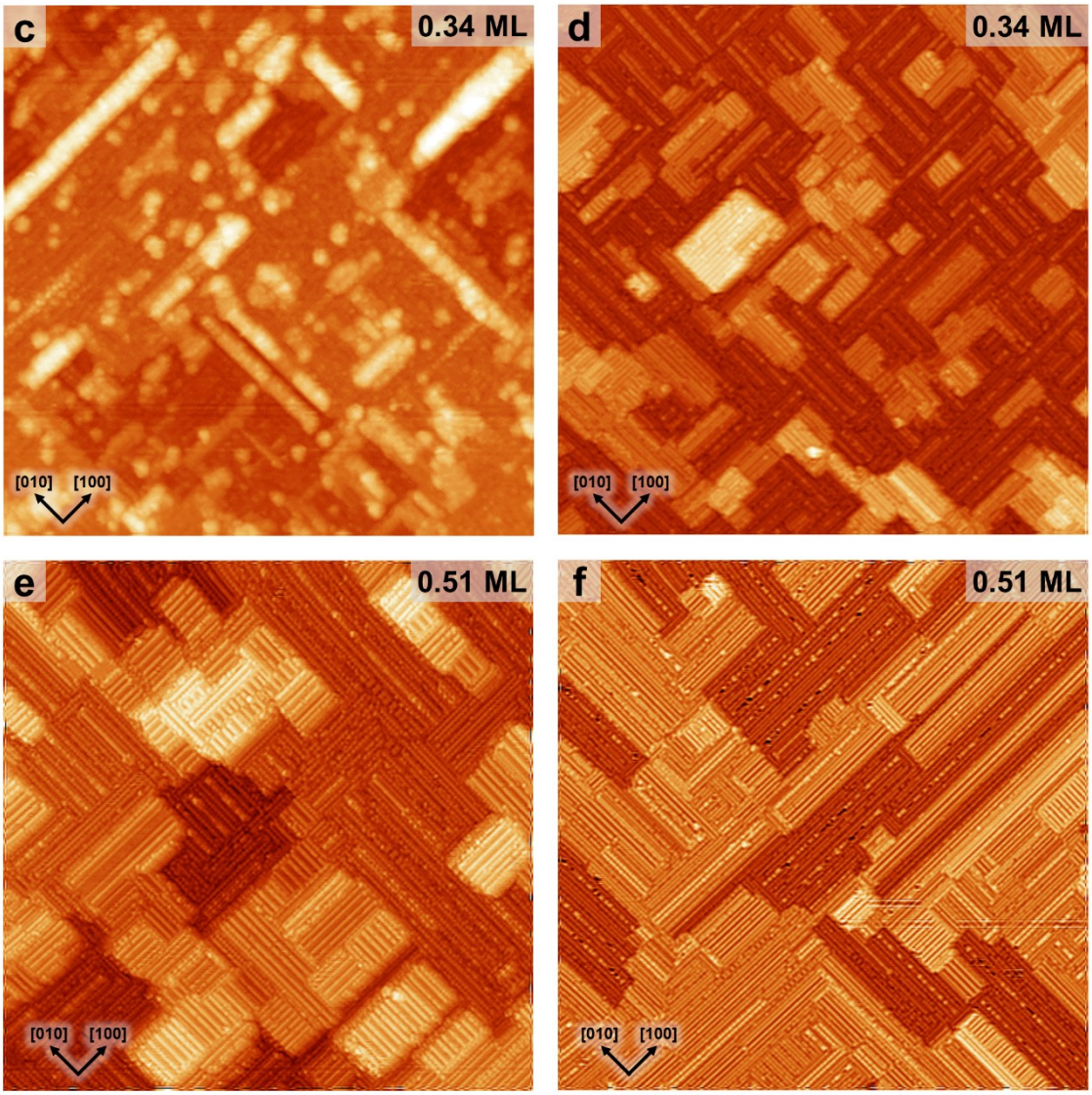


Fig. 4.3 Ti deposition and UHV annealing at different temperatures and durations facilitate the growth of anatase islands on the $SrTiO_3$(001) substrate. (a) STM image of small anatase islands formed on the $SrTiO_3$(001) substrate before Ti deposition. These islands are highlighted (image size: 150 × 150 nm^2, V_s = +1.603V, I_t = 0.265 nA). (b-e) STM images of the sample surface after room-temperature Ti deposition followed by post-deposition anneals at different temperatures: (b) 0.34 ML Ti deposited and annealed at 600°C for 30 minutes (image size: 80 × 80 nm^2, V_s = +1.438 V, I_t = 0.21 nA). (c) 0.34 ML Ti deposited and annealed at 650°C for 4 hours (image size: 100 × 100 nm^2, V_s = +1.5 V, I_t = 0.25 nA); (d) 0.34 ML Ti deposited and annealed at 750°C for 4 hours (image size: 150 × 150 nm^2, V_s = +1.603 V, I_t = 0.235 nA); (e) 0.51 ML Ti deposited and anneal at 800°C for 1 hour (image size: 100 × 100 nm^2, V_s = +1.652 V, I_t = 0.25 nA); (f) 0.51 ML Ti deposited and annealed at 850°C for 1 hour (image size: 150 × 150 nm^2, V_s = +1.609 V, I_t = 2.43 nA).

Next, another 0.34 ML of Ti was deposited and the sample was annealed at 850°C for 2 hours. 20 minutes after the sample was cooled down to room temperature, it was taken out of UHV into atmosphere. The coverage of anatase was significantly increased after the sample was exposed to the ambient environment and re-inserted into the UHV-STM chamber. Next, 0.17 ML of Ti was deposited and the sample was post annealed at 850°C for 1.5 hours. After this treatment, the sample surface was mostly covered by anatase (Fig. 4.4a). The total amount of Ti deposited onto the sample surface was 1.02 ML since the first Ti deposition.

Surface reconstructions were observed on the anatase film after thermal treatment (Fig. 4.4). The surface reconstructions on anatase TiO_2 are driven by the release of tensile stresses from the anatase surface Ti(5) and O(2) bonds [230]. The 5 and 2 in brackets denote the coordination numbers of the atoms. A zoomed-in STM image of the anatase surface is shown in Fig. 4.4b. A line profile measured across the bright ridges in Fig. 4.4b is shown in Fig. 4.4e. The separation of the ridges is 14.58±0.18 Å, i.e., four times the TiO_2 anatase unit cell constant (a_{TiO_2}= 3.78 Å) (Fig. 4.4e). From both the top-view (Fig. 4.4c) and 3D (Fig. 4.4d) images, it can be seen that the ridges consist of oval spots, which are highlighted by the blue and red dots in the images. The periodicity of the ovals is 3.68±0.09 Å (one TiO_2 anatase unit cell). The measurements indicate that the anatase grown on $SrTiO_3$(001) is typically (1 × 4) reconstructed. Faint rows were observed between the bright ridges indicated by arrows in Fig. 4.4f and g. The separation between two faint rows is 3.67±0.12 Å (equal to a_{TiO_2} of anatase).

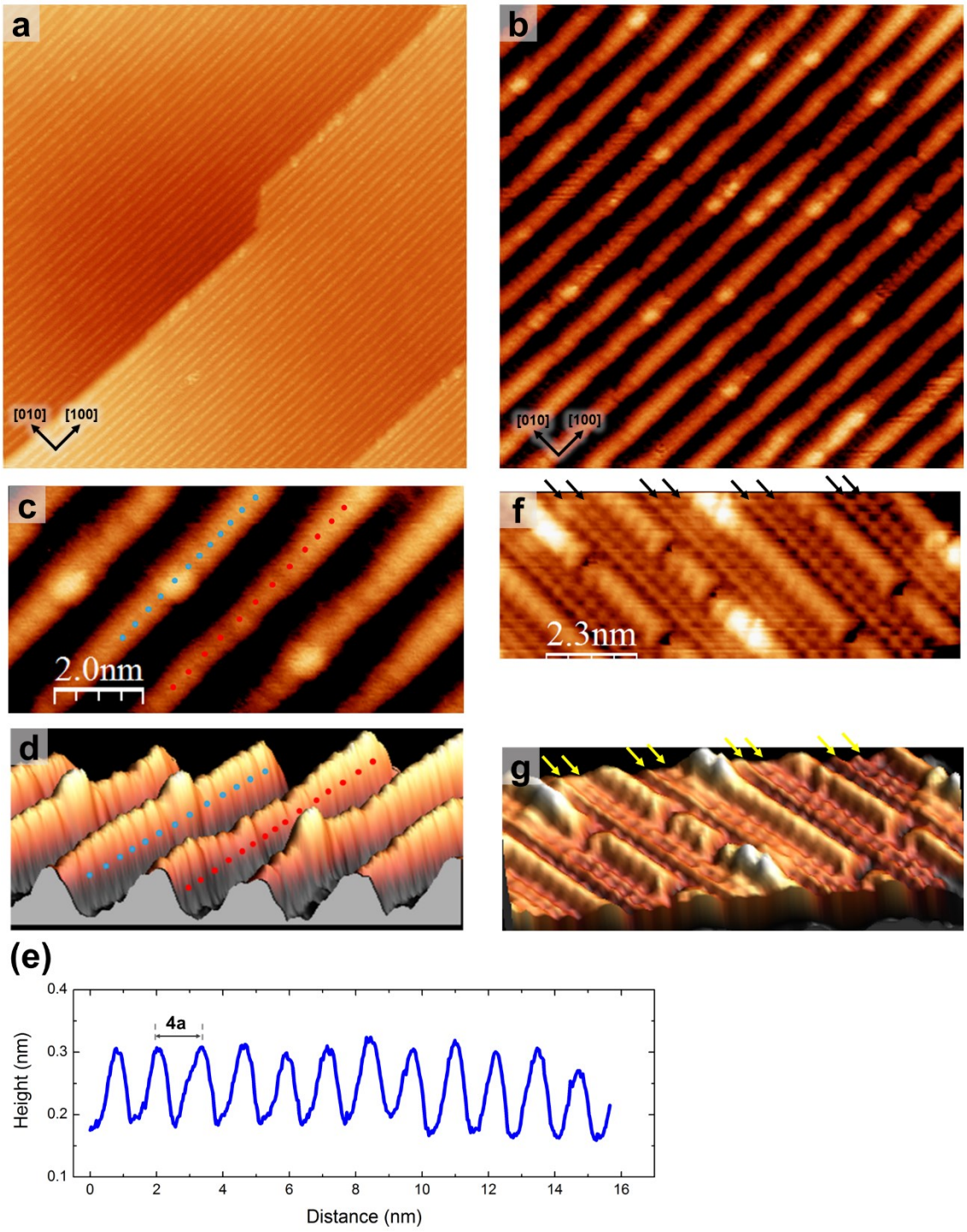


Fig. 4.4 (a) STM image of anatase structures on three terraces (image size: 80 × 80 nm^2, imaging conditions: V_s = +1.61 V, I_t = 0.225 nA). (b) Processed STM image of the anatase surface (image size: 20 × 20 nm^2, imaging conditions: V_s = +1.61 V, I_t = 0.225 nA). (c) Zoomed-in STM image showing details of the anatase structure. The periodic ovals in the anatase ridges are highlighted. (d) 3D view of the ridge structure. (e) Profile measured across the ridges showing the periodicity is four times the TiO_2 anatase unit cell lattice constant (a = 3.78 Å). (f) STM image of the faint-row structure between the bright ridges (highlighted by arrows). (g) 3D view of faint-row structures and ridges.

Several models have been proposed for the anatase (001)-(1 × 4) reconstruction including the microfacet model (MFM) [214], added-and-missing row (AMR) model [215], ad-molecule model (ADM) [230] and some modified ADMs [199,228]. Among these, the ad-molecule model (ADM) originally proposed by Lazzeri and Selloni [230] (Fig. 4.5a) is widely accepted and was recently proved by Yuan *et al.* when they conducted real-time observations of the surface reconstruction of TiO_2(001) using environmental transmission electron microscopy (ETEM) [229]. By referring to the ADM model proposed by Lazzeri and Selloni [230], we built a model for the epitaxial relationship of the anatase (1 × 4) reconstruction on $SrTiO_3$(001) (Fig. 4.5c, d and e). The colour scales for the atoms in the different layers are summaried in Fig. 4.5f. Ti atoms from the top layer to the bulk are represented by different colour scales of red. The O atoms are in blue and Sr atoms are in green.

As shown in the side-view models in Fig. 4.5 c and d, due to the lattice mismatch (anatase TiO_2(001)‖$SrTiO_3$(001)= -3.3%), the anatase unit cells in touch with $SrTiO_3$(001) is under tension and slightly expanded compared to that of the free-standing unit cell constant (a_{TiO_2}= 3.78 Å). As suggested by Lazzeri and Selloni, the bright rows are derived from the surface Ti(4) atoms and faint rows correspond to the Ti(5) surface atoms [230] (Fig. 4.5a). The 3D view of (1 × 4) reconstructed anatase grown on $SrTiO_3$(001) is presented in Fig. 4.5e. The rows of TiO_3 species periodically replace every fourth row of bridging O on unreconstructed anatase (001) surfaces (Fig. 4.5b), resulting in the (1 × 4) reconstruction (Fig. 4.5e). The top rows with TiO_3 species are protrusive and correspond to the bright ridges observed in the STM images (Fig. 4.4b).

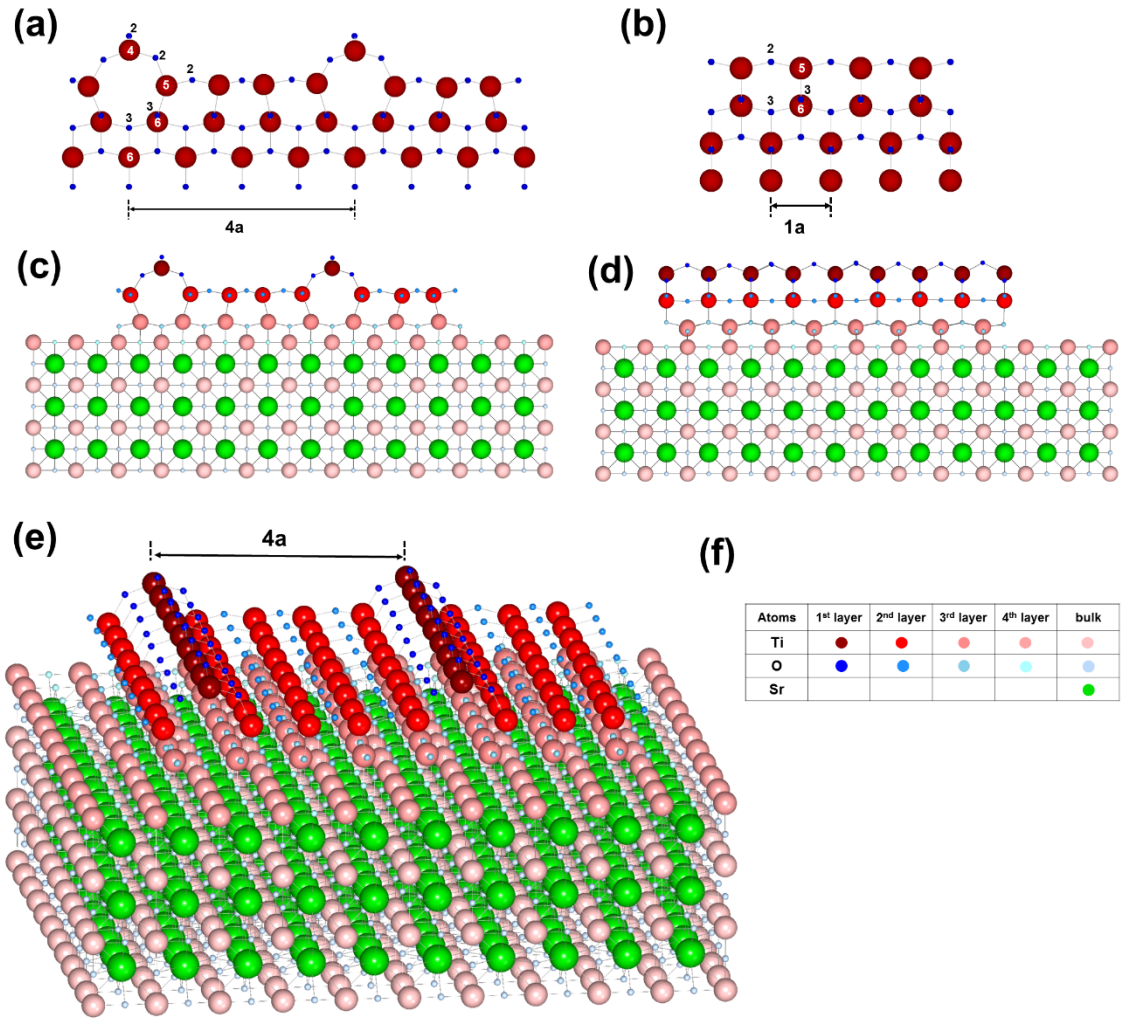


Fig. 4.5 (a) ADM Model of anatase TiO_2(001) with the (1 × 4) reconstruction [230]. (b) Side view of ball-and-stick model of unreconstructed anatase TiO_2(001). (c) and (d) Side view models. (e) 3D model of the epitaxially grown TiO_2(001)-(1 × 4) on $SrTiO_3$(001). (f) Summary of the colour codes of atoms in the different layers. Ti atoms are in red, O atoms are in blue and Sr atoms are in green.

Screw dislocations were observed in anatase TiO_2 and highlighted in Fig. 4.6a. The Burgers vector of the screw dislocations is in the [001] direction and is perpendicular to the anatase (001) surface. A close-view image and a 3D image, in Fig. 4.6b and c, show that a step is formed around the dislocation with the height of 4.26±0.07 Å, corresponding to half of anatase unit cell (i.e., 4.76 Å). The slight offset of the measurement to the true value is due to the calibration factor of z-piezo in the STM. A height profile was measured along the direction indicated by the arrow in Fig. 4.6a. There appears a kink in the trend line of the

height profile as pointed out by the arrow in Fig. 4.6d. The surface close to the screw dislocation is lifted up by around 0.68° due to the lattice distortion caused by the shear stress around the region. Some regions of the anatase surface have two types of domains, A and B, aligned along [100] and [010] respectively (Fig. 4.7a and b). They are at 90° to each other and are (1 × 4) and (4 × 1) reconstructed respectively.

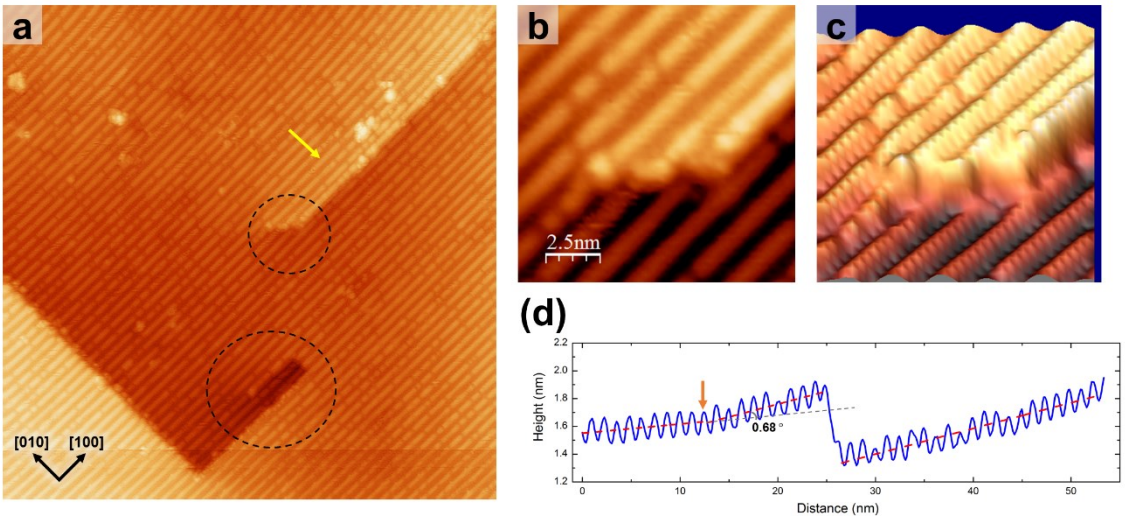


Fig. 4.6 (a) STM image of screw dislocations formed on the anatase surface (outlined by the black dash circles) (image size: 80 × 80 nm^2, imaging conditions: V_s = +1.6 V, I_t = 0.225 nA). (b) Zoomed-in STM image of one screw dislocation. (c) 3D of the screw dislocation in Fig. 4.6b. (d) Height profile measured along the direction of the arrow in Fig. 4.6a across the step caused by the screw dislocation.

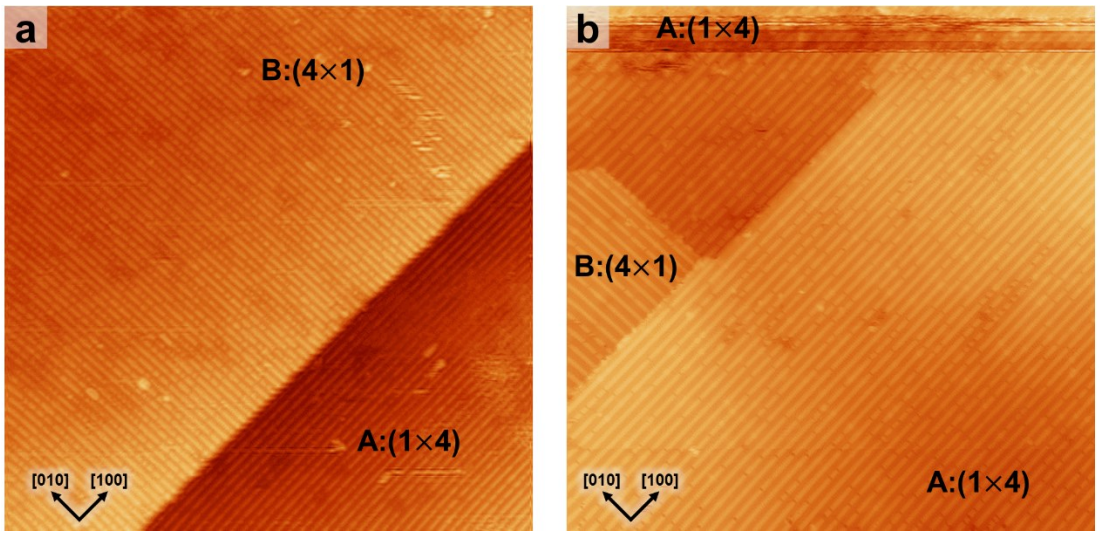


Fig. 4.7 Two types of anatase domains are found, type A: (1 × 4) reconstruction and domain B: (4×1) reconstruction. (a) Image size: 100×100 nm^2, imaging conditions: V_s = +1.619 V, I_t = 0.24 nA; (b) Image size: 80 × 80 nm^2, imaging conditions: V_s = +1.404 V, I_t = 0.215 nA.

4.3.3 Anatase (1 × 3) nanostructures

Ti was deposited on the nanostructured $SrTiO_3$(001) substrate at room temperature for 120 seconds (quantity: 0.34 ML) and post-deposition annealed at 800°C for 30 minutes. This treatment process gave rise to the formation of complex nanostructures on $SrTiO_3$(001) (Fig. 4.8a). This complex nanostructure is comprised of close-packed parallel bright anatase ridges and a single outer row at either side made up of dots. In addition, the dot-anatase nanostructures all have the same width of 6.78 ± 0.05 nm and only vary in length. Eight complex nanostructures are highlighted in Fig. 4.8a.

Fig. 4.8b shows one complex nanostructure from Fig. 4.8a highlighted by the yellow rectangle. Fig. 4.8c is the line profile measured across the anatase ridges in the direction along the arrow in Fig. 4.8b. The separation between neighbouring ridges is 11.48 ± 0.10 Å, which corresponds to three times the $SrTiO_3$(001) lattice constant. Similar to anatase islands, these anatase nanostructures adopt the lattice constant of the substrate $SrTiO_3$(001) unit cell and show a (1 × 3) reconstruction (Fig. 4.8c). The anatase ridges are aligned in the <100> directions. Referring to the ADM model of the anatase TiO_2(001)-(1 × 4) reconstruction proposed by Lazzeri and Selloni [230], we built the anatase TiO_2(001)-(1 × 3) reconstruction model as shown in Fig. 4.8d. In this (1 × 3) model, rows of TiO_3 species periodically replace every third row of the bridging O atoms on the unreconstructed anatase TiO_2(001) surface as shown in the model in Fig. 4.5b.

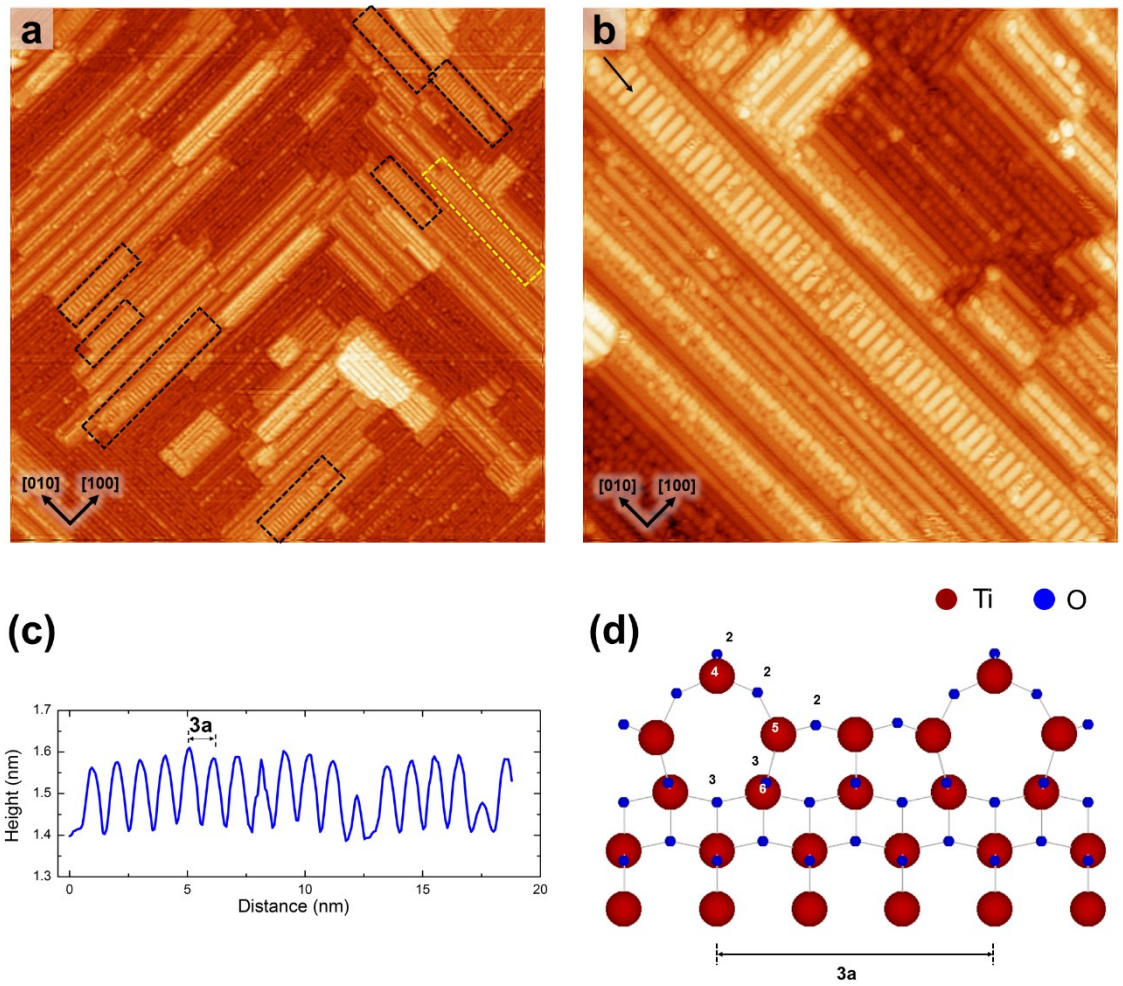


Fig. 4.8 (a) STM image showing the formation of complex anatase (1 × 3) nanostructures on the $SrTiO_3$(001) substrate. Anatase nanostructures are highlighted by dashed rectangles (image size: 150 × 150 nm^2, imaging conditions: V_s = +1.799 V, I_t = 0.24 nA). (b) STM image of the zoomed-in anatase (1 × 3) nanostructure highlighted by the yellow rectangle in Fig. 4.8a (image size: 50 × 50 nm^2, imaging conditions: V_s = +1.799 V, I_t = 0.24 nA). (c) Line profile measured across the anatase ridges showing the (1 × 3) reconstruction. (d) Side view of the (1 × 3) reconstructed anatase nanostructure according to the ADM model (Ref. [230]).

A zoomed-in image of this complex nanostructure is shown in Fig. 4.9a and its 3D image is presented in Fig. 4.9b. Each nanostructure has close-packed anatase ridges with the (1 × 3) reconstruction and outer rows with dots separated by 0.78 ± 0.02 nm, i.e., twice the $SrTiO_3$(001) unit cell constant. The separation of the side dots from these complex nanostructures is identical to that of trilines and tetralines. The anatase ridges is around 2 Å

higher than dots (Fig. 4.9c), which corresponds to one interplanar spacing (i.e., 2.38 Å) of anatase unit cell, suggesting anatase ridges present one more Ti layer above dots structure.

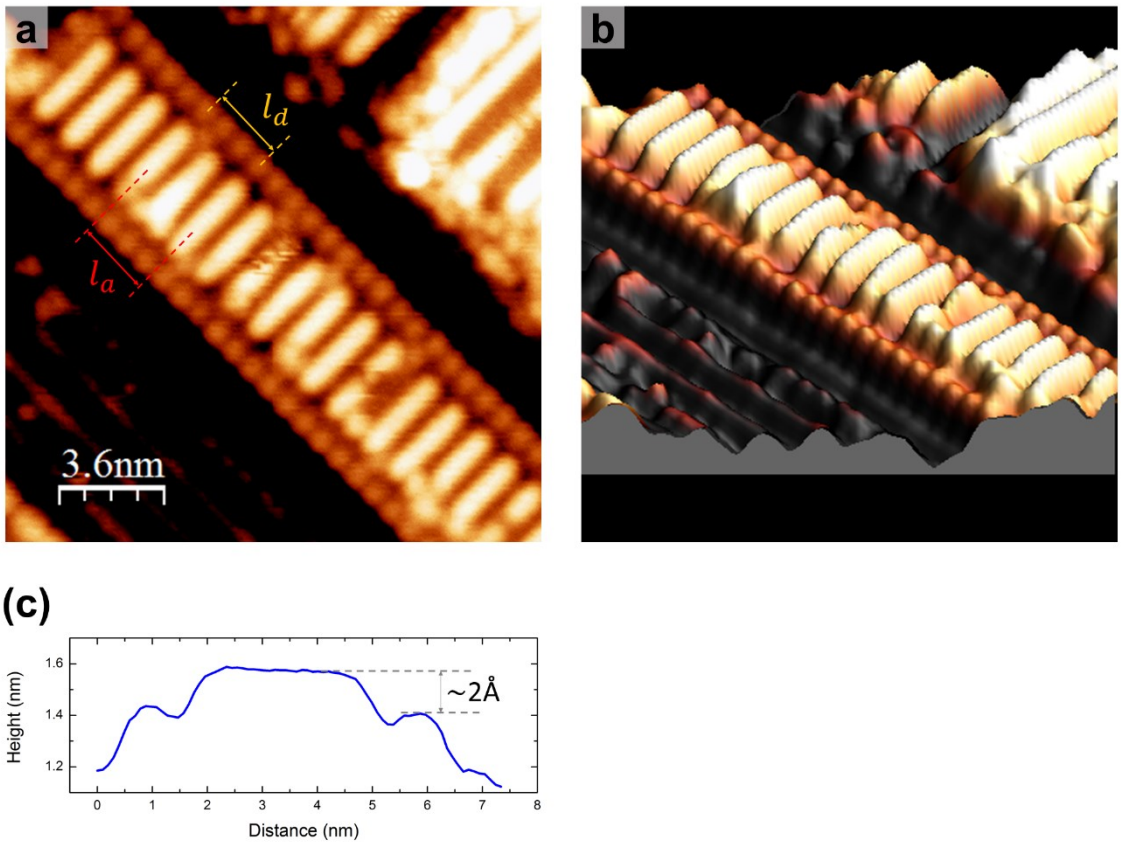


Fig. 4.9 (a) Processed STM image of the complex anatase (1 × 3) nanostructure and (b) the corresponding 3D view. (c) Height profile measured across two dots and one anatase ridge.

Using to the DFT-modelled nanoline structures from Marshall *et al.* [13,85] and the ADM model proposed by Lazzeri and Selloni [230], we propose a model for our complex (1 × 3) anatase nanostructure grown on $SrTiO_3$(001) (Fig. 4.10a). The Ti atoms are in red and become lighter from surface to the bulk. The side view of this complex nanostructure is depicted in Fig. 4.10b and c. It shows that the anatase (1 × 3) nanostructure have one more TiO_x layer above dots, which is consistent with our measurement in Fig. 4.9c.

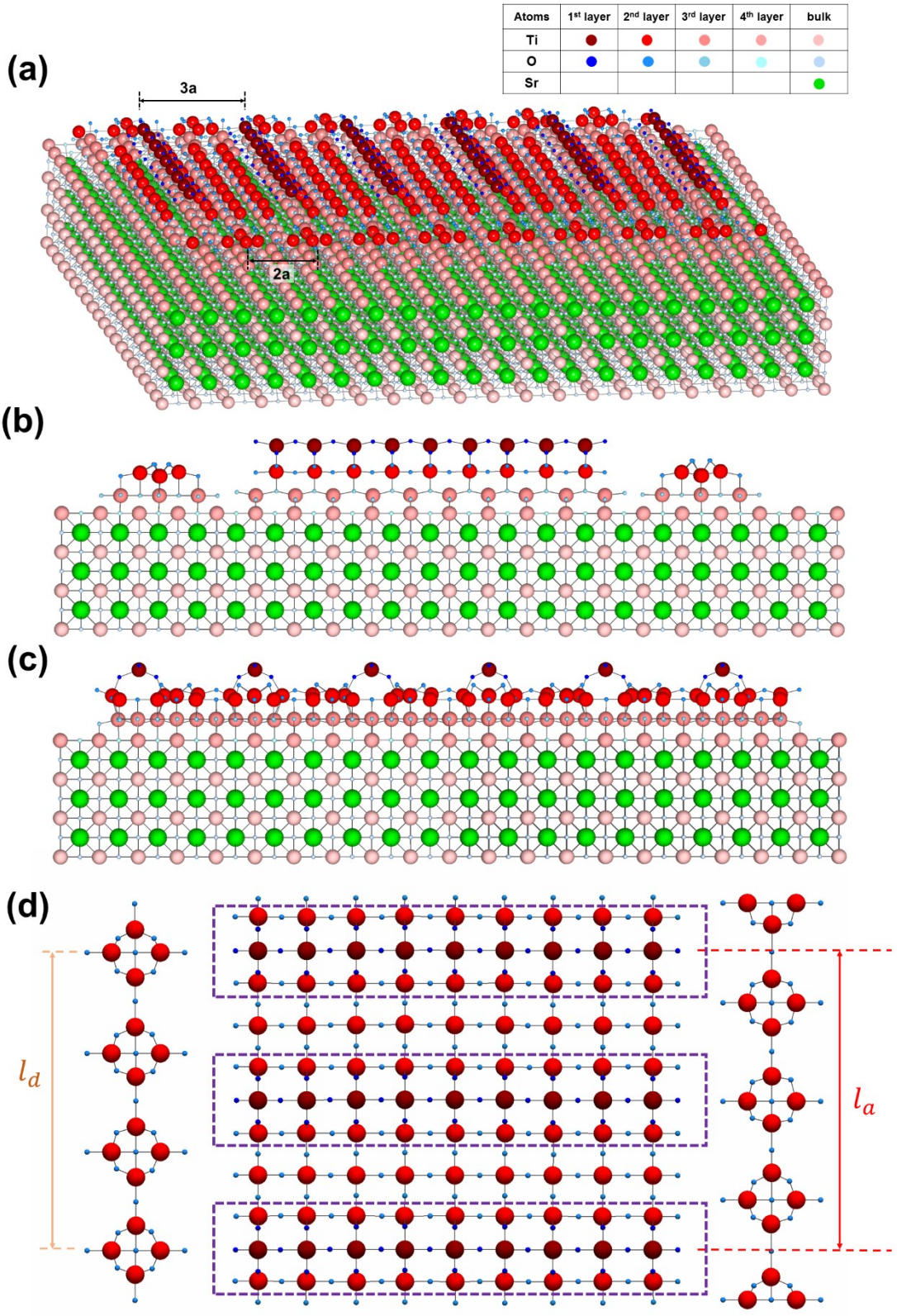


Fig. 4.10 Atomic model of the complex anatase (1 × 3) nanostructure grown on $SrTiO_3$(001). (a) 3D model; (b) and (c) Side-view models; (d) First two layers of atomic arrangement of the complex anatase nanostructure. The same distances between l_a of the anatase ridges and l_d of the dots are represented. Summary of the colour codes of atoms in the different layers is shown in the top-right corner. Ti atoms are in red, O atoms are in blue and Sr atoms are in green.

The top view of the atomic model from first two Ti-O layer shows that every fourth dot from the side row is aligned with every third anatase ridge as indicated by the same distances labelled in l_a and l_d (Fig. 4.10d). This agrees with our measurements where the periodicity of the dots is 0.78±0.02 nm (i.e., $2a_{SrTiO_3}$) and periodicity of the anatase ridges is 1.15±0.01 nm (i.e., $3a_{SrTiO_3}$). The distance across three anatase ridges ($l_a$in Fig. 4.9a) equals to that across four dots ($l_d$in Fig. 4.9a)

4.4 Discussion

4.4.1 Formation of anatase TiO_2 on $SrTiO_3$

We have shown that the anatase TiO_2(001) phase can form on $SrTiO_3$(001) by the epitaxial growth method. Sputtering $SrTiO_3$(001) by Ar^+ ions produces the nonstoichiometric surface. Annealing the sample in reduced atmosphere (UHV) causes Ti and O segregation towards the $SrTiO_3$(001) surface [12]. This leads to Ti enrichment and enables the epitaxial growth of self-assembled reconstructed TiO_x nanolines on the $SrTiO_3$(001) substrate. DFT calculations by Marshall *et al*. [85] and Becerra-Toledo *et al.* [146] illustrate that these TiO_x-rich nanolines grown on $SrTiO_3$(001) consist of three TiO_x layers, where the topmost layer sits on an intermediate TiO_2 layer, which sits on top of the bulk TiO_2 surface. This TiO_x-terminated surface provides a favourable template for the continuous growth of TiO_2 structures when sufficient Ti and O precursors are segregated towards the surface. This epitaxial growth of TiO_2 is induced by extensive annealing in UHV. TiO_2 has three polymorphs and its anatase phase has a very close lattice parameter to that of

$SrTiO_3$(001). The small lattice mismatch of 3.3% favours the formation of the stable anatase structure with the high-energy (001) surface exposed.

The epitaxially-grown anatase islands are stressed in tension by the $SrTiO_3$(001) substrate. The strain can be released by forming mismatch dislocation at the interface. The simplified schematic of the semi-coherent interface between anatase TiO_2(001) and $SrTiO_3$(001) is depicted to calculate the misfit dislocation density (Fig. 4.11).

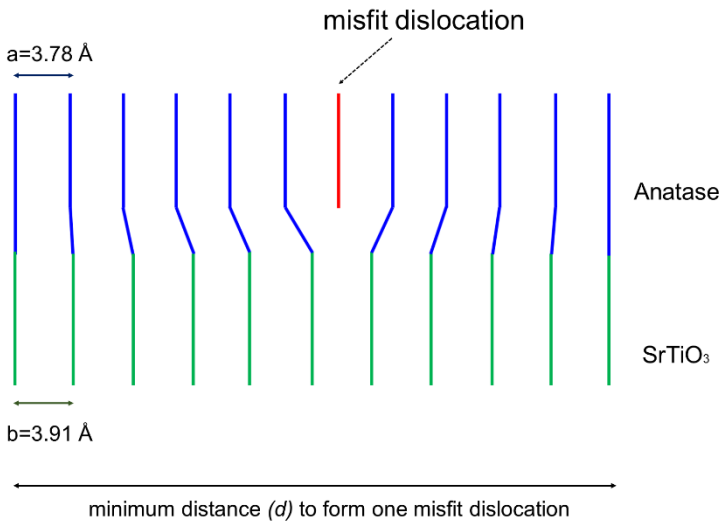


Fig. 4.11 Simplified schematic showing the misfit dislocation formed at interface between anatase TiO_2(001) and $SrTiO_3$(001). Both anatase and $SrTiO_3$ unit cells are present in the side view.

The minimum distance (d) required to form one dislocation, consist of $(n + 1)$ anatase unit cells, which are elastically strained with n unit cells of $SrTiO_3$(001). One additional plane is formed in the anatase caused by misfit dislocation. The following relationship can be obtained,

$$d = (n + 1) \times a \tag{4.1}$$

$$d = n \times b \tag{4.2}$$

Combining Eq. 4.1 and Eq. 4.2 gives $(n+1) \times a = n \times b$ (4.3)

Which, a and b denote the lattice constants of anatase and $SrTiO_3$ respectively.

Substituting $a = 3.78$ Å and $b = 3.91$ Å into Eq. 4.3, gives $n = 29$.

Therefore, the minimum distance (d) to form one dislocation is

$$d = 29 \times 3.91 \text{ Å} = 11.3 \text{ nm}$$

Most of anatase islands observed in our sample at the initial growth stage are smaller than 11.3 nm, which the misfit dislocations are unexpected to form at the interface. The anatase islands are therefore elastically strained by $SrTiO_3$ surface in lateral directions in agreement with our STM measurement which shows the anatase islands adopt the lattice constant of $SrTiO_3$ unit cell (a = 3.91 Å).

Upon low temperature anneals, Ti and O atoms are less mobile. Additionally introduced Ti precursors preferentially adhere to existing anatase nuclei and grow in height in order to reduce the tensile strain built-up in anatase. This matches our STM observation that anatase islands formed at low temperatures stack onto each other (Fig. 4.3d and e). We observed elongated flat anatase islands when the sample was treated at 850°C (Fig. 4.3f). This is because the detachment and attachment of Ti and O from the original anatase islands are thermally assisted at higher temperatures [22]. This leads to their preferential growth along the ridges and hence the formation of elongated flat islands.

Anatase islands prepared by our method are widely spaced. Each island acts as a preferential nucleation site for island growth into a film. Screw dislocations are often observed in the anatase film, indicative of the spiral growth mechanism. A screw dislocation is a line defect, involving the distortion of the Ti-O interatomic bonds and the displacements of Ti and O atoms [346], which causes the formation of steps on the surface. The steps have high surface

energies and act as the favourable sites for atoms to bond to [347]. With Ti and O atomic precursors continuously attaching to the sides of the steps, the steps move forwards [348] and this leads to the formation of new TiO_2 layers. The dislocation steps advance around the dislocation core and generate a spiral pattern during the growth of anatase layers. This continuous step movement on the sample surface enable rapid growth of anatase film in a high coverage.

The size of anatase films are larger than 11.3 nm which enables the formation of misfit dislocations at interface to release the strain. This is confirmed by our STM measurement which anatase films present the original unit cell size (a = 3.78 Å) and relaxed on the $SrTiO_3$(001) surface.

4.4.2 Formation of anatase TiO_2-(1 × 3) nanostructure

According to the AES and core-level XPS results for nanolines studied by Deak *et al.* [12] and Marshall *et al.* [13,85], Ti is enriched in the backbone of trilines and tetralines. The Ti enrichment also increased with increasing annealing temperatures and durations. Higher temperatures assist the segregation of Ti and O towards the surface in the reduced atmosphere (UHV). Fig. 4.12 compares the atomic-layer structures of trilines [85] and the anatase (1 × 3) reconstruction on $SrTiO_3$(001). The first TiO_x layers on them are different due to the different surface reconstructions. Layer 2 and 3 of the anatase (1 × 3) nanostructure (Fig. 4.12 b2 and b3) show the same atomic arrangements as those of the triline backbone structure (highlighted by the dashed rectangle in Fig. 4.12. a2 and a3). The same subsurface atomic arrangements (layer 2 and 3) indicate that the backbone can

reconstruct to form the anatase (1 × 3) structure once there are sufficient Ti and O atoms upon thermal treatments.

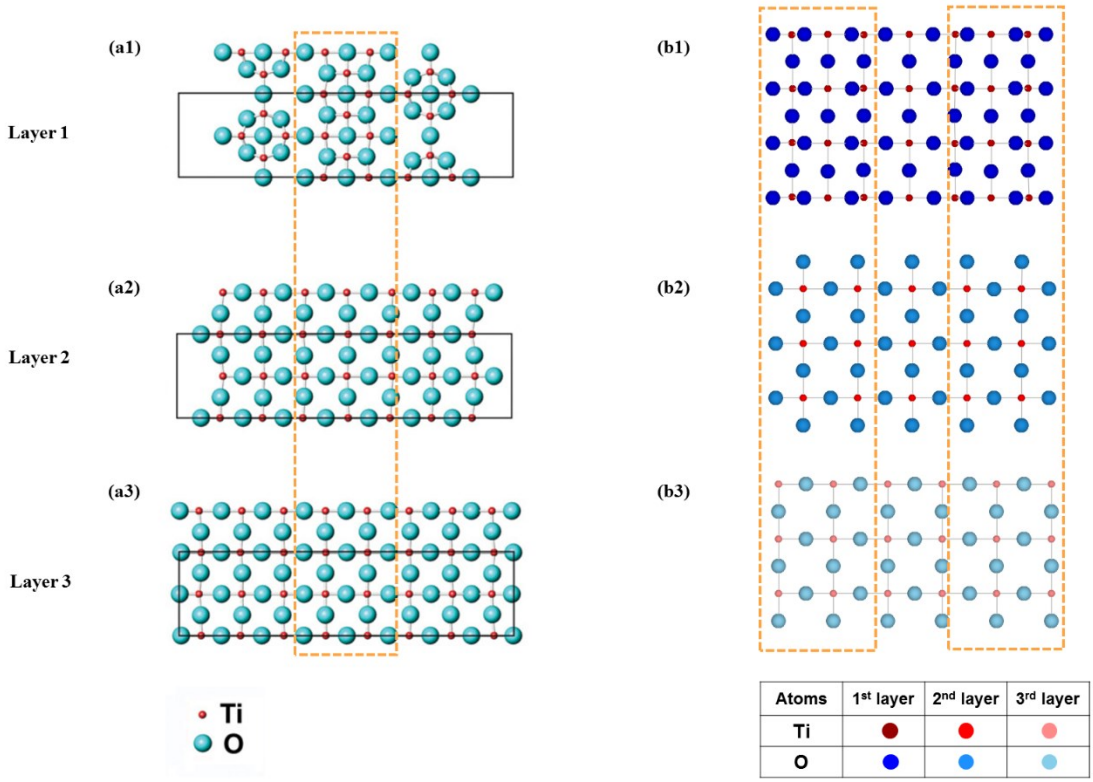


Fig. 4.12 Comparison of TiO_x layered structures of the triline and the anatase (1 × 3) reconstruction. (a) Triline structure. The atomic arrangement of the triline backbone is highlighted by the dashed rectangle (adapted from Ref. [85]). (b) Anatase (1 × 3) reconstruction. The atomic arrangements of bright ridges are highlighted by the dashed rectangle.

Surface reconstructions on anatase TiO_2 are always observed and driven by the release of tensile stresses in anatase surface Ti(5) and O(2) bonds [230]. The (1 × 4) reconstruction was mostly observed on anatase (001) surfaces [21,191,199,214,223,228-230] because it has a relatively lower surface energy (0.51 J/m^2) compared to those of (1 × 5) (γ = 0.53 J/m^2) and (1 × 3) (γ = 0.58 J/m^2) reconstructions [230]. Anatase (1 × 3) is less stable compared to (1 × 4) and (1 × 5) and is difficult to observe in large areas. This is also confirmed by our STM observation (Fig. 4.1a) where small areas of (1 × 3) reconstruction

were observed on anatase islands while most of them exhibited the (1 × 4) reconstruction. However, an exception of long-range anatase (1 × 3) was observed (Fig. 4.8a) and it is stable on $SrTiO_3$(001) when both sides of the anatase ridges are decorated by single-dot rows. This suggests a possible way to stabilise the metastable (1 × 3) reconstruction by forming this complex nanostructure.

Misfit dislocation appears not happen in this complex anatase (1 × 3) nanostructure as it still has the same periodicity as $SrTiO_3$(001) across the ridges. This may due to the strong effect of edge energy on these narrow structures even through their length is beyond the critical value (d = 11.3 nm) of formation of misfit dislocation. The anisotropic growth of anatase (1 × 3) nanostructures may be caused by the anisotropic strain built in the anatase from the $SrTiO_3$(001)substrate, where this structure is strained across the ridges and possibly relaxed along the ridges. Further investigation such as DFT calculation is required to obtain a full understanding of this system.

4.5 Conclusion

Nanostructured $SrTiO_3$(001) with TiO_x terminated surfaces can be used as the substrate for anatase nucleation. High-quality and flat anatase films with the high-energy (001) surface exposed can be produced via heterogeneous epitaxial growth due to the small lattice mismatch between anatase (001) and $SrTiO_3$(001). The anatase islands epitaxially grown on $SrTiO_3$(001) are strained and adopted the $SrTiO_3$(001) lattice constant (a_{SrTiO_3}= 3.91 Å). The anatase films are relaxed on $SrTiO_3$(001) surface and presents its original unit cell size (a_{TiO_2}= 3.78 Å). Anatase islands grown on $SrTiO_3$(001) have two orientations along the

[010] and [100] directions. Each single island is composed of a mixture of (1 × 3) and (1 × 4) reconstructions.

Complex anatase (1 × 3) nanostructures were formed when sufficient Ti and O segregated to the surface. These complex nanostructures all present the same width of 6.78±0.05 nm, which suggests a stable configuration of long-range anatase (1 × 3) reconstructions. The anisotropic growth of anatase and the formation of elongated shapes across the ridges may be caused by the anisotropic stresses applied to (1 × 3) nanostructures.

Further deposition of Ti on anatase islands facilitates the island growth. Oxygen dosing (by exposing the sample to the atmosphere in our case) produces well distributed flat anatase films on the $SrTiO_3$(001) substrate. The anatase structure is comprised of parallel ridges along the <100> crystallographic directions and faint rows between the ridges. The anatase exhibits two types of domains with (1 × 4) and (4 × 1) reconstructions. Screw dislocations are often found on anatase surfaces indicating the spiral growth mechanism. This anatase phase is stable up to 950°C with the (1 × 4) reconstruction. These surfaces are ideally suited to the study of epitaxially-grown metal nanoparticles (e.g., Pd).

Furthermore, considering the high density of defects on anatase TiO_2(001) surfaces, it will be useful to chemically modify the surface to further improve the adsorption capacity, selectivity and surface reactivity of anatase for catalytic applications.

Chapter 5

Growth of Pd on Ordered Diline-(6 × 2) Substrates

5.1 Introduction

Atomic resolution scanning tunnelling microscopy (STM) of the $SrTiO_3$(001) surface revealed that certain surface treatments gave rise to the formation of a variety of nanolines [11-13,85,86]. These self-assembled nanolines are highly-ordered structures aligned in <100> crystallographic directions, which remain stable at room temperature. If the nanolines are found to be electrically conducting, they are likely to be used as nanowires. If they are insulating, the patterned surfaces can be used as templates for the growth of self-assembled molecular, semiconducting or metallic structures. Auger spectroscopy showed that the nanolines are TiO_x-rich [12]. Oxide-supported metal nanocrystals have become functionally important in catalysis [17,23-25], gas sensing [243] and optical applications [244]. Pd nanocrystals are widely used as catalysts, whose catalytic activity is sensitive to their shape. Different atomic arrangements of Pd nanocrystals could affect their catalytic properties [27]. The Pd nanocrystals have a face centred cubic structure with a lattice constant of 3.89 Å. The lattice mismatch between Pd and $SrTiO_3$(001) is only 0.5%. Therefore, it is possible to control the shapes and sizes of Pd nanocrystals by epitaxially growing them on nanostructured $SrTiO_3$(001) substrates.

In this chapter, we report STM studies of Pd nanocrystals grown on a diline-terminated $SrTiO_3(001)$ support at different temperatures. The sizes of Pd nanocrystals grown at different temperatures were measured and compared. The adhesion energy of Pd nanocrystal was calculated to characterise the bonding properties between Pd and dilines.

5.2 Experimental methods

Dilines were grown on 0.5 wt% Nb doped $SrTiO_3(001)$ substrates. The diline samples were prepared by Ar^+ ion sputtering for 10 minutes at a beam energy of 1.0 keV and an ion current of 4.5 μA. The sputtered samples were further annealed in UHV at 860°C for 1.5 hours to form diline structures. Pd was deposited on the diline-terminated samples at three different temperatures: 450°C, 600°C and 650°C using an e-beam evaporator. After each experiment, Pd was evaporated from the diline substrate to get the clean surface ready for the next deposition. The details of the Pd deposition and annealing conditions are summarised in Tab. 5.1. All annealing was carried out in the UHV (base pressure 10^{-8} Pa).

Tab. 5.1 Summary of Pd deposition and annealing conditions

		Dilines-1	**Dilines-2**	**Dilines-3**
Deposition	Filament current (A)	4.12	4.10	4.11
	Emission (mA)	11.4	11.3	11.9
	Flux (nA)	15.1	26.9	25.5
	Time (s)	150	180	180
	Substrate temperature (°C)	450	600	650
Post annealing	Temperature/ duration	450/15mins	600/1hr	650/1hr
	Environment	UHV	UHV	UHV

5.3 Results

5.3.1 Diline-terminated $SrTiO_3$(001) surfaces

Dilines were formed on $SrTiO_3$(001) after 1.5 hours of annealing at 860°C. Fig. 5.1a shows the surface structure with dilines aligning along the [010] and [100] crystallographic directions. As shown in Fig. 5.1b, each diline is made up of two parallel rows. Dilines have well-ordered (6 × 2) domains, one of which is highlighted by the rectangular unit cell in Fig. 5.1b as a typical example. Zig-zag (Fig. 5.1c) and square configurations (Fig. 5.1d) were observed in dilines as previously reported in Ref.[11]. Both configurations can co-exist in the same row. A change of structure from the zig-zag (left) to the square configuration (right) is shown in Fig. 5.1c with the defect indicated by the red arrow. This well-structured and flat dilines surface is suitable for Pd nanocrystal growth.

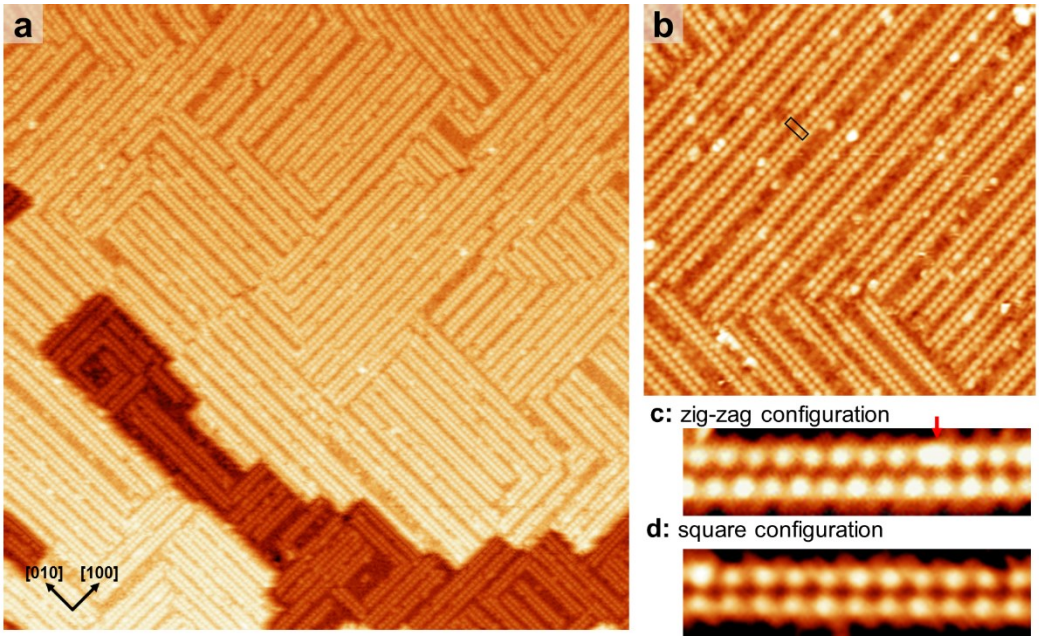


Fig. 5.1 (a) STM image of diline-structured sample surface (image size: 100 × 100 nm^2, imaging conditions: V_s = +1.865 V, I_t = 0.24 nA). (b) Surface with (6 × 2) dilines (image size: 40 × 40 nm^2, imaging conditions: V_s = +1.823 V, I_t = 0.184 nA). (c) Zoom-in STM image of the diline with zig-zag configuration (image size: 10 × 2.5 nm^2). A defect is pointed by the red arrow. (d) Zoom-in STM image of the diline with square configuration (image size: 10 × 2.5 nm^2).

5.3.2 Growth of Pd nanocrystals on dilines substrates

Fig. 5.2 shows the STM image of Pd nanocrystals grown on the dilines at different temperatures. The Pd nanocrystals grew into the hexagonal disk shape on dilines. When the sample was annealed at 450°C, the Pd nanocrystals observed have a wide range of sizes (Fig. 5.2a). The majority of the hexagonal Pd nanocrystals are elongated along the orientations of the dilines in the [010] and [100] directions as indicated by the arrows in Fig. 5.2a. The height of a typical Pd nanocrystal (e.g., "crystal i") was measured to be 0.99 nm (Fig. 5.2d). The similar brightness of most crystals in Fig. 5.2a to "crystal i" indicates similar heights. The Pd nucleation site density was found to decrease after increasing the deposition temperature to 600°C and 650°C (Fig. 5.2b and c). When the Pd nanocrystals were annealed at 600°C, fewer small-sized nanocrystals (width less than 5 nm) were found (Fig. 5.2b). These small crystals still had an elongated shape as indicated by the arrows in Fig. 5.2b. Two different levels of brightness of Pd nanocrystals were observed: one represented by "crystal i" and the other by "crystal ii" as labelled in Fig. 5.2b. From the height comparison shown in Fig. 5.2e, a significant height difference is observed between "crystal i" (3.39 nm high) and "crystal ii" (1.22 nm high). More Pd nanocrystals grew into the regular hexagonal shape upon higher-temperature annealing (650°C) (Fig. 5.2c). Most Pd nanocrystals grown on dilines have similar sizes. They still show two different levels of brightness as labelled by "i" and "ii" in Fig. 5.2c. The heights are 2.98 nm for "crystal i" and 2.02 nm for "crystal ii", as measured from profiles in Fig. 5.2f. Bright dots (i.e., moiré dots) were observed on the Pd nanocrystals surfaces after anneals at 600°C and 650°C (highlighted in Fig. 5.2b and c). This indicates the formation of superstructures due to encapsulation of Pd nanocrystals, the details of which will be discussed in Ch. 7.3.1.

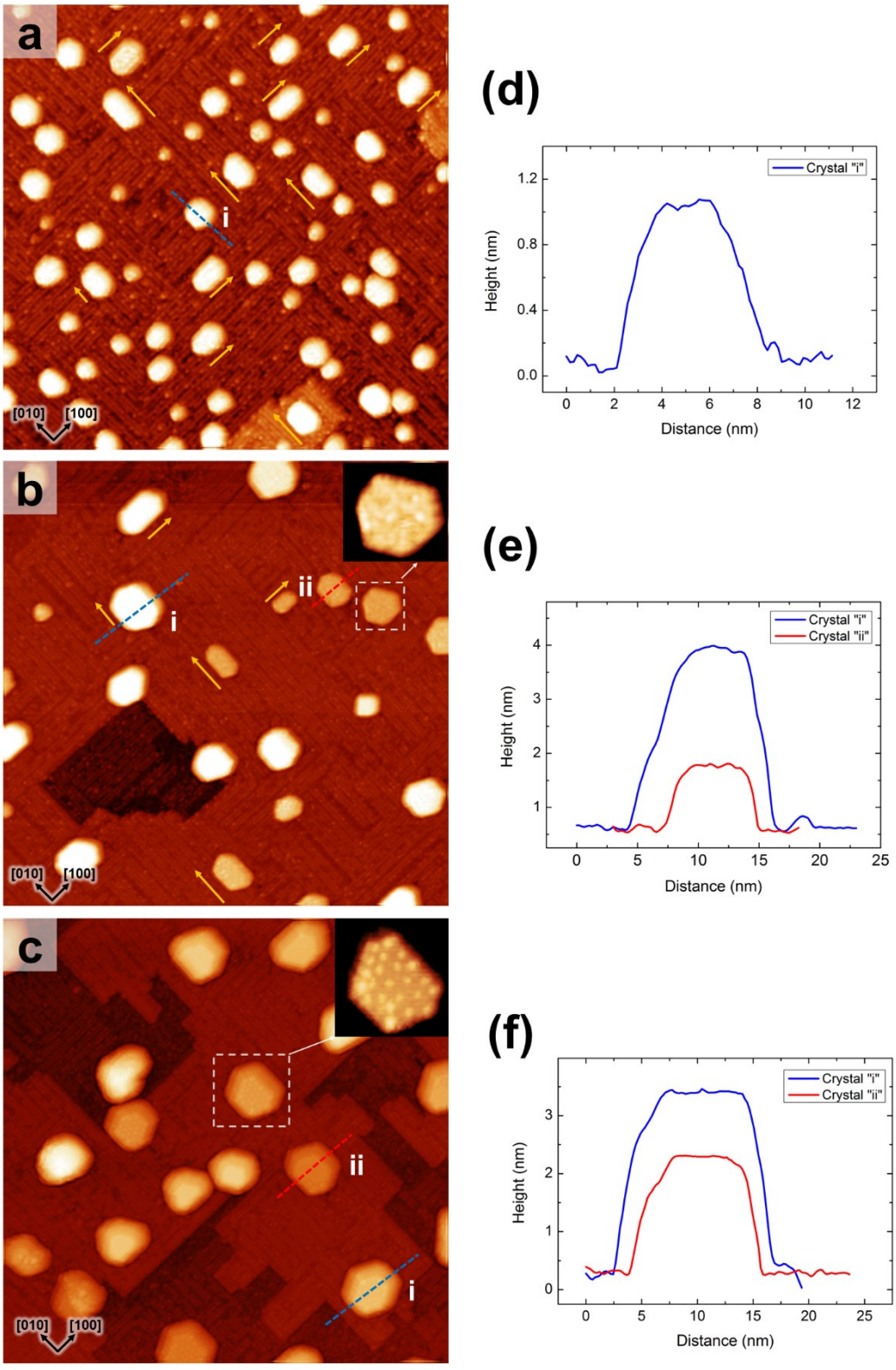


Fig. 5.2 STM images of Pd nanocrystals grown on diline surfaces at (a) 450°C for 15 mins (image size: 100 × 100 nm^2, imaging conditions: V_s = +1.73 V, I_t = 0.3 nA), (b) 600°C for 1 hour (image size: 120 × 120 nm^2, imaging conditions: V_s = +1.727 V, I_t = 0.155 nA), and (c) 650°C for 1 hour (image size: 120 × 120 nm^2, imaging conditions: V_s = +2 V, I_t = 0.3 nA). Line profiles are measured along dash lines across the crystals from (d) crystal i in Fig. 5.2a, (e) crystals i and ii in Fig. 5.2b and (f) crystals i and ii in Fig. 5.2c.

5.3.3 Size distributions of Pd nanocrystals

1) Height distribution

The size of Pd nanocrystals increased with the annealing temperature. 268 Pd crystals were measured from the 450°C treatment, 86 crystals from the 600°C treatment and 123 crystals from the 650°C treatment. The histograms of the height distributions of the Pd nanocrystals are shown in Fig. 5.3. The heights of most Pd crystals grown at 450°C are either 9.31±0.58 Å or 10.91±0.58 Å, which are respectively equal to 4 and 5 times the Pd(111) interplanar spacing (2.25 Å), i.e., 4 layers (4L) and 5 layers (5L) of the Pd(111) plane (Fig. 5.3a). The average Pd crystal height was increased after the sample was annealed at 600°C. Two distinct peaks were observed in the height distribution histograms (Fig. 5.3b). The majority of Pd crystals are 13.21 ± 0.67 Å (6L) and 27.02 ± 0.45 Å (12L) which correspond to 6 and 12 times the Pd(111) interplanar spacing. The bimodal distribution of crystal heights is possibly attributed to the encapsulation of Pd nanocrystals upon high temperature treatment. Encapsulation occurs to reduce the surface energy of Pd nanocrystals. The encapsulated Pd nanocrystals with relative low surface energies tend to grow flatter compared to bare Pd nanocrystals. Therefore, the first peak (13.2±0.67 Å (6L)) and the second peak (27.02±0.45 Å (12L)) could be those of encapsulated and bare Pd nanocrystals, respectively. The Pd nanocrystals grew even higher after being annealed at 650°C. 73% of the Pd crystals are comprised of 11 to 17 layers of Pd, whose crystal heights are in the range of 24.962±0.56 Å (11L) to 38.28±0.78 Å (17L). However, 4% of the Pd nanocrystals are 49.30±0.59 Å (22L) high, which is the origin of the small peak of the crystal heights above 19 layers in Fig. 5.3c. Because the heights of Pd nanocrystals are integral multiples of the Pd(111) interplanar spacing (2.25 Å), this indicates that the top facet of Pd nanocrystals is the (111) plane. Therefore, the shape of Pd nanocrystal is

characteristic of a (111) top facet, with three (111) side facets and three (001) side facets. The interface with the substrate is also a (111) plane and the interfacial crystallography is described as $(111)_{Pd} \parallel (001)_{SrTiO_3}$ $[110]_{Pd} \parallel [110]_{SrTiO_3}$.

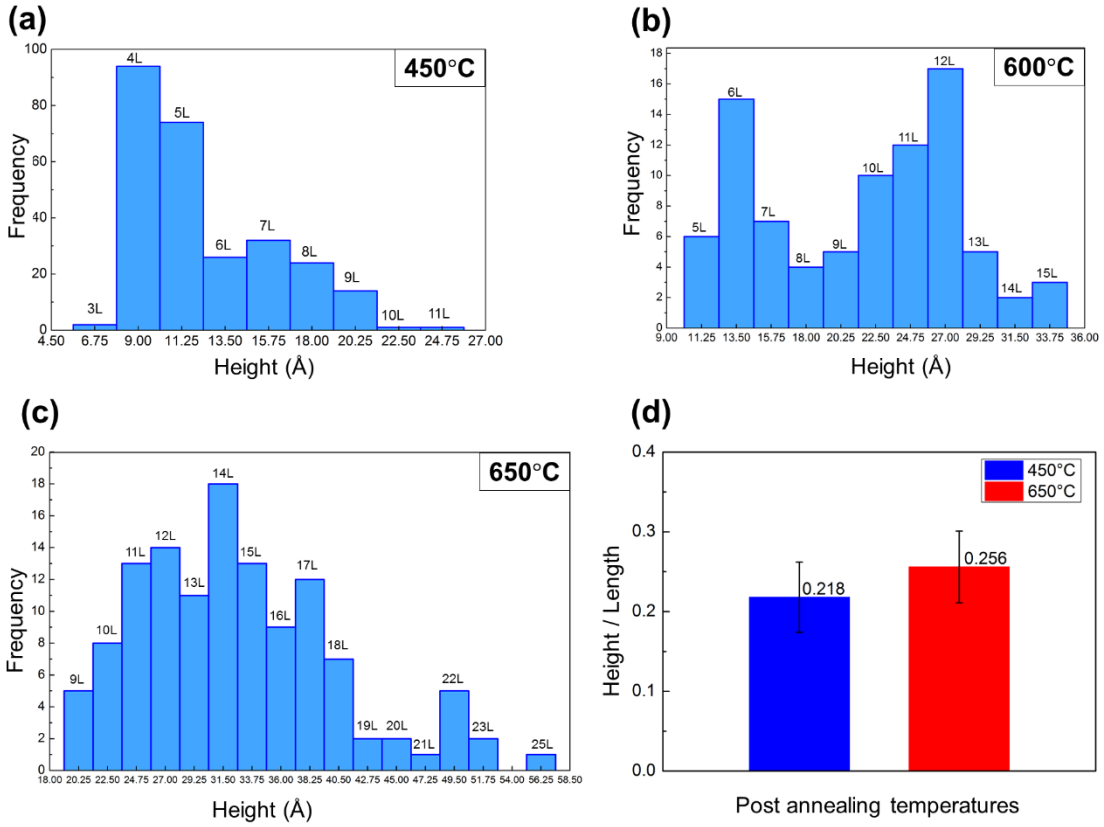


Fig. 5.3 Histograms showing the distribution of Pd nanocrystal heights. The number of Pd(111) layers is labelled on top of each bar. Post-annealing treatment temperatures were (a) 450°C for 15 mins, (b) 600°C for 1 hour and (c) 650°C for 1 hour. Panel (d) compares the average height-to-length ratios of hexagonal Pd nanocrystals annealed at 450°C and 650°C.

The height-to-length ratios of the hexagonally-shaped Pd nanocrystals annealed at 450°C and 650°C were measured, and the averages are shown in Fig. 5.3d. The length was measured on the base facet from the middle of the (001) side to the opposite (111) side. 57 Pd nanocrystals were measured from the 450°C treatment, giving an average ratio of h/l = 0.218±0.044; 52 Pd nanocrystals were measured from the 650°C treatment, resulting in an average ratio of h/l = 0.256±0.045. The errors denote the standard deviations of the

measurements. The difference between the ratios suggests that the Pd nanocrystals favoured growth in width at low temperatures and growth in height at high temperatures.

2) Equilibrium h/w ratio of symmetrical Pd nanocrystals

In order to obtain the equilibrium *h/w* ratio of bare Pd nanocrystals, we chose the Pd nanocrystals which were annealed at 450°C for 15 minutes and free of encapsulation. 29 Pd nanocrystals in the symmetrical truncated triangular shapes were chosen. One of typical example is shown in Fig. 5.4a.

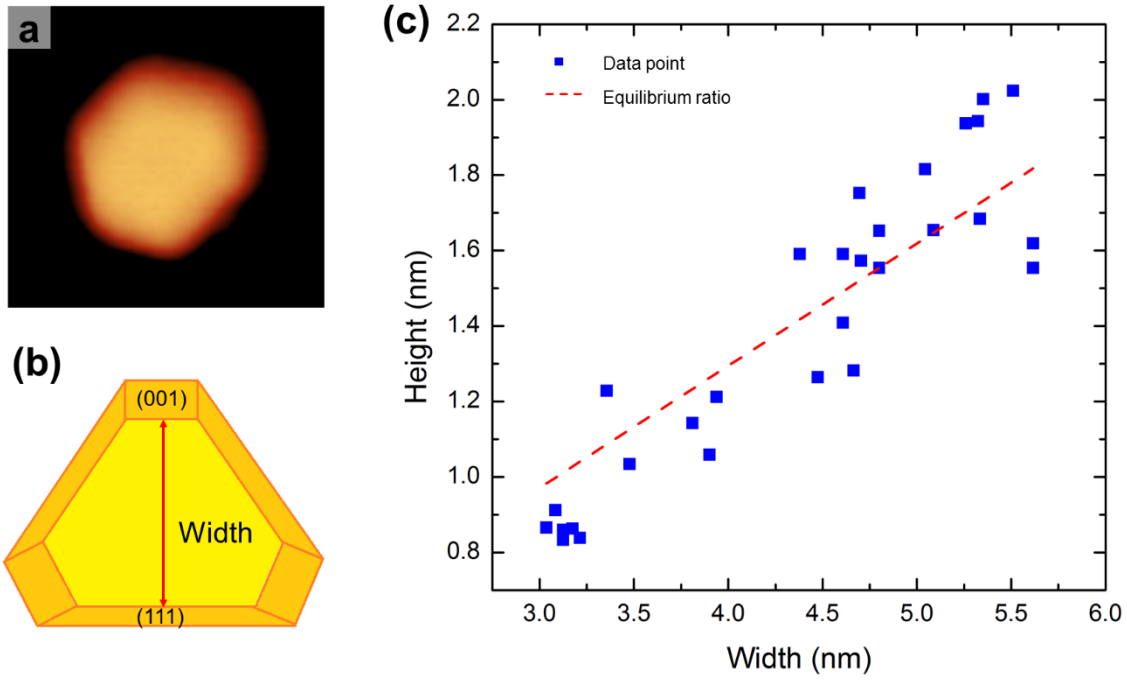


Fig. 5.4 (a) STM image of a typical Pd nanocrystal with a truncated triangular shape formed at 450°C after 15 minutes annealing (image size: 12.3 × 12.4 nm^2, imaging conditions: V_s = +2 V, I_t = 0.3 nA). (b) Top view of a truncated triangular Pd nanocrystal. Its width was measured on the top facet from the middle of the (001) side to the middle of the opposite (111) side. (c) Plot of the heights and widths of 29 selected bare Pd nanocrystals with a truncated triangular shape. Pd nanocrystals with width less than 3nm are not seen because they are unstable. The gradient of the dashed line corresponds to the equilibrium ratio h/w = 0.32 ± 0.04, where the error denotes the standard deviation. The fitting line was obtained by fixing the intercept at 0.

The height and width of these 29 bare Pd nanocrystals were measured. To get a more accurate measurement, the width was measured on the top facet from the middle of the (001) side to the opposite (111) side (Fig. 5.4b). Fig. 5.4c shows the linear relationship between height and width, indicating the formation of equilibrium-shaped Pd nanocrystals. The equilibrium ratio is indicated by the gradient of the red dashed line (Fig. 5.4c), where $h/w = 0.32 \pm 0.04$, the error denotes the standard deviation.

3) SD to LD ratio of elongated Pd nanocrystals

Most Pd nanocrystals annealed at 450°C show elongated shapes along the orientation of the dilines. Two typical elongation orientations of Pd nanocrystals, [100] and [010], are shown in Fig. 5.5a and b. The heights of the majority of the elongated nanocrystals are 9.32 ± 0.57 Å (4L) and 10.90 ± 0.58 Å (5L) as shown by the height distribution histogram in Fig. 5.5c. The proportion of elongated nanocrystals was reduced as the crystals grew taller. The sizes of the elongated crystals were measured along the long distance (LD) and the short distance (SD) as illustrated in Fig. 5.5d. The measured SD was plotted against LD in Fig. 5.5e, showing a linear trend with a SD/LD ratio of 0.72 ± 0.09. The error denotes the standard deviation.

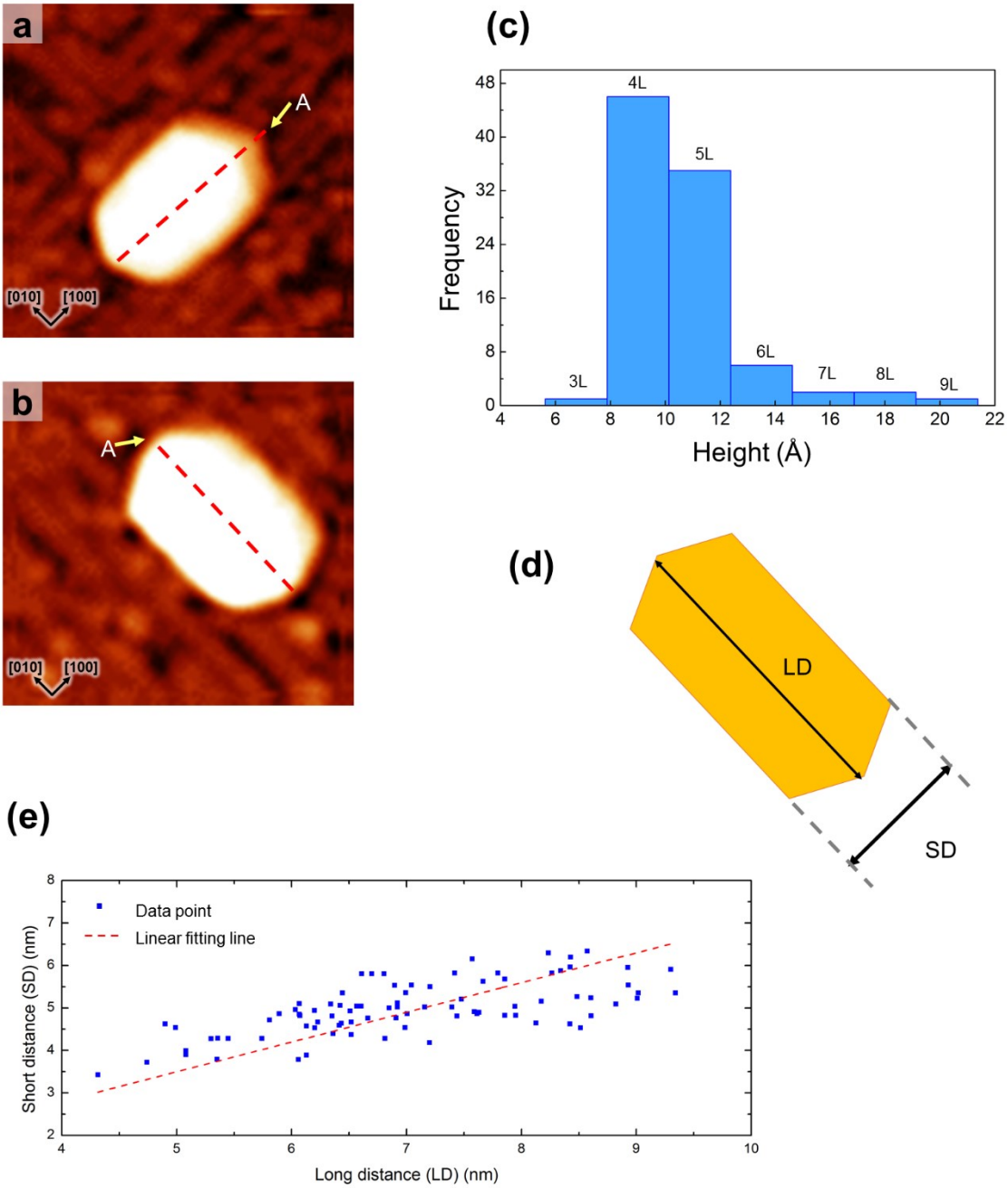


Fig. 5.5 Typical elongated Pd nanocrystals growing in the (a) [100] crystallographic direction (image size: 16 × 15 nm^2, imaging conditions: V_s = +1.73 V, I_t = 0.3 nA) and (b) [010] crystallographic direction (image size: 12 × 11 nm^2, imaging conditions: V_s = +1.73 V, I_t = 0.3 nA). The sample was annealed at 450°C for 15 minutes. (c) Height distribution histogram of elongated Pd nanocrystals. The number of layers is marked on top of each bar. (d) Top view of an elongated Pd nanocrystal schematically showing the measurements of the long distance (LD) and the short distance (SD). (e) Plot of SD vs LD with a red linear fitting line. The fitting line was obtained by fixing the intercept at 0. The gradient of fitting line gives the SD/LD ratio of 0.72±0.09. The error denotes the standard deviation.

5.4 Discussion

Ar^+ ion sputtering produces non-stoichiometric surfaces which causes surface reconstructions on $SrTiO_3$(001) substrates. A higher sputtering energy (1.0 keV) was used to produce more defective surfaces which were suitable for drastic surface reconstructions. The drastic surface reconstructions facilitate the formation of nanostructures, i.e., dilines in our study. Plenty of defects were found on the diline surface (Fig. 5.1a). These defects provided the nucleation sites for Pd nanocrystals. The Pd deposition was carried out on warm substrates to encourage nucleation, and post-deposition anneals at three different higher temperatures encouraged Pd growth.

5.4.1 Growth of elongated Pd nanocrystals

At the lowest nucleation and growth temperature (450°C), most Pd nanocrystals grew into elongated shapes along the orientation of the substrate dilines, i.e., the [010] and [100] crystallographic directions. The elongated crystals have good epitaxy with the substrate with their two long sides parallel to the dilines. The composition of dilines has been studied by Marshall, *et al*. [85] using DFT modelling. Their model is used in this discussion section to study the substrate effect on the Pd nanocrystal shape (Fig. 5.6). In general, the formation of dilines requires the reconstruction of the top three layers of bulk $SrTiO_3$ as shown in the side-view model (Fig. 5.6f). The composition of the first layer of dilines is shown in Fig. 5.6b. Each dot observed in the STM image (Fig. 5.6a) is comprised of 4 Ti and 7.5 O atoms. The second layer has TiO_2 stoichiometry (Fig. 5.6c) sitting on the bulk TiO_2 surface, which is the third layer shown in Fig. 5.6d. The fourth layer is the bulk SrO plane (Fig. 5.6 e).

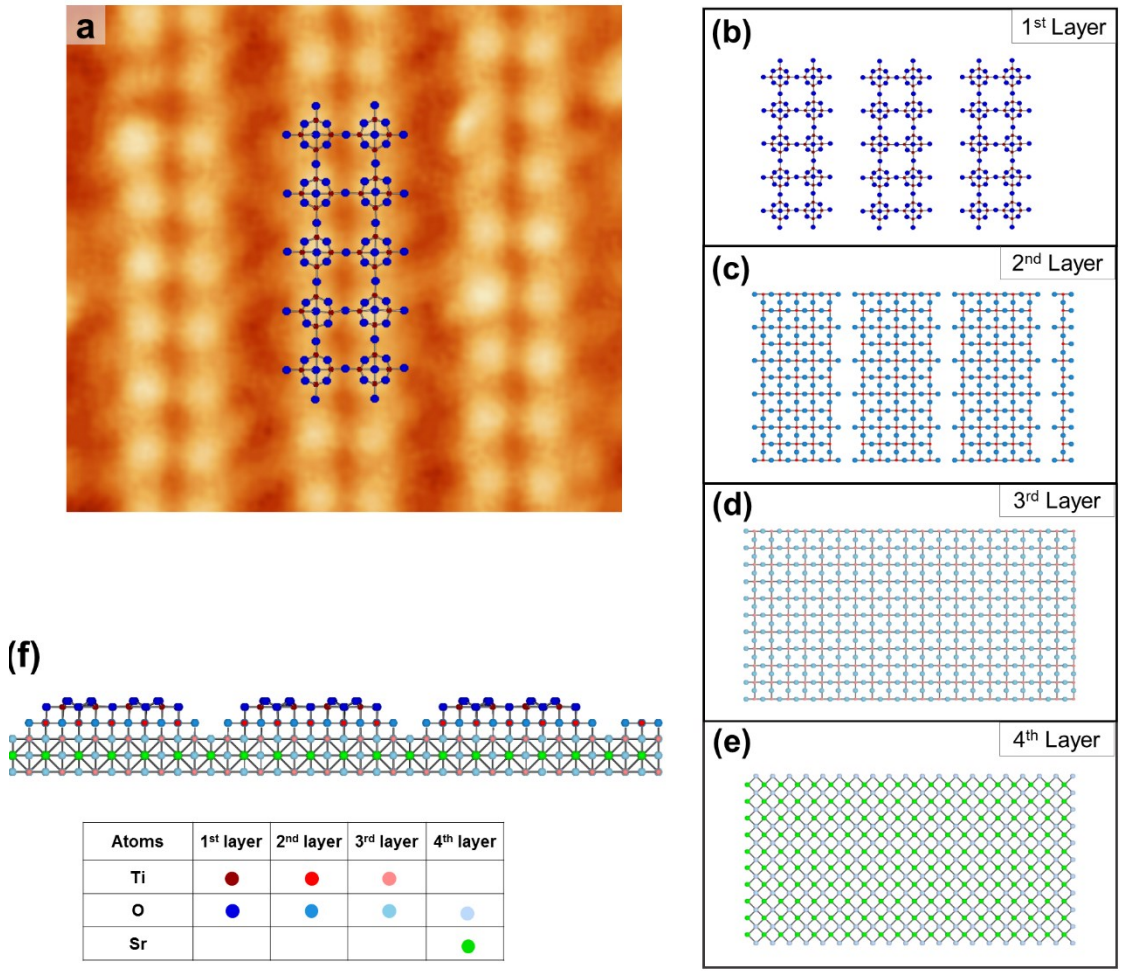


Fig. 5.6 (a) STM image showing the diline structures with the ball-and-stick model overlying part of the image. (b)-(e) Ball-and-stick models of the top four layers of the diline structures as top views. The top two layers sit above the bulk TiO_2 surface (adapted from Ref. [85]). The Ti atoms are in red; O atoms are in blue; Sr atoms are green. The colour brightness of atoms in the different layers is summarised in the table below Fig. 5.6f.

The growth mechanism of the elongated Pd nanocrystals on dilines is illustrated in Fig. 5.7. Taking dilines with a [100] orientation as an example, the trench-like channels are observed between dilines in the [100] direction as indicated by the back arrows in the side-view image in Fig. 5.7a. After Pd atoms are adsorbed on the diline surface (Fig. 5.7b), they become mobile at elevated temperatures. Surface diffusion of Pd adatoms occurs during sample annealing, which involves hopping and jumping of Pd atoms to neighbouring adsorption sites. Because the substrate has ordered linear structures, the surface diffusion of Pd on

dilines could be affected by the substrate structures in the [100] (along the rows) and [010] (across the rows) directions. The possible adsorption sites of Pd on different layers of dilines are marked by the numbers in Fig. 5.7b. The activation energy for in-channel diffusion is normally smaller than cross-channel diffusion due to the higher energy barrier to jump over the side channel walls [349]. This means that the diffusion of Pd along the channel (along [100]) requires less energy than across the dilines (along [010]). When Pd adsorbs in the channel between two dilines (marked by "0"), it prefers to diffuse along the channel (along [100]) such as diffusing to the next adsorption site "1" in the same channel. If a Pd atom is adsorbed on top of the diline (position 3 or 4), the fast diffusion direction is still along the dilines (along [100]). If we assume that the dilines, which are comprised of two TiO_x layers, are the small atomic steps above the substrate, those Pd atoms located on top of the first layer are required to overcome the additional Ehrlich–Schwoebel barrier in order to diffuse and descend to the lower substrate (path from "4" to "5"). This energy barrier is higher than the energy required to diffuse on the flat surface. The fast diffusion path along the dilines inside the channels of the dilines is also confirmed by our STM results. As labelled by dash lines A in Fig. 5.5a and b, the longest diffusion distance in the elongated Pd nanocrystals is located in the channel between two dilines. Therefore, the anisotropic in-channel and cross-channel diffusions of Pd limit the growth of Pd nanocrystals across the dilines and consequently lead to the elongated crystal shapes (Fig. 5.7c). The simplified model of elongated Pd nanocrystals preferentially grown along the dilines is shown in Fig. 5.7d.

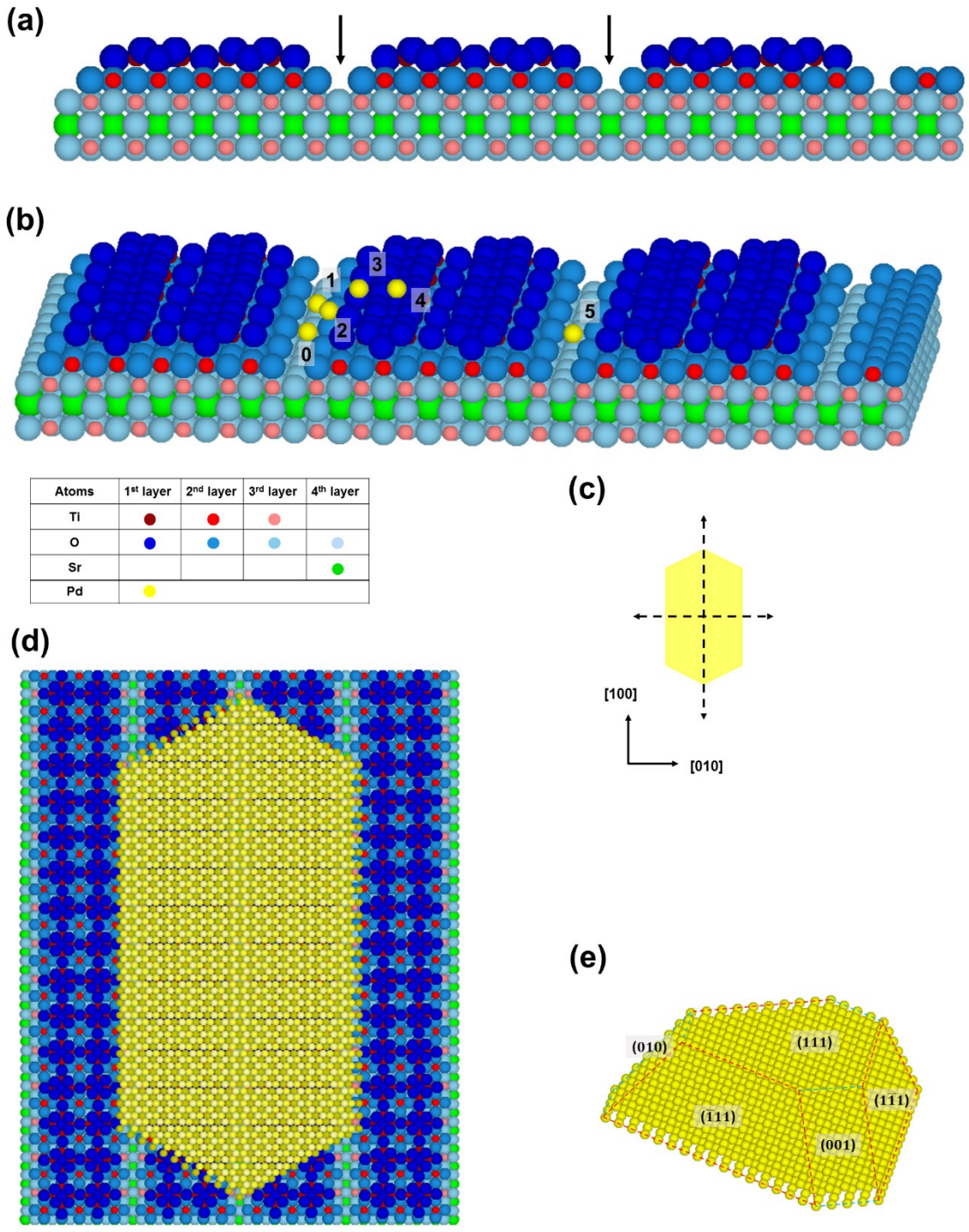


Fig. 5.7 (a) Hard-ball model of dilines grown on a $SrTiO_3$(001) substrate (side view). (b) Pd adsorption sites on different layers in dilines. (c) Schematic top view of the growth directions of an elongated Pd nanocrystal. (d) Simplified model of an elongated Pd nanocrystal grown on dilines (top view). (e) 3D model of a hexagonal Pd nanocrystal. The colours for different atoms in different layer are summarised in the table below Fig. 5.7b.

For the same Pd-diline system, surface diffusivity of Pd is strongly dependent on temperature too. Within limited time, the diffusion distance of Pd is determined by the surface diffusivity at that specific temperature. The anneals at a relatively low temperature (450°C) limit the diffusion distance of Pd atoms where most Pd nanocrystals are small and 4-5 layers in height. Because these crystals are small, the diline substrate plays a more important part in the epitaxial growth of Pd, where Pd nanocrystals grow with two sides parallel to the dilines. Increasing the contact area between Pd crystals and the dilines could significantly minimise the total surface energy of the Pd-diline system.

As the annealing temperature increases, the diffusivity of Pd on dilines increases. As Pd atoms become more mobile on the diline surface, their diffusion distance become longer within a certain time period. These Pd atoms far apart from each other could then diffuse together and form larger nanocrystals. When Pd layers become thicker, the channels between dilines become filled up by Pd atoms. The diffusion barrier from the diline channel walls become less dominant as the relative height difference between Pd nanocrystals and dilines is reduced. Also, Ostwald ripening occurs at higher annealing temperatures when the growth of larger nanocrystals occurs at the expense of smaller nanocrystals. This is the reason why we saw smaller Pd nanocrystals vanishing and larger nanocrystals growing even larger (Fig. 5.2b). Once most Pd atoms have sufficient energy to freely diffuse on the diline surface, Pd nanocrystals start to grow towards the regular hexagonal shape. The diffusion phenomenon of crystal growth in height becomes more dominant by the self-diffusion of Pd atoms on Pd(111) and (001) surfaces. The side facets of hexagonally-shaped Pd nanocrystals are (111) and (001) planes, whose surface energies were calculated by DFT to be $\gamma_{111} = 1.64$ J/m^2 and $\gamma_{001} = 1.86$ J/m^2 respectively [350]. Because the Pd(001) plane has a higher surface energy than the (111) plane, Pd(111) usually grows larger than the (001) surface in order to minimise the total surface energy of the Pd nanocrystal. This explains

why the hexagonal shapes initially presented larger areas of the (111) facet and smaller areas of the (001) facet (Fig. 5.2b and c). The model of the hexagonal Pd nanocrystal in this intermediate stage is shown in Fig. 5.7e.

5.4.2 Adhesion energy of Pd nanocrystals on dilines

From the experimental results, we know that hexagonal Pd nanocrystals have one (111) top facet, three (111) side facets, three (001) side facets and a (111) interface with dilines. The work of adhesion (W_{adh}) (i.e., adhesion energy) characterises the bonding properties between the nanocrystals and the support [44]. The adhesion energy of Pd on dilines is defined by the amount of work required (energy per unit area) to separate the Pd nanocrystal from the dilines. It is assumed that there are no plastic or diffusional modifications [44].

After the Pd nanocrystal is placed on dilines, an interface with the area A_i is created between them (marked in red in Fig. 5.8a). The total energy of system 1 is:

$$E_1 = \gamma_{Pd(111)}A_{111} + \gamma_{Pd(001)}A_{001} + \gamma_i A_i + \gamma_{s(001)}A_{s1} \quad (5.1)$$

where $\gamma_{Pd(111)}$ and $\gamma_{Pd(001)}$ = surface energies of the Pd(111) and (001) planes;

A_{111} = the total area of one Pd(111) top facet and three (111) side facets;

A_{001} = the total area of three Pd{001} side facets;

$\gamma_{s(001)}$ = the surface energy of dilines;

A_{s1} = the surface area of the dilines, excluding the area of Pd-diline interface.

When separating Pd from dilines, we assume that the shape of Pd nanocrystal does not change. The base (111) surface with an area of A_b is created on the Pd nanocrystal. As described in Fig. 5.8b, the total energy in system 2 when the Pd and dilines are apart is:

$$E_2 = \gamma_{Pd(111)}A_{111} + \gamma_{Pd(111)}A_b + \gamma_{Pd(001)}A_{001} + \gamma_{s(001)}A_{s2} \quad (5.2)$$

The energy change between systems 1 and 2, derived from Eq. 5.1 and Eq. 5.2, is

$$E = E_2 - E_1 = \gamma_{Pd(111)} A_b - \gamma_i A_i + \gamma_{s(001)} (A_{s2} - A_{s1}) \quad (5.3)$$

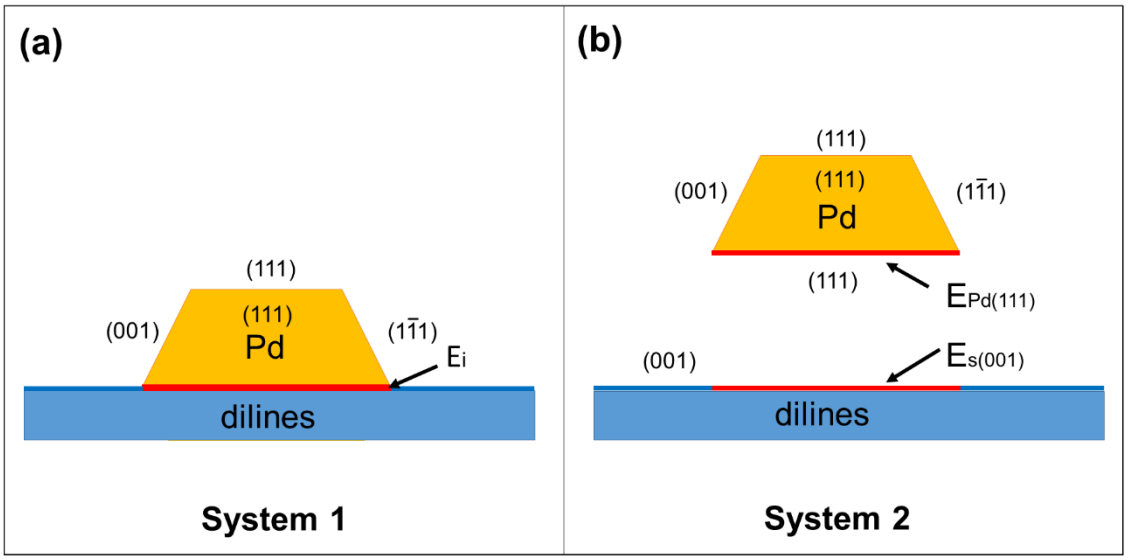


Fig. 5.8 Model of the free energy of adhesion shown by the process of separating Pd from dilines (side view). (a) Before separation, the interface area between Pd and dilines is marked in red. (b) After separation, the areas of the same size are created on the Pd(111) base facet and diline surface, marked in red.

Because the crystal shape remains the same, the base area (A_b) (marked in red in Fig. 5.8b) of the Pd nanocrystal is equal to the interface area A_i (marked in red in Fig. 5.8a). The change in the exposure area of dilines is $A_{s2} - A_{s1} = A_i$.

Equation. 5.3 can be rewritten as:

$$E = E_2 - E_1 = \gamma_{Pd(111)} A_i - \gamma_i A_i + \gamma_{s(001)} A_i \quad (5.4)$$

The energy change per unit area, i.e., adhesion energy (W_{adh}) can be obtained by dividing Eq. 5.4 by A_i on both sides:

$$W_{adh} = \gamma_{Pd(111)} - \gamma_i + \gamma_{s(001)} \quad (5.5)$$

As described in the formation mechanism of nanocrystals in Ch. 3.6.1, the general surface energy γ^*defined by Winterbottom [231] can be rewritten as $\gamma^* = \gamma_i - \gamma_{s(001)}$ (Eq. 5.6). Substitution into Eq. 5.5 gives

$$W_{adh} = \gamma_{Pd(111)} - \gamma^* \tag{5.7}$$

According to Silly *et al*. [55], γ^* for the equilibrium hexagonal shape of Pd nanocrystals can be written as a function of $\gamma_{Pd(001)}$, $\gamma_{Pd(111)}$ and the height (h)-to-width (w) ratio:

$$\gamma^*_{Hexa} = \sqrt{\frac{3}{2}}\frac{h}{w}\gamma_{Pd(001)} - \gamma_{Pd(111)} \tag{5.8}$$

Substituting our experimentally determined value $\frac{h}{w}$ = 0.32±0.04 (Fig. 5.4c) and using the DFT-calculated value of Pd surface energy by Methfessel *et al.* [350], where $\gamma_{Pd(001)}$ = 1.86 J/m^2 and $\gamma_{Pd(111)}$ = 1.64 J/m^2, we obtain

$$\gamma^*_{Hexa} = \text{-}0.91\pm0.09 \text{ J/m}^2$$

Substituting the value of γ^*_{Hexa} into Eq. 5.7 gives us

$$W_{adh} = 2.55\pm0.09 \text{ J/m}^2$$

Silly *et al*. [55] calculated γ^*_{Hexa} for Pd nanocrystals formed on $c(4 \times 2)$-$SrTiO_3(001)$ substrate to be γ^*_{Hexa} = -0.73±0.12 J/m^2. Equation 5.7 gives an adhesion energy of Pd grown on $c(4 \times 2)$-$SrTiO_3(001)$ of W_{adh} = 2.37±0.12 J/m^2. Comparing our results with Silly *et al*.'s, we can conclude that more energy is required to separate Pd nanocrystals from dilines (6×2)-$SrTiO_3(001)$ (W_{adh} = 2.55±0.09 J/m^2) than from $c(4 \times 2)$-$SrTiO_3(001)$ (W_{adh} = 2.37±0.12 J/m^2). This indicates a stronger adhesion of Pd on dilines than on $c(4 \times 2)$-$SrTiO_3(001)$ substrates.

5.5 Conclusion

We prepared diline-terminated $SrTiO_3$(001) surfaces with close-packed rows aligning in [010] and [100] crystallographic directions. This patterned surface can be used as a suitable substrate for the epitaxial growth of Pd nanocrystals. The height distributions of the Pd nanocrystals grown at three different temperatures (450°C, 600°C and 650°C) were measured. Most Pd annealed at 450°C were measured to be 9.31±0.58 Å and 10.91±0.58 Å high, which are equal to 4 (4L) and 5 layers (5L) of Pd(111). Pd annealed at 600°C had two distinct heights 13.21±0.67 Å (6L) and 27.02±0.45 Å (12L). The heights of most Pd nanocrystals grown at higher temperature 650°C are in the range of 24.962±0.56 Å (11L) to 38.28±0.78 Å (17L). Pd nanocrystals prefer to grow in width, rather than in height at low temperatures and the other way round at higher annealing temperatures. The annealing temperatures influence the growth shapes of hexagonal Pd nanocrystals. Dilines have a strong effect on constraining the growth shape of Pd at low temperatures, when elongated nanocrystals are formed along the dilines. As the temperature increases, elongated Pd nanocrystals start to grow across the dilines towards, forming the hexagonal shape under equilibrium conditions. This demonstrates the importance of the selection of suitably patterned substrates and the annealing temperature on the size and morphology of nanocrystals. The adhesion energy of Pd-dilines is calculated to be 2.55±0.09 J/m^2.

Chapter 6

Growth of Pd on Anatase Substrates

6.1 Introduction

Metal nanoparticles grown on well-ordered metal oxide surfaces are widely used in heterogeneous catalysis. One popular system uses TiO_2 as the support to grow transition metal nanocrystals or clusters such as Au, Pt and Pd. Most research was carried out on the well-studied rutile TiO_2, especially on its (110) surface [191,262-264]. The anatase surface is found to be more catalytically active than the rutile surface. Studies related to the metal particles grown on well-ordered anatase TiO_2 surfaces are still scarce. These studies mainly focused on the catalytic property of the metal-anatase system [26,254,267-269]. Studies on the interaction between noble metal nanocrystals (such as Pd and Pt) on oxide supports (especially TiO_2 substrates) have drawn increasing attention in the last thirty years. Pd nanocrystals have become popular as catalysts, whose catalytic activity is sensitive to the nanocrystal shape. Their catalytic properties can be improved by modifying the morphology of the Pd nanocrystals [27]. Therefore, understanding the compositions, morphologies and locations of metal Pd nanocrystals grown on anatase substrates plays a vital role in optimising catalytic performance in the metal-oxide catalyst system.

In this chapter, STM studies of bare and encapsulated Pd nanocrystals grown on anatase substrates are reported. The morphologies and sizes of these Pd nanocrystals grown at different temperatures were studied and compared. The adhesion energy of Pd nanocrystals

was calculated to characterise the bonding between Pd and anatase. The surface energy changes of encapsulated Pd nanocrystals were calculated and compared to those of bare Pd nanocrystals.

6.2 Experimental Methods

Anatase TiO_2(001)-terminated $SrTiO_3$(001) samples were used as the substrate for the growth of Pd nanocrystals. The details of anatase preparation were described in Ch. 4.2. Pd was deposited on anatase (001) surfaces at 300°C and 400°C using an e-beam evaporator. Post-deposition anneals of the samples were carried out at various temperatures and for various durations. After each experiment, Pd was evaporated from the anatase substrate to get the clean surface ready for the next deposition. The details of the Pd deposition and post-deposition anneals are summarised in Tab. 6.1. All anneals were carried out in UHV (base pressure 10^{-8} Pa).

Tab. 6.1 Summary of Pd deposition and annealing conditions

		Anatase-1	**Anatase-2**	**Anatase-3**	**Anatase-4**	**Anatase-5**
Deposition	Filament current (A)	4.11	4.1	4.11	4.11	4.11
	Emission (mA)	13.9	14.1	12.7	13.6	12.6
	Flux (nA)	32.4	56	0.85	1	0.42
	Time (s)	40	20	20	20	20
	Substrate temperature (°C)	300	300	400	300	300
Post annealing	Temperature/ duration (°C/hour(s))	300/0.5hr	300/0.5hr	400/1hr 450/1hr 500/3hrs 550/2hrs	300/30mins 300/2hrs 350/3hrs 550/1hr 550/3hrs	600/1hr
	Environment	UHV	UHV	UHV	UHV	UHV

6.3 Results

6.3.1 Shapes and size distributions of Pd

1) Height distribution

Pd was deposited on the warm anatase substrates (T = 300°C and 400°C) and post annealed for different time durations. Fig. 6.1 shows the surface of sample "Anatase-2" after a post-deposition anneal at 300°C for 30 minutes. Pd nanocrystals in truncated triangular (marked as i), rectangular (marked as ii), and elongated hexagonal (marked as iii) shapes were observed (Fig. 6.1a). The heights of Pd nanocrystals in these three shapes are shown in Fig. 6.1b. Line profiles were measured across these three different Pd nanocrystals along the dash lines in Fig. 6.1a. The height of the truncated triangular Pd nanocrystal (profile in blue line) is 17.96±0.43 Å, corresponding to 8 layers of the Pd(111) plane (2.25 Å). The truncated triangular Pd nanocrystal consists of a (111) top facet, three (111) and three (001) side facets. The interface with the anatase substrate is a Pd(111) plane. There are three Pd nanocrystals in hut shapes with a typical height of 39.27±0.76 Å (profile in red line), which is fourteen times of the Pd(011) interplanar spacing (i.e., 2.75 Å). The base facet being rectangular, suggest that the hut Pd nanocrystal has two (111) side facets, two (001) end facets and an (011) base facet at the interface with the anatase substrate. The height of the elongated hexagonal Pd nanocrystal (profile in green) is 15.51±0.23 Å, which is close to seven layers of the Pd(111) plane. Similar to the truncated triangular shape, the elongated hexagonal Pd nanocrystal has a (111) top facet, three (001) and (111) side facets and a (111) base facet at the interface with anatase.

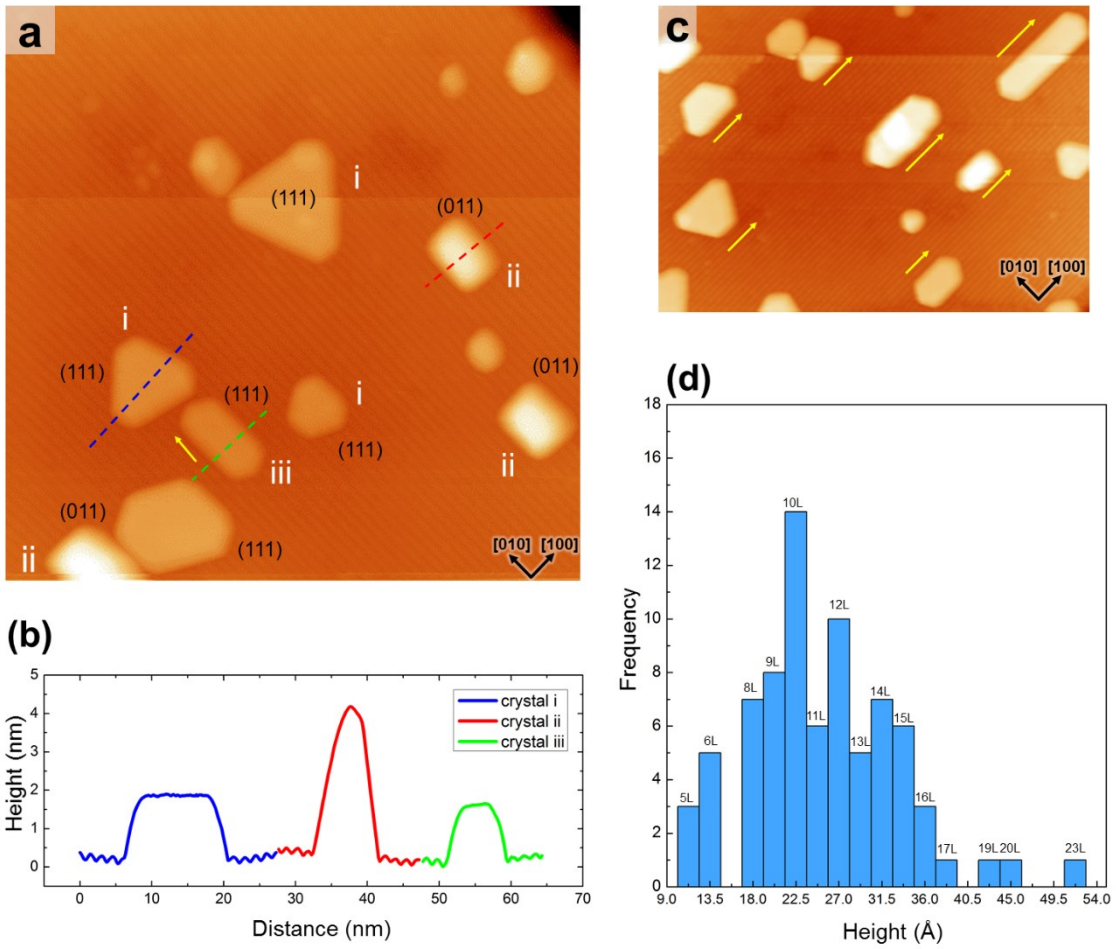


Fig. 6.1 (a) STM image of Pd nanocrystals grown on sample "Anatase-2". The sample was prepared by Pd deposition at 300°C for 20s followed by a post-deposition anneal at the same temperature for 30 minutes (image size: 100 × 100 nm^2, imaging conditions: V_s = +1.678 V, I_t = 0.27 nA). (b) Line profiles measured along the dashed lines across Pd nanocrystals of the three different shapes indicated in Fig. 6.1a. (c) STM image of elongated Pd nanocrystals observed on the same sample (image size: 120 × 85 nm^2, imaging conditions: V_s = +1.678 V, I_t = 0.27 nA). (d) Height histogram of Pd nanocrystals nucleated and grown at 300°C for 30 minutes. The height was measured from samples "Anatase-1, 2 and 4" with corresponding layer numbers labelled.

More elongated Pd nanocrystals were observed in the different regions of the same sample. They are highlighted by the yellow arrows in Fig. 6.1c. These Pd nanocrystals grew preferentially along the [100] direction of the anatase substrate. As discussed in Ch. 5.4.1, the growth of Pd particles elongating along the [100] direction of the substrate is attributed to the faster and preferential in-channel diffusion, compared to cross-channel diffusion of Pd on anatase. The height distribution of Pd nanocrystals nucleated and grown at 300°C for

30 minutes from samples "Anatase-1, 2 and 4" is shown in Fig. 6.1d. The average height of these Pd nanocrystals is 25.50±5.92 Å. Most of the measured Pd nanocrystals have heights corresponding to 8 to 15 layers of Pd(111).

In the sample "Anatase-3" which was firstly annealed at 400°C, most of the Pd nanocrystals have a truncated triangular shape and are found at step edges of the anatase surface (Fig. 6.2a). The sample was further annealed at 550°C. From the STM image (Fig. 6.2b), Pd nanocrystals are still found at step edges close to the screw dislocations on anatase.

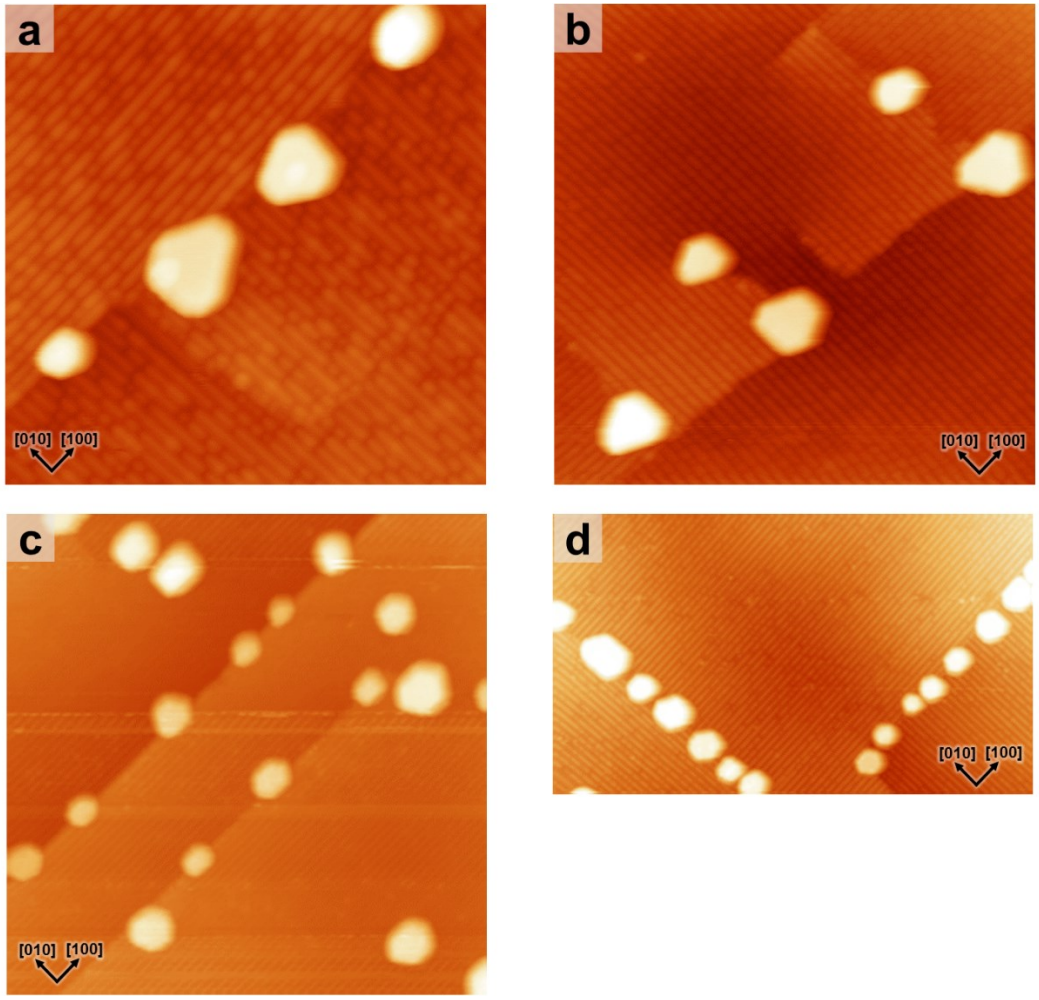


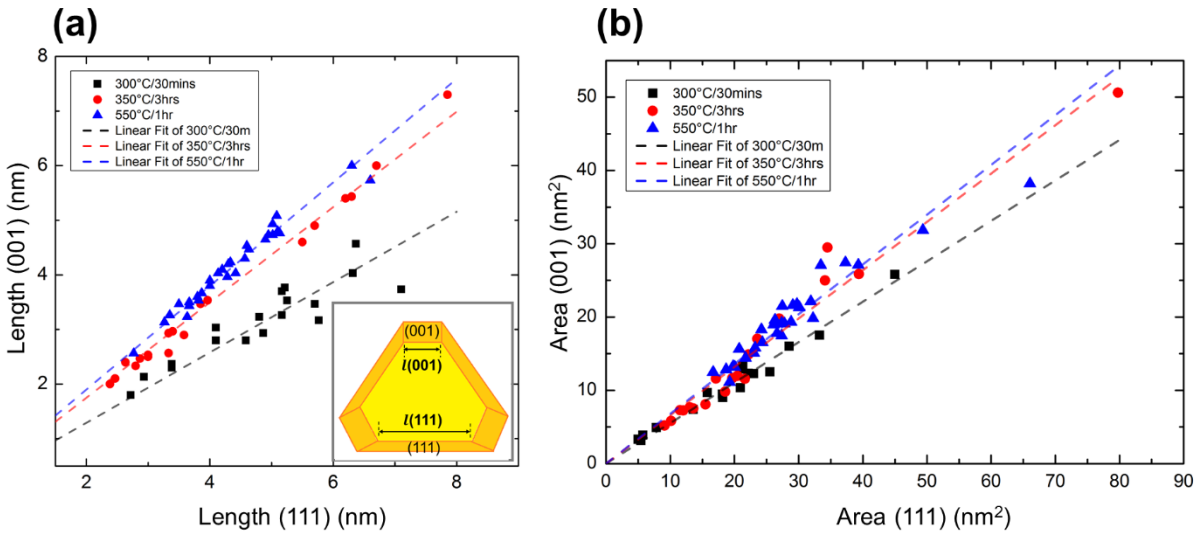
Fig. 6.2 (a) STM image of Pd nanocrystals grown on "Anatase-3" after a 1-hour anneal at 400°C (image size: 60 × 60 nm^2, imaging conditions: V_s = +2.251 V, I_t = 0.215 nA). (b) STM image of the same "Anatase-3" sample after a further anneal at 550°C for 2 hours (image size: 80 × 80 nm^2, imaging conditions: V_s = +1.634 V, I_t = 0.17 nA). (c,d) STM images of Pd nanocrystals grown on "Anatase-4" after a 3-hour anneal at 550°C (image sizes (c) 100 × 100 nm^2 and (d) 120 × 70 nm^2; imaging conditions: (c) V_s = +1.79 V, I_t = 1.275 nA and (d) V_s = +1.79 V, I_t = 1.3 nA).

Fig. 6.2c shows the Pd nanocrystals grown on sample "Anatase-4". After this sample was post annealed at 550°C for 3 hours, some Pd nanocrystals had changed from a truncated triangular shape into a hexagonal shape. The average height of the hexagonal crystals is 3.59±0.58 nm, which is an integer multiple of the Pd(111) interplanar spacing (i.e., 0.225 nm). This indicates that the hexagonal Pd nanocrystals have a (111) top facet, three (001) and (111) side facets and a (111) base facet. Most of the nanocrystals in this sample are also located at step edges. The preferential Pd growth along step edges was also observed in other regions of the same sample (Fig. 6.2d).

2) Measurements of (001) and (111) side lengths

The lengths of the (001) and (111) sides of the Pd nanocrystals annealed at 300°C, 350°C and 550°C were measured. The side lengths of the top facet were measured along $l(001)$ and $l(111)$ as illustrated in Fig. 6.3a. Because the surface energy of the (001) facet (γ_{001} = 1.86 J/m^2) is higher than that of the (111) facet (γ_{111} = 1.64 J/m^2), the size of $l(001)$ should be smaller than $l(111)$. The $l(001)$ values are plotted against $l(111)$ under different treatment conditions in Fig. 6.3a. The gradients of the linear fits, the ratios $l(001)$:$l(111)$, under different treatment conditions are summarised in Fig. 6.3c. It shows an increase of $l(001)$:$l(111)$ ratio, towards 1, for an increase in annealing temperature. A ratio of "1" corresponds to the regular hexagonal shape. The change of $l(001)$:$l(111)$ ratio suggests that Pd nanocrystals tend to grow from the truncated triangular shape to the near-hexagonal shape as the annealing temperature and time were increased. It should be noted that the ratio approaches 1, but never reaches 1 because the (001) and (111) sides of the Pd unit cell (fcc) present different atomic arrangements. The surface areas of the (001) and (111) facets were calculated and plotted in Fig. 6.3b. The gradient of the fitted line is the ratio between the

two facet areas, $A(001)$:$A(111)$. It shows that the area of the (001) facet increases relative to that of the (111) facet with increasing annealing temperatures (Fig. 6.3d). The ratio $A(001)$:$A(111)$ is less than 1 because the surface energy of the (001) facet is higher than that of the (111) facet, resulting in a relatively smaller facet area, to minimise the total surface free energy of the Pd nanocrystals under equilibrium conditions.



(c)

$l(001)$:$l(111)$	Average	Standard deviation
300°C/30mins	0.66	0.06
350°C/3hrs	0.86	0.04
550°C/1hrs	0.95	0.03

(d)

$A(001)$:$A(111)$	Average	Standard deviation
300°C/30mins	0.57	0.06
350°C/3hrs	0.63	0.09
550°C/1hrs	0.69	0.05

Fig. 6.3 (a) Plot of $l(001)$ versus $l(111)$ under different treatment conditions. The side lengths of the (111) and (001) facets were measured as shown in the bottom right corner. The intercept of fitted line was fixed at 0. The $l(001)$:$l(111)$ ratios for the different treatment conditions are summarised in (c). (b) Plot of the side surface areas of the (001) and (111) facets under different treatment conditions. Each fitted line has fixed intercept at 0. The $A(001)$:$A(111)$ ratios for the different treatment conditions are summarised in (d).

3) Measurements of volumes

The volumes of Pd nanocrystals annealed at different temperatures and / or for different time durations were measured from sample "Anatase-4". Fig. 6.4a shows the results from the sample annealed at 350°C and 550°C for the same annealing time (3 hours). It shows that the average size of Pd nanocrystals significantly increased at a higher annealing temperature. Small crystals (less than 50 nm^3) were less seen and more crystals have large size (~550-650 nm^3). At the higher temperature, large nanocrystals grow at the expense of smaller ones due to Ostwald ripening. The volume distributions are shown in Fig. 6.4b for a sample treated at the same temperature (550°C) for 1 hour and 3 hours respectively. The sizes of the most Pd nanocrystals are in the 200-300 nm^3 range for both annealing durations. At the same time, some large crystals (600-700 nm^3) formed as the annealing time increased.

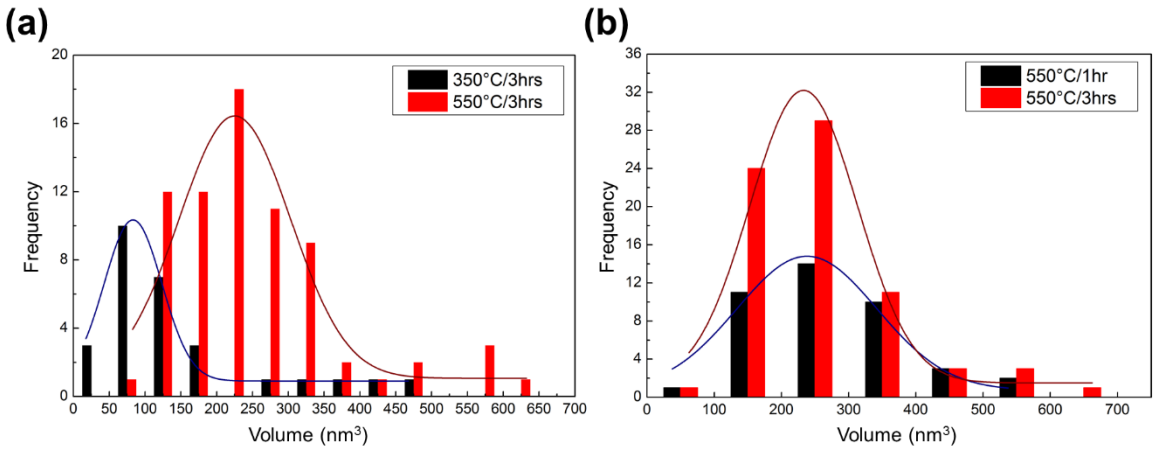


Fig. 6.4 Volume distributions of Pd nanocrystals which were grown (a) at different temperatures for the same annealing time and (b) at the same temperature for different annealing times.

4) Measurements of rotation angles

In Ch. 5.3.2, we observed the encapsulation of Pd nanocrystals supported on dilines after the sample was annealed at above 600°C. The same phenomenon occurred in the system in which Pd nanocrystals were supported on an anatase substrate after the sample was annealed at above 600°C (see Ch. 7). Fig. 6.5a shows the STM images of a typical bare Pd nanocrystal grown on anatase. The top facet is flat and terminated by the Pd(111) plane. A typical encapsulated Pd nanocrystal supported on anatase is shown in Fig. 6.5b. Bright dots were observed on the top facets, indicating the formation of a superstructure. The details of the experimental results of encapsulated Pd nanocrystals on anatase are presented in Ch.7.3.2.

The rotation angles, the smallest angle between one of the Pd nanocrystal sides and anatase, were measured for both bare and encapsulated nanocrystals. Fig. 6.5c and d show the orientation distributions of the smallest rotation angles. An example measurement is illustrated in each of Fig. 6.5 a and b, in which Pd nanocrystal sides are labelled with blue arrows and the anatase directions are labelled with white arrows.

83 bare Pd nanocrystals annealed at 300°C for 30 minutes were measured. The histogram of the orientations is shown in Fig. 6.5c. The nanocrystal sizes are indicated by different colours (Fig. 6.5c). A wide range of the orientations between 0° and 31° were observed, with peaks located at 0-1° and 15-17°. When the rotation angles were compared between different crystal sizes, it was found that 66% of small Pd nanocrystals ($w < 11$ nm) tend to align well (0-5°) with the anatase substrate with only a small proportion (16%) rotated by more than 15°. However, for big Pd nanocrystals ($w \geq 11$ nm) there is poor alignment with the substrate, with more than 36% of the nanocrystal presenting rotations larger than 15°. When annealed for the same amount of time, larger Pd nanocrystals grew faster than smaller

ones, the former of which seem to have insufficient time to adjust themselves to the most favourable (i.e., lowest-energy) position. That is why larger crystals show poorer epitaxy with the anatase substrate.

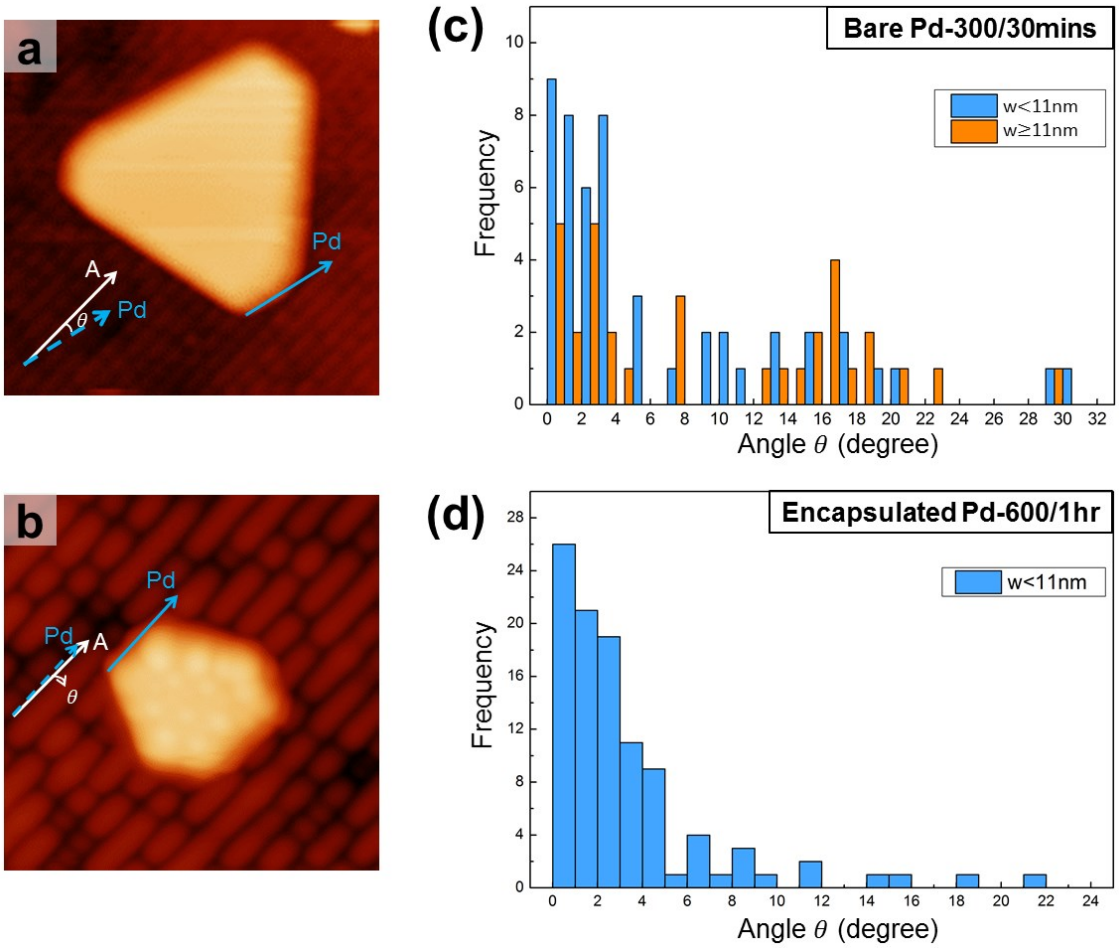


Fig. 6.5 (a) STM image of a typical bare Pd nanocrystal formed at 300°C after being annealed for 30 minutes (image size: 32 × 32 nm^2, imaging conditions: V_s = +1.678 V, I_t = 0.27 nA). (b) STM image of a typical encapsulated Pd nanocrystal after being annealed at 600°C for 1 hour (image size: 20 × 20 nm^2, imaging conditions: V_s = +2.63 V, I_t = 1.325 nA). Examples of rotation measurements are shown with the orientation of Pd sides measured along blue arrows and the orientation of anatase measured along the white arrows. (c) Orientation distribution histogram for bare Pd nanocrystals treated at 300°C for 30 minutes. The histogram was plotted for crystal width w < 11 nm (blue bars) and w ≥ 11 nm (orange bars). (d) Orientation distribution histogram for encapsulated Pd nanocrystals annealed at 600°C for 1 hour. These encapsulated Pd nanocrystals were all narrower than 11 nm.

102 encapsulated Pd nanocrystals were measured after sample "Anatase-5" was annealed at 600 °C for 1 hour. These nanocrystals were all narrower than 11 nm. 85% of the nanocrystals have rotation angles in the range 0-5°, showing good epitaxy with the anatase substrate (Fig. 6.5d). When the orientations of small Pd nanocrystals (w < 11 nm) treated at lower (Fig. 6.5c) and higher temperatures (Fig. 6.5d) were compared, it was found that the higher-temperature treatment facilitated the Pd nanocrystals to re-adjust their orientations from unfavourable to favourable orientations (0-5°), i.e., the lowest-energy positions.

6.3.2 Height-to-width (*h*/*w*) ratio of Pd nanocrystals

As described in Sec. 6.3.1, most Pd nanocrystals have a truncated triangular shape at low temperatures (below 400 °C), a typical example of which is shown in Fig. 6.6a. Hexagonally-shaped Pd nanocrystals were mostly found at higher annealing temperatures (above 500 °C) with a typical example shown in Fig. 6.7a. A further increase in the annealing temperature to 600°C caused the encapsulation of Pd nanocrystal with bright dots on the top facets (Fig. 6.8a). In order to obtain the equilibrium height-to-width (*h/w*) ratio of bare and encapsulated Pd nanocrystals, the heights and widths of the symmetrically-shaped Pd nanocrystals treated at 300 and 550°C (bare) and 600°C (encapsulated) were measured. The widths were measured on the Pd top facets from the middle of the (001) side to the opposite (111) side (c in Fig. 6.6-Fig. 6.8).

1) Bare Pd - truncated triangular shape

53 truncated triangular Pd nanocrystals were selected from sample "Anatase-2", which was annealed at 300°C for 30 minutes. The heights and widths of these nanocrystals were measured and plotted in Fig. 6.6b. The *h/w* ratio is 0.19±0.03. The uncertainty denotes the standard deviation. The data points are widely scattered, suggesting that these Pd nanocrystals had not reached their equilibrium shape.

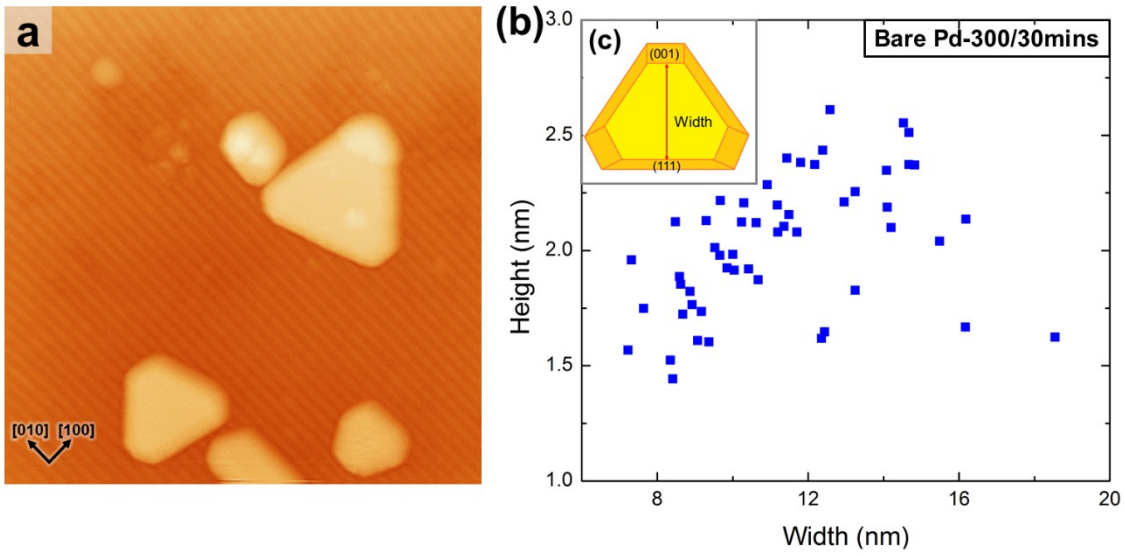


Fig. 6.6 (a) STM image of typical truncated triangular-shaped Pd nanocrystals formed on sample "Anatase-2". The sample was annealed at 300°C for 30 minutes (image size: 70 × 70 nm^2, imaging conditions: V_s = +1.678 V, I_t = 0.27 nA). (b) Plot of height versus width of 53 Pd nanocrystals with a truncated triangular shape. (c) Top view of a truncated triangular Pd nanocrystal. Its width was measured on the top facet from the middle of (001) side to the middle of the opposite (111) side.

2) Bare Pd - hexagonal shape

The widths and heights of 11 Pd nanocrystals with a hexagonal shape were measured from sample "Anatase-4", annealed at 550°C for 3 hours. The height was plotted against the width in Fig. 6.7b. It shows a linear relation given by the red dashed line, suggesting the formation of equilibrium-shaped Pd nanocrystals. The gradient of the red dashed line

represents the equilibrium ratio of *h/w*, which is 0.54±0.02. The uncertainty denotes the standard deviation.

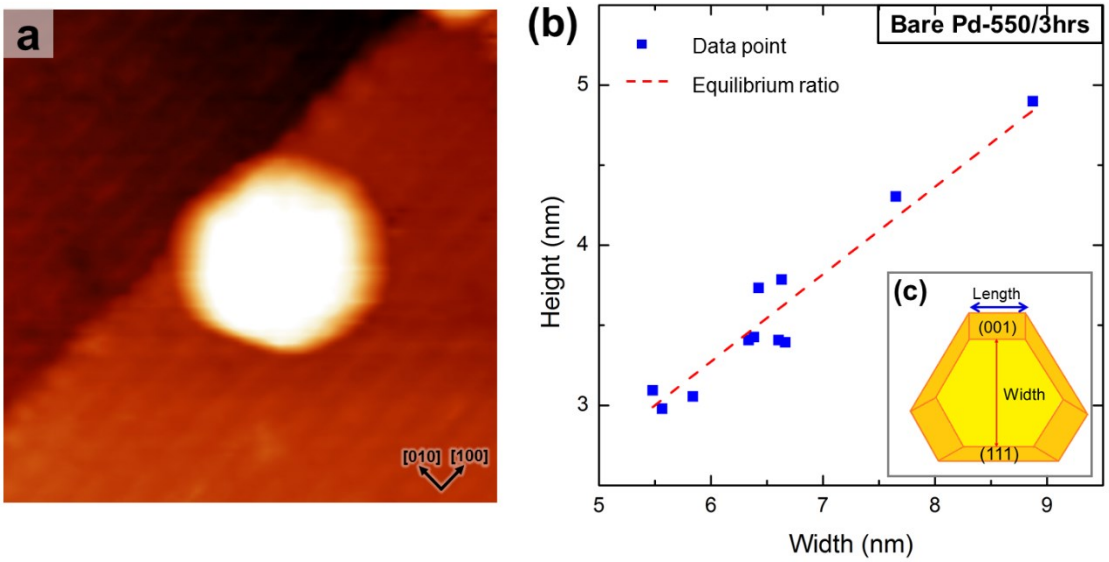


Fig. 6.7 (a) STM image of typical hexagonal Pd nanocrystals formed on sample "Anatase-4". The sample was annealed at 550°C for 3 hours (image size: 30 × 30 nm^2, imaging conditions: V_s = +2.329 V, I_t = 0.15 nA). (b) Plot of height versus width of 11 hexagonal Pd nanocrystals. The gradient of the fitted dashed line corresponds to the equilibrium ratio *h/w* = 0.54±0.02, where the uncertainty denotes the standard deviation. The intercept was fixed at 0. (c) Top view of a hexagonal-shaped Pd nanocrystal. Its width was measured on the top facet from the middle of (001) side to the middle of the opposite (111) side. The side length of (001) facet was measured on top facet of Pd nanocrystals.

3) Encapsulated Pd

High-temperature treatments caused the encapsulation of Pd nanocrystals, with superstructures formed on the top facet. The details of the study of the superstructures can be found in Ch. 7.3.2. The encapsulation of Pd nanocrystals was achieved by a 1-hour anneal at 600°C. The widths and heights of 31 encapsulated Pd nanocrystals were measured. The plot of the height against width shows a linear relationship, which implies these nanocrystals have reached their equilibrium shapes (Fig. 6.8b). The equilibrium *h/w* ratio was obtained from the gradient of linear fitted line, which is 0.45±0.01, where the uncertainty denotes the standard deviation.

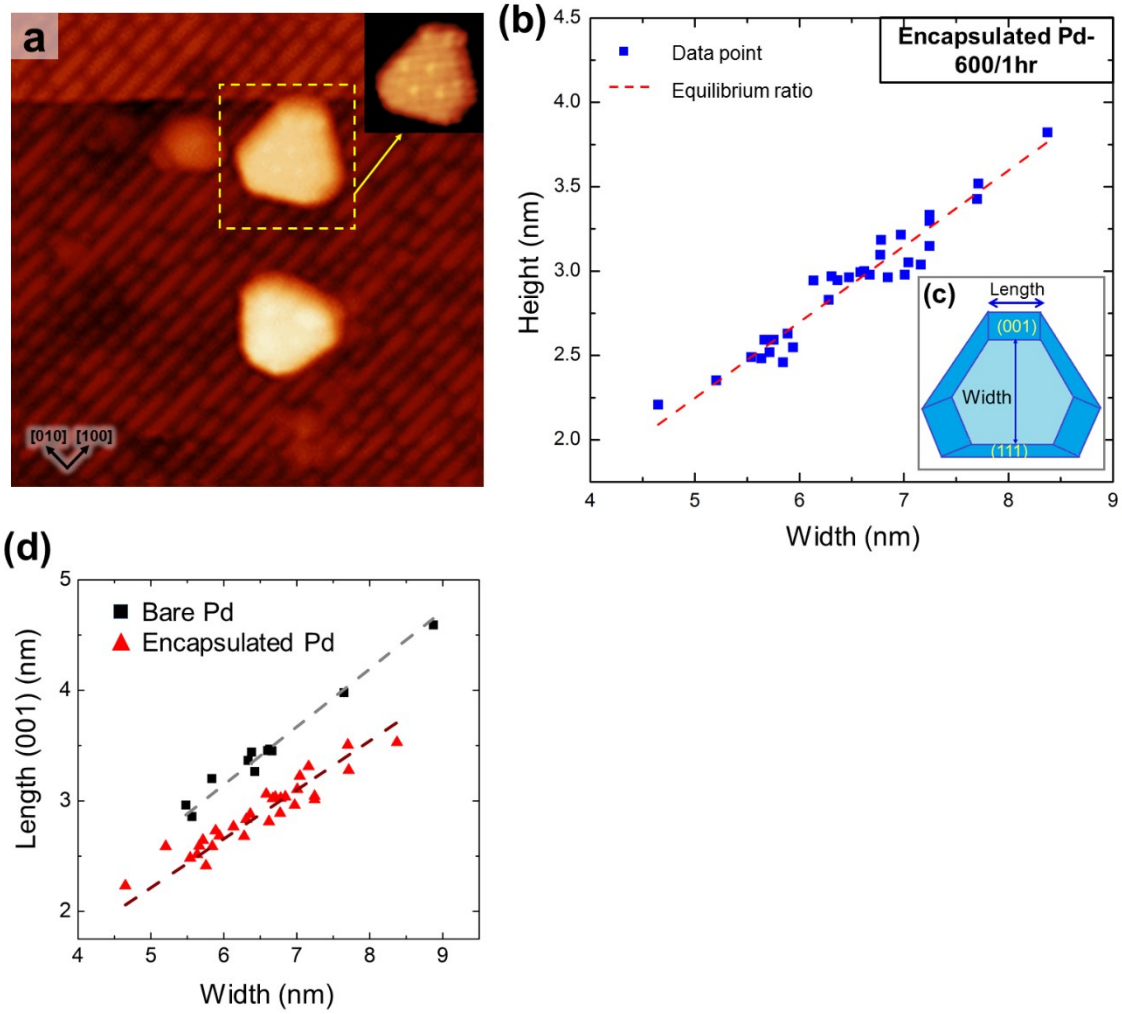


Fig. 6.8 (a) STM image of typical encapsulated Pd nanocrystals formed on "Anatase-5". The sample was annealed at 600°C for 1 hour. The bright spots were observed on top facet as shown in the right corner (image size: 40 × 40 nm^2, imaging conditions: V_s = +2.5 V, I_t = 0.8 nA). (b) Plot of height versus width of 31 encapsulated Pd nanocrystals. The gradient of the fitted dashed line corresponds to the equilibrium ratio h/w = 0.45±0.01, where the uncertainty denotes the standard deviation. The intercept was fixed at 0. (c) Top view of an encapsulated Pd nanocrystal. Its width was measured on the top facet from the middle of (001) side to the middle of the opposite (111) side. The side length of (001) facet was measured on top facet of Pd nanocrystals. (d) Plot of length of (001) facet versus width for bare and encapsulated Pd nanocrystals.

The (001) side length for both bare hexagonal and encapsulated Pd nanocrystals was measured from top facet as indicated in Fig. 6.7c and Fig. 6.8c respectively. The results between (001) side length (l) and crystal width (w) are plotted in Fig. 6.8d. It shows a linear

relationship between the length and width, which l/w = 0.53±0.01 for bare hexagonal Pd nanocrystals and l/w = 0.45±0.02 for encapsulated Pd nanocrystals.

Pd nanocrystals are found to grow flatter at low temperature. As atoms land on the surface at low temperature (e.g., 300°C), they are likely to move along the surface and attached to the edge of the existing atom clusters. The more favoured lateral movement of the deposited atoms encourages the growth of nanocrystal in lateral size rather than height due to lack of energy for atoms to jump onto other atoms. This is also found by Silly *et al.* [55] who observed the limited growth rate of crystals in height, but not width, at low temperatures. This tendency postpone the formation of the equilibrium shape of Pd nanocrystal at low temperature. Therefore, our measurement of *h/w* ratio for Pd nanocrystals grown at 300°C should be smaller than that of the equilibrium crystal formed at the same temperature.

When the sample was annealed at higher temperature, Pd atoms become more energetically favoured to climb onto others and grow higher in the meantime move freely in lateral direction. Pd nanocrystals formed at high temperature should be easier to reach their equilibrium shape than those grown at low temperature. As the measurements in Fig. 6.6b, Fig. 6.7b and Fig. 6.8b are compared, only Pd nanocrystals grown at 550 and 600°C shows the linear relationships between height and width, indicating these nanocrystals have reached their equilibrium shape. Therefore, the equilibrium *h/w* ratios of Pd nanocrystals grown at 550°C and 600°C are used for further calculation in Sec. 6.4.

6.4 Discussion

6.4.1 Adhesion energy of Pd nanocrystals on anatase

The dimensions of equilibrium bare Pd nanocrystals with hexagonal shapes were used to calculate the adhesion energy of Pd supported on anatase. The adhesion energy (W_{adh}) between Pd nanocrystals and the anatase substrate is derived in Ch. 5.4.2, where

$$W_{adh} = \gamma_{Pd(111)} - \gamma_i + \gamma_{s(001)}, \tag{5.5}$$

and

$$W_{adh} = \gamma_{Pd(111)} - \gamma^*. \tag{5.7}$$

For the equilibrium Pd nanocrystals of the hexagonal shapes, γ^* can be written as a function of $\gamma_{Pd(001)}$, $\gamma_{Pd(111)}$ and the height (h)-to-width (w) ratio [55]:

$$\gamma^* = \sqrt{\frac{3}{2}}\frac{h}{w}\gamma_{Pd(001)} - \gamma_{Pd(111)}. \tag{5.8}$$

The experimentally determined values, h/w = 0.54±0.02 (Fig. 6.7b) for hexagonally shaped Pd were substituted into Eq. 5.8. The Pd surface energies from the DFT calculations by Methfessel *et al.* [350] were used, where $\gamma_{Pd(001)}$ = 1.86 J/m^2 and $\gamma_{Pd(111)}$ = 1.64 J/m^2.

We obtained

$$\gamma^*_{hexa} = -0.41 \pm 0.05 \text{ J/m}^2.$$

Substituting the values of γ^* into Eq. 5.7 gives us the adhesion energy of Pd nanocrystals grown on anatase TiO_2(001) substrate is

$$W_{adh(hex)} = 2.05 \pm 0.05 \text{ J/m}^2.$$

6.4.2 Comparison of surface energies between bare and encapsulated Pd nanocrystals

Our results have shown that a thin TiO_x film was formed on Pd nanocrystal surfaces after encapsulation occurred (Ch. 7.3.2). TiO_x films can grow on both Pd(001) and Pd(111) surfaces [351], which suggests that the side facets of Pd nanocrystal were covered by TiO_x as well as the top facet. The surface energies of bare and encapsulated Pd nanocrystals in equilibrium shapes supported on anatase were compared. Tab. 6.2 summarises the experimental values of *h/w* and *l/w* obtained in Sec. 6.3.2.

Tab. 6.2 Summary of experimental *h/w* and *l/w* values

Systems	**Annealing conditions**	**Experimental *h/w* ratios**	**Experimental *l/w* ratios**
Bare Pd	550°C/3hrs	0.54±0.02	0.53±0.01
Encapsulated Pd	600°C/1hr	0.45±0.01	0.45±0.02

In the particle-substrate system, Winterbottom analysis [231] suggests that the ratio between the surface energy of any free surface facet (γ_{hkl}) and the perpendicular distance (h_{hkl}) from the Wulff point is constant (i.e., $\gamma_{hkl} = \lambda h_{hkl}$). Applying to a free equilibrium Pd nanocrystal indicated in Fig. 6.9, we obtain,

$$\frac{\gamma_{111}}{\gamma_{001}} = \frac{h_{111}}{h_{001}} \tag{6.1}$$

The relative surface energies between Pd(111) and (001) facets from Eq. 6.1 can be determined from the dimensions of the equilibrium nanocrystal in Eq. 6.2.

$$\frac{\gamma_{111}}{\gamma_{001}} = \frac{h_{111}}{h_{001}} = \frac{(w\times cos\alpha+\frac{1}{2}l)\times sin\alpha}{w\times sin\alpha} = \frac{1}{2}\frac{l}{w} + \frac{1}{\sqrt{3}} \tag{6.2}$$

Where l is the (001) side length and w is the width of an equilibrium shaped Pd nanocrystal, α is the angle between Pd(001) and Pd(111) planes with $sin\alpha = \sqrt{\frac{2}{3}}$ and $cos\alpha = \sqrt{\frac{1}{3}}$.

Equation 6.2 indicates that the relative surface energy ratio of (111) and (001) facets (i.e., $\frac{\gamma_{111}}{\gamma_{001}}$) is proportional to the length-to-width ratio (i.e., $\frac{l}{w}$) of an equilibrium Pd nanocrystal i.e., $\frac{\gamma_{111}}{\gamma_{001}} \propto \frac{l}{w}$. Applying experimental results of l/w (Tab. 6.2) for both bare and encapsulated Pd into Eq. 6.2 gives the $\frac{\gamma_{111}}{\gamma_{001}}$ ratio of 0.84 and 0.80 respectively. It shows that the relative surface energy ratio (i.e., $\frac{\gamma_{111}}{\gamma_{001}}$) is reduced after the Pd nanocrystal is encapsulated.

As described in Ch. 5.4.2, in the particle-substrate system, the value of general surface tension γ^*, which is defined as $\gamma^* = \gamma_i - \gamma_{s(001)}$, is determined by the morphology and surface energies of the particle (Eq. 5.8):

$$\gamma^* = \sqrt{\frac{3}{2}}\frac{h}{w}\gamma_{Pd(001)} - \gamma_{Pd(111)} \tag{5.8}$$

The general surface tension of bare Pd (γ_b^*) supported on anatase can be written in Eq. 6.3. Note that the subscript "b" means bare Pd.

$$\gamma_b^* = \sqrt{\frac{3}{2}}\frac{h_b}{w_b}\gamma_{b(001)} - \gamma_{b(111)} \quad \text{(Bare Pd on anatase)} \tag{6.3}$$

When a Pd nanocrystal was annealed at high temperatures, it was covered by a thin TiO_x layer (i.e., encapsulation). The cross section of an encapsulated Pd nanocrystal (in orange) supported on its (111) plane on the anatase substrate is depicted in Fig. 6.9. The TiO_x overlayer is marked in blue. The free part of the Pd nanocrystal is in light yellow.

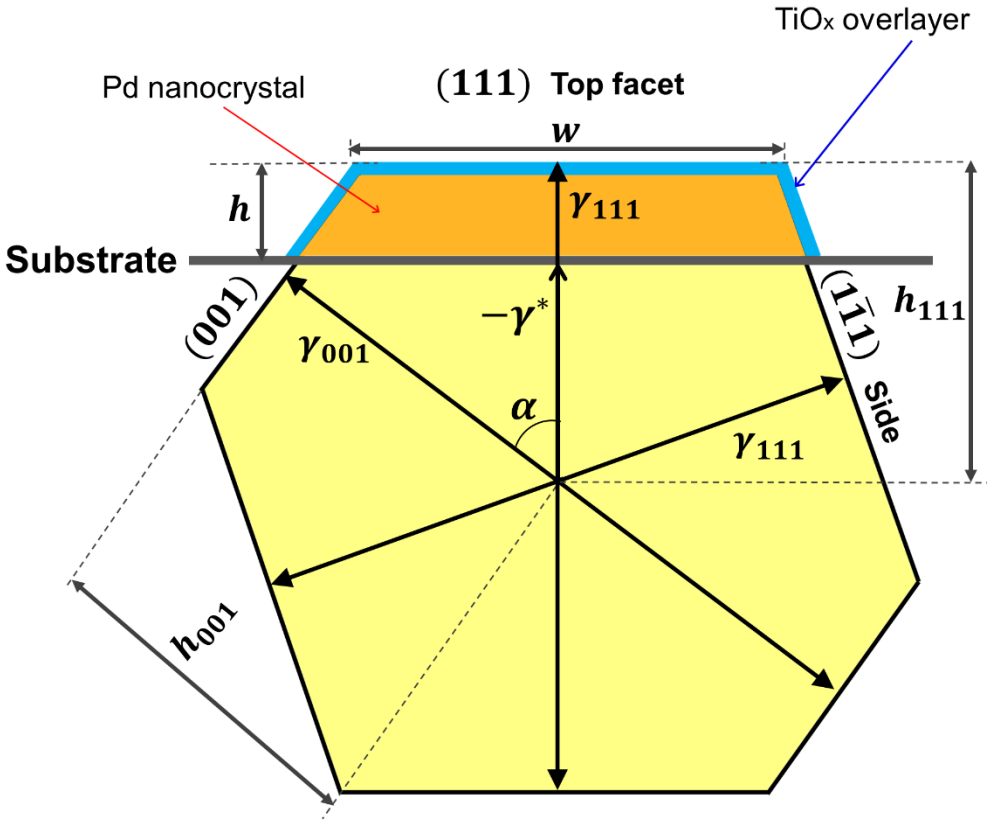


Fig. 6.9 Cross section of a Pd nanocrystal based on the Wulff construction. The encapsulated part of the Pd nanocrystal is in orange with a TiO_x overlayer in blue. The free part of the Pd nanocrystal is in light yellow (adapted from Ref. [44]).

Equation 6.4 can be derived by applying Eq. 5.8 to the encapsulated Pd-anatase system. Note that the subscript "e" means encapsulated Pd.

$$\gamma_e^* = \sqrt{\frac{3}{2}}\frac{h_e}{w_e}\gamma_{e(001)} - \gamma_{e(111)} \tag{6.4}$$

Inserting $\frac{\gamma_{e(111)}}{\gamma_{e(001)}} = 0.80$ into Eq. 6.4 gives rise to Eq. 6.5.

$$\gamma_e^* = \sqrt{\frac{3}{2}}\frac{h_e}{w_e}\gamma_{e(001)} - 0.8\gamma_{e(001)} \tag{6.5}$$

In the particle-substrate system, the value of general surface energy γ^* is defined as $\gamma^* = \gamma_i - \gamma_{s(001)}$ [231], where γ_i is the interfacial energy and $\gamma_{s(001)}$ is the surface energy of

substrate (i.e., anatase). The interface between Pd(111) and anatase (001) does not change after encapsulation, which results in the constant interfacial energy (γ_i). As a result, $\gamma_b^* = \gamma_e^*$ since the value of general surface energy (γ^*) for the Pd-anatase system remains the same from the bare Pd-anatase to the encapsulated Pd-anatase. Equations 6.3 and 6.5 imply Eq. 6.6.

$$\gamma_{e(001)} = \frac{\sqrt{\frac{3}{2}}\frac{h_b}{w_b}\gamma_{b(001)} - \gamma_{b(111)}}{\sqrt{\frac{3}{2}}\frac{h_e}{w_e} - 0.8} \tag{6.6}$$

Using the DFT-calculated values of Pd surface energies by Methfessel *et al*. [350] for the bare Pd nanocrystal where $\gamma_{b(001)} = 1.86$ J/m^2 and $\gamma_{b(111)} = 1.64$ J/m^2; and our experimental h/w ratios (Tab. 6.2), we obtain $\gamma_{e(001)} = 1.61 \pm 0.23$ J/m^2 and $\gamma_{e(111)} = 1.29 \pm 0.19$ J/m^2.

In terms of thermodynamics, Pd nanocrystals have the tendency to minimize the total surface free energy as they grow on the anatase substrate. The encapsulation of Pd nanocrystals was observed when the samples were annealed above 600°C. The surface energy of encapsulated Pd was calculated by comparison with the bare Pd crystals. The results show that the surface energies of encapsulated Pd crystals in (111) and (001) facets (i.e., $\gamma_{e(111)} = 1.29 \pm 0.19$ J/m^2 and $\gamma_{e(001)} = 1.61 \pm 0.23$ J/m^2) are lower than those of the bare Pd(111) and Pd(001) (i.e., $\gamma_{b(111)} = 1.64$ J/m^2 and $\gamma_{b(001)} = 1.86$ J/m^2) respectively. This indicates that covering a bare Pd nanocrystal with a monolayer TiO_x film, which is formed at high temperatures, could certainly reduce the total surface free energy of the system. The complete wetting of the TiO_x film on the Pd surface also indicates that the surface energy of TiO_x is lower than that of the Pd nanocrystals. Thus, encapsulation occurred to reduce the total surface free energy of the system by forming an oxide layer. The surface energy of Pd nanocrystal after encapsulation is reduced by 0.35 ± 0.19 J/m^2

compared to that of bare Pd(111), which is the dominant surface of Pd nanocrystals grown on an anatase substrate. The surface energy of (001) facets is slightly reduced by 0.25±0.23 J/m^2.

6.5 Conclusion

Pd nanocrystals can grow epitaxially on anatase substrates, with one side parallel to the <100> crystallographic directions of anatase. The epitaxy of most Pd nanocrystals was significantly improved after high-temperature anneals. Annealing temperatures influence the shapes of the Pd nanocrystals. They form truncated triangular shapes with low h/w ratios (0.19±0.03) at low temperatures (300°C). Increasing the annealing temperature leads to an increase in the areas ratio of the (001) and (111) sides (i.e., A(001):A(111)) as well as the side length ratio l(001):l(111). Pd nanocrystals tend to grow into a near-hexagonal shape with a h/w ratio of 0.54±0.02 at high temperatures (550°C). The increase in h/w ratio suggests that Pd nanocrystals prefer to grow in width rather than in height at low temperatures, and the other way round at higher annealing temperatures. The adhesion energy of Pd-anatase is calculated to be 2.05 ± 0.05 J/m^2. The encapsulation of Pd nanocrystals occurred at high temperatures (above 600°C). When Pd nanocrystals were annealed at high temperatures, the energy reduction mainly came from the encapsulation of Pd nanocrystal with a TiO_x overlayer with a lower surface energy. In that case, the surface energy of dominant (111) facets is reduced by 0.35±0.19 J/m^2, from 1.64 J/m^2 for bare Pd nanocrystals to 1.29 ± 0.19 J/m^2 for encapsulated Pd nanocrystals. The surface energy reduction of (001) facets is 0.25±0.23 J/m^2, from 1.86 J/m^2 for bare Pd nanocrystals to 1.61±0.23 J/m^2 for encapsulated Pd nanocrystals.

Chapter 7

Encapsulation of Pd on Dilines and Anatase Substrates

7.1 Introduction

Noble metal nanocrystals grown on oxide supports are a popular system in heterogeneous catalysis [234-236]. Studies of the interaction between noble metal nanocrystals and oxide supports have drawn increasing attention in the recent thirty years, especially for noble metal nanocrystals (e.g. Pt [28-31] and Pd [32-36]) supported on titanium oxide substrates. Several studies illustrated that Ti atoms become mobile at elevated temperatures and tend to migrate to the metal nanocrystal surfaces during high temperature treatments. This brings the system into the strong metal-support interaction state (SMSI). The metal-oxide system under SMSI state is characterised by the encapsulation of metal nanocrystals under a thin oxide layer, leading to the reduction of the total surface energy of the metal nanocrystals. This phenomenon is especially attractive and fundamentally important for scientific studies to understand the catalytic activities. On the one hand, SMSI-related encapsulation reduces the chemisorption ability of CO and H_2 [34,232,237]. On the other hand, competitive hydrogenation versus hydrogenolysis reactions are greatly favoured in SMSI systems [29]. This allows tailored selectivity for catalytic reactions [36,239,240].

In this chapter, we report STM studies of Pd nanocrystals (typical width 3-15 nm) and larger islands (typical width 100-200 nm) grown on titanium oxide supports terminated by dilines and anatase. We show that moiré patterns formed on encapsulated Pd surfaces. The crystal models are also depicted to illustrate the formation of the different moiré patterns.

7.2 Experimental method

Pd nanocrystals were grown on two different substrates with dilines or anatase terminations. Preparation methods to form dilines and anatase structures were described in Ch. 5.2 and Ch. 4.2 respectively. An e-beam evaporator was used to evaporate Pd onto the substrates. The detailed preparation conditions are summarised in Tab. 7.1. Pd was deposited on the diline substrate at temperatures of 600°C and 650°C, followed by post-deposition anneals at the deposition temperature for 1 hour. Pd was also deposited on the anatase substrate at 300°C followed by a post-deposition anneal at 600°C for 1 hour. Further deposition by increasing the flux and time encourages the formation of large Pd nanocrystals. Pd islands were prepared by two annealing steps. Firstly, Pd was deposited onto the anatase sample at 300°C followed by a 1-hour anneal at 500°C. Next, the sample was annealed at 860°C for 1.5 hours. All anneals were carried out in UHV with a base pressure of 10^{-8} Pa. The surface structures were characterised by STM and image analysis softwares (WSxM [352], FabViewer, ImageJ and Gwyddion). The crystal models were built in CrystalMaker.

Tab. 7.1 Summary of sample preparation conditions

		Pd nc. (width 3-15 nm) **on dilines**		**Pd nc.** (width 3-15nm) **on anatase**	**Pd isl.** (width 100-200nm) **on anatase**
Pd deposition	Filament current (A)	4.10	4.11	4.11	4.32
	Emission (mA)	11.3	11.9	12.6	20.7
	Flux	26.9 nA	25.5 nA	421.1 pA	1.9 nA
	Time (s)	180	180	20	30
	Substrate temperature (°C)	600	650	300	300
Post anneal	Temperature/ duration	600/1hr	650/1hr	600/1hr	500/1hr+860/1.5hrs
	Environment	UHV	UHV	UHV	UHV
Note: nc. means nanocrystal; isl. means island.					

7.3 Results

7.3.1 Encapsulation of Pd nanocrystals supported on dilines

Encapsulation was observed on Pd nanocrystals when the sample was annealed at 600°C and 650°C. Bright dots (i.e., moiré dots) were observed in STM indicating the formation of the superstructures on Pd nanocrystal surfaces (Fig. 7.1 and Fig. 7.2). Fig. 7.1 shows the Pd nanocrystals after the sample was annealed at 600°C. Two types of superstructures, named as the hexagonal superstructure (A in Fig. 7.1b) and the wagon wheel superstructure (B in Fig. 7.1b) coexisted on the Pd nanocrystal surface with their unit cells highlighted. The bright lines connecting the moiré dots in the wagon wheel superstructure became visible after the imaging conditions were adjusted (Fig. 7.1c). The orientation of the moiré dots in the hexagonal superstructure is indicated by the yellow arrow (labelled as “h”) and that of the wagon wheel superstructure is indicated by the blue arrow (labelled as “w”) in Fig. 7.1b. The reference orientation was taken as the $[10\bar{1}]$ close-packed direction of the Pd

nanocrystal (the white arrow in Fig. 7.1b labelled as "Pd"). The relative rotations of moiré dots to the Pd surface are ~0° and 1.5° for the wagon wheel and the hexagonal superstructures, respectively.

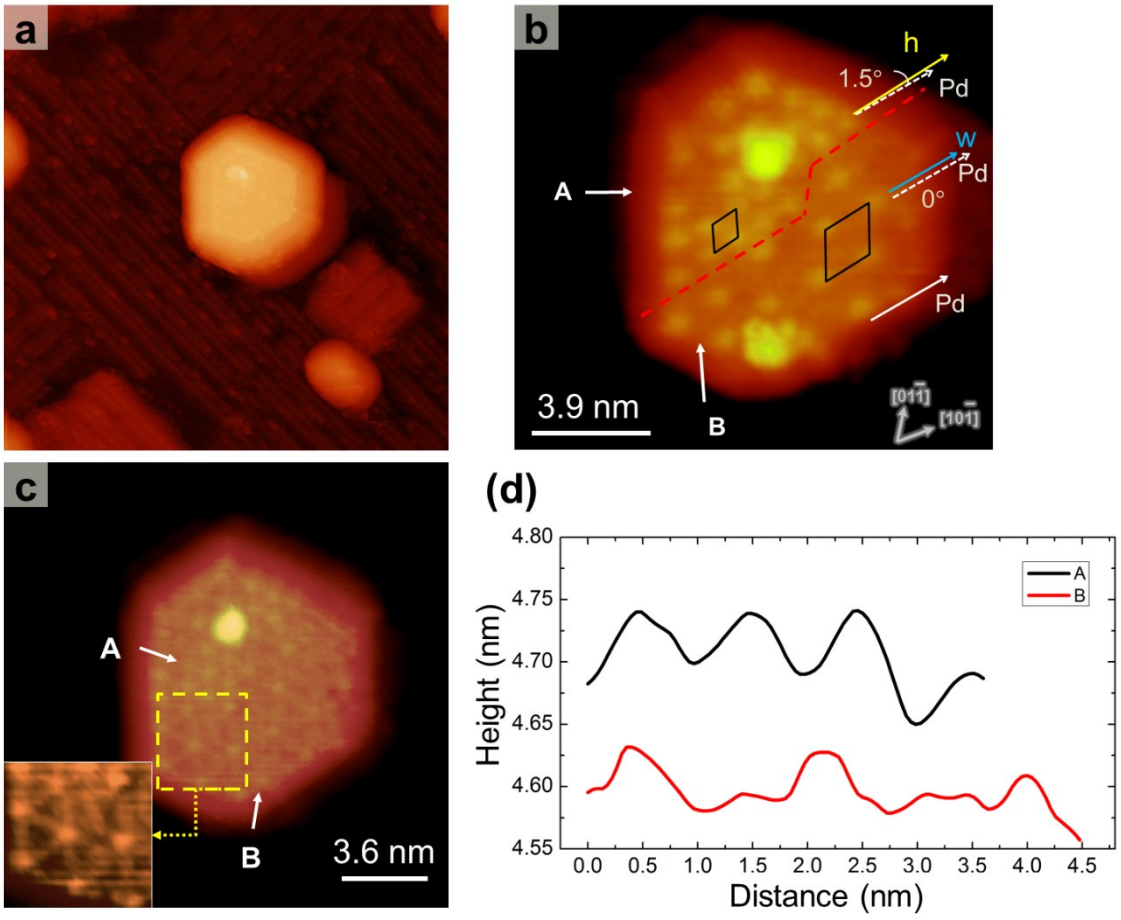


Fig. 7.1 (a) STM image of a typical encapsulated Pd nanocrystal supported on dilines after the sample was annealed at 600°C for 1 hour (image size: 50 × 50 nm^2, imaging conditions: V_s = +1.603 V, I_t = 0.265 nA). (b) and (c) Zoomed-in STM images showing the detailed structures on the encapsulated Pd nanocrystal surface with the hexagonal (pointed by A) and wagon wheel (pointed by B) superstructures. The bright lines connecting the moiré dots in the wagon wheel superstructure became visible after the STM imaging conditions were changed from (b) V_s = +1.727 V, I_t = 0.26 nA to (c) V_s = +1.621 V, I_t = 0.245 nA. (d) Line profiles measured along the close-packed directions in the hexagonal superstructure (arrow A in Fig. 7.1c) and the wagon wheel superstructure (arrow B in Fig. 7.1c).

As shown in the line profiles along the moiré dots in the hexagonal and wagon wheel superstructures (Fig. 7.1d), the spacing between two adjacent dots in the wagon wheel structure is almost twice as big as that in the hexagonal structure. The dimension of the hexagonal superstructure unit cell is 10.95 ± 0.45 Å, corresponding to a $(4 \times 4)R1.5°$ superstructure with respect to the Pd(111) surface. The unit cell of the wagon wheel superstructure is a slightly distorted hexagon with a lattice parameter of 18.50 ± 0.93 Å. The reconstruction type of the wagon wheel superstructure is defined in the 650°C treatment, where a more regular shape has formed.

More Pd nanocrystals were encapsulated after the sample was further annealed at 650°C. Some of the encapsulated Pd nanocrystals with moiré dots on the surface are circled in Fig. 7.2a. Only the wagon wheel superstructure was observed after Pd nanocrystals were annealed at 650°C (see zoomed-in image of these circled crystals). The 3D image of the encapsulated Pd nanocrystals is presented in Fig. 7.2b. The protruding dots, where they appear brighter in the STM image in Fig. 7.2a, are found at the crystal surfaces (Fig. 7.2b). A line profile measured along the arrow in image Pd-B shows the equal spacing of around 19 Å between adjacent moiré dots (Fig. 7.2c). The relative rotation between the moiré dots and the Pd layer is $0°$ as indicated in image Pd-A of Fig. 7.2. The wagon wheel superstructure has a lattice constant of 19.36 ± 0.63 Å, corresponding to a (7×7) superstructure with respect to the Pd(111) surface.

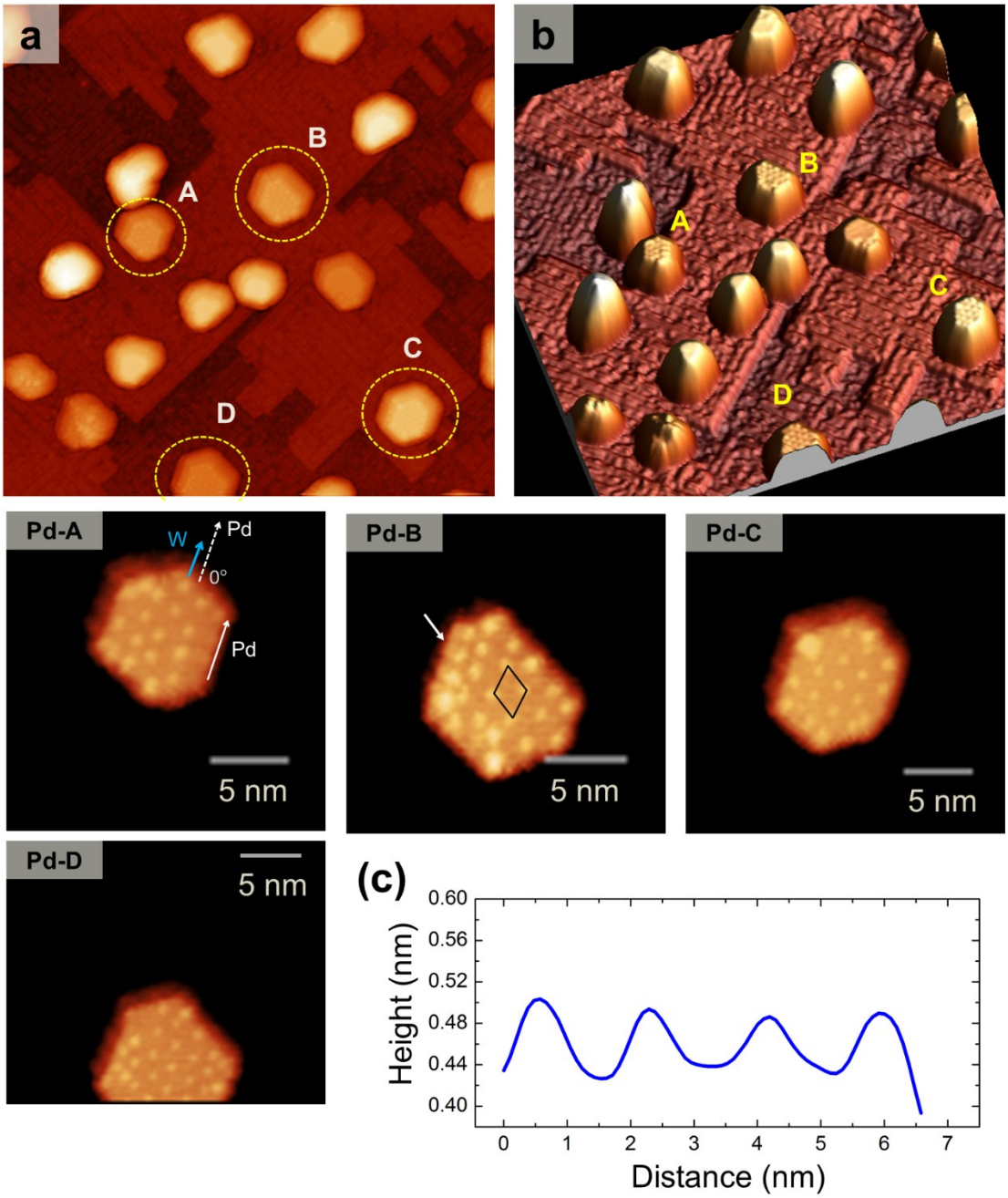


Fig. 7.2 (a) STM image of encapsulated Pd nanocrystals supported on dilines after a 1-hour anneal at 650°C (image size: 120 × 120 nm^2, imaging conditions: V_s = +2 V, I_t = 0.3 nA). Zoomed-in images of four Pd nanocrystals circled in Fig. 7.2a are presented under Fig. 7.2a. The wagon wheel superstructure was observed on these crystal surfaces. (b) 3D interpretation of the STM image in Fig. 7.2a. (c) Line profile measured along the moiré dots on the Pd crystal surface pointed by the arrow in image Pd-B.

7.3.2 Encapsulation of Pd nanocrystals supported on anatase

Encapsulation also occurs on Pd nanocrystals supported on the anatase substrate after high-temperature treatments. After the sample was annealed in UHV at 600°C for 1 hour, moiré dots were observed on the top surface of Pd nanocrystals. These encapsulated Pd nanocrystals are pointed by the arrows in Fig. 7.3a. The close view of one encapsulated Pd nanocrystal is shown in Fig. 7.3b with the 3D image shown in Fig. 7.3c. The protruded dots observed in the 3D image are those which appear brighter on the crystal surface in STM.

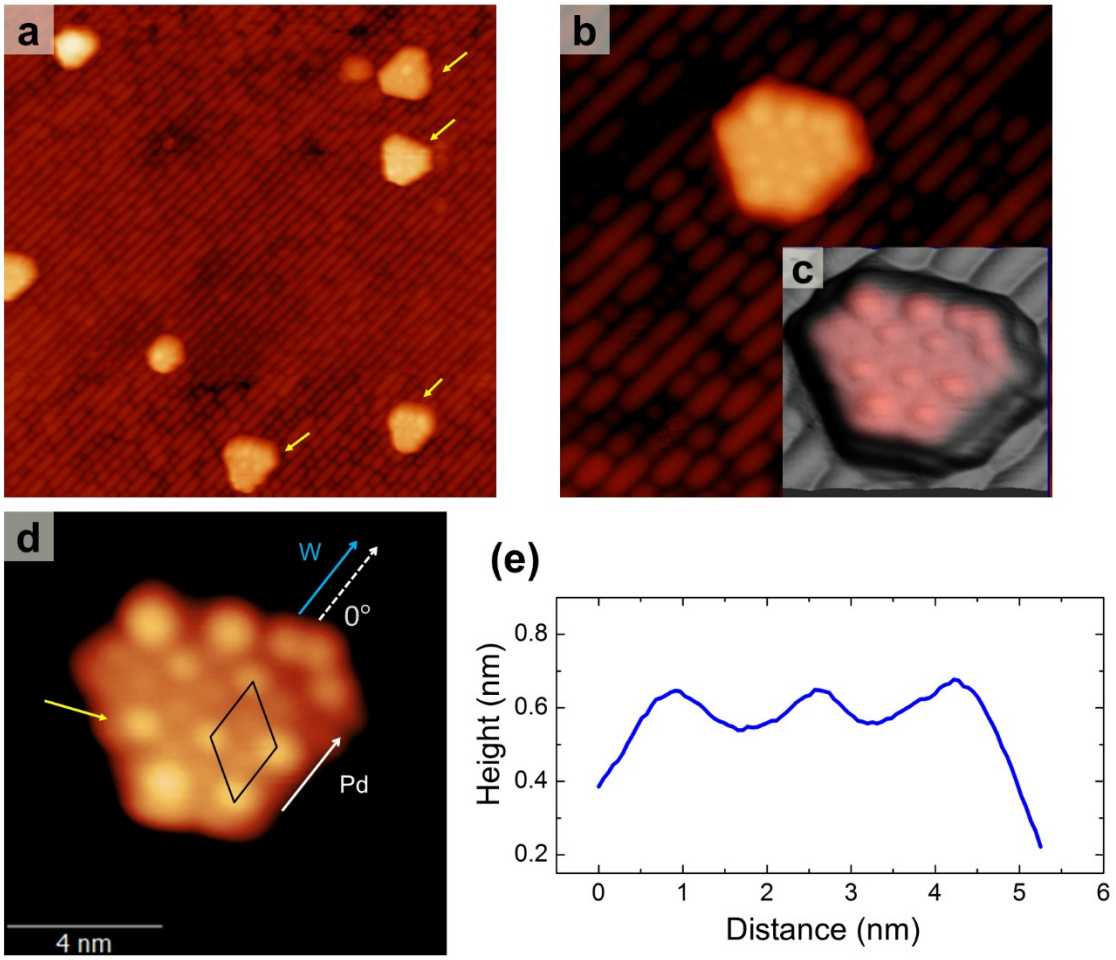


Fig. 7.3 (a) STM image of encapsulated Pd nanocrystals supported on anatase after the sample was annealed at 600°C for 1 hour (image size: 80 × 80 nm^2, imaging conditions: V_s = +2.5 V, I_t = 0.825 nA). The encapsulated crystals are pointed by yellow arrows. (b) One typical encapsulated Pd nanocrystal surface with the wagon wheel superstructure (image size: 30×30 nm^2, imaging conditions: V_s = +2.63 V, I_t = 1.325 nA). (c) 3D view of the encapsulated Pd nanocrystal. (d) Processed STM image showing the detailed surface structure in Fig. 7.3b. (e) Line profile measured along the moiré dots as marked in Fig. 7.3d.

The processed image shows clear moiré dots with a unit cell highlighted (Fig. 7.3d). The moiré dots are separated by the same distance of around 18 Å as shown in the line profile (Fig. 7.3e). These ordered moiré dots form the wagon wheel superstructure with a periodicity of 18.70 ± 0.80 Å. The orientation of these moiré dots is parallel to the orientation of close-packed Pd atoms (relative ~0° rotation) as labelled in Fig. 7.3d. This also gives rise to the formation of the (7×7) wagon wheel superstructure with respect to the Pd(111) surface.

7.3.3 Encapsulation of Pd islands supported on anatase

Pd was deposited on the anatase substrate at 300°C. Pd islands were formed on the anatase substrate after the sample was post annealed in UHV at 500°C for 1 hour and 860°C for 1.5 hours. The heights of these Pd islands are 22.81 ± 0.60 nm. Fig. 7.4a shows the formation of Pd islands observed in STM. These Pd islands have flat top surfaces without any particular shapes. Some clusters were found at the edges of the island surfaces. One example of the island heights, measured from the Pd island along the red dashed line in Fig. 7.4a, is 23.22 nm as shown in the height profile in Fig. 7.4c. Two types of moiré patterns were observed in the zoomed-in STM image of the flat island surface (Fig. 7.4b). One moiré pattern is made of bright moiré dots and the other is formed with dark patterns among the dots. The orientation of the moiré dots was measured along the yellow arrow (labelled as "h"). The close-packed direction of the Pd atoms shares the same direction as the edge of the Pd nanocrystal and is pointed by the white arrow (labelled as "Pd") in Fig. 7.4b. The relative rotation between the moiré dots and the Pd layer is ~1.5°.

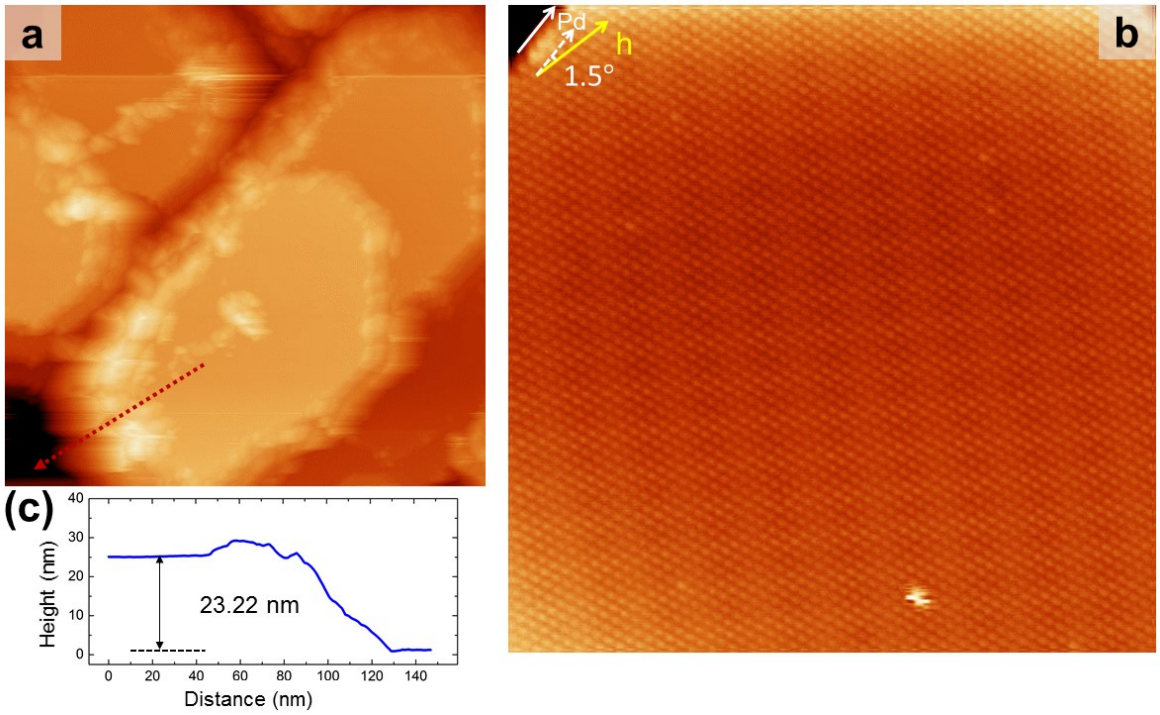


Fig. 7.4 (a) STM image of encapsulated Pd islands supported on anatase after the sample was annealed at 500°C for 1 hour and 850°C for 1.5 hours (image size: 300 × 300 nm^2, imaging conditions: V_s = +2 V, I_t = 0.155 nA). (b) STM image showing the surface with two types of moiré patterns on the encapsulated Pd island (image size: 60 × 60 nm^2, imaging conditions: V_s = +1.97 V, I_t = 0.235 nA). (c) Line profile measured along the direction pointed in Fig. 7.4a shows the height of the Pd island.

A zoomed-in STM image of the moiré dots is shown in Fig. 7.5a. These well-ordered moiré dots form a hexagonal superstructure. The measured separation between neighbouring dots is 10.95±0.45 Å, where the error denotes the standard deviation in the measurements. The hexagonally-arranged moiré dots, with the unit cell highlighted by black rhombus in Fig. 7.5a, present a (4 × 4)*R*1.5° superstructure with respect to the Pd(111) surface.

The Fourier transformed image of Fig. 7.5a is shown in Fig. 7.5b. The FFT image represents the reciprocal space vectors of the structures. Two periodical features are observed in the 2D-FFT image. Six bright spots (marked by blue circles) are of the 6-fold symmetry and four spots (marked by yellow circles) have a 2-fold symmetry. These six spots are relatively further away from the origin in the FFT image, indicating a smaller lattice parameter in the

real space. The 6-fold symmetrical spots also confirm that the moiré dots observed in STM have a hexagonal arrangement. As shown in the inset of Fig. 7.5b, each 6-fold symmetrical spot has the 2-fold symmetrical spots as satellites. The 2-fold symmetrical spots are closer to the centre, which indicates a large periodicity in real space. Compared to the STM images, the 2-fold symmetrical spots are related to the dark pattern among moiré dots with a unit cell size of $(6.98 \pm 0.14) \times (8.81 \pm 0.07)$ nm^2 (highlighted by a yellow rhombus in Fig. 7.5a).

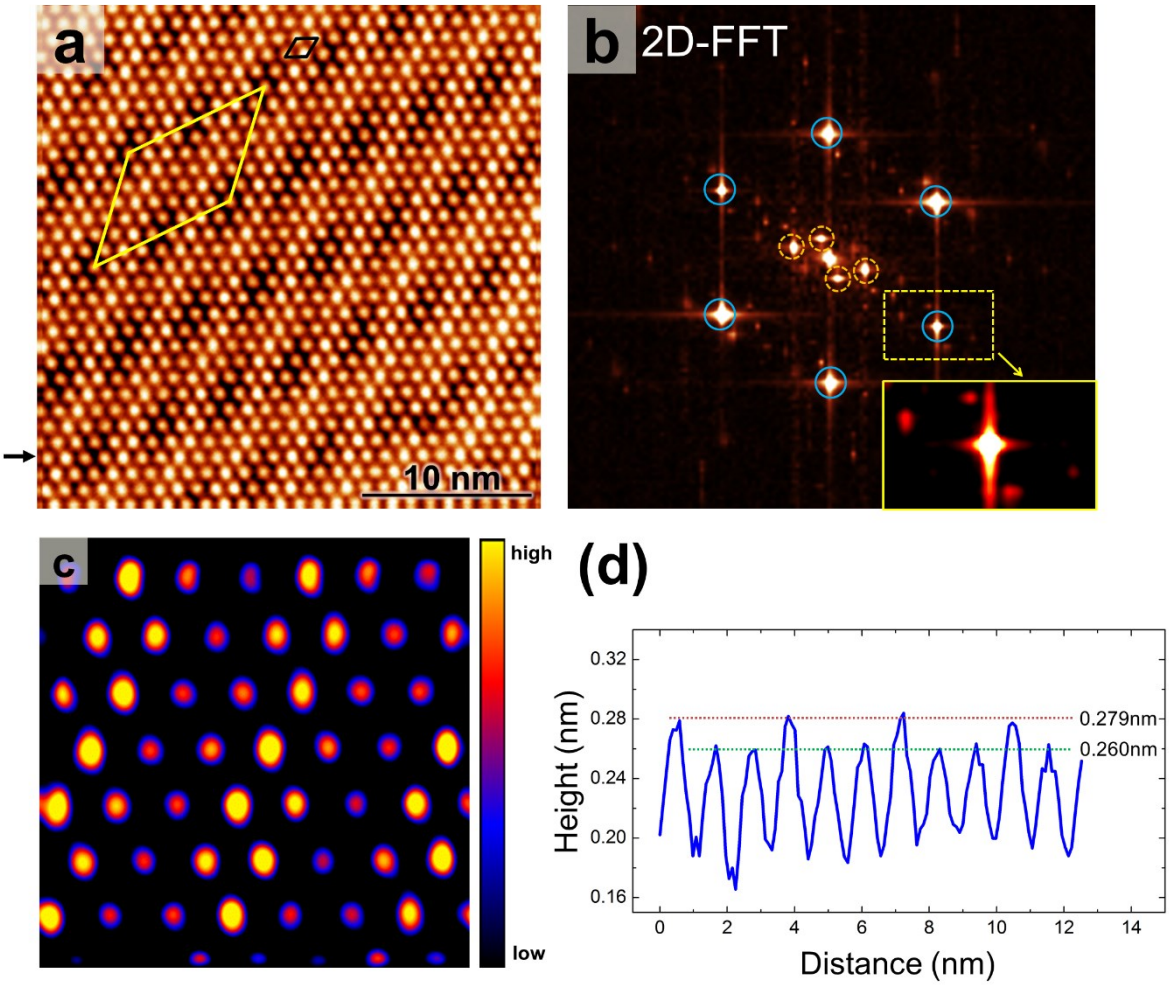


Fig. 7.5 (a) Processed STM image of hexagonal surface structure formed on encapsulated Pd island (imaging conditions: $V_s = +2.135$ V, $I_t = 0.165$ nA). (b) 2D Fast Fourier Transform (FFT) of STM image in Fig. 7.5a. The inset shows the detail of a big bright spot (marked in rectangle) with its satellites. (c) Zoomed-in STM image of the hexagonal surface structure with the colour range adjusted. The colour scale represents the height difference. (d) Line profile measured along the direction pointed by the black arrow in Fig. 7.5a.

Along the horizontal direction in the STM image Fig. 7.5a, every third dot appears brighter. The toucan colour palette was applied on the STM image with a wider range of colours to represent the relative heights of the dots more clearly (Fig. 7.5c). The higher dots are in yellow and the relatively lower dots are in pink. The brighter yellow dots show a zig-zag arrangement in the large-scale hexagonal superstructure. The height profile (Fig. 7.5d) was measured along the direction pointed in Fig. 7.5a. The even brighter moiré dots are approximately 19 pm higher than other bright moiré dots.

When the tip was moved closer to the sample surface by reducing the STM imaging voltage and increasing the tunnelling current, bright lines connecting neighbouring moiré dots were revealed as shown in Fig. 7.6a. The atomically resolved moiré dots in the same region are shown in Fig. 7.6b. The same unit cells are marked by the rhombi in both images. The bright dots in Fig. 7.6b are Ti atoms. Ti atoms appear brighter in empty-state imaging because they have a higher density of states than oxygen atoms. Fig. 7.6c shows a closer view of the arrangement of the surface Ti atoms. When the moiré dots in Fig. 7.6a are compared with the Ti atoms in Fig. 7.6c, it can be seen that each moiré dot is comprised of seven Ti atoms in total. The interpretation of one moiré dot is shown in the inset of Fig. 7.6a. Six Ti atoms are located at the hexagon vertices and one atom locates at the centre. The distance between the moiré dots should be three times the spacing across four Ti atoms. The Ti atoms exhibit a nearly hexagonal structure. Height profile (Fig. 7.6d) measured along the Ti atoms (Fig. 7.6c) shows equal spacing between neighbouring atoms. The spacing between these Ti atoms is 3.66 ± 0.08 Å, in the range of 2.9-3.8 Å which is reported in many literatures [29,30,32,33,353,354]. The orientations of Pd atoms and Ti atom are labelled by white and red arrows respectively (Fig. 7.6b). The relative rotation between these two layers is $\sim 1.5°$.

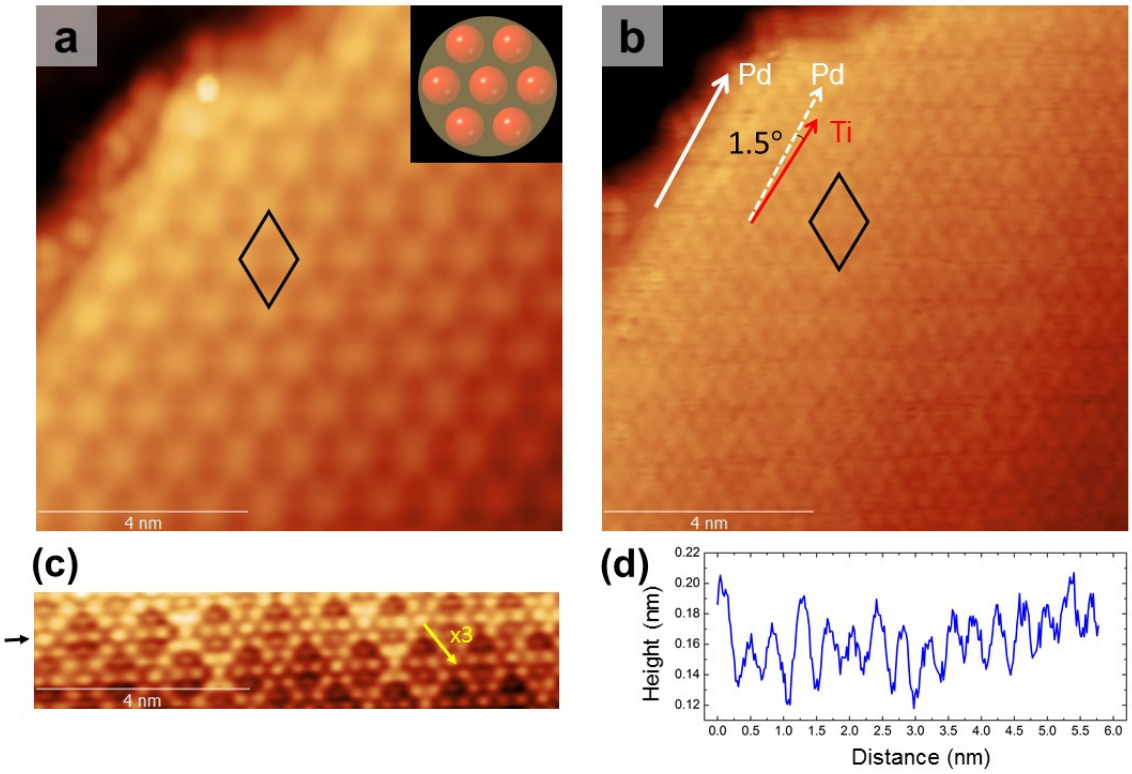


Fig. 7.6 (a) STM image of moiré dots and bright lines connecting the dots (imaging conditions: V_s = +0.453 V, I_t = 0.522 nA). The composition of each moiré dot is interpreted by the image in the inset. The red balls are Ti atoms and the big light yellow circle covering the red balls represents a bright moiré dot whose brightness is attributed to the seven Ti atoms. (b) Atomically resolved moiré dots in Fig. 7.6a (imaging conditions: V_s = +0.664 V, I_t = 0.577 nA). (c) Processed STM image showing the atomically resolved moiré dots (cropped image) (imaging conditions: V_s = +0.479 V, I_t = 0.582 nA). (d) Line profile measured along the atoms in the direction pointed by the black arrow in Fig. 7.6c.

Moiré dots with different brightness were observed, for example the bright moiré dots (marked as "i") and the even brighter moiré dots (marked as "ii") in Fig. 7.7b. The atomically resolved dots with different brightness is shown in Fig. 7.7a. Some Ti atoms appear brighter compared to others under empty state STM imaging. Two levels of brightness are highlighted by "i" and "ii" in Fig. 7.7a. The zoomed-in images of these two configurations are shown in Fig. 7.7a(i) and (ii) with the schematic structures next to them. Both yellow and red balls represent the bright Ti atoms in atomically resolved STM image, where the even brighter Ti atoms are in yellow. Specifically, Fig. 7.7a(i) shows only one central Ti atom being brighter and Fig. 7.7a(ii) shows the bottom three Ti atoms being

brighter. The moiré dots with a normal brightness (labelled as "i" in Fig. 7.7b and Fig. 7.7c) contain only one brighter Ti located at the centre. The moiré dots consisting of three brighter Ti atoms correspond to those which are even brighter observed in STM with an example labelled as "ii" in Fig. 7.7b and Fig. 7.7c.

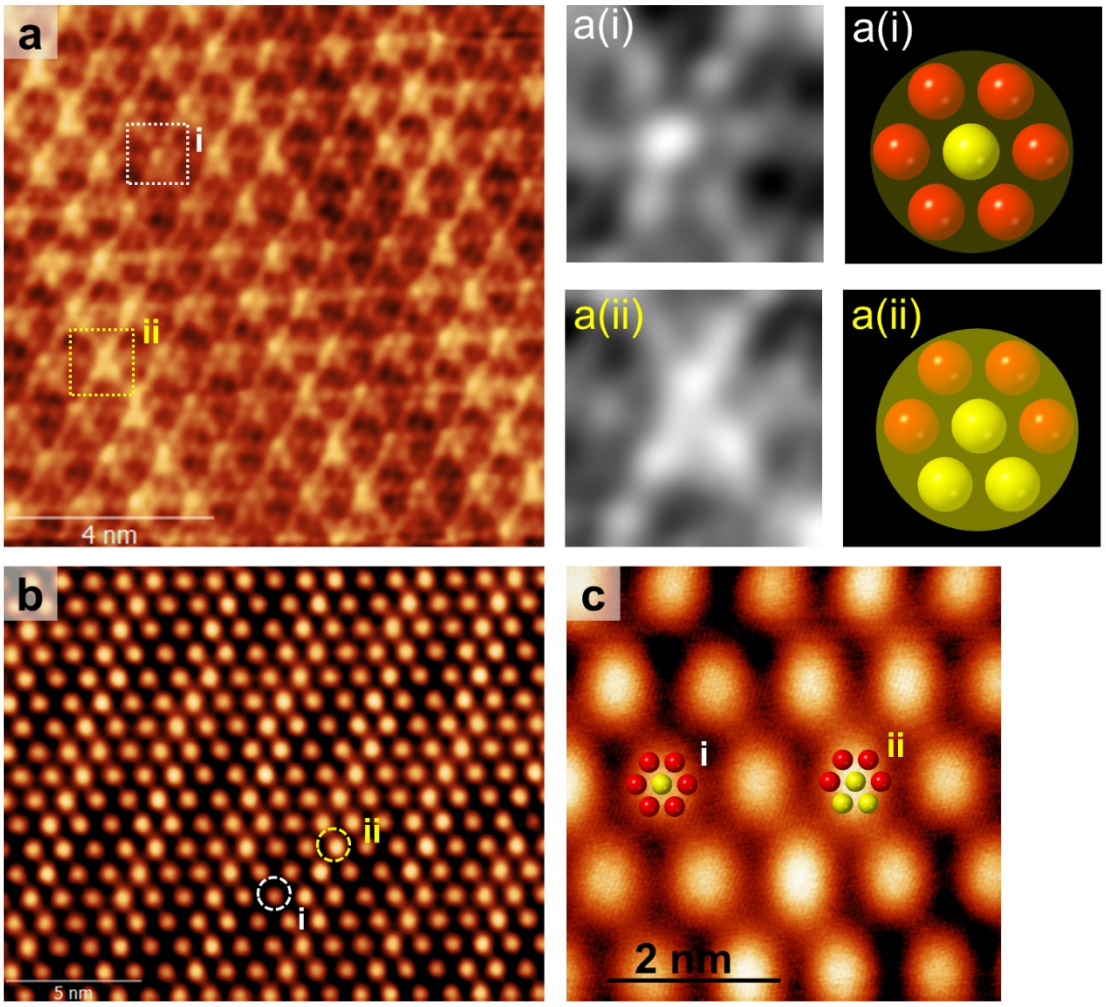


Fig. 7.7 (a) Processed STM image showing the atomically resolved moiré dots with different brightness. Two configurations were observed as labelled by "i" and "ii" in Fig. 7.7a, one with one brighter central Ti atom, and the other with three brighter Ti atoms at the bottom. The zoomed-in images of the marked regions are shown to the right of Fig. 7.7a, to show the two configurations in more detail. Both yellow and red balls represent bright Ti atoms in STM image, where the even brighter one is indicated by the yellow balls. (b) Processed STM image showing the moiré dots with different brightness. One example of a bright moiré dot and an even brighter moiré dot are labelled as "i" and "ii" respectively. (c) Schematic compositions of moiré dots i and ii.

7.4 Discussion

7.4.1 Stacking sequence of encapsulated layer on Pd(111)

Encapsulation of noble metals (abbrev. NM) on titanium oxide substrate has been observed after high-temperature treatments [29-36]. Several studies showed that the encapsulated layer has the composition of TiO_x ($0 < x < 1.4$) [29-33]. The stacking sequence of the TiO_x layer formed on the noble metal surface was debated among the researchers. It is generally found in two types: O-Ti-NM [34,35,64,355-358] or Ti-O-NM [32,33], from the topmost layer to the innermost layer.

The O-Ti-NM stacking sequence is the most reasonable one to interpret the atomic model of encapsulated TiO_x layer on the Pd(111) surface. The evidence to support this is: 1) The relative heat of formation for the oxide ($-\Delta H_f$) of Ti (500-550 kJ/mol) is higher than that of Pd (50-100 kJ/mol). This means that Ti is more active than Pd to form more stable oxides [64]; 2) the relative bond energy of O-Ti (672.4 ± 9.2 kJ/mol) is higher than that of O-Pd (380.7 ± 83.7 kJ/mol). O is preferentially associated with Ti because the Ti-O bond is more stable than the Pd-O bond [358]. Thus, the affinity of Ti to oxygen is higher than to Pd; 3) O desorbs more easily from Pd than from Ti. Significant O desorption from Pd occurs at $\sim$700K and it only happens on TiO_2 at temperature above 800K. It is likely for O to adsorb onto Ti at higher annealing temperatures [34,355]; 4) the signal values in EPR (Electron Spin Resonance) spectra less than 2 are assigned to Ti^{3+}. The EPR study of Pd on rutile and anatase showed a characteristic Ti^{3+} peak which is generated by the Ti^{3+} ion located at the contact with the Pd surface. It also shows that SMSI occurs at the contact between Ti^{3+} and the Pd substrate [35].

Only few studies reported a Ti-O-NM stacking sequence, and the atomic models built are not sufficiently strongly supported. The atomic model built by Bennett *et al*. [33] shows the Ti terminated layer with a Ti-O-Pd sequence. In this model Ti is exposed to the vacuum because the electrons are expected to tunnel between the tip and Ti atoms. This stacking sequence is not convincing because the contrast in STM images is influenced by both electronic and topographic effects. For example, the dominant electronic effect makes Ti atoms (with a high electronic density of state) appear brighter under empty state STM imaging even though Ti atoms locate topographically lower than the surrounding O atoms [56]. The model reported by Silly *et al*. was described as an O layer sandwiched between Ti and Pd layers without more detailed explanations to support this structure [32].

Therefore, with the stronger evidence from literature, the atomic models of the O-Ti-Pd stacking sequence is applied to interpret the superstructures observed in our study.

7.4.2 Atomic models of the superstructures and moiré patterns

1) Mathematical calculations

After the samples were annealed at above 600°C, the Pd-dilines and Pd-anatase systems enter the strong metal-support interaction (SMSI) state, characterised by the encapsulation of Pd nanocrystals and islands with a TiO_x layer. These structures are attributed to the moiré patterns which are formed by the superposition of the Pd(111) layer (a = 2.75 Å) and the Ti adlayer.

An algebraic approach suggested by Silly *et al*. [32] is applied to calculate the coincidence between Pd and Ti lattices. The coincidence of the two superposed lattices is determined by the following equation [359]:

$$\begin{pmatrix} s & \frac{1}{2}s \\ 0 & \frac{\sqrt{3}}{2}s \end{pmatrix}\begin{pmatrix} h \\ k \end{pmatrix} = \begin{pmatrix} cos\theta & -sin\theta \\ sin\theta & cos\theta \end{pmatrix}\begin{pmatrix} a & \frac{1}{2}a \\ 0 & \frac{\sqrt{3}}{2}a \end{pmatrix}\begin{pmatrix} m \\ n \end{pmatrix} \quad (7.1)$$

The solutions for Eq. 7.1 are [32]:

$$\theta = arctan\left(\frac{\sqrt{3}(km-hn)}{2hm+hn+km+2kn}\right) \quad (7.2)$$

$$a = s\sqrt{\frac{h^2+hk+k^2}{m^2+mn+n^2}} \quad (7.3)$$

where s is the interatomic distance in the substrate layer,

a is the interatomic distance in adlayer,

θ is the rotational angle between the substrate and the adlayer,

h, k and m, n are integral multiples of the substrate and adlayer interatomic distances which lead to the coincidence between two lattices.

The moiré periodicity (r) and the relative rotational angle between the moiré pattern and the substrate (ϕ) are suggested by Silly *et al*. [32]:

$$r = \frac{s}{2}\sqrt{(2h+k)^2+3k^2} \quad (7.4)$$

$$\phi = arctan\left(\frac{\sqrt{3}k}{2h+k}\right) \quad (7.5)$$

where s is the interatomic distance in the substrate layer,

r is the periodicity of moiré pattern,

ϕ is the rotational angle between the moiré pattern and the substrate,

h and k are integral multiples of the substrate and the adlayer interatomic distances which lead to the coincidence between two lattices.

The purpose of using the calculation above is to solve for a, θ, r and ϕ, which should be as close to the experimental values measured in STM images as possible. This is achieved by

altering the integer numbers h, k, m and n in Eq. 7.2-7.5. The solutions which lead to reasonable calculated values of a, θ, r and ϕ are summarised in Tab. 7.2.

Tab. 7.2 Summary of parameters in experimental measurements and calculations on superstructures.

	Pd nc. on diline				**Pd nc. on anatase**		**Pd isl. on anatase**	
Structures	Hexagonal		Wagon wheel		Wagon wheel		Hexagonal	
	Meas.	Calc.	Meas.	Calc.	Meas.	Calc.	Meas.	Calc.
h,k,m,n	-	33,1,25,0	-	7,0,6,0	-	7,0,6,0	-	33,1,25,0
Ti periodicity (*a*)		3.69	-	3.21	-	3.21	3.66±0.08	3.69
Pd periodicity (*s*)	-	2.75	-	2.75	-	2.75	2.75	2.75
Moiré periodicity (*r*)	10.95±0.45	92.16	19.36±0.63	19.25	18.70±0.80	19.25	89.11±1.74	92.16
Moiré rotation (ϕ)	1.5°	1.5°	0°	0°	0°	0°	1.5°	1.5°
Ti to Pd rotation (θ)	-	1.5°	0°	0°	0°	0°	1.5°	1.5°
Moiré dots spacing*	10.95±0.45	11.06	19.36±0.63	19.26	18.70±0.80	19.26	11.01±0.40	11.06

Note:

1) The unit for periodicity is angstrom (Å), and the unit for rotation is degree (°).
2) "Meas." means data from STM measurements, and "cals." means data from calculations.
3) "*": The spacing between bright spots is measured from STM images and the atomic models

2) Atomic models of the wagon wheel and hexagonal superstructures

Atomic models of each superstructure were built using the parameters from calculations in Tab. 7.2. Specifically, a layer of hexagonal Pd(111) with a lattice constant of 2.75 Å is used as the substrate. A layer of Ti atoms with the calculated periodicity is placed on the top of the Pd(111) layer. The rotation between the Ti and Pd layers is applied according to the parameter θ from the calculations. The atomic models of the superstructures are shown in Fig. 7.8, Fig. 7.9, Fig. 7.13 and Fig. 7.15. The Pd atoms are in blue and the Ti atoms are in

red. Superposition of the Ti and Pd layers with different lattice constants results in the formation of moiré patterns corresponding to the wagon wheel and hexagonal superstructures observed in STM. After building the atomic models, the model images are then blurred to identify the unit cells of these moiré dots. As the electronic effects are neglected, these blurred images are simple illustrations only rather than the simulation of the STM images.

Wagon wheel superstructure

The wagon wheel superstructure has a hexagonal superstructure and it emerged when the sample was annealed at 600°C. The Pd nanocrystals become fully covered with the wagon wheel superstructure after the sample was annealed at 650°C. Fig. 7.8a shows the STM image of the wagon wheel structure formed at 650°C. The periodicity of moiré pattern measured from the STM images is 19.36±0.63 Å. A similar wagon wheel superstructure formed on anatase-supported Pd nanocrystals upon anneals at 600°C (Fig. 7.9a). The periodicity measured from STM images is 18.70±0.80 Å.

The indices $h = 7$, $k = 0$, $m = 6$, $n = 0$, $s = 2.75$ Å, $\theta = 0°$ and $a = 3.21$ Å were applied to reproduce the moiré pattern with these features on Pd nanocrystals supported on dilines and anatase. The calculation gives a periodicity of 19.25 Å for the moiré pattern, which matches the STM observation (19.36±0.63 Å and 18.70±0.80 Å). Fig. 7.8b and Fig. 7.9b are the atomic models of the wagon wheel superstructure in Fig. 7.8a and Fig. 7.9a, respectively. In each atomic model, a hexagonal adlayer of Ti atoms ($a = 3.21$ Å) is placed on the Pd(111) layer ($s = 2.75$ Å). There is no rotation between the Ti adlayer and the Pd substrate. A group of Ti atoms located near the top of the Pd nanocrystals contribute to the bright moiré dots in the wagon wheel structure. Other Ti atoms located near the 2-fold bridging sites between

Pd atoms form the bright connecting lines between neighbouring bright moiré dots. Because of the small height difference (~28.6 pm) of Ti atoms located between the bridging site and on top of Pd atoms, the bridging site Ti atoms can only be detected when the tip is moved closer to the sample. The distance between the sample and tip is linked to tunnelling current by an inverse exponential relationship and is proportional to the voltage. This is the reason why the bright lines are only revealed as imaging conditions are changed to a higher current or a lower voltage (Fig. 7.1c). The spacing between bright moiré dots measured in the atomic models (bc in Fig. 7.8 and Fig. 7.9) is 19.26 Å, which is close to the value measured from the STM image (19.36±0.63 Å and 18.70±0.80 Å). The unit cells of the moiré dots are highlighted by the rhombi. A similar wagon wheel structure was observed by Silly *et al.* [32] when Pd nanocrystals were grown on nanolines. Our model built to interpret the wagon wheel structure is consistent with his model [32].

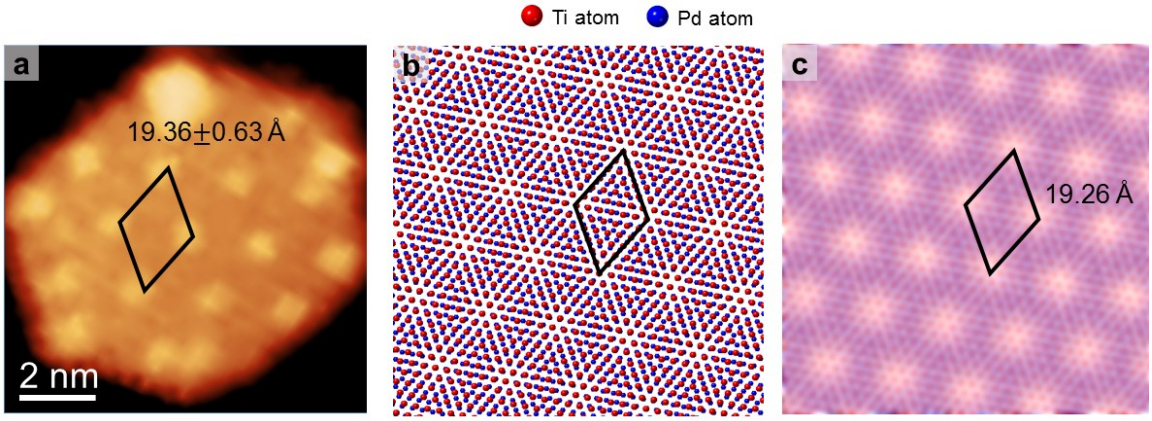


Fig. 7.8 (a) STM image of the wagon wheel superstructure formed by encapsulated Pd nanocrystals on the diline substrate. (b) Model of the wagon wheel superstructure. A hexagonally arranged adlayer of Ti atoms (a = 3.21 Å) is placed on the Pd(111) layer (s = 2.75 Å) with no rotation between the two layers. Ti atoms are red and Pd atoms are blue. (c) Schematic illustration of the STM observation. The image is obtained by blurring Fig. 7.8b to show the position of moiré dots. The unit cells in both the STM image and the model are highlighted.

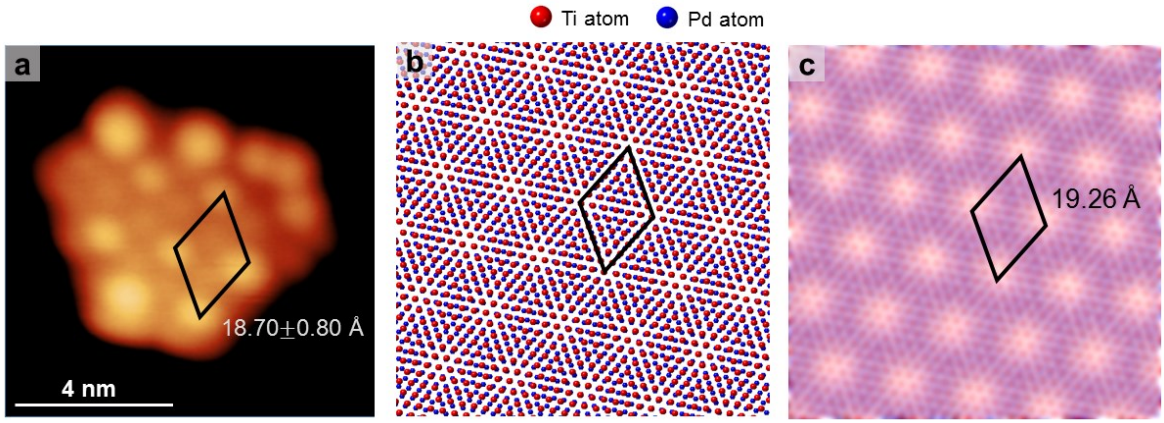


Fig. 7.9 (a) STM image of the wagon wheel superstructure formed by encapsulated Pd nanocrystals on the anatase substrate. (b) Model of wagon wheel superstructure. A hexagonally arranged adlayer of Ti atoms (a = 3.21 Å) is placed on the Pd(111) layer (s = 2.75 Å) with no rotation between the two layers. Ti atoms are red and Pd atoms are blue. (c) Schematic illustration of the STM observation. The image is obtained by Fig. 7.9b to show the position of moiré dots. The unit cells in both the STM image and the model are highlighted.

Hexagonal superstructure

Pd islands were largely covered by moiré patterns after the sample was annealed at 860°C. The dimension of the hexagonal unit cell formed on anatase is 11.01±0.4 Å. In the atomically resolved STM image, the Ti atom spacing is 3.66±0.08 Å (Fig. 7.6).

The calculation equations in Sec. 7.3.2 apply when Ti atoms are hexagonally packed in the adlayer. However, the 2-fold symmetrical dark pattern observed in STM (Fig. 7.5a) indicates that these Ti unit cells in the adlayer are not perfectly hexagon but slightly compressed in one direction. In order to obtain a suitable atomic model for the hexagonal superstructure, we use the indices h = 33, k = 1, m = 25, n = 0 and s = 2.75 Å to obtain the lattice constant of the Ti hexagonal structure that is close enough to the measured value from STM images (3.66±0.08 Å). The parameters for calculations are a = 3.69 Å, θ = 1.5°, ϕ = 1.5° and r = 92.16 Å. The compression is then applied in the Ti unit cell by varying the angle α which affects the distance d shown in Fig. 7.10. A compressed Ti hexagonal

adlayer (a = 3.69 Å and variable α, $\alpha \in [60°, 70°]$) is placed on top of the Pd(111) layer (s = 2.75 Å) with a relative rotation of 1.5°. A series of atomic models with different α values were built and then blurred to interpret the STM observation. Fig. 7.11 summaries a series of blurred atomic model images by varying the angle α from 60° to 70° with increments of 1°, where α = 60° represents the hexagonal Ti unit cell. The bright spots in the blurred images are related to the moiré dots observed in STM. A clear dark pattern is observed in the images where α = 60° and α = 61° (Fig. 7.11). Next, the angle α was further narrowed between α = 60° and α = 61° with increments of 0.1° (Fig. 7.12). From the series of blurred images shown in Fig. 7.12, only the image with α = 60.3° shows a clear and well-ordered dark pattern. The model in which α = 60.3° is therefore used for further analysis.

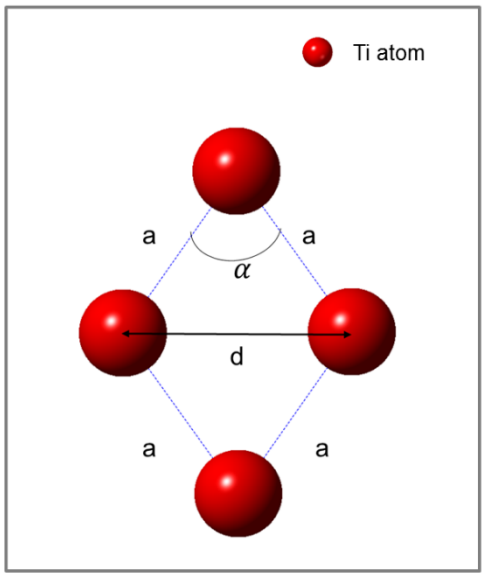


Fig. 7.10 Schematic diagram showing the parameters in a typical Ti unit cell used in the model.

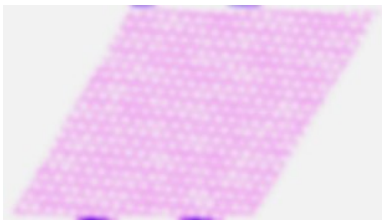
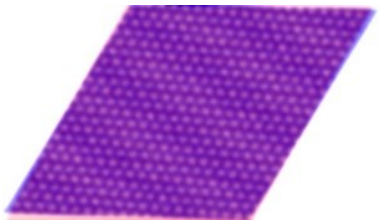
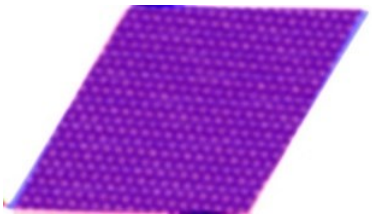
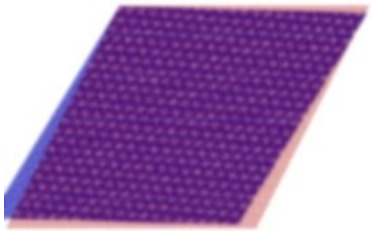
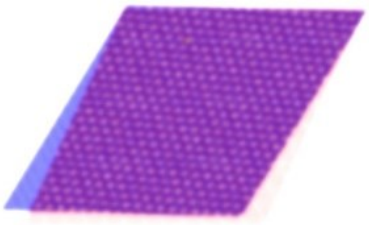
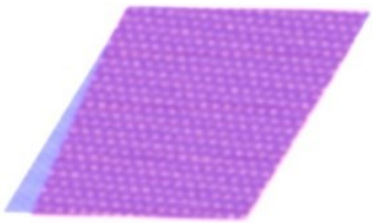
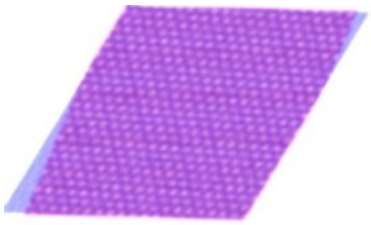
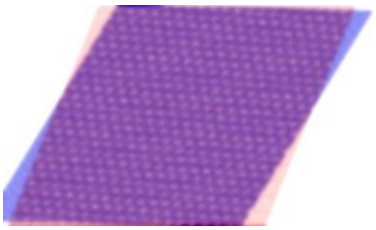
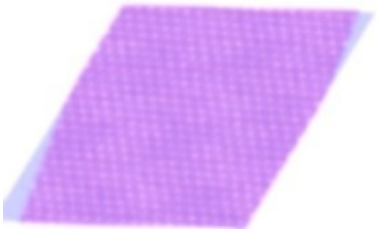
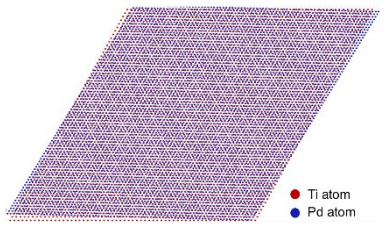
α=60°	α=61°	α=62°
		
α=63°	**α=64°**	**α=65°**
		
α=66°	**α=67°**	**α=68°**
		
α=69°	**α=70°**	**Example: atomic model (α=61°)**
		

Fig. 7.11 Blurred atomic models with the angle α varying between 60°-70° with increments of 1°.

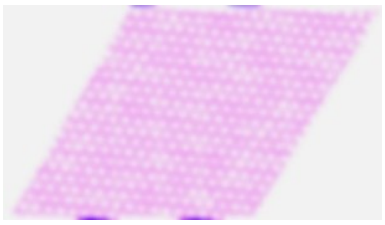
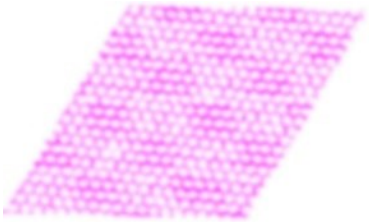
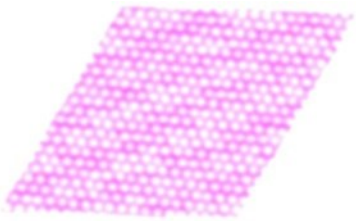
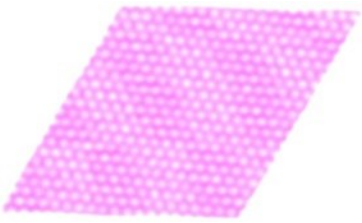
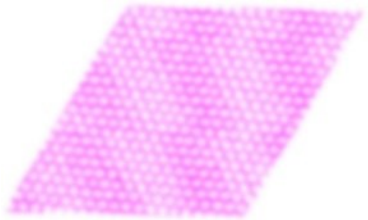
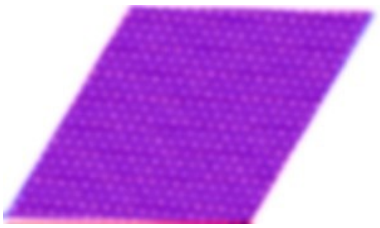
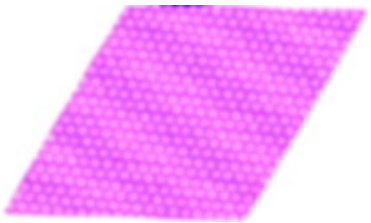
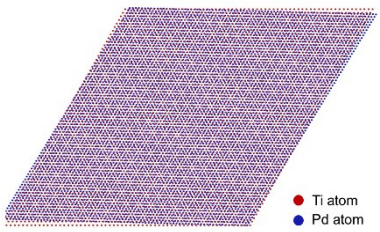
α=60.0°	α=60.1°	α=60.2°
		
α=60.3°	**α=60.4°**	**α=60.5°**
		
α=60.6°	**α=60.7°**	**α=60.8°**
		
α=60.9°	**α=61.0°**	**Example: atomic model (α=60.3°)**
		

Fig. 7.12 Blurred atomic models with the angle α varying between 60°-61° with increments of 0.1°.

Fig. 7.13 shows the comparison of the STM image and the atomic model with $\alpha = 60.3°$. A layer of compressed hexagonal Ti structure (a = 3.69 Å and $\alpha = 60.3°$) is placed on the hexagonal Pd(111) layer (s = 2.75 Å) with a rotation of 1.5° between the two layers. The atomic model is blurred to resemble the moiré dots observed in STM. The unit cell of the moiré dots is highlighted. The spacing between bright spots measured from the model is 11.06 Å, which is consistent with STM measurement (11.01±0.40 Å). Besides, the dark pattern observed in the STM image (Fig. 7.13a) can be reproduced in this atomic model (see blurred image in Fig. 7.13c). The size of the dark pattern unit cell is 6.91 × 8.64 nm^2 which are close to the experimentally measured values from STM images, (6.98±0.14) × (8.81±0.07) nm^2.

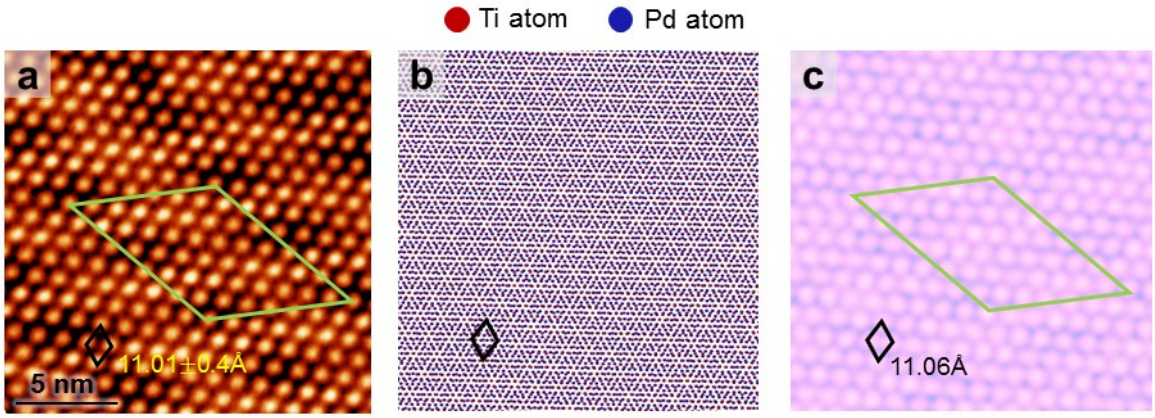


Fig. 7.13 (a) STM image of the hexagonal superstructure with a dark pattern. (b) Large-scale atomic model of the hexagonal superstructure. A layer of compressed hexagonal Ti structure (a = 3.69 Å and $\alpha = 60.3°$) is placed on the Pd(111) substrate (s = 2.75 Å) with a rotation of 1.5° between the two layers.(c) Blurred atomic model to resemble the moiré dots and the well-ordered dark pattern observed in STM.

From the STM image of the atomically resolved moiré dots (Fig. 7.6c), we find that Ti atoms have different brightness. This is due to the different topographical positions of Ti atoms located on the Pd atoms. Fig. 7.14a is a typical unit cell in the Ti adlayer with the atomic model in Fig. 7.14b. Three positions are generally found in this model, which are

the on-top site, the bridging site and the 3-fold hollow site of Pd atoms. They are marked by "1", "2" and "3" next to Ti atoms respectively. The relative positions of Ti atoms in the model shown in the Fig. 7.14b are linked to the corresponding positions in STM image (Fig. 7.14a). Ti atoms located at the top of Pd atoms (position 1) are brighter than other Ti atoms shown in Fig. 7.14a. The brightness for Ti atoms located at the Pd bridging site (position 2) are slightly reduced. The bridging site Ti atoms are observed as the bright lines connecting the moiré dots in the STM image (Fig. 7.6a). Ti atoms located at the 3-fold hollow site (position 3) of Pd atoms are faint under empty-state STM imaging.

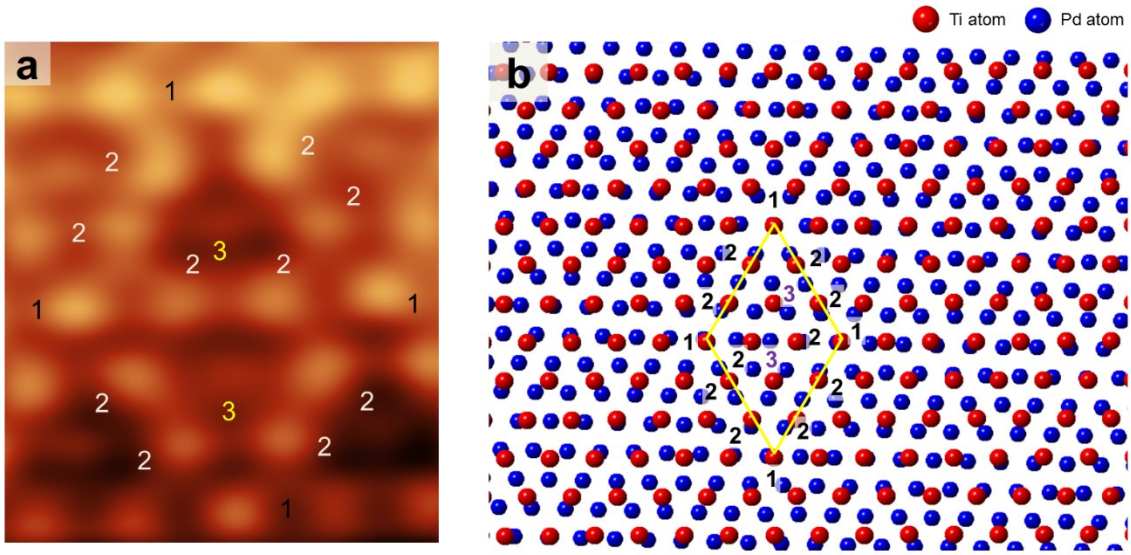


Fig. 7.14 (a) STM image of a typical Ti unit cell. The numbers labelled next to the Ti atoms are the positions of the Ti atoms relative to the Pd atoms. "1" means Ti is on top of Pd; "2" means Ti is at the bridging site of Pd; "3" means Ti is at the 3-fold hollow site of Pd. (b) Atomic model of the hexagonal superstructure and corresponding Ti positions in Fig. 7.14a. A layer of compressed hexagonal Ti structure (a = 3.69 Å and α = 60.3°) is placed on the Pd(111) layer (s = 2.75 Å) with a rotation of 1.5° between the Ti and Pd layers.

The hexagonal superstructure observed on Pd nanocrystals has a periodicity of 10.95 ± 0.45 Å with a rotation of 1.5° to the Pd substrate layer (Fig. 7.15a). The moiré pattern with these features can be reproduced using the same indices as the one which

produced the hexagonal superstructure formed on Pd-anatase islands, where $h = 33$, $k = 1$, $m = 25$, $n = 0$ and $s = 2.75$ Å, $a = 3.69$ Å, $\theta = 1.5°$, $\phi = 1.5°$ and $\alpha = 60.3°$. Fig. 7.15b shows the atomic model of the hexagonal superstructure in Fig. 7.15a. Fig. 7.15c is the blurred image of Fig. 7.15b to resemble the STM observation. The periodicity of the moiré dots in atomic model is 11.06 Å, which matches the STM observation of 10.95±0.45 Å.

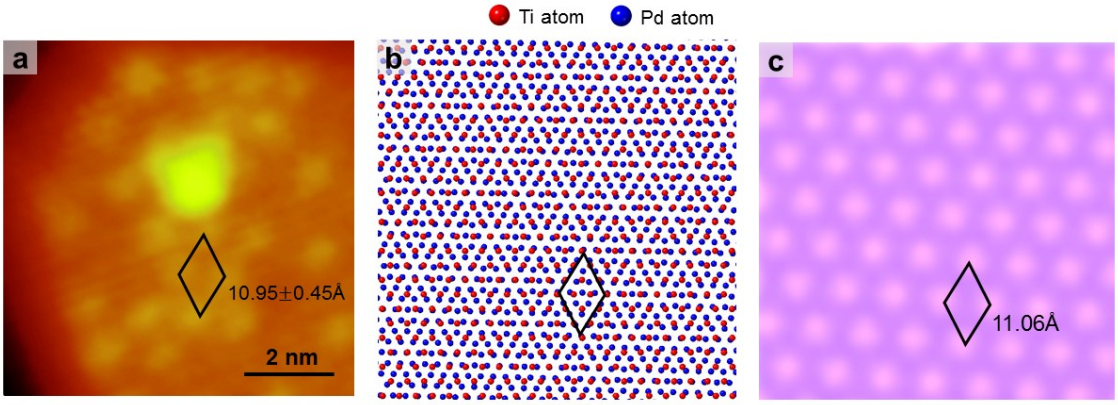


Fig. 7.15 (a) STM image of the hexagonal superstructure formed on encapsulated Pd nanocrystal supported on dilines. (b) Atomic model of the hexagonal superstructure. A layer of compressed hexagonal Ti structure ($a = 3.69$ Å and $\alpha = 60.3°$) is placed on the Pd(111) substrate ($s = 2.75$ Å) with rotation of 1.5° between the two layers. Ti atoms are red and Pd atoms are blue. (c) Schematic illustration of the STM observation. The image is obtained by blurring Fig. 7.15b to show the position of moiré dots. The unit cells in both the STM image and the model are highlighted.

A similar hexagonal superstructure was observed by Silly *et al*. [32] when Pd nanocrystals were grown on mixed nanolines. The periodicity of the hexagonal superstructure was reported to be 10.5±0.2 Å. However, it seems that the atomic model does not perfectly match this structure. The spacing between bright moiré dots measured from their model is 8.65 Å, which is significantly less than the experimental value. In our case, Pd nanocrystals were grown on the diline surface. Dilines are one type of the nanolines formed on the $SrTiO_3$(001) surface which should be the same system as the one used by Silly *et al* [32]. The spacing between bright dots in our atomic model is 11.06 Å, which is much closer to

our STM observation (periodicity 10.95±0.45 Å). Therefore, our model better interprets the hexagonal superstructure formed on encapsulated Pd nanocrystals supported on dilines.

In general, Ti atoms which sit on top of Pd atoms or at the bridging sites of the Pd(111) layer are topographically higher than those sit at the 3-fold hollow sites. Because STM is topographically-sensitive, those Ti atoms which sit topographically higher should appear brighter in STM images. For those Ti atoms located at the 3-fold hollow sites of Pd atoms are relatively lower than the other two types, appearing fainter under STM (Fig. 7.14). As we observed from STM images, the moiré dots in these superstructures have different levels of brightness. The number of brighter constituent Ti atoms could influence the overall brightness of the moiré dots. According to the atomically-resolved moiré dot image (Fig. 7.7), the bright moiré dots (example as dot "i") have only one brighter Ti atom at the topographically higher position. The even brighter moiré dots (example as dot "ii") are those containing three brighter Ti atoms located at topographically higher positions.

It is claimed in some studies that the bright moiré dots originate from those Ti atoms which sit directly atop of the underlying atoms [32]. However, our atomically-resolved image shows that the brightness of the moiré dots is an overall effect of the brightness attributed to the number of brighter Ti atoms. Our results may broaden the understanding of the origin of the moiré pattern (e.g., moiré dots) formed on the encapsulated noble metals supported on oxides in the SMSI state.

7.5 Conclusion

In this study, we prepared the hexagonal (4 × 4)*R*1.5° and the wagon wheel (7 × 7) superstructures on top of encapsulated Pd nanocrystal surfaces. They were formed by high-temperature treatments above 600°C, which brings the diline- and anatase-supported Pd nanocrystals into the SMSI state. The system under the SMSI state is characterised by the encapsulation of Pd with a thin oxide layer. Atomic models were built to explain the formation of the moiré patterns of the hexagonal and the wagon wheel superstructure, which are attributed to the superposition of the Pd(111) layer (s = 2.75 Å) and the Ti adlayer. The atomically resolved moiré dots were obtained in STM, showing each moiré dot is comprised of seven Ti atoms. The moiré dots have two atomic configurations which lead to the different levels of the overall brightness. The bright moiré dots (e.g., dot "i") have only one brighter Ti atom located at the centre. The even brighter moiré dots (e.g., dot "ii") are those which contain three brighter Ti atoms. The brightness of the Ti atoms is related to their relative positions on the Pd atoms, where topographically higher positions yield the brighter Ti atoms in STM.

Chapter 8

Growth of MoS_2 on $SrTiO_3$ Substrates

8.1 Introduction

MoS_2 is one of the typical layered transition metal dichalcogenides (TMDs) and its monolayer has obtained great attention. Monolayer MoS_2 is a direct-bandgap semiconductor with a bandgap energy of 1.8 eV [298]. It exhibits strong adsorption in the solar spectrum region, enhanced PL quantum yield after indirect-to-direct band transition [298], large in-plane carrier mobility [299] and high current on/off ratios [285,291,300]. All these properties enable 2D MoS_2 to be fabricated for optical and optoelectronics devices [285,291,295,360]. Several materials have been used as the substrates to grow monolayer MoS_2. They are SiO_2/Si [298,308-314,330,332], sapphire [308,333,334], *h*-BN [61,335], Au [323,335-337], mica [335,338], graphite [335,339], graphene [340], $SrTiO_3$ [341-343] and $LaAlO_3$ [341,344]. Due to the amorphous nature and relatively high surface roughness of the substrates such as SiO_2/Si, 2D MoS_2 crystals grown on them are randomly oriented and their electrical and mechanical properties are usually deteriorated. This is due to the formation of a large number of grain boundaries, which are suggested to be detrimental to the electrical [361,362] and mechanical [363,364] properties of the 2D materials.

Growth of MoS_2 via van der Waals epitaxy on single crystal substrates with atomically smooth surfaces is a feasible method to control the crystal orientation and uniformity to

form a large-area single crystalline monolayer [333,334]. This enables the production of high-quality monolayer MoS_2 crystals with controlled shapes and electrical and mechanical properties with great potential in the next generation of nanoelectronics and optoelectronic applications [338].

In this chapter, we report the epitaxial growth of monolayer MoS_2 crystals on $SrTiO_3$(111) and (001) substrates. The morphology of MoS_2 crystals was studied by SEM and STM. The orientations of MoS_2 crystals grown both on (111) and (001) substrates were examined. PL spectroscopy was also conducted to compare the as-grown and annealed MoS_2 crystals on both substrates. The substrate-introduced-strains in MoS_2 crystals on both (111) and (001) surfaces were studied by PL and Raman. The influence of different substrate lattice symmetries on the morphologies of MoS_2 crystals are discussed.

8.2 Experimental Methods

$SrTiO_3$ single crystal doped with 0.5wt% Nb and terminated with epi-polished (111) and (001) surfaces were used in this experiment. $SrTiO_3$(111) samples were prepared to terminate with (4 × 4) and (3 × 3) reconstructions. These surface reconstructions were produced by Ar^+ ions sputtering at 0.5 keV for 8 minutes followed by an anneal at 1050°C for 3 hours in 4.5×10^{-4} Pa of O_2. The $SrTiO_3$(001) sample was sputtered for 10 minutes at 0.5 keV and then annealed in UHV at 1100°C for 1 hour, to produced the *c*(4 × 2) reconstructed surface.

Both reconstructed $SrTiO_3$(111) and $SrTiO_3$(001) samples were taken out of UHV and sent to the Nanostructured Materials Group, Oxford for the growth of MoS_2 crystals. The atmosphere pressure chemical vapour deposition (APCVD) method was applied to grow

monolayer MoS_2 crystals on the $SrTiO_3$ substrates. The details of the set-up of the apparatus are described in Ref. [313]. Molybdenum trioxide (MoO_3) powder (≥ 99.5%, Sigma-Aldrich) and sulphur (S) powder (≥ 99.5%, Sigma-Aldrich) were used as precursors. 300 mg S and 20 mg MoO_3 were loaded in two separate ceramic boats. S was placed upstream of the tube. The $SrTiO_3$ sample was placed downstream with respect to the precursors. 500 sccm argon was firstly flushed through the CVD system to drive off the oxygen. Then, S vapour was pre-introduced at 190°C for 15 minutes under a flow rate of 150 sccm with Ar gas. Pre-introducing the CVD system with sufficient S led to the growth of MoS_2 crystals with S terminations. Next, the MoO_3 precursor was heated to 300°C and it reacted with S. The MoS_2 was grown on $SrTiO_3$ at a substrate temperature of 782°C. The reaction lasted for 30 minutes followed by rapid cooling. The argon flow rate during the reaction was kept at the 100 sccm.

STM (JSPM-4500S) and SEM (Hitachi-4300) were carried out to inspect the sample surfaces. In SEM an accelerating voltage of 3.0 kV was used. PL and Raman measurements were obtained using a confocal Raman microscope (JY Horiba LabRAM ARAMIS). The excitation wavelength and laser power are 532 nm and 12.5 mW, respectively. The laser spot size is ~1 μm and the acquisition time is 5 s. SEM, PL and Raman were performed by Wenshuo Xu from the Nanostructured Materials Group, Oxford. The results of her measurements are also included in this chapter because they are critical to the development of a full understanding of the MoS_2 on $SrTiO_3$ system.

8.3 Results

8.3.1 MoS_2 on $SrTiO_3$(111) substrate

The first substrate we used was $SrTiO_3$(111). The surface was reconstructed to (4 × 4) and (3 × 3) after the sample was sputtered by Ar^+ ions and annealed in oxygen. Fig. 8.1a shows a large area of the atomically-smooth reconstructed $SrTiO_3$(111) surface. Two types of surface reconstructions, (3 × 3) and (4 × 4) were formed and labelled as region α and β respectively. Most regions of sample were covered with the (4 × 4) reconstruction with small amounts of the (3 × 3) reconstruction observed close to step edges. The height profile, measured across the terraces along the arrow in Fig. 8.1a, shows step heights of 0.24±0.01 nm, corresponding to the (111) interplanar spacing of the $SrTiO_3$ unit cell (Fig. 8.1d). A close-up image of the (3 × 3) reconstruction is shown in Fig. 8.1b with a unit cell highlighted by a black rhombus. The lattice parameter measured in this image is 1.70±0.03 nm, consistent with that of the (3 × 3) reconstruction. The (3 × 3) reconstruction has big bright dots comprised of three smaller ones and the large spots are connected by bridging dots. Fig. 8.1c shows a close-up image of the (4 × 4) reconstruction with a unit cell highlighted. The lattice parameter measured from the image is 2.26±0.04 nm which is consistent with that of the (4 × 4) reconstruction. The (4 × 4) reconstruction is comprised of a network of big bright dots surrounded by three dots.

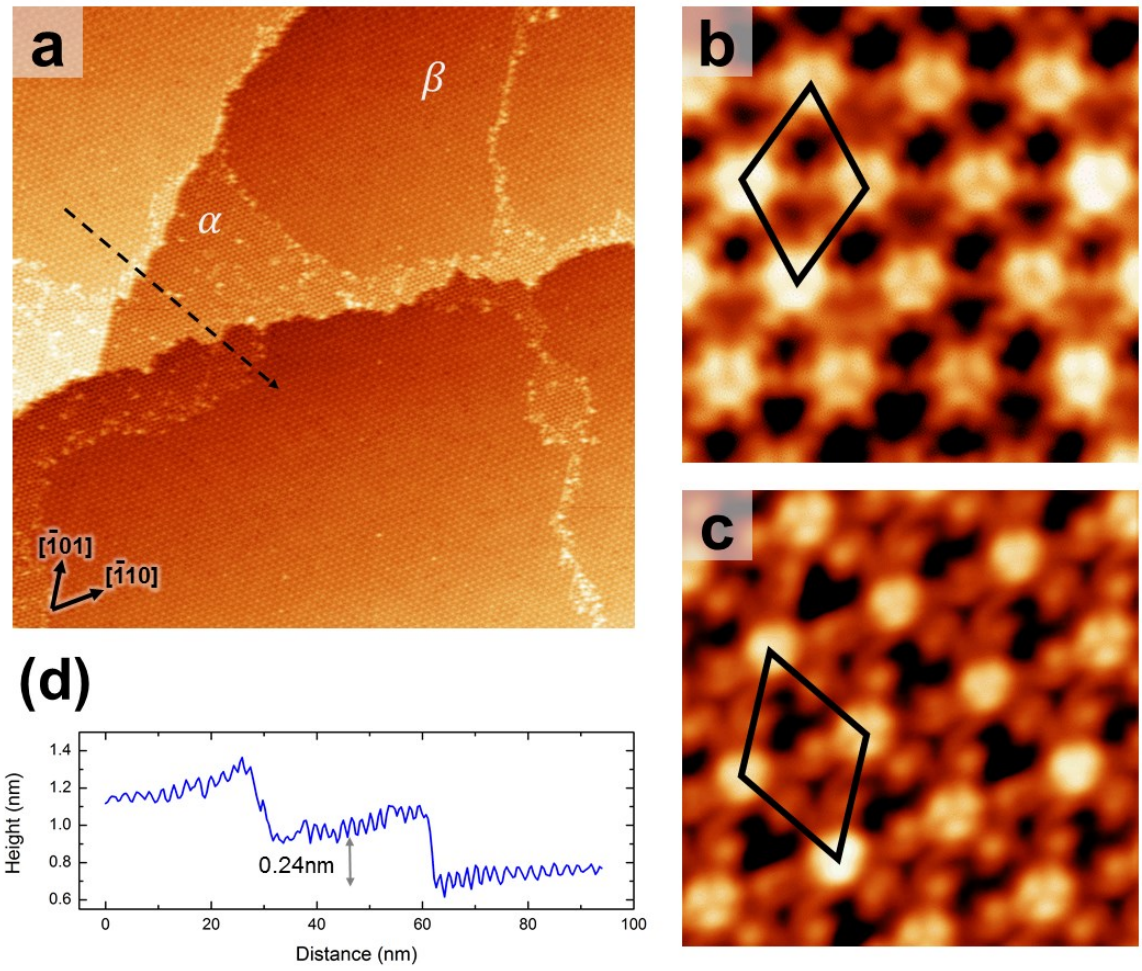


Fig. 8.1 (a) STM image of the $SrTiO_3$(111) surface terminated with (4 × 4) (e.g., region β) and (3 × 3) (e.g., region α) reconstructions (image size: 200 × 200 nm^2, imaging conditions: V_s = +2.308 V, I_t = 0.225 nA). (b) Close-up STM image of the (3 × 3) reconstruction with a unit cell highlighted. This image was taken from a different $SrTiO_3$(111) sample (image size: 7.0 × 7.0 nm^2). This image was processed using Smart Align software [365] by averaging 4 STM images with imaging conditions of V_s = +2.326 V, I_t = 0.35 nA. (c) Close-up STM image of the (4 × 4) reconstruction with a unit cell highlighted. This image was taken from the same $SrTiO_3$(111) sample as Fig. 8.1a (image size: 8.8 × 8.8 nm^2). This image was processed using Smart Align software [365] by averaging 14 STM images with imaging conditions of V_s = +2.308 V and I_t = 0.225 nA. (d) Height profile taken across three terraces on the $SrTiO_3$(111) surface in the direction along the black arrow in Fig. 8.1a.

(4×4) and (3×3) reconstructed $SrTiO_3(111)$ was used as the substrate for the growth of MoS_2 crystals. Note that $SrTiO_3$ will no longer be reconstructed once it is in air, however, the STM images show that any polishing damage has been removed allowing the crystallography to extend to the surface of the sample. The as-grown MoS_2 sample was inspected by the SEM. As shown in Fig. 8.2a, a small number of extremely large (>20 μm) and a large number of small (<3 μm) MoS_2 crystals were observed in the large-scale image. A close-up image of the region with small MoS_2 crystals is shown in Fig. 8.2b. These small MoS_2 crystals have lateral sizes smaller than 3 μm, and they have a side of the triangles aligning with the direction labelled by the red arrows in Fig. 8.2b. Both large and small MoS_2 crystals exhibit zig-zag edges which are the most energetically stable edge structures of MoS_2 [329]. As our samples were grown in an S-rich environment, these triangular MoS_2 crystals should have three S-terminated zig-zag (S-zz) edges.

The orientations of 296 MoS_2 crystals of the size 5-15μm were measured because PL and Raman measurements were conducted on the similar-sized crystals. The orientation was measured in terms of the angle θ as illustrated in the inset of Fig. 8.2c. It shows two distinct favourable orientations at $\theta = 0°$ and $60°$ in the orientation histogram (Fig. 8.2c). The images of the $0°$ and $60°$ orientated triangular crystals are depicted on top of the corresponding bars.

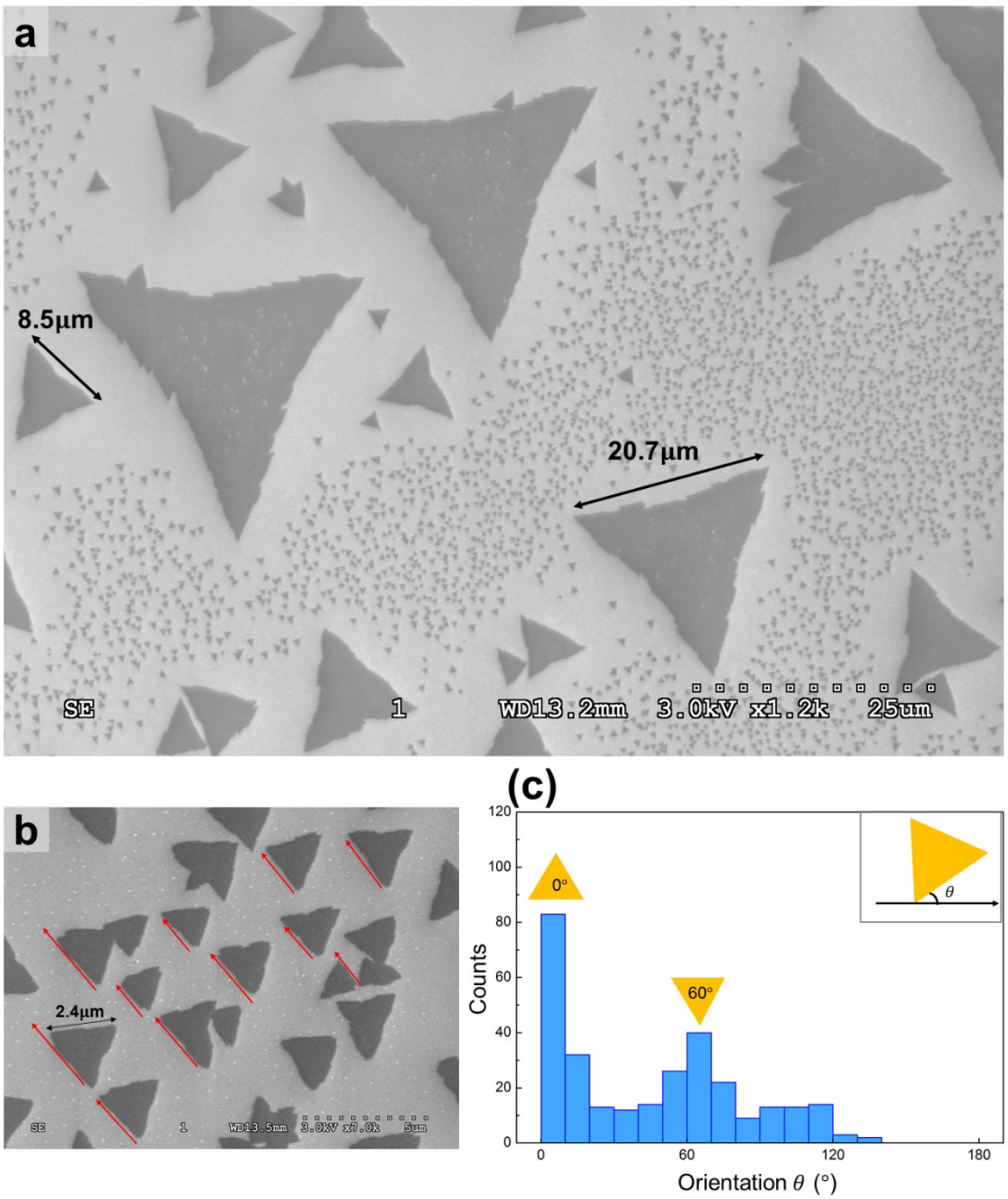


Fig. 8.2 As-grown MoS_2 crystals on the $SrTiO_3$(111) substrate by APCVD growth method: (a) SEM image showing two distinct sizes of MoS_2 crystals. (b) SEM image of small MoS_2 crystals showing the preferential alignment in the direction along the red arrows. SEM images (a) and (b) were obtained by Wenshuo Xu from Professor Warner's group. (c) Orientation histogram of 296 triangular MoS_2 crystals of the sizes 5-15μm. The angle θ was measured according to the schematic diagram shown in the inset.

The as-grown MoS_2 sample was then put into UHV-STM. Several anneals were carried out and the surface was examined by STM. Due to the limited field of view in STM, only the smaller MoS_2 crystals (lateral size smaller than 1.5 μm) can be completely seen. Fig. 8.3a shows a typical STM image of small MoS_2 crystals grown on the $SrTiO_3$(111) substrate. A small MoS_2 crystal (lateral size around 188 nm) is highlighted in Fig. 8.3a. Most MoS_2 crystals in this STM image have two sides aligning with the crystallographic directions $[\bar{1}01]$ and $[\bar{1}10]$ on $SrTiO_3$(111). This suggests good epitaxy with the substrate and the favourable alignments with the $[\bar{1}01]$ and $[\bar{1}10]$ (i.e. <110>) directions. By comparison with the orientation histogram in Fig. 8.2c, the most favourable 0° and 60° oriented MoS_2 crystals correspond to the alignments with <110> directions. Two typical epitaxially-aligned MoS_2 crystals are shown in Fig. 8.3b and c, at 60° to each other.

A larger MoS_2 crystal (lateral size of 373 nm) shows slightly poorer alignment with the substrate (Fig. 8.3a). After being annealed for the same amount of time, larger MoS_2 crystals grew faster than smaller ones, the former of which seem to have insufficient time to adjust themselves to the most favourable (i.e., lowest-energy) positions. That is why some larger crystals show poorer epitaxy with the $SrTiO_3$(111) substrate. The height was measured across a MoS_2 crystal indicated by a red arrow in Fig. 8.3a. The height of 0.8 nm (Fig. 8.3d), in the range of 0.6-0.9 nm reported by many literatures [313-316], suggesting a monolayer MoS_2 crystal.

Fig. 8.3e shows the atomically resolved STM image of MoS_2 structure. It shows the hexagonally arranged bright dots with spacing of 3.12 ± 0.07 Å. The bright dots are S atoms as suggested by the recent work on STM calculation in the Refs. [318-322]. The distance between neighbouring spots (i.e., 3.12 ± 0.07 Å) is close to the true value of S-S distance in the MoS_2(0001) basal plane (i.e., 3.16 Å) and consistent with experimental measurement

reported in literature [314,323,366]. The atomic structure is overlaid on the triangular MoS_2 crystals to identify the lattice orientation and is not to scale (Fig. 8.3b).

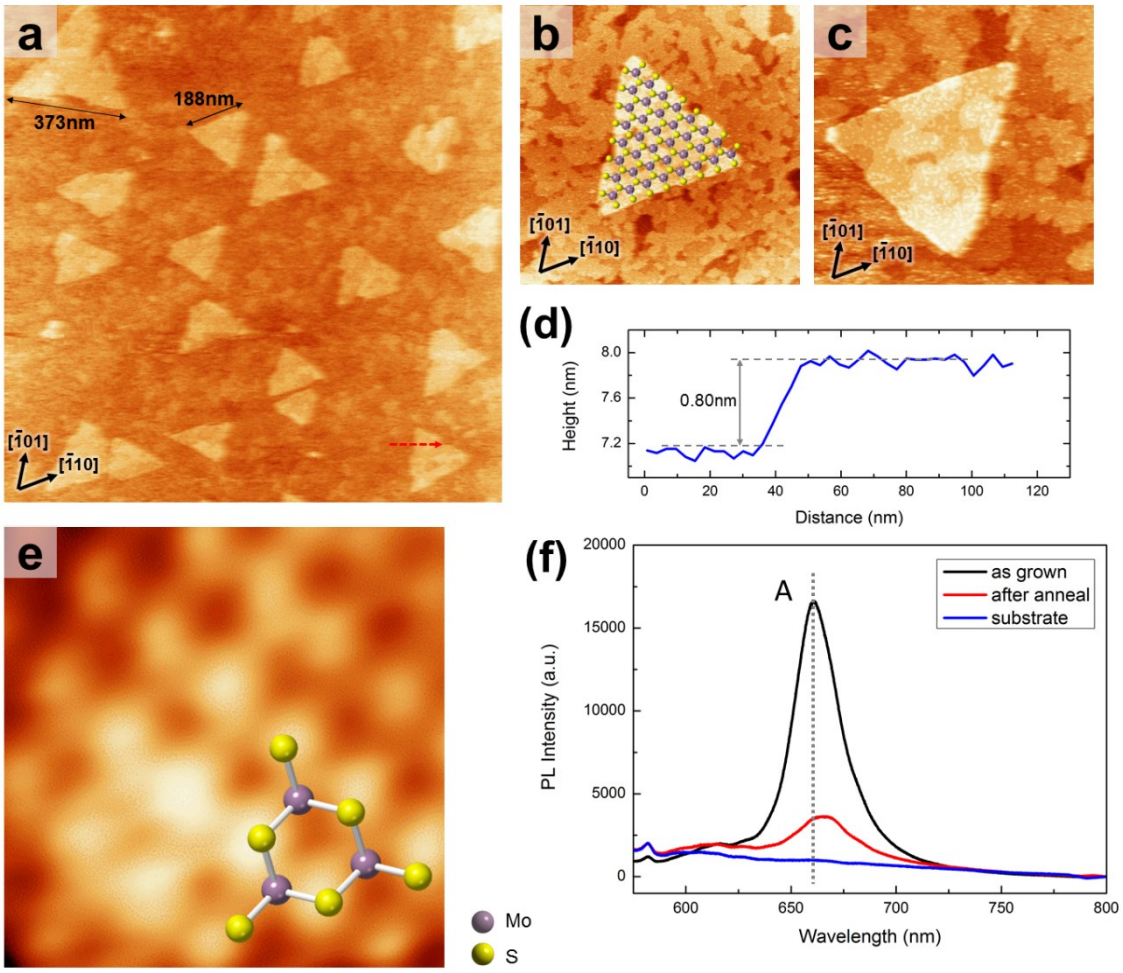


Fig. 8.3 (a) STM image of MoS_2 grown on $SrTiO_3(111)$ with crystals preferentially aligned with <110> directions (image size: 1500 × 1500 nm^2, imaging conditions: V_s = +1.541 V, I_t = 0.085 nA). (b) and (c) Two favourable orientations of the MoS_2 crystals grown on $SrTiO_3(111)$ at 60° to each other (image size: (b) 800 × 800 nm^2 and (c) 400 × 400 nm^2, imaging conditions: (b) V_s = +1.711 V, I_t = 0.04 nA and (c) V_s = +2.828 V, I_t = 0.015 nA). The MoS_2 atomic structure inside the crystal indicates the lattice orientation within the single MoS_2 crystal and is not to scale. (d) Height profile measured across one MoS_2 crystal showing a height of 0.8 nm. (e) Atomically-resolved STM image of MoS_2 structure. The bright dots are S atoms. The atomic structure is overlaid on the STM image (image size: 1.56 × 1.56 nm^2). This image was processed using Smart Align software [365] by averaging 4 STM images with imaging conditions of V_s = +1.098 V, I_t = 0.155 nA and 2 STM images with imaging conditions of V_s = +1.116 V, I_t = 0.15 nA. (f) PL spectra on as-gown (black line) and annealed (red line) MoS_2 crystals, and compared to that of on substrate (blue line).

PL was conducted on both as-grown and annealed MoS_2 samples. Because the laser spot size is around 1 μm, large crystals (>5 μm) were chosen for PL measurement to ensure the signal was generated from the MoS_2 rather than from substrate. The PL from a fresh (111) substrate was also measured and the spectrum was plotted for comparison. As shown in the PL spectra in Fig. 8.3f, the as-grown sample shows remarkably high PL intensity of the A excitonic peak at a wavelength of 660.8 nm (1.877 eV). This corresponds to a phonon energy between 1.8-1.9 eV, which is characteristic of the monolayer MoS_2, as reported in many literatures [298,314,332,335,341]. The peak position was slightly red-shifted to 666.8 nm (1.86 eV) after the sample was annealed at 450°C for 1 hour. By contrast, the intensity of PL peak was significantly reduced for the annealed sample. The weaker PL intensity is attributed to a poorer crystalline quality, which suggests that the quality of MoS_2 was reduced by thermal anneals.

A moiré pattern was observed on the MoS_2 sample with an example highlighted in Fig. 8.4a. The moiré pattern is comprised of hexagonally arranged bright dots. The spacing between neighbouring dots is 4.13 ± 0.12 nm. In layered MoS_2, Mo and S atoms are bound with strong covalent bonds. MoS_2 layers interact via weak van der Waals forces which allow for inter-layer rotations. The moiré pattern is likely attributed to the misorientation in the bilayer MoS_2. The atomic model is built with a relative rotation of 4.5° between the two MoS_2 layers (Fig. 8.4b). The periodicity measured from the model is 4.12 nm which is consistent with our experimental measurements (4.13 ± 0.12 nm). Moiré patterns formed via variable rotation angles in bilayer MoS_2 (e.g., at folded region) were observed which may suggest that there is no fixed rotation values to form MoS_2 moiré patterns [312,338,342,344].

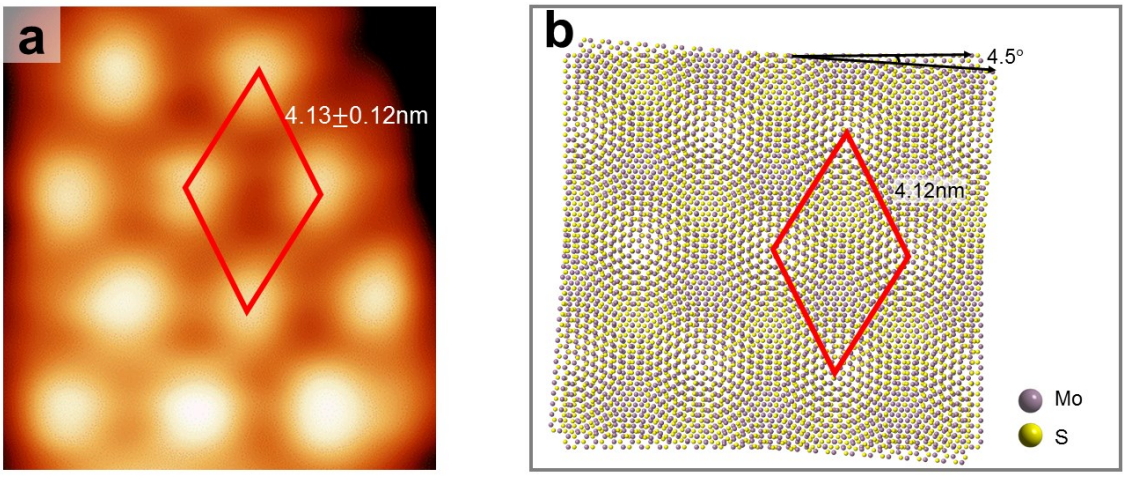


Fig. 8.4 (a) STM image of the moiré pattern formed on MoS_2-$SrTiO_3$(111) surface (image size: 13.8 × 14.7 nm^2, imaging conditions: V_s = +2.199 V, I_t = 0.015 nA). (b) Atomic model of the moiré pattern interpreted by relative rotations of 4.5° in bilayer MoS_2. The unit cells are highlighted.

8.3.2 MoS_2 on $SrTiO_3$(001) substrate

MoS_2 was also grown on the $SrTiO_3$(001) substrate. The c(4×2) reconstruction of this surface was prepared by Ar^+ ion sputtering followed by UHV annealing. The atomic flat $SrTiO_3$(001) surface reconstructed to the c(4 × 2) structure is shown in Fig. 8.5a. It shows several flat terraces with straight step edges aligned with the [010] and [100] directions. Step heights measured across three terraces along the black arrows show a value of 1.92 nm (five bulk unit cells) (Fig. 8.5c). The close-up STM image of the c(4 × 2) reconstruction is shown in Fig. 8.5b, with a unit cell highlighted by the red rhombus. The size of a c(4 × 2) unit cell measured from STM image is 8.74±0.25 Å.

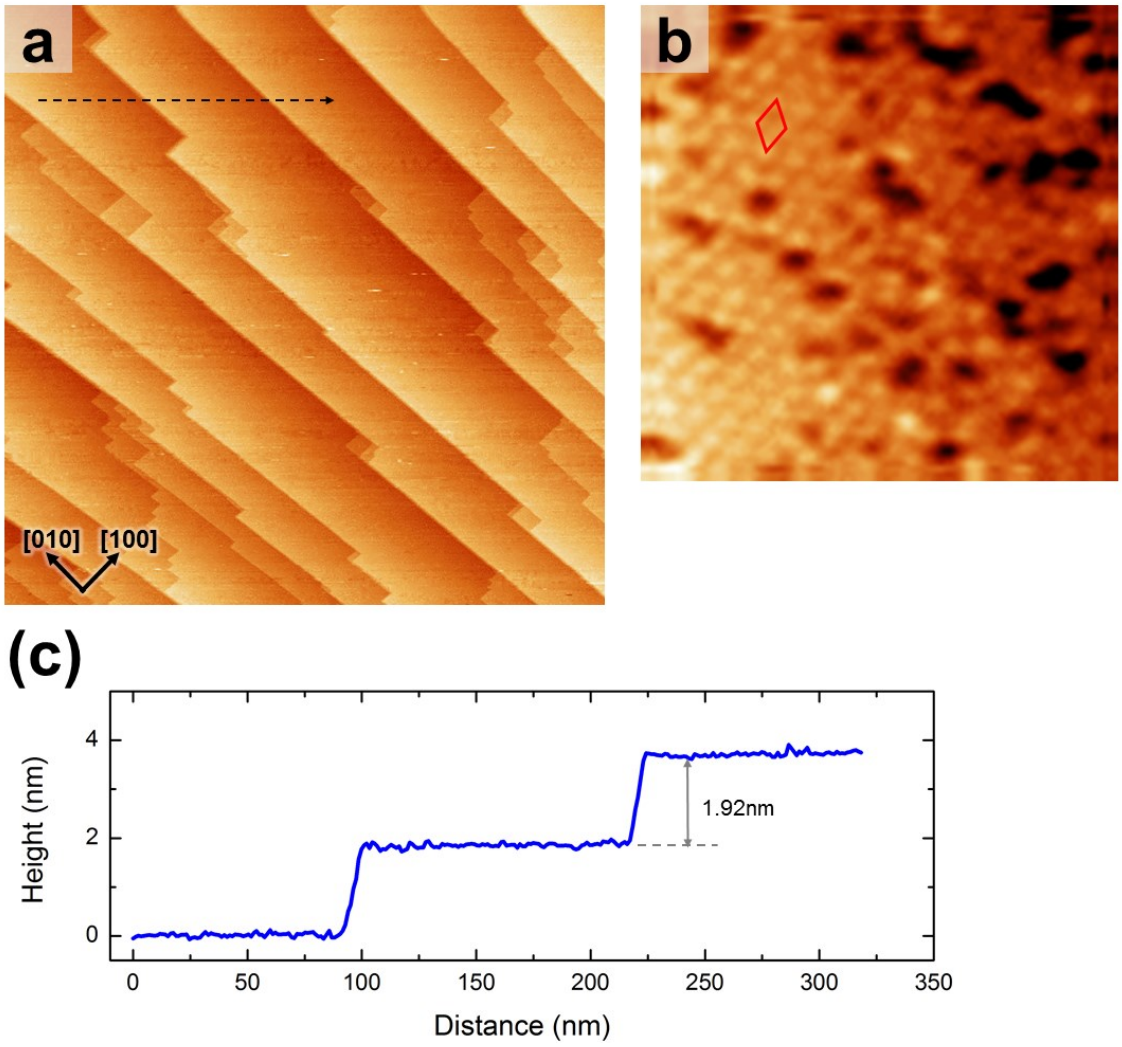


Fig. 8.5 (a) STM image of the $c(4 \times 2)$ reconstruction formed on the $SrTiO_3(001)$ surface (image size: 600×600 nm^2, imaging conditions: $V_s = +2.69$ V, $I_t = 0.09$ nA). (b) Close-up STM image showing the details of the $c(4 \times 2)$ reconstruction with a unit cell highlighted (image size: 15×15 nm^2, imaging conditions: $V_s = +1.5$ V, $I_t = 0.1$ nA). (c) Height profile measured across three terraces in the direction indicated by the arrow in Fig. 8.5a.

MoS_2 crystals were grown on the $SrTiO_3(001)$ substrate by APCVD method. The as-grown MoS_2 sample was inspected by SEM. From the large-scale image (Fig. 8.6a), two distinct sizes of the MoS_2 crystals were observed. A small quantity of MoS_2 crystals with size larger than 5 μm are surrounded by a large number of small crystals. Most big MoS_2 crystals present a right-angled triangular shape with the size of ~5-10 μm and some of them are highlighted by the blue marks in Fig. 8.6a.

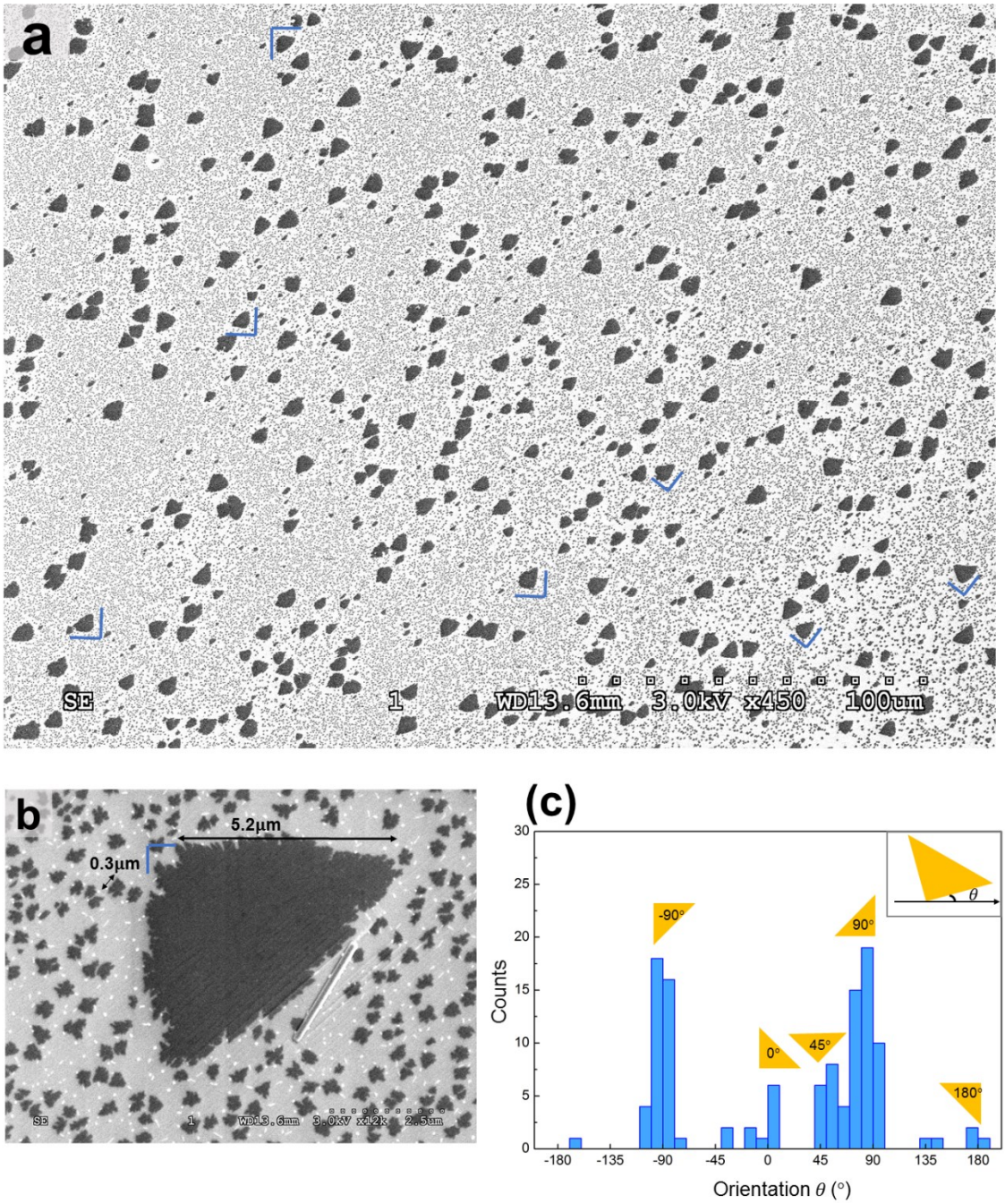


Fig. 8.6 SEM images of as-grown MoS_2 crystals on the $SrTiO_3$(001) substrate by APCVD growth method: (a) Large-scale image showing two distinct crystal sizes. The right-angled crystals are highlighted by the blue marks. (b) Close-up SEM image showing the details of small crystals (~0.3 μm) in fractal shapes and a big right-angled triangular crystal (5.2 μm) with rough edges. SEM images (a) and (b) were obtained by Wenshuo Xu from Professor Warner's group. (c) Orientation histogram of 118 right-angled triangular crystals. The angle θ was measured as illustrated in the inset. The simplified crystal images corresponding to the favourable orientations are labelled on top of the bars.

The close-up SEM image with an example of the right-angled triangular crystal is shown in Fig. 8.6b. The right-angled triangular crystal in this image has a lateral size of 5.2 μm with very rough edges. Compared to big crystals, the small crystals (~0.3 μm) show fractal shapes and are randomly orientated. The orientations of 118 right-angled triangular crystals in Fig. 8.6a were measured. The measurements were taken according to the schematic diagram illustrated in the inset of Fig. 8.6c. The orientation histogram shows five favourable orientations at θ = -90°, 0°, 45°, 90° and 180° (Fig. 8.6c). The corresponding simplified MoS_2 crystal images are depicted on top of the bars.

The as-grown MoS_2 sample was introduced into UHV-STM for more detailed characterisation. The sample was gently annealed at temperatures of 615°C and 810°C for 30 minutes and 1 hour respectively. Fig. 8.7a shows the surface structure after the sample was annealed at 615°C. The MoS_2 crystal present an irregular shape with a size around 368 nm. The surface of the MoS_2 crystal is continuously extended across the substrate terraces with step edges visible. The clear and big zig-zag edges were found as marked by the yellow dashed lines. The same sample was further annealed at 810°C. The sample temperature near the end of the sample was hotter (>810°C). Both regions (T = 810°C and >810°C) were imaged and the STM results are shown in Fig. 8.7b-d. In the region where T = 810°C, the crystal is still a continuous film (Fig. 8.7b). While in the region where T > 810°C, the edge of the crystal started to degrade and form particles as pointed by the black arrow in Fig. 8.7c. In the region which was annealed to even higher temperatures, the continuous film of MoS_2 was broken down and left with particles which maintains the original shape of the MoS_2 crystals (highlighted by dashed rectangles in Fig. 8.7d). These particles could be Mo rich with little or no S due to the desulphurisation of MoS_2 at high temperatures (e.g., 1203°C reported by Liu *et al*. [367]). Further studies are required to distinguish the compositions of the particles, for example by using AES.

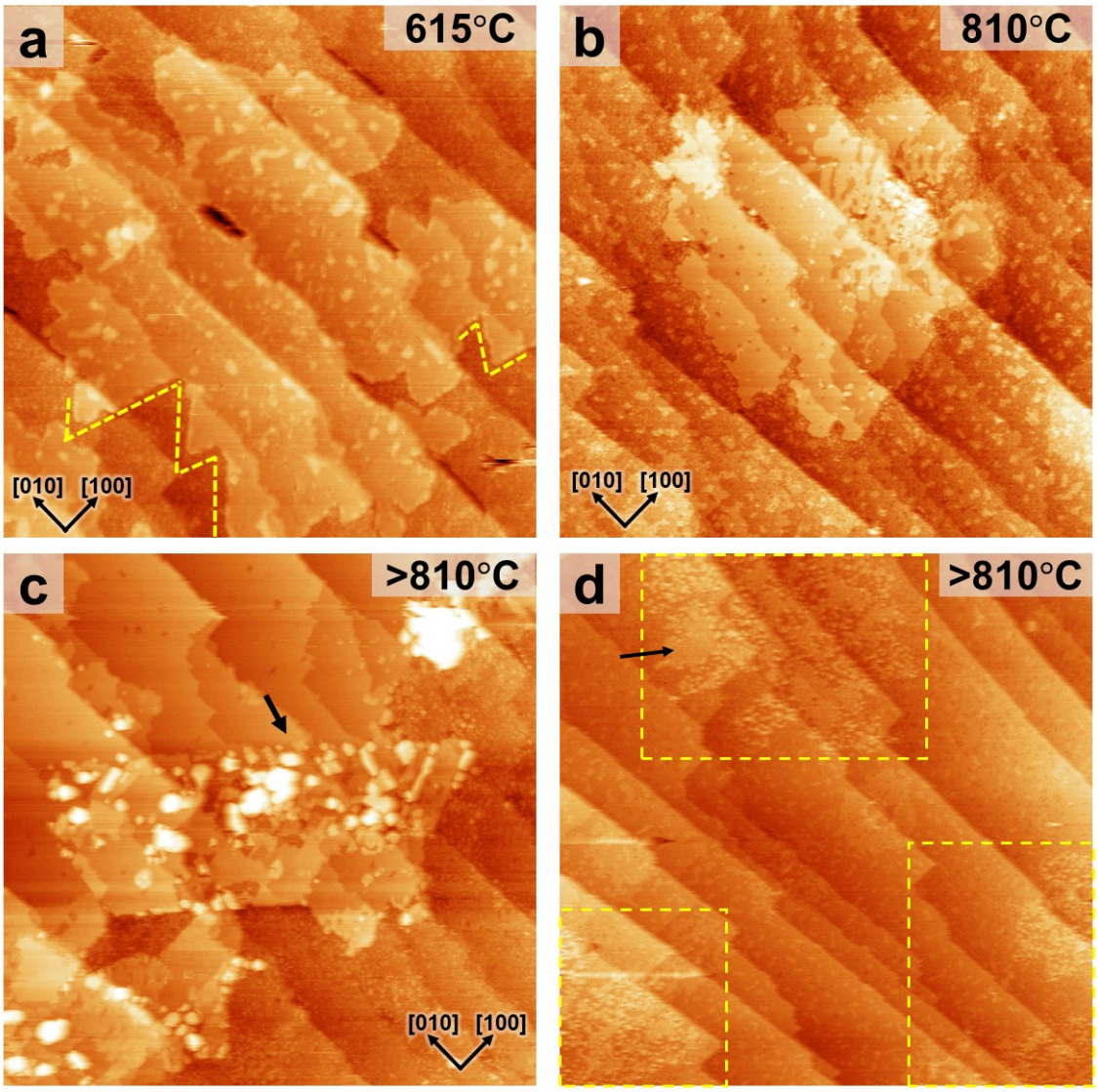


Fig. 8.7 STM images of MoS_2 crystals grown on the $SrTiO_3(001)$-$c(4 \times 2)$ substrate after thermal treatments: (a) After first anneal at 615°C for 30 minutes (image size: 400 × 400 nm^2, imaging conditions: V_s = +2.288 V, I_t = 0.027 nA). (b) After second anneal at 810°C for 1 hour (image size: 500 × 500 nm^2, imaging conditions: V_s = +2 V, I_t = 0.05 nA). (c) The region where the sample temperature was higher than 810°C during the second anneal. The particles were found along the edges of the crystal (pointed by arrow) (image size: 400 × 400 nm^2, imaging conditions: V_s = +2.55 V, I_t = 0.105 nA). (d) The region where the sample temperature was hotter than that of region (c). Particles were observed in the crystals and are highlighted by yellow dashed rectangles (image size: 800 × 800 nm^2, imaging conditions: V_s = +2 V, I_t = 0.075 nA).

The as-grown and annealed MoS_2 samples were measured by PL and the spectra are plotted in Fig. 8.8a. A strong PL A peak was observed at 665.7 nm (1.863 eV). The peak intensities measured on the annealed crystals were significantly reduced. A very weak PL signal with the peak A at 666.7 nm (1.860 eV) was detected from the crystal annealed at 810°C (red line in Fig. 8.8a). The region of the PL spectra highlighted by the green dashed rectangle is zoomed in and shown in Fig. 8.8b. No characteristic peak A of MoS_2 phase was observed on the crystals annealed to above 810°C (blue line in Fig. 8.8b). This suggests that the composition of the crystal has been changed by the high-temperature anneal. The gentle bump on the PL curve (blue line) compared to the substrate (pink line) may be caused by the region on the crystal which was still left with small pieces of the MoS_2 material. This agrees with our STM observation where most crystals transformed into particles with small pieces of MoS_2 films left (e.g., pointed by black arrows in Fig. 8.7d) in the hotter region ($T > 810°C$).

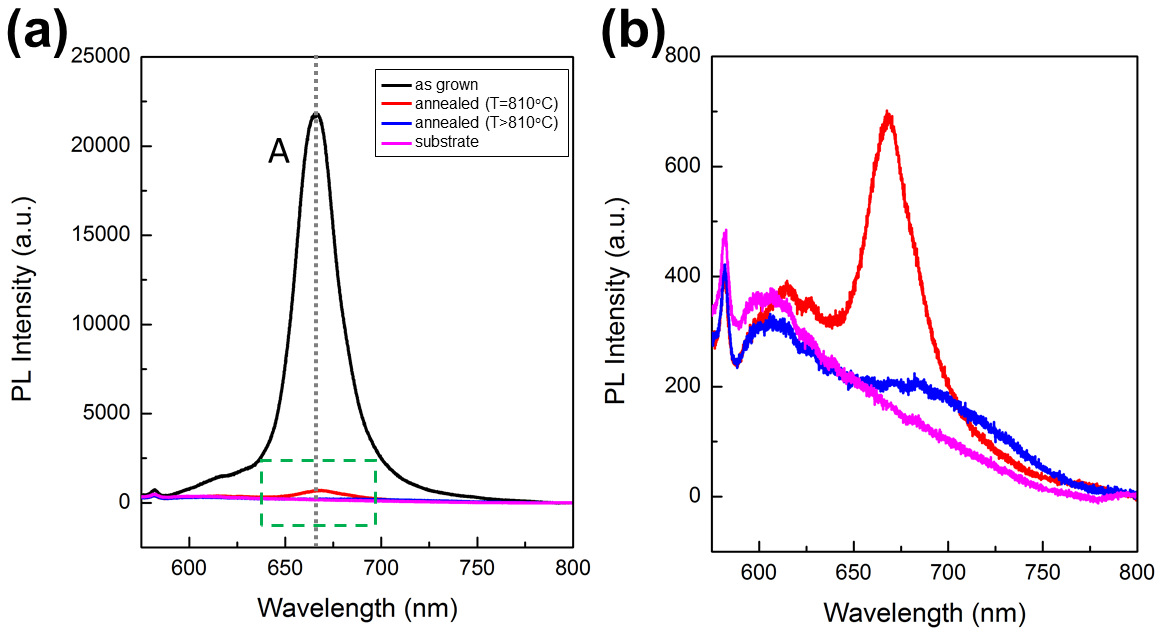


Fig. 8.8 (a) PL spectra of the monolayer MoS_2 on $SrTiO_3$(001): as-grown (black line), annealed at 810°C region (red line), annealed at >810°C (blue line) and that of the substrate (pink line). (b) Close-up of the PL spectra in the region highlighted by the green rectangle in Fig. 8.8a. This data was obtained by Wenshuo Xu from Professor Warner's group.

8.3.3 Comparison between (111) and (001) substrates

The PL and Raman of as-grown MoS_2 on both $SrTiO_3$(111) and (001) substrates were measured. Fig. 8.9a compares the PL spectra measured from MoS_2 on $SrTiO_3$(111) and $SrTiO_3$(001). The peak A for MoS_2 grown on (111) and (001) substrate locate at 660.8 nm (1.88 eV) and 666.3 nm (1.86 eV) respectively. A redshift (20 meV) is observed on (001) relative to that of on (111), mainly attributed to the larger strain built up in the MoS_2 crystals grown on the $SrTiO_3$(001) substrate. The higher strain bends the band structure, which results in the reduced band gap [368].

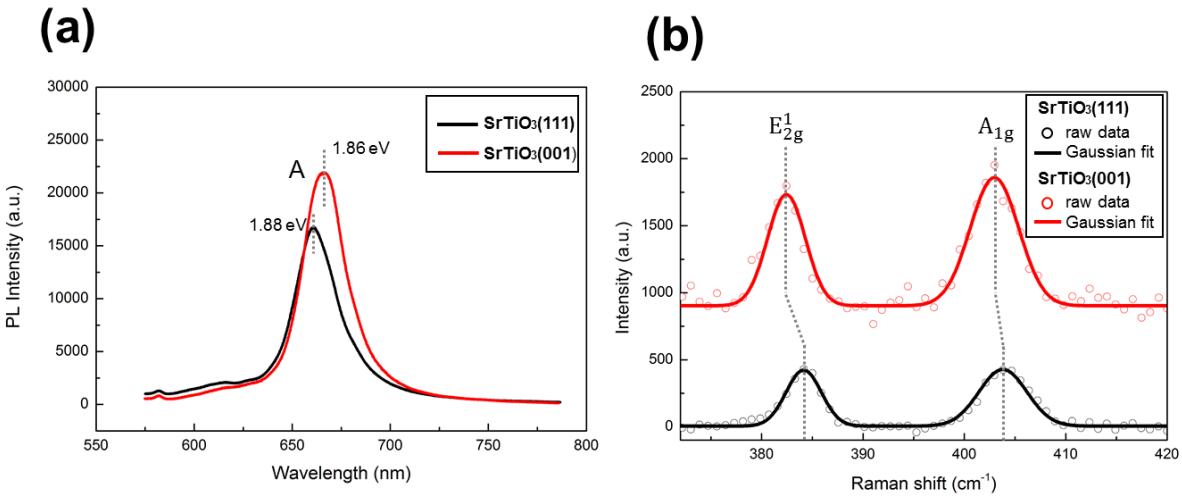


Fig. 8.9 (a) PL spectra and (b) Raman spectra of monolayer MoS_2 on $SrTiO_3$(111) (black line) and $SrTiO_3$(001) (red line) substrates. All measurements were conducted on as-grown samples. This data was obtained by Wenshuo Xu from Professor Warner's group.

Two characteritic active modes, i.e., in-plane E^1_{2g} and out-of-plane A_{1g} modes were observed on the (111) susbstrate (E^1_{2g} = 384.2 cm^{-1} and A_{1g} = 403.8 cm^{-1}) and the (001) substrate (E^1_{2g} = 382.5 cm^{-1} and A_{1g} = 403.0 cm^{-1}) respectively (Fig. 8.9b). The frequency difference (Δk) between E^1_{2g} and A_{1g} is 19.6 cm^{-1} and 20.6 cm^{-1} for the (111) and (001) substrates respectively, confirming monolayer MoS_2 [303,313,330]. As shown in Fig. 8.9b,

a notable redshift (softening) of E^1_{2g} mode (1.8 cm^{-1}) was observed on the (001) substrate relative to that on the (111) substrate. Because the E^1_{2g} mode originates from the in-plane vibration of two S atoms with respect to the Mo atom, the peak position of this mode could be influenced by the substrate and the red-shift of this mode indicates an increase in the strain [326,341]. Thus, the red-shift of the E^1_{2g} mode of MoS_2 grown on the (001) substrate is likely to be attributed to the increased strain in the crystal induced by the (001) substrate.

8.4 Discussion

The $SrTiO_3$(111) surface has a hexagonal atomic arrangement (three-fold symmetry) with a lattice constant of 5.52 Å. The (001) surface of cubic $SrTiO_3$ crystal typically exhibits four-fold symmetry with a square lattice constant of 3.91 Å. Monolayer MoS_2 which presents a three-fold symmetrical atomic arrangement in either the S or Mo layer has an in-plane lattice constant of 3.16 Å in the (0001) basal plane. It was reported that van der Waals epitaxy allows the growth of monolayer MoS_2 on both similar symmetry, e.g., *c*-plane sapphire [333,334], Au(111) [323,336,337] and mica [338], and different symmetry substrates, e.g., $SrTiO_3$(001) [342,343] and $LaAlO_3$(100) [341,344].

MoS_2 can easily achieve an equilibrium regular triangular shape by growing epitaxially on the $SrTiO_3$(111) substrate as both present hexagonal in-plane lattice structures. In addition to the symmetry coincidence, $SrTiO_3$(111) also presents a perfect lattice registry with MoS_2(0001). The in-plane periodicity of $SrTiO_3$(111) (i.e., 5.52 Å) is approximately 7/4 of MoS_2(0001) (3.16 Å). As described in Sec. 8.3.1, the regular triangle crystals are preferentially aligned along the <110> directions on $SrTiO_3$(111). The commensurate structure of MoS_2 on $SrTiO_3$(111) is shown in Fig. 8.10a. This forms a coincident

superlattice with (7 × 7) MoS_2(0001) on (4 × 4) $SrTiO_3$(111) ($\theta = 0°$), with a lattice mismatch of 0.18%. MoS_2 is compressively stressed on $SrTiO_3$(111). The regular triangular-shaped MoS_2 crystals can be formed via this type of registry and this agrees with our orientation measurements which show two favourable orientations at 0° and 60° (Fig. 8.2c).

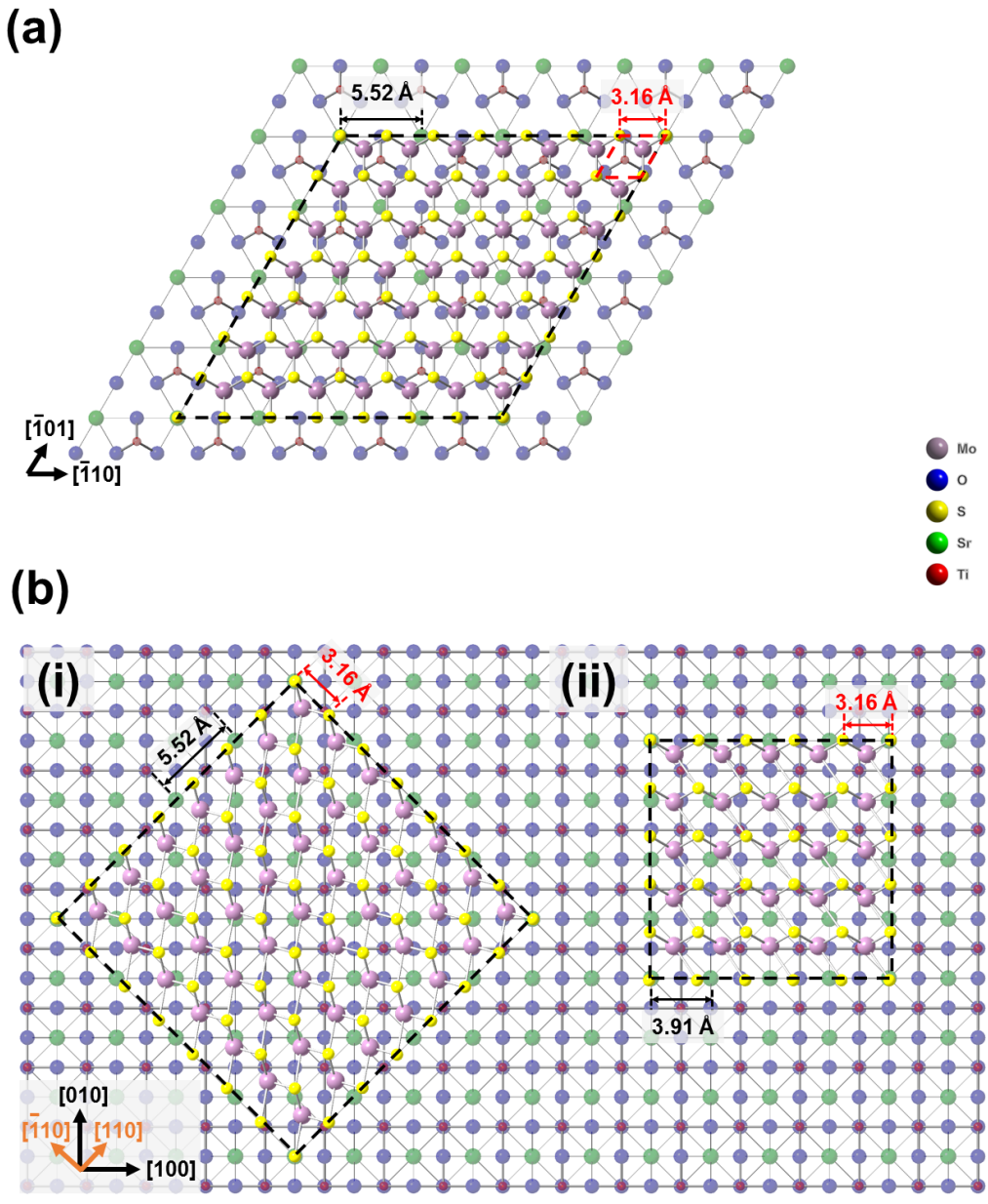


Fig. 8.10 Top view of the commensurate structures of monolayer MoS_2 on (a) the $SrTiO_3$(111) lattice where a supercell of (7 × 7) MoS_2 was used to accommodate a (4 × 4) $SrTiO_3$(111); (b) the $SrTiO_3$(001) lattice: (i) a distorted (7 × 7) MoS_2 used to accommodate a ($4\sqrt{2} \times 4\sqrt{2}$) $SrTiO_3$(001), (ii) a distorted (5 × 5) MoS_2 used to accommodate a (4 × 4) $SrTiO_3$(001).

Compared to the regular triangular-shaped MoS_2 crystals grown on $SrTiO_3$(111) surface, due to the lattice symmetry disparity, MoS_2 crystals of the right-angled triangular shape are found on the $SrTiO_3$(001) substrate. It is different from the regular triangular shape reported in most literatures [311,329,330,333,334,338]. As described in Sec. 8.3.2, the orientation histogram shows that the right-angle sides of the crystal are aligned such that θ = -90°, 0°, 45°, 90° and 180°. The notable favourite set of orientations of 90° and 45° may suggest two possible commensuration structures shown in Fig. 8.10b. Panel i in Fig. 8.10b describes a distorted square supercell of (7 × 7) MoS_2 accommodated on a ($4\sqrt{2} \times 4\sqrt{2}$) $SrTiO_3$(001). This registry gives a misfit of 0.18%. Another possible commensuration is shown in panel ii of Fig. 8.10b. This is achieved by accommodating a distorted (5 × 5) MoS_2 cell on a (4 × 4) $SrTiO_3$(001) and showing a 1.02% misfit. Both 0.18% and 1.02% misfits suggest that MoS_2 is compressively stressed on $SrTiO_3$(001) substrate. There is a 45° rotation between two registries which agrees with our orientation measurements showing a peak at 45°. As considered the commensuration degrees in registries i and ii, the misfit is significantly lower in the former which may indicate a relatively more favourable orientation. In other words, the favourable orientations corresponding to θ = -90°, 0°, 90° and 180° are likely to be those MoS_2 crystals with right-angled sides aligned with the <110> directions on $SrTiO_3$(001). The remaining peaks indicate those MoS_2 crystals with right-angle sides aligning with the <100> directions on $SrTiO_3$(001).

In a dissimilar symmetric arrangement system, the hexagonally arranged MoS_2 lattice needs a heavy distortion in order to accommodate the $SrTiO_3$(001) substrate with a square symmetric lattice. The distortion could be caused by the relatively stronger interaction between MoS_2 and $SrTiO_3$(001). The possible interactions are 1) van der Waals interaction to control the lattice orientation in order to reach high-degree lattice commensurability [333]

2) formation of the edge bonding linkage (such as Mo-S-Ti and Mo-O-Ti linkages [369]) between MoS_2 and the TiO_x-terminated $SrTiO_3$(001) substrate.

This strong interaction forces the lattice distortion of MoS_2 adlayer in order to accommodate the symmetry the $SrTiO_3$(001) substrate. The strong distortion of MoS_2 lattice produces more built-in strains in the right-angled MoS_2 crystals, in agreement with our PL and Raman measurements (Fig. 8.9a and b). The increased strain level is evidenced by the redshift of A peak in PL and the softening of the E_{2g}^1 mode in Raman spectra of MoS_2-$SrTiO_3$(001) compared to those of MoS_2-$SrTiO_3$(111).

8.5 Conclusion

Monolayer MoS_2 was grown on atomically-smooth (111)- and (001)-terminated $SrTiO_3$ single-crystal substrates. MoS_2 crystals grown on the $SrTiO_3$(111) substrate with a similar symmetry have well-defined regular triangular shapes. They have favourable orientations at 0° and 60°, i.e., they edges are aligned with the <110> directions of the substrate. This is formed by symmetry coincidence and the high degree of lattice commensuration i.e., (7 × 7) MoS_2(0001) on (4 × 4) $SrTiO_3$(111) with a 0.18% misfit. MoS_2 crystals with right-angled triangular shapes were formed on the $SrTiO_3$(001) substrate with a different symmetry, with favourable orientations at θ = -90°, 0°, 45°, 90° and 180°. Formation of MoS_2 crystals of the right-angled shapes is attributed to the strong substrate interaction causing the significant lattice distortion. MoS_2 crystals grown on the $SrTiO_3$(001) substrate is more strained than those grown on (111) as evidenced by the red-shift of the A peak in PL and the softening of the E_{2g}^1 mode in Raman spectra for the former. Two possible commensurate structures to interpret the strained right-angled triangular shape and the orientations were

proposed. The registries (i) distorted (7 × 7) MoS_2 on ($4\sqrt{2} \times 4\sqrt{2}$) $SrTiO_3$(001), (ii) distorted (5 × 5) MoS_2 on (4 × 4) $SrTiO_3$(001) would induce misfits of 0.18% and 1.02% respectively. This could suggest the favourable orientations for MoS_2 crystal edges to align with are the <110> and <100> directions on $SrTiO_3$(001). A moiré pattern with periodicity 4.13±0.12 nm was observed due to the relative rotation of 4.5° between two MoS_2 layers. Thermal treatments reduced the quality of MoS_2 monolayers as detected by the significantly reduced PL intensity. The fractal morphology with rough edges of MoS_2 grown on $SrTiO_3$(001) could provide a large exposed active edge site which are suggested to be capable in electrocatalytic hydrogen evolution reaction applications [344].

Chapter 9

Conclusions

9.1 Overview

This thesis reports experimental investigations on anatase nanostructures, epitaxially-grown Pd nanocrystals and monolayer MoS_2 crystals. Two types of substrates, $SrTiO_3$(001) and $SrTiO_3$(111), were used in this work. $SrTiO_3$(001) was reconstructed into dilines and anatase terminated surfaces, which were used for the growth of Pd nanocrystals. Both surface reconstruction treated $SrTiO_3$(001) and (111) were used as the substrates to grow MoS_2 crystals. The morphologies of anatase, Pd and MoS_2 crystals were characterised using STM or SEM. The substrate-induced strain in MoS_2 crystals were studied using Raman and PL.

The work has encompassed a variety of investigations including the morphology of the epitaxial nanostructures, their epitaxy relationship with substrate and the SMSI in Pd-diline and Pd-anatase systems. The calculations regarding the adhesion energy and surface energy change through encapsulation were conducted, providing an understanding of the interactions between metal nanocrystals with oxide supports. The conclusions made through the experimental investigations (from Chapter 4 to Chapter 8) are summarised in this chapter.

9.2 Anatase Nanostructures and Film

Scanning tunnelling microscopy (STM) revealed that upon extensive UHV annealing leading to significant TiO_x surface enrichment, the TiO_2(001) anatase phase was nucleated on the nanostructured $SrTiO_3$(001) surface. The small lattice mismatch of 3.3% between TiO_2 anatase and $SrTiO_3$(001) enables the growth of otherwise unstable anatase TiO_2 with the high-energy (001) surface exposed. Each single epitaxial anatase island is composed of a mixture of (1 × 3) and (1 × 4) reconstructions and is strained on the $SrTiO_3$(001) substrate because dislocations, which release the strain, are unexpected to form at the interface for such a small island (width < 11.3 nm). The complex anatase (1 × 3) nanostructures were formed with the same width of 6.78±0.05 nm, which indicates a stable configuration of long-range anatase (1 × 3) reconstruction on $SrTiO_3$(001) surface.

The presence of widely spaced anatase islands provides preferential sites for large coverage of islands growth. The growth process is also assisted by Ti deposition, oxygen dosing (exposing the sample to the atmosphere in our case) and extensive UHV annealing, to produce well distributed flat anatase films on the $SrTiO_3$(001) substrate. The anatase film exhibits (1 × 4) reconstructions comprised of parallel ridges along <100> crystallographic directions. Anatase TiO_2(001) film epitaxially grown on $SrTiO_3$(001) surfaces are relaxed and present its original lattice constant (a = 3.78 Å). Screw dislocations are often found on anatase, which enable the fast growth of film by the spiral growth mechanism. This anatase structure with (1 × 4) reconstruction is stable up to 950°C. The high quality and flat anatase surfaces are ideally suited to study epitaxially-grown metal nanoparticles (e.g., Pd).

9.3 Epitaxial Pd Nanocrystals

Pd, as one of the popular metals used as catalyst motivated us to study its morphology and interaction with dilines and anatase substrates. Pd nanocrystals were grown on ordered dilines and anatase substrates. These two substrates are atomically flat and with close-packed rows on the surface aligning in <100> crystallographic directions, which enable us to explore the epitaxy relationship in these systems. Most Pd nanocrystals grown on both dilines and anatase are characterised by a (111) top facet, three (111) side facets, three (001) side facets and a (111) interface with the substrate. Pd nanocrystals prefer to grow in width rather than in height at low temperatures and the other way round at higher annealing temperatures. The elongated Pd nanocrystals were formed at low temperatures i.e., 450°C and 300°C on dilines and anatase respectively. The elongation is along the rows due to a faster and preferential in-channel diffusion than cross-channel diffusion of Pd on both substrates at low temperature. As temperature increases, elongated Pd nanocrystals started to grow across the dilines and anatase rows towards forming a more equilibrium hexagonal shape. Besides, Pd nanocrystals in truncated triangular shapes were also formed on anatase substrate at 300 °C. Pd nanocrystals formed at higher temperature are closer to its equilibrium shape and were therefore used to calculate the adhesion energy, giving the values of 2.55 ± 0.09 J/m^2 and 2.05 ± 0.05 J/m^2 for Pd-dilines and Pd-anatase respectively.

The orientation of Pd nanocrystals with respect to the anatase substrate was study as an indication of the epitaxial relationship in this system. It shows that small crystals ($w <$ 11 nm) have a good epitaxy with the substrate, compared to that of big Pd nanocrystals ($w \geq$ 11 nm) with more than 36% of the nanocrystal presenting rotations larger than 15°. In addition, higher-temperature treatment allows the Pd nanocrystals to re-adjust their

orientations from unfavourable to favourable orientations (0-5°), i.e., the lowest-energy positions, which obtained a good epitaxy with substrate.

Two SMSI states have been prepared for Pd nanocrystals supported on dilines and anatase by high temperature treatment (above 600°C). A (7 × 7) wagon wheel and a (4 × 4)R1.5° hexagonal superstructures are formed with respect to the Pd(111) surface. The formation of these two superstructures is attributed to the moiré patterns caused by supposition of Ti and Pd layers. Atomic models were built to interpret the moiré patterns with hexagonal and wagon wheel superstructure. Specifically, the wagon wheel superstructure is formed by the superposition of a hexagonal adlayer of Ti atoms (a = 3.21 Å) and a Pd(111) layer (s = 2.75 Å) with no inter-layer rotation. The hexagonal superstructure is produced by placing a layer of compressed hexagonal Ti lattices (a = 3.69 Å and α = 60.3°) on the Pd(111) substrate (s = 2.75 Å) with relative 1.5° inter-layer rotation. The moiré dots consist of seven Ti atoms with two configurations according to the atomic resolved STM images. The brightness of the moiré dot is attributed to the overall brightness of the Ti atoms in either of two configurations. The bright moiré dot has only one brighter Ti atom located at the centre of the seven Ti atoms. The even brighter moiré dots are those containing three brighter Ti atoms. According to the STM observation and atomic models, the brightness of the Ti atoms is related to the relative positions where they sit on the Pd atoms, which topographically high position yield the brighter Ti atoms.

A typical Pd-TiO_2 system i.e., Pd-anatase with bare and encapsulated Pd nanocrystals were studied, showing a reduction of 0.35±0.19 J/m^2 in surface energy for the dominant (111) facets, from 1.64 J/m^2 for bare Pd nanocrystals to 1.29±0.19 J/m^2 for encapsulated Pd nanocrystals supported on anatase. The reduction of surface energy proves that

encapsulation can reduce the surface energy of the metal nanocrystals (e.g., Pd) supported on TiO_2 by forming a thin oxide layer (TiO_x).

9.4 Epitaxial Monolayer MoS_2 crystals

$SrTiO_3$ substrates were prepared with surface reconstructions, leading to the atomically flat and crystallinity revealed surfaces, which are suitable for the growth of high quality monolayer MoS_2 crystals and study of the epitaxial relationship. Both (111) and (001) terminated surfaces were used because they present very different lattice structures i.e., hexagonal and square lattices structure respectively.

MoS_2 crystals grown on the $SrTiO_3$(111) substrate with a similar three-fold symmetry have well-defined regular triangular shapes. They have favourable orientations at 0° and 60°, i.e., they edges are aligned with <110> directions of the substrate. This is formed by symmetry coincidence and the high degree of lattice commensuration i.e., (7×7) MoS_2(0001) on (4×4) $SrTiO_3$(111) with a 0.18% misfit. MoS_2 crystals with right-angled triangular shapes were formed on the symmetry-disparate $SrTiO_3$(001) substrate, with favourable orientations at $\theta =$ -90°, 0°, 45°, 90° and 180°. Formation of right-angled shapes is attributed to the strong substrate interaction causing significant lattice distortion. MoS_2 crystals grown on the $SrTiO_3$(001) substrate are more strained than those grown on (111), as evidenced by the red-shift (20 meV) of the A peak in PL and the softening of the E^1_{2g} mode (1.8 cm^{-1}) in Raman spectra for the former. Two possible commensurate structures to interpret the strained right-angled triangular shape and the orientations are (i) distorted (7×7) MoS_2 on $(4\sqrt{2} \times 4\sqrt{2})$ $SrTiO_3$(001) and (ii) distorted (5×5) MoS_2 on (4×4) $SrTiO_3$(001) with

misfits of 0.18% and 1.02% respectively. This could suggest the MoS_2 crystal edges are favoured to align with the <110> and <100> directions on $SrTiO_3$(001).

9.5 Future work

The experimental observation of the formation of anatase (1 × 3) nanostructures in a long range order has been demonstrated in this work. Anatase (1 × 3) presents a higher surface energy (γ = 0.58 J/m^2) compared to that of (1 × 4) and (1 × 5) reconstructions (γ = 0.51 J/m^2 and 0.53 J/m^2 respectively) [230]. The higher surface energy may simply lead to a more active surface for chemical reactions. It is important to find an approach to form a stable anatase (1 × 3) phase as it may improve catalysis efficiency. We have currently established the collaboration with Prof. Laurence Marks group in Northwestern University where the DFT modelling on this structure is under investigation. We hope to fully understand the stabilisation mechanism of this metastable phase from theoretical aspects and to produce large anatase (1 × 3) surfaces which will be useful in catalysis application. Besides, we found the anatase (1 × 3) nanostructure is strained on $SrTiO_3$(001) surface. Because STM can only probe the surface atomic layer, high resolution transmission electron microscopy (HR-TEM) could be applied to directly visualise and study the interface between two materials and understand how the interaction performs.

We have performed the STM characterisations and have demonstrated the formation of hexagonal and wagon wheel superstructures on the Pd nanocrystals in SMSI state. In addition, it is practically important to understand the composition and stoichiometry of the encapsulated layer on Pd nanocrystals for example by X-ray photoelectron spectroscopy (XPS). Moreover, it is suggested that noble metals-oxide supports in the SMSI state exhibit

the capability in the selective catalytic reactions [36,239,240]. The size and surface structures could influence how the Pd-anatase catalyst performs in chemical reactions. This motivates further studies involving the chemical testing on the encapsulated Pd-anatase system. For example, one could study the performance of hexagonal or wagon wheel structured Pd nanocrystals with different sizes in the hydrogenation reaction (e.g., alkynes to alkenes). This could possibly contribute to fine chemical productions and industrial polymerisation processes.

Both anatase TiO_2(001) and Pd show an outstanding capability as catalysts. Exploring two possible future research directions mentioned above is promising to achieve the full potential of this heterogeneous material in catalysis applications.

References:

[1] Henrich, V. E., Dresselhaus, G. and Zeiger, H. J. *Surface Defects and the Electronic Structure of $SrTiO_3$ Surfaces*. Phys. Rev. B **17**, 4908, (1978).

[2] Vendik, O. G., Ter-Martirosyan, L. T. and Zubko, S. P. *Microwave Losses in Incipient Ferroelectrics as Functions of the Temperature and the Biasing Field*. J. Appl. Phys. **84**, 993, (1998).

[3] Trainer, M. *Ferroelectricity: Measurement of the Delectric Susceptibility of Strontium Titanate at Low Temperatures*. Am. J. Phys. **69**, 966, (2001).

[4] Frederikse, H. P. R., Thurber, W. R. and Hosler, W. R. *Electronic Transport in Strontium Titanate*. Phys. Rev. **134**, A442, (1964).

[5] Mavroides, J. G., Kafalas, J. A. and Kolesar, D. F. *Photoelectrolysis of Water in Cells with $SrTiO_3$ Anodes*. Appl. Phys. Lett. **28**, 241, (1976).

[6] Nemec, H. et al. *Highly Tunable Photonic Crystal Filter for the Terahertz Range*. Opt. Lett. **30**, 549, (2005).

[7] Hara, T., Ishiguro, T., Wakiya, N. and Shinozaki, K. *Oxygen Sensing Properties of $SrTiO_3$ Thin Films*. Jpn. J. Appl. Phys. **47**, 7486, (2008).

[8] Shen, H., Song, Y. W., Gu, H., Wang, P. C. and Xi, Y. M. *A High-permittivity $SrTiO_3$-based Grain Boundary Barrier Layer Capacitor Material Single-fired Under Low Yemperature*. Mater. Lett. **56**, 802, (2002).

[9] Wang, N. et al. *Enhanced Thermoelectric Performance of Nb-doped $SrTiO_3$ by Nano-inclusion with Low Thermal Conductivity*. Sci. Rep. **3**, 3449, (2013).

[10] Chaudhari, P., Koch, R. H., Laibowitz, R. B., McGuire, T. R. and Gambino, R. J. *Critical-Current Measurements in Epitaxial Films of $YBa_2Cu_3O_{7-x}$ Compound*. Phys. Rev. Lett. **58**, 2684, (1987).

[11] Castell, M. R. *Nanostructures on the $SrTiO_3$ (001) Surface Studied by STM*. Surf. Sci. **516**, 33, (2002).

[12] Deak, D. S., Silly, F., Newell, D. T. and Castell, M. R. *Ordering of TiO_2-based Nanostructures on $SrTiO_3$ (001) Surfaces*. J. Phys. Chem. B **110**, 9246, (2006).

[13] Marshall, M. S. J., Becerra-Toledo, A. E., Marks, L. D. and Castell, M. R. *Surface and Defect Structure of Oxide Nanowires on $SrTiO_3$*. Phys. Rev. Lett. **107**, 086102, (2011).

[14] Marshall, M. S. J. et al. *Structure and composition of linear TiOx nanostructures on $SrTiO_3$ (001)*. Physical Review B **86**, 125416, (2012).

[15] Liu, S., Yu, J. and Jaroniec, M. *Anatase TiO_2 with Dominant High-energy {001} Facets: Synthesis, Properties, and Applications*. Chem. Mater. **23**, 4085, (2011).

[16] Lee, K., Kim, M. and Kim, H. *Catalytic Nanoparticles Being Facet-Controlled*. J. Mater. Chem. **20**, 3791, (2010).

[17] Fan, L. Z. et al. *Single-site Nickel-grafted Anatase TiO_2 for Hydrogen Production: Toward Understanding the Nature of Visible-light Photocatalysis*. J. Catal. **320**, 147, (2014).

[18] Karakitsou, K. E. and Verykios, X. E. *Effects of Altervalent Cation Doping of TiO_2 on its Performance as a Photocatalyst for Water Cleavage*. J. Phys. Chem. **97**, 1184, (1993).

[19] Kavan, L., Gratzel, M., Gilbert, S. E., Klemenz, C. and Scheel, H. J. *Electrochemical and Photoelectrochemical Investigation of Single-crystal Anatase*. J. Am. Chem. Soc. **118**, 6716, (1996).

[20] Lazzeri, M., Vittadini, A. and Selloni, A. *Erratum: Structure and Energetics of Stoichiometric TiO_2 Anatase Surfaces*. Phys. Rev. Lett. **65**, 119901, (2001).

[21] Silly, F. and Castell, M. R. *Formation of Single-domain Anatase TiO_2(001)-(1×4) Islands on $SrTiO_3$(001) After Thermal Annealing*. Appl. Phys. Lett. **85**, 3223, (2004).

[22] Marshall, M. S. J. and Castell, M. R. *Shape Transitions of Epitaxial Islands During Strained Layer Growth: Anatase TiO_2 on $SrTiO_3$*. Phys. Rev. Lett. **102**, 146102, (2009).

[23] Haruta, M. *Size-and Support-ependency in the Catalysis of Gold*. Catal. Today **36**, 153, (1997).

[24] Sun, J. Y. et al. *Controlled Growth of Ni Nanocrystals on $SrTiO_3$ and Their Application in the Catalytic Synthesis of Carbon Nanotubes*. Chem. Commun. **49**, 3748, (2013).

[25] Sun, B., Vorontsov, A. V. and Smirniotis, P. G. *Role of Platinum Deposited on TiO_2 in Phenol Photocatalytic Oxidation*. Langmuir **19**, 3151, (2003).

[26] Bian, Z. F., Tachikawa, T., Kim, W., Choi, W. and Majima, T. *Superior Electron Transport and Photocatalytic Abilities of Metal-Nanoparticle-Loaded TiO_2 Superstructures*. J. Phys. Chem. C **116**, 25444, (2012).

[27] Zhang, H., Jin, M. S., Xiong, Y. J., Lim, B. and Xia, Y. N. *Shape-Controlled Synthesis of Pd Nanocrystals and Their Catalytic Applications*. Acc. Chem. Res. **46**, 1783, (2013).

[28] Berko, A., Szoko, J. and Solymosi, F. *Effect of CO on the Morphology of Pt Nanoparticles Supported on TiO_2 (110)-(1×n)*. Surf. Sci. **566**, 337, (2004).

[29] Dulub, O., Hebenstreit, W. and Diebold, U. *Imaging Cluster Surfaces with Atomic Resolution: The Strong Metal-support Interaction State of Pt Supported on TiO_2(110)*. Phys. Rev. Lett. **84**, 3646, (2000).

[30] Jennison, D. R., Dulub, O., Hebenstreit, W. and Diebold, U. *Structure of an Ultrathin TiO_x film, Formed by the Strong Metal Support Interaction (SMSI), on Pt Nanocrystals on TiO_2(110)*. Surf. Sci. **492**, L677, (2001).

[31] Steinruck, H. P., Pesty, F., Zhang, L. and Madey, T. E. *Ultrathin Films of Pt on TiO_2(110) - Growth and Chemisorption-Induced Surfactant Effects*. Phys. Rev. B **51**, 2427, (1995).

[32] Silly, F. and Castell, M. R. *Encapsulated Pd Nanocrystals Supported by Nanoline-Structured $SrTiO_3$(001)*. J. Phys. Chem. B **109**, 12316, (2005).

[33] Bennett, R. A. et al. *Surface structures in the SMSI state; Pd on (1×2) Reconstructed TiO_2(110)*. J. Phys. Chem. B **106**, 4688, (2002).

[34] Bowker, M. et al. *Model Catalyst Studies of the Strong Metal-support Interaction: Surface Structure Identified by STM on Pd Nanoparticles on $TiO_2(110)$*. J. Catal. **234**, 172, (2005).

[35] Li, Y. Z. et al. *Strong Metal-support Interaction and Catalytic Properties of Anatase and Rutile Supported Palladium Catalyst Pd/TiO_2*. Chem. Phys. Lett. **372**, 160, (2003).

[36] Weerachawanasak, P., Praserthdam, P., Arai, M. and Panpranot, J. *A Comparative Study of Strong Metal-support Interaction and Catalytic Behavior of Pd Catalysts Supported on Micron- and Nano-sized TiO_2 in Liquid-phase Selective Hydrogenation of Phenylacetylene*. J. Mol. Catal. A: Chem. **279**, 133, (2008).

[37] Castell, M. R. *Scanning Tunneling Microscopy of Reconstructions on The $SrTiO_3(001)$ Surface*. Surf. Sci. **505**, 1, (2002).

[38] Russell, B. C. and Castell, M. R. *Surface of Sputtered and Annealed Polar $SrTiO_3(111)$: TiO_x-rich (n x n) Reconstructions*. J. Phys. Chem. C **112**, 6538, (2008).

[39] Russell, B. C. and Castell, M. R. *(✓13 × ✓13)R13.9° and (✓7 × ✓7)R19.1° Reconstructions of the Polar $SrTiO_3$ (111) Surface*. Phys. Rev. B **75**, 155433, (2007).

[40] Silly, F., Newell, D. T. and Castell, M. R. *$SrTiO_3(001)$ Reconstructions: The (2 × 2) to c(4 × 4) Transition*. Surf. Sci. **600**, L219, (2006).

[41] Jiang, Q. and Zegenhagen, J. *c(6×2) and c(4×2) Reconstruction of $SrTiO_3(001)$*. Surf. Sci. **425**, 343, (1999).

[42] Kubo, T. and Nozoye, H. *Surface Structure of $SrTiO_3$ (100)-(✓5 × ✓5)R26.6°*. Phys. Rev. Lett. **86**, 1801, (2001).

[43] Semagina, N. and Kiwi-Minsker, L. *Recent Advances in the Liquid-Phase Synthesis of Metal Nanostructures with Controlled Shape and Size for Catalysis*. Cat. Rev. **51**, 147, (2009).

[44] Hansen, K. H. et al. *Palladium Nanocrystals on Al_2O_3: Structure and Adhesion Energy*. Phys. Rev. Lett. **83**, 4120, (1999).

[45] *Sciencelearn: Resolving Power of Microscopes (University of Waikato)*. <http://sciencelearn.org.nz/Contexts/Exploring-with-Microscopes/Sci-Media/Images/Resolving-power-of-microscopes>, (2012).

[46] Binnig, G., Rohrer, H., Gerber, C. and Weibel, E. *Tunneling through a Controllable Vacuum Gap* Appl. Phys. Lett. **40**, 178, (1982).

[47] Castell, M. R. in *Nanocharacterisation* (eds Kirkland, A. I. andHutchison, J. L.) (Royal Society of Chemistry, 2007).

[48] Tersoff, J. and Hamann, D. R. *Theory and Application for the Scanning Tunneling Microscope*. Phys. Rev. Lett. **50**, 1998, (1983).

[49] Tersoff, J. and Hamann, D. R. *Theory of the Scanning Tunneling Microscope*. Phys. Rev. B **31**, 805, (1985).

[50] Leach, R., Weckenmann, A., Coupland, J. and Hartmann, W. *Interpreting the Probe-surface Interation of Surface Measuring Instruments, or What is a Surface?* Surf. Topogr.: Metrol. Prop. **2**, 035001, (2014).

[51] Marshall, M. S. J. *Nanostructured Strontium Titanate Surfaces* PhD thesis, University of Oxford, (2009).

[52] *Instructions: JSPM-4500S Ultrahigh Vacuum Scanning Tunneling Microscope*. (JEOL Ltd., 2000).

[53] *EX03 Ion Gun System: Operating Manual*. (VG Microtech, 2000).

[54] Chen, C. J. *Introduction to Scanning Tunneling Microscopy*. 2nd edn, (Oxford University Press, 2008).

[55] Silly, F. and Castell, M. R. *Selecting the Shape of Supported Metal Nanocrystals: Pd Huts, Hexagons, or Pyramids on $SrTiO_3(001)$*. Phys. Rev. Lett. **94**, 046103, (2005).

[56] Diebold, U., Anderson, J. F., Ng, K. O. and Vanderbilt, D. *Evidence for the Tunneling Site on Transition-metal Oxides: $TiO_2(110)$*. Phys. Rev. Lett. **77**, 1322, (1996).

[57] *Instructions: TM-57543 SPM Software for Windows System*. (JEOL, 2001).

[58] *MINI E-BEAM EVAPORATOR Model EGCO4: Serial No. S1944/GB5766 Operating and Service Manual*. (OXFORD APPLIED RESEARCH, 2000).

[59] Gfroerer, T. H. in *Encyclopedia of Analytical Chemistry* (ed Meyers, R. A.) Ch. 9209, (John Wiley & Sons Ltd, 2000).

[60] Lupoi, J. S. *Developments in Enzyme Immobilization and Near-infrared Raman Spectroscopy with Downstream Renewable Energy Applications* PhD thesis, Iowa State University, (2012).

[61] Wang, S. S., Wang, X. C. and Warner, J. H. *All Chemical Vapor Deposition Growth of MoS_2: h-BN Vertical van der Waals Heterostructures*. Acs Nano **9**, 5246, (2015).

[62] Smith, M. B. et al. *Crystal Structure and the Paraelectric-to-ferroelectric Phase Transition of Nanoscale $BaTiO_3$*. J. Am. Chem. Soc. **130**, 6955, (2008).

[63] Dewar, M. *Characterization and Evaluation of Aged 20Cr32Ni1Nb Stainless Steels* PhD thesis, University of Alberta, (2013).

[64] Henrich, V. E. and Cox, P. A. *The Surface Science of Metal Oxides*. 1st edn, (Cambridge University Press 1994).

[65] Setvin, M., Wagner, M., Schmid, M., Parkinson, G. S. and Diebold, U. *Surface Point Defects on Bulk Oxides: Atomically-resolved Scanning Probe Microscopy*. Chem. Soc. Rev. **46**, 1772, (2017).

[66] Pena, M. A. and Fierro, J. L. G. *Chemical Structures and Performance of Perovskite Oxides*. Chem. Rev. **101**, 1981, (2001).

[67] Bhalla, A. S., Guo, R. and Roy, R. *The Perovskite Structure-A Review of Its Role in Ceramic Science and Technology*. Mater. Res. Innov. **4**, 3, (2000).

[68] May, K. G. *Surface Structural Changes of Perovskite Oxides during Oxygen Evolution in Alkaline Electrolyte* BEng thesis, MacMaster University, (2010).

[69] Mao, Y., Zhou, H. and Wong, S. S. *Synthesis, Properties, and Applications of Perovskite-Phase Metal Oxide Nanostructures*. Mater. Matters. **5.2**, 50, (2010).

[70] Koripella, C. R. *Dielectric Beyond Barium Titanate*. Kemet Electronics Corp. **2**, 1, (1992).

[71] Lantto, V., Saukko, S., Toan, N. N., Reyes, L. F. and Granqvist, C. G. *Gas Sensing with Perovskite-like Oxides Having ABO_3 and BO_3 Structures*. J. Electroceram. **13**, 721, (2004).

[72] Bibes, M. and Barthelemy, A. *Oxide Spintronics*. IEEE Trans. Electron. Dev. **54**, 1003, (2007).

[73] Henrich, V. E. *The Surfaces of Metal-Oxides*. Rep. Prog. Phys. **48**, 1481, (1985).

[74] Erdman, N. et al. *The Structure and Chemistry of the TiO_2-rich Surface of $SrTiO_3(001)$*. Nature **419**, 55, (2002).

[75] *http://www.chem.qmul.ac.uk/surfaces/scc/scat6_1.htm*.

[76] Kolasinski, K. K. *Surface Science : Foundations of Catalysis and Nanoscience* 3rd edn, (Wiley 2012).

[77] Kern, K. in *Surface Science: Principles and Applications Institute of Physics* (eds Howe, R. F., Lamb, R. N., andWandelt, K.) (Springer-Verlag, 1993).

[78] Michaelides, A. and Scheffler, M. *An Introduction to the Theory of Metal Surfaces* (Univerisity College London).

[79] Yamada, T. K., Tamura, H., Shishido, M., Irisawa, T. and Mizoguchi, T. *Surface Reconstruction of Clean bcc-Fe{110}: A Quasi-Hexagonal Top-Layer with Periodic Height Modulation*. Surf. Sci. **603**, 315, (2009).

[80] Nix, R. M. *An Introduction to Surface Chemistry*, <http://www.chem.qmul.ac.uk/surfaces/scc/> (2013).

[81] Somorjai, G. A. and Li, Y. *Introduction to Surface Chemistry and Catalysis*. 2nd edn, (John Wiley & Sons, Inc, 2010).

[82] Freund, H. J., Kuhlenbeck, H. and Staemmler, V. *Oxide Surfaces*. Rep. Prog. Phys. **59**, 283, (1996).

[83] Cappus, D. et al. *Polar Surfaces of Oxides-Reactivity and Reconstruction*. Surf. Sci. **337**, 268, (1995).

[84] Bonnell, D. A. *Local Structure and Properties of Oxide Surfaces: Scanning Probe Analyses of Ceramics*. J. Am. Ceram. Soc. **81**, 3049, (1998).

[85] Marshall, M. S. J. et al. *Structure and Composition of Linear TiO_x Nanostructures on $SrTiO_3$ (001)*. Phys. Rev. B **86**, 125416, (2012).

[86] Marsh, H. L., Deak, D. S., Silly, F., Kirkland, A. I. and Castell, M. R. *Hot STM of Nanostructure Dynamics on $SrTiO_3$ (001)*. Nanotechnology **17**, 3543, (2006).

[87] Deak, D. S. *Molecular Ordering on Nanostructured Strontium Titanate* PhD thesis, University of Oxford, (2007).

[88] Parak, W. J., Manna, L., Simmel, F. C., Gerion, D. and Alivisatos, P. in *Nanoparticles, from Theory to Application* (ed Schmid, Gunter) 4-49 (Wiley-Vch Verlag GmbH & Co. KGaA, 2004).

[89] Sierka, M. *Synergy between Theory and Experiment in Structure Resolution of Low-dimensional Oxides*. Prog. Surf. Sci. **85**, 398, (2010).

[90] Chen, H. G., Lian, H. D., Hung, S. P. and Wang, C. F. *Epitaxial Growth of Self-ordered ZnO Nanostructures on Sapphire Substrates by Seed-assisted Hydrothermal Growth*. J. Cryst. Growth **362**, 231, (2013).

[91] Chen, Z. et al. *Effect of N_2 Flow Rate on Morphology and Structure of ZnO Nanocrystals Synthesized Via Vapor Deposition*. Scr. Mater. **52**, 63, (2005).

[92] Djurisic, A. B. and Leung, Y. H. *Optical Properties of ZnO Nanostructures*. Small **2**, 944, (2006).

[93] Fan, D. H., Zhu, Y. F., Shen, W. Z. and Lu, J. J. *Synthesis and Optical Properties of Hierarchical Pure ZnO Nanostructures*. Mater. Res. Bul. **43**, 3433, (2008).

[94] Gu, Y., Kuskovsky, I. L., Yin, M., O'Brien, S. and Neumark, G. F. *Quantum Confinement in ZnO Nanorods*. Appl. Phys. Lett. **85**, 3833, (2004).

[95] Hong, S. S., Joo, T., Park, W. I., Jun, Y. H. and Yi, G. C. *Time-resolved Photoluminescence of The Size-controlled ZnO Nanorods*. Appl. Phys. Lett. **83**, 4157, (2003).

[96] Manzoor, U. and Kim, D. K. *Size Control of ZnO Nanostructures Formed in Different Temperature Zones by Varying Ar flow Rate with Tunable Optical Properties*. Physica. E Low Dimens. Syst. Nanostruct. **41**, 500, (2009).

[97] Sharma, M. and Jeevanandam, P. *Magnesium Doping in Hierarchical ZnO Nanostructures and Studies on Optical Properties*. Superlattices Microstruct. **52**, 1083, (2012).

[98] Pal, U. et al. *Synthesis and Optical Properties of ZnO Nanostructures with Different Morphologies*. Opt. Mater. **29**, 65, (2006).

[99] Al-Gaashani, R., Radiman, S., Tabet, N. and Daud, A. R. *Optical Properties of SnO_2 Nanostructures Prepared Via One-step Thermal Decomposition of Tin (II) Chloride Dihydrate*. Mater. Sci. Eng. B-Adv. **177**, 462, (2012).

[100] Tawale, J. S., Gupta, G., Mohan, A., Kumar, A. and Srivastava, A. K. *Growth of Thermally Evaporated SnO_2 Nanostructures for Optical and Humidity Sensing Application*. Sens. Actuator B-Chem. **201**, 369, (2014).

[101] Mattsson, A., Lejon, C., Bakardjieva, S., Stengl, V. and Osterlund, L. *Characterisation, Phase Stability and Surface Chemical Properties of Photocatalytic Active Zr and Y Co-doped Anatase TiO_2 Nanoparticles*. J. Solid State Chem. **199**, 212, (2013).

[102] Rafi ud, d. et al. *Superior Catalytic Effects of Nb_2O_5, TiO_2, and Cr_2O_3 Nanoparticles in Improving the Hydrogen Sorption Properties of $NaAlH_4$*. J. Phys. Chem. C **116**, 11924, (2012).

[103] Hu, W. B. et al. *Synthesis and Characterization of In_2O_3 Nanocube via A Solvothermal-calcination Route*. Mater. Chem. Phys. **118**, 277, (2009).

[104] Senthilkumar, R., Ravi, G., Sanjeeviraja, C., Arivanandan, M. and Hayakawa, Y. in *Solid State Physics, Vol 57* Vol. 1512 *AIP Conference Proceedings* (eds Chauhan, A. K., Murli, C., andGadkari, S. C.) 648 (Amer Inst Physics, 2013).

[105] Wang, X. G., Zhang, H. L., Liu, L. L., Li, W. J. and Cao, P. *Controlled Morphologies and Growth Direction of WO_3 Nanostructures Hydrothermally Synthesized with Citric Acid*. Mater. Lett. **130**, 248, (2014).

[106] Park, S. et al. *Synthesis of Au-functionalized SnO_2 Nanotubes Using TeO_2 Nanowires as Templates and Their Enhanced Gas Sensing Properties*. Appl. Phys. A **110**, 471, (2013).

[107] Zhang, Q. B. et al. *CuO Nanostructures: Synthesis, Characterization, Growth Mechanisms, Fundamental Properties, and Applications*. Prog. Mater. Sci. **60**, 208, (2014).

[108] Chand, P., Gaur, A. and Kumar, A. *Structural, Optical and Ferroelectric Behavior of CuO Nanostructures Synthesized at Different pH Values*. Superlattices Microstruct. **60**, 129, (2013).

[109] Zaien, M., Omar, K. and Hassan, Z. *Synthesis of Dendrite-like Petals of CdO Nanostructure*. Optoelectron. Adv. Mat. **5**, 982, (2011).

[110] Fua, X. Q. et al. *A Three-dimensional Hierarchical CdO Nanostructure: Preparation and Its Improved Gas-diffusing Performance In Gas Sensor*. Sens. Actuator B-Chem. **184**, 260, (2013).

[111] Wang, J. Z., Xu, C. H., You, Y. F. and Wang, J. P. in *Resources and Sustainable Development, Pts 1-4* Vol. 734-737 *Advanced Materials Research* (eds Wu, J., Lu, X., Xu, H., andNakagoshi, N.) 2256 (Trans Tech Publications Ltd, 2013).

[112] Shi, Z. H. et al. *Preparation and Photoelectronic Properties of Alpha-Fe_2O_3 Nanostructure Films on Titanium Foils*. Chinese J. Inorg. Chem. **28**, 1338, (2012).

[113] Ramana, C. V., Troitskaia, I. B., Atuchin, V. V., Ramos, M. and Ferrer, D. *Electron Microscopy Characterization of Hexagonal Molybdenum Trioxide (MoO_3) Nanorods*. J. Vac. Sci. Technol. **28**, 726, (2010).

[114] Hu, J. T., Odom, T. W. and Lieber, C. M. *Chemistry and Physics in One Dimension: Synthesis and Properties of Nanowires and Nanotubes*. Acc. Chem. Res. **32**, 435, (1999).

[115] Iijima, S. *Helical Microtubules of Graphitic Carbon*. Nature **354**, 56, (1991).

[116] Guha, P., Chakrabarti, S. and Chaudhuri, S. *Synthesis of Beta-Ga_2O_3 Nanowire from Elemental Ga Metal and Its Photoluminescence Study*. Physica. E Low Dimens. Syst. Nanostruct. **23**, 81, (2004).

[117] Li, X. C. and Tay, B. K. *Facile Fabrication of Si Nanowire Arrays for Solar Cell Application*. J. Nanosci. Nanotechnol. **11**, 10539, (2011).

[118] Iwai, H. et al. *Si Nanowire FET and Its Modeling*. Sci. China Inform. Sci. **54**, 1004, (2011).

[119] Dayeh, S. A. and Picraux, S. T. *Direct Observation of Nanoscale Size Effects in Ge Semiconductor Nanowire Growth*. Nano Lett. **10**, 4032, (2010).

[120] Muller, T., Heinig, K. H. and Schmidt, B. *Formation of Ge Nanowires in Oxidized Silicon V-grooves by Ion Beam Synthesis*. Nucl. Instrum. Methods Phys. Res. B **175**, 468, (2001).

[121] Kumar, R. and Thakur, N. *Formation and Characterization of SiO_2 Nanowire Groups on Si Substrate by SLS Mechanism*. Optoelectron. Adv. Mat. **3**, 343, (2009).

[122] Hu, L. et al. *MgO Nanowire Growth from Mg Metal and SiO_2*. J. Nanosci. Nanotechnol. **4**, 1071, (2004).

[123] Wu, Z., Hahm, M. G., Jung, Y. J. and Menon, L. *Epitaxially Grown GaN Nanowire Networks*. J. Mater. Chem. **19**, 463, (2009).

[124] Wang, J. C., Zhan, C. Z. and Li, F. G. *The Synthesis of Highly Oriented GaN Nanowire Arrays*. Appl. Phys. A Mater. Sci. Process. **76**, 609, (2003).

[125] Li, Z. J., Zhang, M. and Meng, A. *Synthesis and Mechanism of Single-crystalline Beta-SiC Nanowire Arrays on A 6H-SiC Substrate*. CrystEngComm **13**, 4097, (2011).

[126] Zhang, L. C., Ruan, Y. F., Wang, D. L. and Qiu, C. X. *Synthesis and Photoluminescence Properties of ZnO Nanowire Arrays*. Cryst. Res. Technol. **46**, 405, (2011).

[127] Wang, C. H. et al. *Synthesis of Uniform ZnO Nanowire Arrays over a Large Area*. (Crc Press-Taylor & Francis Group, 2008).

[128] Flory, F., Escoubas, L. and Berginc, G. *Optical Properties of Nanostructured Materials: A Review*. J Nanophotonics. **5**, 052502, (2011).

[129] Wang, L. and Zhu, Y. F. *Effects of Nanostructure on Catalytic Degradation of Ethanol on $SrCO_3$ Catalysts*. J. Phys. Chem. B **109**, 5118, (2005).

[130] Bell, A. T. *The Impact of Nanoscience on Heterogeneous Catalysis*. Science **299**, 1688, (2003).

[131] Goesmann, H. and Feldmann, C. *Nanoparticulate Functional Materials*. Angew. Chem. Int. Ed. **49**, 1362, (2010).

[132] Lee, H., Kim, C., Yang, S., Han, J. W. and Kim, J. *Shape-Controlled Nanocrystals for Catalytic Applications*. Catal. Surv. Asia **16**, 14, (2012).

[133] Somorjai, G. A. and Kliewer, C. J. *Reaction Selectivity in Heterogeneous Catalysis*. React. Kinet. Catal. Lett. **96**, 191, (2009).

[134] Haruta, M., Kobayashi, T., Sano, H. and Yamada, N. *Novel Gold Catalysts for the Oxidation of Carbon Monoxide at a Temperature far Below 0 °C*. Chem. Lett., 405, (1987).

[135] Tessonnier, J. P. and Su, D. S. *Recent Progress on the Growth Mechanism of Carbon Nanotubes: A Review*. ChemSusChem **4**, 824, (2011).

[136] Kumar, M. and Ando, Y. *Chemical Vapor Deposition of Carbon Nanotubes: A Review on Growth Mechanism and Mass Production*. J. Nanosci. Nanotechnol. **10**, 3739, (2010).

[137] Luo, W. D., Duan, W. H., Louie, S. G. and Cohen, M. L. *Structural and Electronic Properties of n-doped and p-doped $SrTiO_3$*. Phys. Rev. B **70**, (2004).

[138] Guo, X. G. et al. *Electronic Band Structure of Nb Doped $SrTiO_3$ from First Principles Calculation*. Phys. Lett. **317**, 501, (2003).

[139] Liang, Y. et al. *Hetero-epitaxy of Perovskite Oxides on GaAs(001) by Molecular Beam Epitaxy*. Appl. Phys. Lett. **85**, 1217, (2004).

[140] Arras, R., Ruiz, V. G., Pickett, W. E. and Pentcheva, R. *Tuning the Two-dimensional Electron Gas at the $LaAlO_3/SrTiO_3$(001) Interface by Metallic Contacts*. Phys. Rev. B **85**, 125404, (2012).

[141] Annadi, A. et al. *Anisotropic Two-dimensional Electron Gas at The $LaAlO_3/SrTiO_3(110)$ Interface*. Nat. Commun. **4**, 1, (2013).

[142] Wu, C., Kruska, K. and Castell, M. R. *Initial Growth Stages of Titanium and Barium Oxide Films on $SrTiO_3(001)$*. Surf. Sci. **618**, 94, (2013).

[143] Johnston, K., Castell, M. R., Paxton, A. T. and Finnis, M. W. *$SrTiO_3(001)(2\times1)$ Reconstructions: First-principles Calculations of Surface Energy and Atomic Structure Compared with Scanning Tunneling Microscopy Images*. Phys. Rev. B **70**, 085415, (2004).

[144] Silly, F. and Castell, M. R. *Self-assembled Supported Co Nanocrystals: the Adhesion Energy of Face-centered-cubic Co on $SrTiO_3(001)$-(2×2)*. Appl. Phys. Lett. **87**, 053106, (2005).

[145] Lin, Y. et al. *The (2×2) Reconstructions on The $SrTiO_3$ (001) surface: A Combined Scanning Tunneling Microscopy and Density Functional Theory Study*. Surf. Sci. **605**, L51, (2011).

[146] Becerra-Toledo, A. E., Marshall, M. S. J., Castell, M. R. and Marks, L. D. *$c(4\times2)$ and Related Structural Units on the $SrTiO_3(001)$ Surface: Scanning Tunneling Microscopy, Density Functional Theory, and Atomic Structure*. J. Chem. Phys **136**, 214701, (2012).

[147] Erdman, N. et al. *Surface Structures of $SrTiO_3(001)$: A TiO_2-rich Reconstruction with A $c(4\times2)$ Unit Cell*. J. Am. Chem. Soc. **125**, 10050, (2003).

[148] Jiang, Q. and Zegenhagen, J. *$SrTiO_3(001)$-$c(6\times2)$: A Long-range, Atomically Ordered Surface Stable in Oxygen and Ambient Air*. Surf. Sci. **367**, L42, (1996).

[149] Newell, D. T., Harrison, A., Silly, F. and Castell, M. R. *$SrTiO_3$ (001)-$(\sqrt{5}\times\sqrt{5})$-R26.6° Reconstruction: A Surface Resulting from Phase Separation in A Reducing Environment*. Phys. Rev. B **75**, 205429, (2007).

[150] Kubo, T. and Nozoye, H. *Surface Structure of $SrTiO_3(100)$*. Surf. Sci. **542**, 177, (2003).

[151] Matsumoto, T., Tanaka, H., Kawai, T. and Kawai, S. *STM-imaging of A $SrTiO_3(100)$ Surface with Atomic-scale Resolution*. Surf. Sci. **278**, L153, (1992).

[152] Naito, M. and Sato, H. *Reflection High-energy Electron Diffraction Study on the $SrTiO_3$ Surface Structure*. Physica C Supercond. **229**, 1, (1994).

[153] Haruyama, Y., Aiura, Y., Bando, H., Nishihara, Y. and Kato, H. *Annealing Temperature Dependence on the Electronic Structure of the Reduced $SrTiO_3$ (111) Surface*. J. Electron. Spectrosc. Relat. Phenom. **88-91**, 695, (1998).

[154] Saghayezhian, M. et al. *Polar Compensation at the Surface of $SrTiO_3$ (111)*. Phys. Rev. B **93**, 125408, (2016).

[155] Marks, L. D., Chiaramonti, A. N., Rahman, S. U. and Castell, M. R. *Transition from Order to Configurational Disorder for Surface Reconstructions on $SrTiO_3(111)$*. Phys. Rev. Lett. **114**, 226101, (2015).

[156] Chiaramonti, A. N., Lanier, C. H., Marks, L. D. and Stair, P. C. *Time, Temperature, and Oxygen Partial Pressure-dependent Surface Reconstructions on $SrTiO_3(111)$: A Systematic Study of Oxygen-rich Conditions*. Surf. Sci. **602**, 3018, (2008).

[157] Feng, J., Zhu, X. and Guo, J. *Reconstructions on $SrTiO_3$(111) Surface Tuned by Ti/Sr Deposition*. Surf. Sci. **614**, 38, (2013).

[158] Lo, W. J. and Somorjai, G. A. *Temperature-dependent Surface Structure, Composition, and Electronic Properties of the Clean $SrTiO_3$(111) Crystal Face: Low-energy-electron Diffraction, Auger-electron Spectroscopy, Electron Energy Loss, and Ultraviolet-photolelectron Spectroscopy Studies*. Phys. Rev. B **17**, 4942, (1978).

[159] Ferrer, S. and Somorjai, G. A. *UPS and XPS Studies of the Chemisorption of O_2, H_2 and H_2O on Reduced and Stoichiometric $SrTiO_3$(111) Surfaces; The Effects of Illumination*. Surf. Sci. **94**, 41, (1980).

[160] Ferrer, S. and Somorjai, G. A. *Evidence for Photodissociation of Water Vapor on Reduced Strontium Titanate (111) Surfaces in a High Vacuum Environment*. J. phys. Chem. **85**, 1464, (1981).

[161] Tanaka, H. and Kawai, T. *Surface Structure of Reduced $SrTiO_3$ (111) Observed by Scanning Tunneling Microscopy*. Surf. Sci. **365**, 437, (1996).

[162] Sigmund, W. M. et al. *A Titanium-rich (111) Surface of $SrTiO_3$ Single Crystals by Thermal Annealing*. Appl. Phys. A **64**, 219, (1997).

[163] Sekiguchi, S. et al. *Structure Analysis of $SrTiO_3$ (111) Polar Surfaces*. Jpn. J. Appl. Phys. **37**, 4140, (1998).

[164] Sekiguchi, S. et al. *Atomic Force Microscopic Observation of $SrTiO_3$ Polar Surface*. Solid State Ion. **108**, 73, (1998).

[165] Gomann, A. et al. *Electronic Structure and Topography of Annealed $SrTiO_3$(111) Surfaces Studied with MIES and STM*. Appl. Surf. Sci. **252**, 196, (2005).

[166] Pojani, A., Finocchi, F. and Noguera, C. *Polarity on the $SrTiO_3$ (111) and (110) Surfaces*. Surf. Sci. **442**, 179, (1999).

[167] Pojani, A., Finocchi, F. and Noguera, C. *A Theoretical Study of the Unreconstructed Polar (111) Face of $SrTiO_3$*. Appl. Surf. Sci. **142**, 177, (1999).

[168] Marks, L. D., Chiaramonti, A. N., Tran, F. and Blaha, P. *The Small Unit cell Reconstructions of $SrTiO_3$(111)*. Surf. Sci. **603**, 2179, (2009).

[169] Ross, F. M., Tromp, R. M. and Reuter, M. C. *Transition States between Pyramids and Domes during Ge/Si Island Growth*. Science **286**, 1931, (1999).

[170] Medeiros-Ribeiro, G., Bratkovski, A. M., Kamins, T. I., Ohlberg, D. A. A. and Williams, R. S. *Shape Transition of Germanium Nanocrystals on a Silicon (001) Surface from Pyramids to Domes*. Science **279**, 353, (1998).

[171] Sone, H., Mishima, T., Miyachi, A., Fukuda, T. and Hosaka, S. *Growth Control of Self-assembled $ErSi_2$ Nanowires on Si(001) and Si(110) Surfaces*. Microelectron. Eng. **84**, 1491, (2007).

[172] Watanabe, R. et al. *Formation and Structure Analysis of Very Long $ErSi_2$ Nanowires Formed on Si(110) Substrates*. Jpn. J. Appl. Phys. **45**, 5535, (2006).

[173] Linsebigler, A. L., Lu, G. Q. and Yates, J. T. *Photocatalysis on TiO_2 surfaces: principles, mechanisms, and selected results*. Chem. Rev. **95**, 735, (1995).

[174] Carp, O., Huisman, C. L. and Reller, A. *Photoinduced Reactivity of Titanium Dioxide*. Prog. Solid State Chem. **32**, 33, (2004).

[175] Thompson, T. L. and Yates, J. T. *Surface Science Studies of the Photoactivation of TiO_2-new Photochemical Processes*. Chem. Rev. **106**, 4428, (2006).

[176] Bankmann, M., Brand, R., Engler, B. H. and Ohmer, J. *Forming of High Surface Area TiO_2 to Catalyst Supports*. Catal. Today **14**, 225, (1992).

[177] Bagheri, S., Muhd Julkapli, N. and Bee Abd Hamid, S. *Titanium Dioxide as a Catalyst Support in Heterogeneous Catalysis*. Scientific World J., 727496 (2014).

[178] Gonzalez, I. D. et al. *A Comparative Study of the Water Gas Shift Reaction over Platinum Catalysts Supported on CeO_2, TiO_2 and Ce-modified TiO_2*. Catal. Today **149**, 372, (2010).

[179] Zhang, T. H. et al. *Application of TiO_2 with Different Structures in Solar Cells*. Chin. Phys. B **21**, (2012).

[180] Garmaroudi, Z. A. and Mohammadi, M. R. *Design of TiO_2 Dye-sensitized Solar Cell Photoanode Electrodes with Different Microstructures and Arrangement Modes of the Layers*. J. Sol-Gel Sci. Technol. **76**, 666, (2015).

[181] Long, H., Chen, A., Yang, G., Li, Y. and Lu, P. *Third-order Optical Nonlinearities in Anatase and Rutile TiO_2 Thin Films*. Thin Solid Films **517**, 5601, (2009).

[182] Wang, W. and Ku, Y. *The Light Transmission and Distribution in an Optical Fiber Coated with TiO_2 Particles*. Chemosphere **50**, 999, (2003).

[183] Ghadiry, M. et al. *Nano-Anatase TiO_2 for High Performance Optical Humidity Sensing on Chip*. Sensors **16**, (2016).

[184] Crossland, E. J. W. et al. *Mesoporous TiO_2 Single Crystals Delivering Enhanced Mobility and Optoelectronic Device Performance*. Nature **495**, 215-219, (2013).

[185] Elshamy, M., Mostafa, H., Said, M. S. and Ieee. in *2014 Ieee 27th Canadian Conference on Electrical and Computer Engineering Canadian Conference on Electrical and Computer Engineering* (2014).

[186] Sanjinés, R. et al. *Electronic Structure of Anatase TiO_2 Oxide*. J. Appl. Phys. **75**, 2945, (1994).

[187] Schuisky, M. et al. *Atomic Layer Chemical Vapor Deposition of TiO_2 Low Temperature Epitaxy of Rutile and Anatase*. J. Electrochem. Soc. **147**, 3319, (2000).

[188] Mo, S. D. and Ching, W. Y. *Electronic and Optical Properties of Three Phases of Titanium Dioxide: Rutile, Anatase, and Brookite*. Phys. Rev. B **51**, 13 023, (1995).

[189] Pang, C. L., Grinter, D. C., Matharu, J. and Thornton, G. *A Scanning Tunneling Microscopy Study of Ultrathin Film Rutile $TiO_2(110)$ Supported on $W(100)$-$O(2\times1)$*. J. Phys. Chem. C **117**, 25622, (2013).

[190] Wang, Y., Shao, X. and Wang, B. *Preparation, Characterization and Photocatalytic Activity of Cr-Doped Rutile $TiO_2(110)$ Single Crystal Thin Films*. Acta Phys-Chim. Sin. **29**, 1363, (2013).

[191] Diebold, U. *The Surface Science of Titanium Dioxide*. Surf. Sci. Rep. **48**, 53, (2003).

[192] Diebold, U. *Structure and Properties of TiO_2 Surfaces: A Brief Review*. Appl. Phys. A **76**, 681, (2003).

[193] Silversmit, G., Poelman, H., Fiermans, L. and De Gryse, R. *An X-ray Photoelectron Diffraction Study of a TiO_2(001) Anatase Single Crystal Mineral*. Solid State Commun. **119**, 101, (2001).

[194] Herman, G. S., Gao, Y., Tran, T. T. and Osterwalder, J. *X-ray Photoelectron Diffraction Study of an Anatase Thin Film: TiO_2(001)*. Surf. Sci. **447**, 201, (2000).

[195] Gong, X. Q., Selloni, A., Batzill, M. and Diebold, U. *Steps on Anatase TiO_2(101)*. Nat. Mater. **5**, 665, (2006).

[196] Sasahara, A., Droubay, T. C., Chambers, S. A., Uetsuka, H. and Onishi, H. *Topography of Anatase TiO_2 Film Synthesized on $LaAlO_3$(001)*. Nanotechnology **16**, S18, (2005).

[197] Ruzycki, N., Herman, G. S., Boatner, L. A. and Diebold, U. *Scanning Tunneling Microscopy Study of the Anatase (100) Surface*. Surf. Sci. **529**, L239, (2003).

[198] De Angelis, F., Di Valentin, C., Fantacci, S., Vittadini, A. and Selloni, A. *Theoretical Studies on Anatase and Less Common TiO_2 Phases: Bulk, Surfaces, and Nanomaterials*. Chem. Rev. **114**, 9708, (2014).

[199] Wang, Y. et al. *Role of Point Defects on the Reactivity of Reconstructed Anatase Titanium Dioxide (001) Surface*. Nat. Commun. **4**, 2214, (2013).

[200] Oropeza, F. E. et al. *Growth of Epitaxial Anatase Nano Islands on $SrTiO_3$(001) by Dip Coating*. Cryst. Growth Des. **13**, 1438, (2013).

[201] Ambrus, Z. et al. *Low Temperature Synthesis, Characterization and Substrate-dependent Photocatalytic Activity of Nanocrystalline TiO_2 with Tailor-Made Rutile to Anatase Ratio*. Appl. Catal. A: Gen. **340**, 153, (2008).

[202] Poelman, H. et al. *XPD Investigation of V_2O_5/TiO_2 Anatase Model Catalysts*. Surf. Sci. **377**, 819, (1997).

[203] Durinck, G. et al. *Observation of Surface Phonons on the (001) and (100) Surfaces of Anatase Minerals*. Solid State Commun. **80**, 579, (1991).

[204] Herman, G. S. and Gao, Y. *Growth of Epitaxial Anatase (001) and (101) Films*. Thin Solid Films **397**, 157, (2001).

[205] Gribb, A. A. and Banfield, J. F. *Particle Size Effects on Transformation Kinetics and Phase Stability in Nanocrystalline TiO_2*. Am. Mineral. **82**, 717-728, (1997).

[206] Wetchakun, N., Incessungvorn, B., Wetchakun, K. and Phanichphant, S. *Influence of Calcination Temperature on Anatase to Rutile Phase Transformation in TiO_2 Nanoparticles Synthesized by the Modified sol-gel Method*. Mater. Lett. **82**, 195, (2012).

[207] Borkar, S. A. and Dharwadkar, S. R. *Temperatures and Kinetics of Anatase to Rutile Transformation in Doped TiO_2 Heated in Microwave Field*. J. Therm. Anal. Calorim. **78**, 761, (2004).

[208] Lazzeri, M., Vittadini, A. and Selloni, A. *Structure and Energetics of Stoichiometric TiO_2 Anatase Surfaces*. Phys. Rev. B **63**, (2001).

[209] Berger, H., Tang, H. and Levy, F. *Growth and Raman Spectroscopic Characterization of TiO_2 Anatase Single Crystals*. J. Crys. Growth **130**, 108, (1993).

[210] Forro, L. et al. *High Mobility Ntype Charge Carriers in Large Single Crystals of Anatase (TiO_2)*. J. Appl. Phys. **75**, 633, (1994).

[211] Tang, H., Berger, H., Schmid, P. E., Levy, F. and Burri, G. *Photoluminescence in TiO_2 Anatase Single Crystals*. Solid State Commun. **87**, 847, (1993).

[212] Tang, H., Prasad, K., Sanjines, R., Schmid, P. E. and Levy, F. *Electrical and Optical Properties of TiO_2 Anatase Thin Films*. J. Appl. Phys. **75**, 2042, (1994).

[213] Hengerer, R., Bolliger, B., Erbudak, M. and Gratzel, M. *Structure and Stability of the Anatase TiO_2 (101) and (001) Surfaces*. Surf. Sci. **460**, 162, (2000).

[214] Herman, G. S., Sievers, M. R. and Gao, Y. *Structure Determination of the Two-domain (1×4) Anatase TiO_2(001) Surface*. Phys. Rev. Lett. **84**, 3354, (2000).

[215] Liang, Y., Gan, S. P., Chambers, S. A. and Altman, E. I. *Surface Structure of Anatase TiO_2(001): Reconstruction, Atomic Steps, and Domains*. Phys. Rev. B **63**, 235402, (2001).

[216] Ciancio, R. et al. *Nanostructure of Buried Interface Layers in TiO_2 Anatase Thin Films Grown on $LaAlO_3$ and $SrTiO_3$ Substrates*. Nanoscale **4**, 91, (2012).

[217] Matsumoto, Y., Miura, Y. and Takata, S. *Thickness-dependent Flat Band Potential of Anatase TiO_2(001) Epitaxial Films on Nb:$SrTiO_3$(001) Investigated by UHV-electrochemistry Approach*. J. Phys. Chem. C **120**, 1472, (2016).

[218] Zhu, M. et al. *A High-resolution Transmission Electron Microscopy Investigation of the Microstructure of TiO_2 Anatase Film Deposited on $LaAlO_3$ and $SrTiO_3$ Substrates by Laser Ablation*. Thin Solid Films **441**, 140, (2003).

[219] Lotnyk, A., Senz, S. and Hesse, D. *Epitaxial Growth of TiO_2 Thin Films on $SrTiO_3$, $LaAlO_3$ and Yttria-stabilized Zirconia Substrates by Electron Beam Evaporation*. Thin Solid Films **515**, 3439, (2007).

[220] Amano, F. et al. *Decahedral Single-crystalline Particles of Anatase Titanium(IV) Oxide with High Photocatalytic Activity*. Chem. Mater. **21**, 2601, (2009).

[221] Shao, R., Wang, C. M., McCready, D. E., Droubay, T. C. and Chambers, S. A. *Growth and Structure of MBE Grown TiO_2 Anatase Films with Rutile Nano-crystallites*. Surf. Sci. **601**, 1582, (2007).

[222] Chen, S. et al. *Ultrahigh Vacuum Metalorganic Chemical Vapor Deposition Growth and in Situ Characterization of Epitaxial TiO_2 Films*. J. Vac. Sci. Technol. A **11**, 2419, (1993).

[223] Tanner, R. E., Sasahara, A., Liang, Y., Altman, E. I. and Onishi, H. *Formic Acid Adsorption on Anatase TiO_2(001)-(1×4) Thin Films Studied by NC-AFM and STM*. J. Phys. Chem. B **106**, 8211, (2002).

[224] Gao, W., Klie, R. and Altman, E. I. *Growth of Anatase Films on Vicinal and Flat $LaAlO_3$(110) Substrates by Oxygen Plasma Assisted Molecular Beam Epitaxy*. Thin Solid Films **485**, 115, (2005).

[225] Murakami, M. et al. *Anatase TiO_2 Thin Films Grown on Lattice-matched $LaAlO_3$ Substrate by Laser Molecular-beam Epitaxy*. Appl. Phys. Lett. **78**, 2664, (2001).

[226] Schmidt, D. A., Ohta, T., Yu, Q. and Olmstead, M. A. *Influence of Perovskite Termination on Oxide Heteroepitaxy*. J. Appl. Phys. **99**, 113521, (2006).

[227] Tersoff, J. and Tromp, R. M. *Shape Transition in Growth of Strained Islands: Spontaneous Formation of Quantum Wires*. Phys. Rev. Lett. **70**, 2782, (1993).

[228] Xia, Y. et al. *Atomic Structure of the Anatase TiO_2(001) Surface*. J. Phys. Chem. Lett. **4**, 2958, (2013).

[229] Yuan, W. et al. *Real-time Observation of Reconstruction Dynamics on TiO_2(001) Surface under Oxygen via an Environmental Transmission Electron microscope*. Nano Lett. **16**, 132, (2016).

[230] Lazzeri, M. and Selloni, A. *Stress-driven Reconstruction of An Oxide Surface: the Anatase TiO_2(001)-(1×4) Surface*. Phys. Rev. Lett. **87**, 266105, (2001).

[231] Winterbottom, W. L. *Equilibrium Shape of a Small Particle in Contact with a Foreign Substrate*. Acta Metall. **15**, 303, (1967).

[232] Tauster, S. J., Fung, S. C. and Garten, R. L. *Strong Metal-Support Interactions. Group 8 Noble Metals Supported on TiO_2*. J. Am. Chem. Soc. **100**, 170, (1978).

[233] Tauster, S. J. *Strong Metal-Support Interations*. Acc. Chem. Res. **20**, 390, (1987).

[234] Zhang, K., Shaikhutdinov, S. and Freund, H. J. *Does the Surface Structure of Oxide Affect the Strong Metal-Support Interaction with Platinum? Platinum on Fe_3O_4(001) versus Fe_3O_4(111)*. ChemCatChem. **7**, 3725, (2015).

[235] Bruix, A. et al. *A New Type of Strong Metal-Support Interaction and the Production of H_2 through the Transformation of Water on Pt/CeO_2(111) and Pt/CeO_x/TiO_2(110) Catalysts*. J. Am. Chem. Soc. **134**, 8968, (2012).

[236] Matsubu, J. C. et al. *Adsorbate-mediated Strong Metal-support Interactions in Oxide-supported Rh Catalysts*. Nat. Chem. **9**, 120, (2017).

[237] Bowker, M., Stone, P., Bennett, R. and Perkins, N. *CO Adsorption on a Pd/TiO_2(110) Model Catalyst*. Surf. Sci. **497**, 155, (2002).

[238] Bonanni, S., Ait-Mansour, K., Brune, H. and Harbich, W. *Overcoming the Strong Metal-Support Interaction State: CO Oxidation on TiO_2(110)-Supported Pt Nanoclusters*. ACS Catal. **1**, 385, (2011).

[239] Haller, G. L. and Resasco, D. E. *Metal-Support Interaction: Group-VIII Metals and Reducilble Oxides*. Adv. Catal. **36**, 173, (1989).

[240] Li, Y. Z. et al. *The Effect of Titania Polymorph on the Strong metal-support Interaction of Pd/TiO_2 Catalysts and Their Application in the Liquid Phase Selective Hydrogenation of Long Chain Alkadienes*. J. Mol. Catal. A: Chem. **216**, 107, (2004).

[241] Kang, J. H., Shin, E. W., Kim, W. J., Park, J. D. and Moon, S. H. *Selective Hydrogenation of Acetylene on TiO_2-added Pd Catalysts*. J. Catal. **208**, 310, (2002).

[242] Silly, F. and Castell, M. R. *Bimodal Growth of Au on $SrTiO_3$(001)*. Phys. Rev. Lett. **96**, 086104, (2006).

[243] Batzill, M. and Diebold, U. *Surface Studies of Gas Sensing Metal Oxides*. Phys. Chem. Chem. Phys. **9**, 2307, (2007).

[244] Della Gaspera, E. et al. *Cooperative Effect of Au and Pt Inside TiO_2 Matrix for Optical Hydrogen Detection at Room Temperature Using Surface Plasmon Spectroscopy*. Nanoscale **4**, 5972, (2012).

[245] Silly, F. and Castell, M. R. *Fe Nanocrystal Growth on $SrTiO_3(001)$*. Appl. Phys. Lett. **87**, 063106, (2005).

[246] Silly, F. and Castell, M. R. *Growth of Ag Icosahedral Nanocrystals on a $SrTiO_3(001)$ Support*. Appl. Phys. Lett. **87**, 213107, (2005).

[247] Silly, F., Powell, A. C., Martin, M. G. and Castell, M. R. *Growth Shapes of Supported Pd Nanocrystals on $SrTiO_3(001)$*. Phys. Rev. B **72**, 165403, (2005).

[248] Fujishima, A., Rao, T. N. and Tryk, D. A. *Titanium Dioxide Photocatalysis*. J. Photochem. Photobiol. C. **1**, 1, (2000).

[249] Chen, X. and Mao, S. S. *Titanium Dioxide Nanomaterials: Synthesis, Properties, Modifications, and Applications*. Chem. Rev. **107**, 2891, (2007).

[250] Rothenberger, G., Moser, J., Gratzel, M., Serpone, N. and Sharma, D. K. *Charge Carrier Trapping and Recombination Dynamics in Small Semiconductor Particles*. J. Am. Chem. Soc. **107**, 8054, (1985).

[251] Tachikawa, T., Fujitsuka, M. and Majima, T. *Mechanistic Insight into The TiO_2 Photocatalytic Reactions: Design of New Photocatalysts*. J. Phys. Chem. C **111**, 5259, (2007).

[252] Tamaki, Y., Hara, K., Katoh, R., Tachiya, M. and Furube, A. *Femtosecond Visible-to-IR Spectroscopy of TiO_2 Nanocrystalline Films: Elucidation of the Electron Mobility before Deep Trapping*. J. Phys. Chem. C **113**, 11741, (2009).

[253] Valden, M., Lai, X. and Goodman, D. W. *Onset of Catalytic Activity of Gold Clusters on Titania with The Appearance of Nonmetallic Properties*. Science **281**, 1647, (1998).

[254] Gong, X. Q., Selloni, A., Dulub, O., Jacobson, P. and Diebold, U. *Small Au and Pt Clusters at the Anatase $TiO_2(101)$ Surface: Behavior at Terraces, Steps, and Surface Oxygen Vacancies*. J. Am. Chem. Soc. **130**, 370, (2008).

[255] Kolmakov, A. and Goodman, D. W. *Scanning Tunneling Microscopy of Gold Clusters on $TiO_2(110)$: CO Oxidation at Elevated Pressures*. Surf. Sci. **490**, L597, (2001).

[256] Min, B. K. and Friend, C. M. *Heterogeneous Gold-based Catalysis for Green Chemistry: Low-temperature CO Oxidation and Propene Oxidation*. Chem. Rev. **107**, 2709, (2007).

[257] Kontapakdee, K., Panpranot, J. and Praserthdam, P. *Effect of Ag Addition on The Properties of Pd-Ag/TiO_2 Catalysts Containing Different TiO_2 Crystalline Phases*. Catal. Commun. **8**, 2166, (2007).

[258] Sikhwivhilu, L. M., Coville, N. J., Naresh, D., Chary, K. V. R. and Vishwanathan, V. *Nanotubular Titanate Supported Palladium Catalysts: The Influence of Structure and Morphology on Phenol Hydrogenation Activity*. Appl. Catal. A Gen. **324**, 52, (2007).

[259] Kitano, M. et al. *Synthesis of Nanowire TiO_2 Thin Films by Hydrothermal Treatment and Their Photoelectrochemical Properties*. Catal. Lett. **119**, 217, (2007).

[260] Rayalu, S. S., Dubey, N., Labhsetwar, N. K., Kagne, S. and Devotta, S. *UV and Visibly Active Photocatalysts for Water Splitting Reaction*. Int. J. Hydrogen Energy **32**, 2776, (2007).

[261] Ni, M., Leung, M. K. H., Leung, D. Y. C. and Sumathy, K. *A Review and Recent Developments in Photocatalytic Water-splitting Using TiO_2 for Hydrogen Production*. Renew. Sustainable Energy Rev. **11**, 401, (2007).

[262] Iddir, H., Skavysh, V., Ogut, S., Browning, N. D. and Disko, M. M. *Preferential Growth of Pt on Rutile TiO_2*. Phys. Rev. B **73**, 041403, (2006).

[263] Yu, X. et al. *Synchrotron-Radiation Photoemission Study of Growth and Stability of Au Clusters on Rutile $TiO_2(110)$-1×1*. Chin. J. Chem. Phys. **22**, 339, (2009).

[264] Lira, E. et al. *Growth of Ag and Au Nanoparticles on Reduced and Oxidized Rutile $TiO_2(110)$ Surfaces*. Top. Catal. **56**, 1460, (2013).

[265] El-Azab, A., Gan, S. and Liang, Y. *Binding and Diffusion of Pt Nanoclusters on Anatase $TiO_2(001)$-(1×4) Surface*. Surf. Sci. **506**, 93, (2002).

[266] Vittadini, A. and Selloni, A. *Small Gold Clusters on Stoichiometric and Defected TiO_2 Anatase (101) and Their Interaction with CO: A Density Functional Study*. J. Chem. Phys. **117**, 353, (2002).

[267] Balasanthiran, C. and Hoefelmeyer, J. D. *Facile Method to Attach Transition Metal Ions to the Surface of Anatase TiO_2 Nanorods*. Chem. Commun. **50**, 5721, (2014).

[268] Shiraishi, Y. et al. *Platinum Nanoparticles Supported on Anatase Titanium Dioxide as Highly Active Catalysts for Aerobic Oxidation under Visible Light Irradiation*. ACS Catal. **2**, 1984, (2012).

[269] Shiraishi, Y., Sakamoto, H., Sugano, Y., Ichikawa, S. and Hirai, T. *Pt-Cu Bimetallic Alloy Nanoparticles Supported on Anatase TiO_2: Highly Active Catalysts for Aerobic Oxidation Driven by Visible Light*. Acs Nano **7**, 9287, (2013).

[270] Fox, M. A. and Dulay, M. T. *Heterogeneous Photocatalysis*. Chem. Rev. **93**, 341, (1993).

[271] Maldotti, A., Molinari, A. and Amadelli, R. *Photocatalysis with Organized Systems for The Oxofunctionalization of Hydrocarbons by O_2*. Chem. Rev. **102**, 3811, (2002).

[272] Palmisano, G., Augugliaro, V., Pagliaro, M. and Palmisano, L. *Photocatalysis: A Promising Route for 21st Century Organic Chemistry*. Chem. Commun., 3425, (2007).

[273] Fagnoni, M., Dondi, D., Ravelli, D. and Albini, A. *Photocatalysis for The Formation of The C-C Bond*. Chem. Rev. **107**, 2725, (2007).

[274] Shiraishi, Y. and Hirai, T. *Selective Organic Transformations on Titanium Oxide-based Photocatalysts*. J. Photochem. Photobiol. C. **9**, 157, (2008).

[275] Chen, M. S. and Goodman, D. W. *Active structure of Supported Au Catalysts (Review)*. Catal. Today **111**, 22, (2006).

[276] Panagiotopoulou, P. and Kondarides, D. I. *Effect of Morphological Characteristics of TiO_2-supported Noble Metal Catalysts on Their Activity for The Water-gas Shift Reaction*. J. Catal. **225**, 327, (2004).

[277] Panagiotopoulou, P., Christodoulakis, A., Kondarides, D. I. and Boghosian, S. *Particle Size Effects On The Reducibility of Titanium Dioxide and Its Relation to The Water-gas Shift Activity of Pt/TiO_2 Catalysts*. J. Catal. **240**, 114, (2006).

[278] Sakurai, H., Ueda, A., Kobayashi, T. and Haruta, M. *Low-temperature Water-gas Shift Reaction Over Gold Deposited on TiO_2*. Chem. Commun., 271, (1997).

[279] Zhang, J. L. et al. *Nucleation and Growth of Palladium Clusters on Anatase TiO_2(101) Surface: A First Principle Study*. J. Phys. Chem. C **112**, 19506, (2008).

[280] Duan, X., Wang, C., Pan, A., Yu, R. and Duan, X. *Two-dimensional Transition Metal Dichalcogenides as Atomically Thin Semiconductors: Opportunities and Challenges*. Chem. Soc. Rev. **44**, 8859, (2015).

[281] Chhowalla, M. et al. *The Chemistry of Two-dimensional Layered Transition Metal Dichalcogenide Nanosheets*. Nat. Chem. **5**, 263, (2013).

[282] Wilson, J. A. and Yoffe, A. D. *The Transition Metal Dichalcogenides Discussion and Interpretation of the Observed Optical, Electrical and Structural Properties*. Adv. Phys. **18**, 193, (1969).

[283] Ghatak, S., Pal, A. N. and Ghosh, A. *Nature of Electronic States in Atomically Thin MoS_2 Field-Effect Transistors*. Acs Nano. **5**, 7707, (2011).

[284] Kam, K. K. and Parkinson, B. A. *Detailed Photocurrent Spectroscopy of the Semiconducting Group VIB Transition Metal Dichalcogenides*. J. Phys. Chem. **86**, 463, (1982).

[285] Radisavljevic, B., Radenovic, A., Brivio, J., Giacometti, V. and Kis, A. *Single-layer MoS_2 Transistors*. Nat. Nanotechnol. **6**, 147, (2011).

[286] Wypych, F. and Schollhorn, R. *1T-MoS2, a New Metallic Modification of Molybdenum Disulfide*. J. Chem. Soc., Chem. Commun., 1386, (1992).

[287] Guo, X. Y., Yang, G. H., Zhang, J. F. and Xu, X. H. *Structural, Mechanical and Electronic Properties of in-plane 1T/2H Phase Interface of MoS_2 heterostructures*. AIP Adv. **5**, 097174, (2015).

[288] Lv, R. et al. *Transition Metal Dichalcogenides and Beyond: Synthesis, Properties, and Applications of Single- and Few-Layer Nanosheets*. Acc. Chem. Res. **48**, 56, (2015).

[289] Novoselov, K. S. et al. *Electric field Effect in Atomically Thin Carbon Films*. Science **306**, 666, (2004).

[290] Wang, Q., Kalantar-Zadeh, K., Kis, A., Coleman, J. N. and Strano, M. S. *Electronics and Optoelectronics of Two-Dimensional Transition Metal Dichalcogenides*. Nat. Nanotechnol. **7**, 699, (2012).

[291] Li, H. et al. *Fabrication of Single- and Multilayer MoS2 Film-Based Field-Effect Transistors for Sensing NO at Room Temperature*. Small **8**, 63, (2012).

[292] Bertolazzi, S., Krasnozhon, D. and Kis, A. *Nonvolatile Memory Cells Based on MoS_2/Graphene Heterostructures*. Acs Nano **7**, 3246, (2013).

[293] Mai, C. et al. *Many-Body Effects in Valleytronics: Direct Measurement of Valley Lifetimes in Single-Layer MoS2*. Nano Lett. **14**, 202, (2014).

[294] Mak, K. F., He, K. L., Shan, J. and Heinz, T. F. *Control of Valley Polarization in Monolayer MoS_2 by Optical Helicity*. Nat. Nanotechnol. **7**, 494, (2012).

[295] Lopez-Sanchez, O., Lembke, D., Kayci, M., Radenovic, A. and Kis, A. *Ultrasensitive Photodetectors Based on Monolayer MoS2*. Nat. Nanotechnol. **8**, 497, (2013).

[296] Perea-Lopez, N. et al. *CVD-grown Monolayered MoS_2 as An Effective Photosensor Operating at Low-voltage*. 2D Mater. **1**, (2014).

[297] Perea-Lopez, N. et al. *Photosensor Device Based on Few-Layered WS_2 Films*. Adv. Funct. Mater. **23**, 5511-5517, (2013).

[298] Mak, K. F., Lee, C., Hone, J., Shan, J. and Heinz, T. F. *Atomically Thin MoS_2: A New Direct-Gap Semiconductor*. Phys. Rev. Lett **105**, (2010).

[299] Fivaz, R. and Mooser, E. *Mobility of Charge Carriers in Semiconducting Layer Structures*. Phys. Rev. **163**, 743, (1967).

[300] Schwierz, F. *Graphene Transistors*. Nat. Nanotechnol. **5**, 487, (2010).

[301] Novoselov, K. S. and Castro Neto, A. H. *Two-dimensional Crystals-based Heterostructures: Materials with Tailored Properties*. Phys. Scripta **T146**, (2012).

[302] Li, H., Wu, J. M. T., Yin, Z. Y. and Zhang, H. *Preparation and Applications of Mechanically Exfoliated Single-Layer and Multi Layer MoS_2 and WSe_2 Nanosheets*. Acc. Chem. Res. **47**, 1067, (2014).

[303] Li, H. et al. *From Bulk to Monolayer MoS_2: Evolution of Raman Scattering*. Adv.Funct. Mater. **22**, 1385, (2012).

[304] Zeng, Z. Y. et al. *Single-Layer Semiconducting Nanosheets: High-Yield Preparation and Device Fabrication*. Angew. Chem. Int. Ed. **50**, 11093, (2011).

[305] Dungey, K. E., Curtis, M. D. and Penner-Hahn, J. E. *Structural Characterization and Thermal Stability of MoS_2 Intercalation Compounds*. Chem. Mater. **10**, 2152, (1998).

[306] Benavente, E., Santa Ana, M. A., Mendizabal, F. and Gonzalez, G. *Intercalation Chemistry of Molybdenum Disulfide*. Coord. Chem. Rev. **224**, 87, (2002).

[307] Eda, G. et al. *Photoluminescence from Chemically Exfoliated MoS_2*. Nano Lett. **11**, 5111, (2011).

[308] Liu, K. K. et al. *Growth of Large-Area and Highly Crystalline MoS_2 Thin Layers on Insulating Substrates*. Nano Lett. **12**, 1538, (2012).

[309] Zhan, Y. J., Liu, Z., Najmaei, S., Ajayan, P. M. and Lou, J. *Large-Area Vapor-Phase Growth and Characterization of MoS_2 Atomic Layers on a SiO_2 Substrate*. Small **8**, 966, (2012).

[310] Lee, Y. et al. *Synthesis of Wafer-scale Uniform Molybdenum Disulfide Films with Control over the Layer Number Using a Gas Phase Sulfur Precursor*. Nanoscale **6**, 2821, (2014).

[311] Schmidt, H. et al. *Transport Properties of Monolayer MoS_2 Grown by Chemical Vapor Deposition*. Nano Lett. **14**, 1909, (2014).

[312] Jeon, J. et al. *Layer-controlled CVD Growth of Large-area two-dimensional MoS_2 Films*. Nanoscale **7**, 1688, (2015).

[313] Wang, S. S. et al. *Shape Evolution of Monolayer MoS_2 Crystals Grown by Chemical Vapor Deposition*. Chem. Mater. **26**, 6371, (2014).

[314] Zhou, X. D. et al. *Atomic-scale Spectroscopy of Gated Monolayer MoS_2*. Nano Lett. **16**, 3148, (2016).

[315] Plechinger, G. et al. *Raman Spectroscopy of the Interlayer Shear Mode in few-layer MoS_2 Flakes*. Appl. Phys. Lett. **101**, (2012).

[316] Lee, C. et al. *Anomalous Lattice Vibrations of Single- and Few-Layer MoS_2*. Acs Nano **4**, 2695, (2010).

[317] Amani, M. et al. *Electrical Performance of Monolayer MoS_2 Field-effect Transistors Prepared by Chemical Vapor Deposition*. Appl. Phys. Lett. **102**, (2013).

[318] Coley, T. R., Goddard, W. A. and Baldeschwieler, J. D. *Theoretical Interpretation of Scanning Tunneling Microscopy Images: Application to the Molybdenum Disulfide Family of Transition Metal Dichalcogenides*. J. Vac. Sci. Technol., B. **9**, 470, (1991).

[319] Kobayashi, K. and Yamauchi, J. *Electronic Structure and Scanning-tunneling-microscopy Image of Molybdenum Dichalcogenide Surfaces*. Phys. Rev. B **51**, 17085, (1995).

[320] Magonov, S. N. and Whangbo, M. H. *Interpreting STM and AFM Images*. Adv. Mater. **6**, 355, (1994).

[321] Kobayashi, K. and Yamauchi, J. *Scanning Tunneling Microscopy Image of Transition-metal-dichalcogenide Surfaces*. Surf. Sci. **357**, 317, (1996).

[322] Fuhr, J. D., Saul, A. and Sofo, J. O. *Scanning Tunneling Microscopy Chemical Signature of Point Defects on the MoS_2(0001) Surface*. Phys. Rev. Lett. **92**, (2004).

[323] Helveg, S. et al. *Atomic-scale structure of single-layer MoS_2 nanoclusters*. Phys. Rev. Lett. **84**, 951, (2000).

[324] Lewandowska, R. (HORIBA Scientific, 2014).

[325] Bertrand, P. A. *Surface-phonon Dispersion of MoS_2*. Phys. Rev. B **44**, 5745, (1991).

[326] Rice, C. et al. *Raman-scattering Measurements and First-principles Calculations of Strain-induced Phonon Shifts in Monolayer MoS_2*. Phys. Rev. B **87**, (2013).

[327] Boukhicha, M., Calandra, M., Measson, M. A., Lancry, O. and Shukla, A. *Anharmonic Phonons in Few-layer MoS_2: Raman Spectroscopy of Ultralow Energy Compression and Shear Modes*. Phys. Rev. B **87**, (2013).

[328] Molina-Sanchez, A. and Wirtz, L. *Phonons in Single-layer and Few-layer MoS_2 and WS_2*. Phys. Rev. B **84**, (2011).

[329] van der Zande, A. M. et al. *Grains and Grain Boundaries in Highly Crystalline Monolayer Molybdenum Disulphide*. Nat. Mater. **12**, 554, (2013).

[330] Najmaei, S. et al. *Vapour Phase Growth and Grain Boundary Structure of Molybdenum Disulphide Atomic Layers*. Nat. Mater. **12**, 754, (2013).

[331] Ji, Q. Q., Zhang, Y., Zhang, Y. F. and Liu, Z. F. *Chemical Vapour Deposition of Group-VIB Metal Dichalcogenide Monolayers: Engineered Substrates from Amorphous to Single Crystalline*. Chem. Soc. Rev. **44**, 2587, (2015).

[332] Splendiani, A. et al. *Emerging Photoluminescence in Monolayer MoS_2*. Nano Lett. **10**, 1271, (2010).

[333] Dumcenco, D. et al. *Large-Area Epitaxial Mono layer MoS_2*. Acs Nano **9**, 4611, (2015).

[334] Ji, Q. Q. et al. *Unravelling Orientation Distribution and Merging Behavior of Mono layer MoS_2 Domains on Sapphire*. Nano Lett. **15**, 198, (2015).

[335] Buscema, M., Steele, G. A., van der Zant, H. S. J. and Castellanos-Gomez, A. *The Effect of the Substrate on the Raman and Photoluminescence Emission of Single-layer MoS_2*. Nano Res. **7**, 561, (2014).

[336] Bollinger, M. V. et al. *One-dimensional Metallic Edge States in MoS_2*. Phys. Rev. Lett. **87**, (2001).

[337] Lauritsen, J. V. et al. *Size-dependent Structure of MoS_2 Nanocrystals*. Nat. Nanotechnol. **2**, 53, (2007).

[338] Ji, Q. Q. et al. *Epitaxial Monolayer MoS2 on Mica with Novel Photoluminescence*. Nano Lett. **13**, 3870, (2013).

[339] Zhang, C. D., Johnson, A., Hsu, C. L., Li, L. J. and Shih, C. K. *Direct Imaging of Band Profile in Single Layer MoS_2 on Graphite: Quasiparticle Energy Gap, Metallic Edge States, and Edge Band Bending*. Nano Lett. **14**, 2443, (2014).

[340] Shi, Y. M. et al. *van der Waals Epitaxy of MoS_2 Layers Using Graphene As Growth Templates*. Nano Lett. **12**, 2784, (2012).

[341] Li, Y. Y. et al. *Photoluminescence of Monolayer MoS_2 on $LaAlO_3$ and $SrTiO_3$ Substrates*. Nanoscale **6**, 15248, (2014).

[342] Zhang, Y. et al. *Dendritic, Transferable, Strictly Monolayer MoS_2 Flakes Synthesized on $SrTiO_3$ Single Crystals for Efficient Electrocatalytic Applications*. Acs Nano **8**, 8617, (2014).

[343] Zhang, Y. et al. *Monolayer MoS_2 Dendrites on a Symmetry-Disparate $SrTiO_3$ (001) Substrate: Formation Mechanism and Interface Interaction*. Adv. Funct. Mater. **26**, 3299, (2016).

[344] Li, C. et al. *Substrate Effect on the Growth of Monolayer Dendritic MoS_2 on $LaAlO_3$ (100) and Its Electrocatalytic Applications*. 2D Mater. **3**, 035001, (2016).

[345] Mak, K. F. et al. *Tightly Bound Trions in Monolayer MoS_2*. Nat. Mater. **12**, 207, (2013).

[346] Jupille, J. and Thornton, G. *Defect at Oxide Surfaces*. Vol. 58 (Springer Series in Surface Science, 2015).

[347] Smereka, P. *Spiral Crystal Growth*. Physica D **138**, 282, (2000).

[348] Cejka, J., Corma, A. and Zones, S. *Zeolites and Catalysis: Synthesis, Reactions and Applications*. Vol. 1 (Wiley-VCH, 2010).

[349] Antczak, G. and Gert, E. *Surface diffusion: Metals, Metal atoms, and Clusters*. (Cambridge University Press, 2010).

[350] Methfessel, M., Hennig, D. and Scheffler, M. *Trends of the Surface Relaxations, Surface Energies, and Work Functions of the 4d Transition Metals*. Phys. Rev. B **46**, 4816, (1992).

[351] Farstad, M. H. et al. *TiOx Thin Films Grown on Pd(100) and Pd(111) by Chemical Vapor Deposition*. Surf. Sci. **649**, 80, (2016).

[352] Horcas, I. et al. *WSXM: a Software for Scanning Probe Microscopy and a Tool for Nanotechnology*. Rev. Sci. Instrum. **78**, 013705, (2007).

[353] Boffa, A. B. et al. *The Growth and Structure of Titanium Oxide Films on Pt(111) Investigated by LEED, XPS, ISS, and STM*. Surf. Sci. **326**, 80, (1995).

[354] Sedona, F. et al. *Ultrathin TiO_x Films on Pt(111): A LEED, XPS, and STM Investigation*. J. Phys. Chem. B **109**, 24411, (2005).

[355] Leisenberger, F. P. et al. *Surface and Subsurface Oxygen on Pd(111)*. Surf. Sci. **445**, 380, (2000).

[356] Xu, J., Sun, K. P., Zhang, L., Ren, Y. L. and Xu, X. L. *A Highly Efficient and Selective Catalyst for Liquid Phase Hydrogenation of Maleic Anhydride to Butyric Acidhly Efficient and Selective Catalyst for Liquid Phase Hydrogenation of Maleic Anhydride to Butyric Acid*. Catal. Commun. **6**, 462, (2005).

[357] Dandekar, A. and Vannice, M. A. *Crotonaldehyde Hydrogenation on Pt/TiO_2 and Ni/TiO_2 SMSI Catalysts*. J. Catal. **183**, 344, (1999).

[358] Lide, D. R. *CRC Handbook of Chemistry and Physics*. (CRC Press, 2005).

[359] Hommrich, J., Humann, S. and Wandelt, K. *Cadmium Underpotential Deposition on Cu(111) - In Situ Scanning Tunneling Microscopy*. Farad. Discuss **121**, 129, (2002).

[360] Feng, J., Qian, X. F., Huang, C. W. and Li, J. *Strain-engineered Artificial Atom as a Broad-spectrum Solar Energy Funnel*. Nat. Photonics **6**, 865, (2012).

[361] Najmaei, S. et al. *Electrical Transport Properties of Polycrystalline Monolayer Molybdenum Disulfide*. Acs Nano **8**, 7930, (2014).

[362] Yazyev, O. V. and Chen, Y. P. *Polycrystalline Graphene and Other Two-dimensional Materials*. Nat. Nanotechnol. **9**, 755, (2014).

[363] Huang, P. Y. et al. *Grains and Grain Boundaries in Single-layer Graphene Atomic Patchwork Quilts*. Nature **469**, 389, (2011).

[364] van der Zande, A. M. et al. *Large-Scale Arrays of Single-Layer Graphene Resonators*. Nano Lett. **10**, 4869, (2010).

[365] Jone, L. et al. *Smart Align - A New Tool for Robust Non-rigid Registration of Scanning Microscope Data*. ADV STRUCT CHEM IMAGING **1:8**, 1, (2015).

[366] Perrot, E., Humbert, A., Piednoir, A., Chapon, C. and Henry, C. R. *STM and TEM Studies of a Model Catalyst: Pd/MoS_2(0001)*. Surf. Sci. **445**, 407, (2000).

[367] Liu, D. C. et al. *Simulation of MoS_2 Crystal Structure and the Experimental Study of Thermal Decomposition*. J Mol. Struct. **980**, 66, (2010).

[368] Conley, H. J. et al. *Bandgap Engineering of Strained Monolayer and Bilayer MoS_2*. Nano Lett. **13**, 3626, (2013).

[369] Kibsgaard, J. et al. *Scanning Tunneling Microscopy Studies of TiO_2-supported Hydrotreating Catalysts: Anisotropic Particle Shapes by Edge-specific MoS_2-support Bonding*. J. Catal. **263**, 98, (2009).